Synergy of Radar, Lidar and Infrared Spectrometry to Retrieve Microphysical and Radiative Properties of Cirrus Clouds

Andreas Reichegger

Munich 2023

Synergy of Radar, Lidar and Infrared Spectrometry to Retrieve Microphysical and Radiative Properties of Cirrus Clouds

Andreas Reichegger

Dissertation
Faculty of Physics
at the Faculty of Physics
of Ludwig Maximilian University
Munich

submitted by
Andreas Reichegger
from Lörrach

Munich, October 2023

1st supervisor: Prof. Dr. Bernhard Mayer
2st supervisor: Prof. Dr. Markus Rapp
Date of submission: 30.10.2023
Date of oral exam: 11.12.2023

Synergie von Radar, Lidar und Infrarotspektrometrie zur Ableitung von Mikrophysikalischen und Strahlungseigenschaften von Cirruswolken

Andreas Reichegger

Dissertation
an der Fakultät für Physik
der Ludwig–Maximilians–Universität
München

vorgelegt von
Andreas Reichegger
aus Lörrach

München 2023

Erstgutachter: Prof. Dr. Bernhard Mayer
Zweitgutachter: Prof. Dr. Markus Rapp
Datum der Abgabe: 30.10.2023
Datum der mündlichen Prüfung: 11.12.2023

"Everybody talks about the weather, but nobody does anything about it."

Mark Twain

Abstract

Clouds are the largest source of uncertainty in climate models. Especially the feedbacks from thin ice clouds (cirrus) have a substantial effect on Earth's radiation budget. They are semi-transparent for incoming solar radiation (cooling effect), but at the same time they can trap outgoing thermal radiation (warming effect). The level of scientific understanding of how these counteracting effects will change in a future warming climate is still low. This is because of the poorly understood processes involved in modelling of ice formation mechanisms and ice cloud evolution. To narrow down these gaps, the microphysical schemes and radiation parameterisations in current climate models have to be constrained by comparisons with ice cloud observations.

Both, active (radar and lidar) and passive (infrared spectrometry) remote sensing observations of ice clouds are available to benchmark the models. While active remote sensing offers comprehensive vertical information content, passive remote sensing provides an integrated measure of the effect of clouds by exploiting radiation emitted from clouds and atmosphere together. The translation from measurements to microphysical cloud properties is accomplished by the usage of ice cloud retrieval algorithms. However, these retrievals are limited in their accuracy by crucial assumptions about microphysical properties like ice crystal shape, and by errors in the used inversion procedure.

The goal of this thesis is to use the synergy of co-located active and passive remote sensing observations to derive microphysical properties of ice clouds and to quantify all known sources of uncertainty. To achieve these tasks, a three-instrument retrieval algorithm - SynCirrus - has been developed. In this process, a radar-lidar inversion is used to derive profiles of ice particle size and ice water content. These microphysical profiles are used as input for radiative transfer calculations, to simulate a spectrum that can be compared with the measured spectrum from the infrared spectrometer. In the course of this spectral analysis, the algorithm can iterate among the relevant microphysical assumptions, to find the best matching assumptions minimizing the spectral residuals between simulation and measurement.

The SynCirrus retrieval includes consistent microphysical assumptions in the inversion and the forward radiative transfer part of the retrieval. To test the SynCirrus retrieval, three studies were performed. First, sensitivity studies of the spectral residuals identified the required data quality criteria for a successful spectral discrimination and for a characterisation of the errors of the inversion method. Second, a radar-lidar retrieval intercomparison study was conducted. Here, the inversion procedure is tested against an established other retrieval approach (VarCloud) using aircraft research flight data, indicating that for good data quality, both retrievals agreed remarkably well. Finally, in a case study using SynCirrus with all instruments at Mount Zugspitze, it was possible to bring radar, lidar and infrared radiance measurements in accordance within the provided uncertainty estimations, for the majority of the cases.

The research presented in this thesis is relevant and important for the goal to improve the microphysical description of ice clouds in climate models. The presented retrieval algorithm SynCirrus can assist to narrow down gaps in the understanding of ice clouds, by providing

high resolved and quality flagged microphysical profiles.

Zusammenfassung

Wolken sind die größte Unsicherheitsquelle bei Klimamodellvorhersagen. Insbesondere die Rückkopplungen von dünnen Eiswolken (Zirren) haben einen erheblichen Einfluss auf den Strahlungshaushalt der Erde. Sie sind halbtransparent für die einfallende Sonnenstrahlung (kühlende Wirkung), können aber gleichzeitig die ausgehende thermische Strahlung absorbieren (wärmende Wirkung). Der wissenschaftliche Kenntnisstand darüber, wie sich diese gegenläufigen Effekte in einem sich erwärmenden Klima verändern werden, ist noch gering. Dies ist zurückzuführen auf die schlecht verstandenen Prozesse bei der Modellierung der Eiskristallbildungsmechanismen innerhalb der Zirren und der Eiswolkenentstehung. Um diese Lücken zu schließen, müssen die mikrophysikalischen Schemata und Strahlungsparametrisierungen in aktuellen Klimamodellen durch Vergleiche mit Eiswolkenbeobachtungen eingeschränkt werden.

Sowohl aktive (Radar und Lidar) als auch passive (Infrarotspektrometrie) Fernerkundungsbeobachtungen von Eiswolken sind für den Vergleich der Modelle verfügbar. Während die aktive Fernerkundung einen umfassenden vertikalen Informationsgehalt bietet, stellt die passive Fernerkundung eine integrierte Messung des Strahlungseffekts von Wolken bereit, indem sie die Strahlung detektiert die von Wolken und Atmosphäre emittiert wurde. Die Übersetzung von Messungen zu mikrophysikalischen Wolkeneigenschaften wird durch die Verwendung von Ableitungsverfahren für Eiswolken erreicht. Allerdings sind diese Algorithmen in ihrer Genauigkeit begrenzt durch entscheidende Annahmen über mikrophysikalische Eigenschaften, wie die Form der Eiskristalle, und durch Fehler im verwendeten Inversionsverfahren.

Das Ziel dieser Arbeit ist es, die Synergie von aktiven und passiven Fernerkundungsbeobachtungen zu nutzen, um mikrophysikalische Eigenschaften von Eiswolken abzuleiten und alle bekannten Quellen der Unsicherheit zu quantifizieren. Um diese Aufgaben zu erfüllen, ist ein Drei-Instrumente Ableitungsverfahren - SynCirrus - entwickelt worden. In diesem Prozess wird eine Radar-Lidar-Inversion verwendet, um Profile der Eispartikelgröße und des Eiswassergehalts abzuleiten. Diese mikrophysikalischen Profile werden als Input für Strahlungstransportberechnungen verwendet, um ein Spektrum zu simulieren, das mit dem gemessenen Spektrum des Infrarotspektrometers verglichen werden kann. Im Zuge dieser Spektralanalyse kann der Algorithmus zwischen den relevanten mikrophysikalischen Annahmen iterieren, um die am besten passenden Annahmen zu finden, die die spektralen Residuen zwischen Simulation und Messung minimieren.

Das SynCirrus Ableitungsverfahren beinhaltet konsistente mikrophysikalische Annahmen im Inversions- und im Vorwärtsmodell (Strahlungstransport) des Algorithmus. Um das SynCirrus Ableitungsverfahren zu testen, wurden drei Studien durchgeführt. Erstens wurden durch Sensitivitätsstudien der spektralen Residuen die erforderlichen Datenqualitätskriterien für eine erfolgreiche spektrale Unterscheidung identifiziert, und eine Charakterisierung der Fehler der Inversionsmethode wurde erarbeitet. Zweitens wurde eine Radar-Lidar-Vergleichsstudie durchgeführt. Hier wird das Inversionsverfahren mit einem anderen etablierten Ableitungsverfahren (VarCloud) unter Verwendung von Forschungsflugzeugdaten getestet. Das Ergebnis zeigt, dass bei guter Datenqualität beide Ableitungsverfahren bemerkenswert

gut übereinstimmen. Letztlich wurde SynCirrus in einer Fallstudie mit allen Instrumenten auf der Zugspitze eingesetzt, es konnten Radar-, Lidar- und Infrarotstrahlungsmessungen innerhalb der angegebenen Unsicherheitsabschätzungen, für die Mehrheit der Fälle, in Einklang gebracht werden.

Die in dieser Arbeit vorgestellte Forschung ist relevant und wichtig für das Ziel, die mikrophysikalischen Beschreibung von Eiswolken in Klimamodellen zu verbessern. Das vorgestellte Ableitungsverfahren SynCirrus kann dazu beitragen, Lücken im Verständnis von Eiswolken zu schließen, indem es hochaufgelöste und mit Qualitätsmerkmalen versehene mikrophysikalische Profile bereitstellt.

Contents

1. Introduction

Clouds are not only beautiful to look at, they also have a big impact on humanity's everyday life by influencing precipitation rate as well as the *Earth's radiation budget* (ERB) and consequently global surface temperature. Climate models predict the increase of the surface temperature between 0.3–1.7 °C (RCP 2.6) up to 2.6–4.8 °C (RCP 8.5), based on representative concentration pathways (RCPs) for different anthropogenic greenhouse gas emissions scenarios (Collins et al., 2013, chap. 12). The difference between 0.3 °C and 2.6 °C as well as 1.7 °C and 4.8 °C may have drastic differences in the frequency of extreme weather events (Bellprat et al., 2019), sea level rise (Rahmstorf, 2010) and the actions and speed required by policymakers and political leaders to release climate protection measures. The uncertainty in global mean temperature rise predictions is closely related to clouds and their behaviour and frequency in a warming climate (Thompson et al., 2017). Therefore, clouds are a subject of great scientific interest, leading the *Intergovernmental Panel on Climate Change* (IPCC) to put a large focus on exploring their impact on Earth's climate in the last two decades:

> " ...cloud feedbacks remain the largest source of uncertainty in climate sensitivity estimates. "
>
> Randall et al. (2007, chap. 8) in IPCC Fourth Assessment Report (AR4)

Especially, the description of high-altitude ice clouds, also called *cirrus* clouds, in climate models contain large uncertainties. These clouds consist of non-spherical ice crystals with highly variable shapes, which can scatter incoming solar radiation back to space (albedo effect) and absorb and re-emit outgoing thermal radiation (greenhouse effect). This can either lead to a cooling or a warming effect within Earth's energy budget, dependent on which effect is dominant:

> " Clouds and aerosols continue to contribute the largest uncertainty to estimates and interpretations of the Earth's changing energy budget. [...] The role of thin cirrus clouds for cloud feedback is not known and remains a source of possible systematic bias. "
>
> Boucher et al. (2013, chap. 7) in IPCC Fifth Assessment Report (AR5)

> " The combined water-vapour and lapse-rate feedback makes the largest single contribution to global warming, whereas the cloud feedback remains the largest contribution to overall uncertainty. "
>
> Forster et al. (2021, chap. 7) in IPCC Sixth Assessment Report (AR6)

The interaction of clouds within the climate systems involve many complex physical processes on different scales ranging from cloud condensation nuclei (nanometre) up to evolved clouds (kilometre) during their lifecycle. Current *Global Circulation Models* (GCM) have a

horizontal resolution of about 100 km. On this scale fully simulating the evolution of a cloud which is governed by the interaction of a number of dynamical, radiative and microphysical processes can not be resolved in such large model grid boxes (Stevens et al., 2013).

To narrow down the mentioned uncertainties, GCMs will require a more realistic description of clouds in terms of more accurate *parameterisation schemes* to include important microphysical cloud processes below the resolution limit of current GCMs, e.g. cirrus-radiation interactions (Ceppi et al., 2017). These parameterisations in turn have to be calibrated with measurements. An instrument based monitoring of atmosphere and clouds can be achieved with *remote sensing* techniques (Yang et al., 2018; Mace and Berry, 2017). They will supply experimental datasets with observables which are sometimes only in a non-linear relationship to the cloud microphysical parameters. Therefore, these required microphysical parameters have to be translated from the measurement data via *cloud retrieval* algorithms (Stein et al., 2011). Future research could use these synergy retrievals to derive long-term datasets on different geographical locations, to constrain cloud parameterisation schemes in GCMs, enable theme to give more meaningful predictions of which role clouds will have in Earth's warming climate system and finally, to predict global warming even more accurately. The work in this thesis focuses on developing a retrieval algorithm (*SynCirrus*), that maps remote sensing observations to microphysical cloud parameters used in climate models.

Further information about the role of ice clouds in Earth's climate, their representation in climate models and their formation mechanisms can be found in Appendix. A, Appendix. B and Appendix. C, respectively.

1.1. State of Scientific Knowledge

Current Status and Challenges of Cirrus Cloud Observations

The instrumental monitoring of microphysical, macrophysical and optical properties of clouds can be divided into *in situ* and *remote sensing* observations. Whereas in situ sensors, on aircrafts or balloons, measure directly in a cloud, remote sensing devices, located on ground, on aircrafts or on satellites, measure cloud properties indirectly by detecting the radiation that interacted with the cloud.

In situ data are generally very precise and often treated as "ground truth", because they deliver detailed information about cirrus cloud bulk properties, like ice crystal size, ice crystal shape, ice crystal mass, ice particle size distribution (PSD) and optical parameters. The ice crystal population is characterised by the PSD and the type of ice crystal is denoted as shape or habit. The spatial sampling of in situ instruments is very poor, because data can only be collected on the flight track, and the collection of data is usually bound to a field campaign and therefore there are no continuously ongoing measurements (Lloyd et al., 2021). Comparing in situ data from different field campaigns can shed light into how ice cloud properties change with environmental conditions (McFarquhar et al., 2017a). Forward scattering spectrometer probes (FSSP) are used to estimate small ice PSDs but sometimes show overestimation of particle size (Heymsfield, 2007). Imaging sensors like optical array probes (OAP) or cloud particle imager (CPI) are often used in aircraft campaigns and can differentiate ice crystals between 100 to 200 µm or 35 to 200 µm, respectively (Baumgardner et al., 2017). Holographic methods can digitally reconstruct number densities, PSD, and sizes between 23 to 1000 µm (Fugal and Shaw, 2009). Right now, there are no universally accepted frameworks of how to process in situ measurements to ensure intercomparison. Therefore there is a need for

a general reference to summarise the most commonly used processing algorithms, including their strengths and weaknesses (McFarquhar et al., 2017a).

Passive Remote sensing devices, like radio- and *spectrometers*, measure radiation which is naturally available. Therefore, these sensors are only capable to provide an integrated measure of the effect of clouds by exploiting radiation emitted from clouds and atmosphere together. As opposed to this, active remote sensors, like *radar* and *lidar*, have their own source of radiation. They emit radiative pulses towards the cloud and measure the time and intensity, after the emitted pulses get reflected back by ice crystals. The magnitude of the returned pulse and their time of flight contains information about the type of scattering particle and their location. A relevant advantage of active sensors is, that their measured signals are range-resolved and can shed light into vertical structure of cirrus cloud properties (Lynch et al., 2002). Due to their different operating wavelengths, they are sensitive to different cloud particle sizes and can provide complementary information from certain parts of the PSD. In detail, the radar is operating on long wavelengths in the millimeter range and is sensitive to the 6^{th} moment of the PSD, whereas the lidar is operating on shorter wavelengths in the nanometer range and is sensitive to the 2^{nd} moment of the PSD. Here, "moment" refers to a weighted integral of the PSD. Based on radar and lidar data it is possible to retrieve important microphysical cloud parameters like the effective ice crystal size (also called effective radius R_{eff}) and the ice water content (IWC). Roughly speaking, R_{eff} is a measure for the size of cloud particles, and IWC is a measure for the amount of cloud particles. These quantities are very sensitive to describe the interaction of radiation with a cloud state in a climate model and therefore necessary for radiative transfer calculations (Lynch et al., 2002).

Satellite based cloud observing platforms, like the aligned A-Train constellation (cloud profiling radar (CPR), Cloud-Aerosol Lidar with Orthogonal Polarisation (CALIOP), Moderate Resolution Imaging Spectroradiometer (MODIS)), allowed for the first time, to reconstruct distributions of upper tropospheric cirrus across the globe (Stephens et al., 2002; Deng et al., 2013). Besides their expansive global view, the additional advantage is that measuring from space, these sensors are not too dependent on atmospheric conditions in the lower troposphere. In this region the highest concentration of aerosols and water vapour occurs. For resolving inhomogeneous cirrus clouds, the difference and size in footprints of radar and lidar can be a challenge (Stephens et al., 2002). To address these footprint shortcomings as result of the formation flying, the single platform EarthCare, launch is scheduled for 2024, will allow for a better co-location of the measurements in order to improve the data quality for synergistic retrieval algorithms (Illingworth et al., 2015). Among other products, EarthCare will supply data for vertical profiles of IWC and ice particle size to enable a deeper and more accurate insight of the role of cirrus clouds in modulating the global shortwave (SW) and longwave (LW) radiation energy flows (Mroz et al., 2023; Mason et al., 2023).

Satellite based observations provide large length scales, horizontal resolution of about 1000 m, but are limited to temporally resolve cloud processes and no observations at all from high latitudes are possible ("pole hole"). For this task, ground-based observations with vertical resolutions of about 60 m, can deliver long-term data on a continuous basis with self-operating systems. But, the biggest advantage of ground-based over satellite observations is the high temporal resolution of long-term data for a given geographical location. They furthermore can provide datasets for thin cirrus clouds, with horizontal resolutions below 300 m (Bühl et al., 2017). There are already long-term monitoring programs, like the Atmospheric Radiation Measurement (ARM) program (Miller et al., 2016) , Cloudnet (Illingworth et al., 2007b) and the Aerosol, Clouds and Trace Gases Research Infrastructure (ACTRIS) (Häme

et al., 2018), that provide ground-based remote sensing data on an operational basis.

Due to their operating principle and used wavelengths, the remote sensing instruments are sensitive to different cloud properties. Unfortunately, all of these devices have some shortcomings in measuring cirrus parameters. For example, radars are more sensitive to ice crystal size (6^{th} moment of PSD, Heymsfield et al. (2014)), but cannot detect small ice crystals, whereas lidars are more sensitive to IWC and extinction (2^{nd} moment of PSD,Vaughan et al. (2004)), but the lidar signal suffers from strong attenuation in optically thick ice clouds, and spectrometers can only give information about integrated cirrus properties (Turner, 2005). To overcome these obstacles, at least partly, *sensor synergy* considerations by combination of data products from different instruments, offer great potential to retrieve cirrus parameters (Ewald et al., 2021). Especially cloud regions where radar and lidar signals are simultaneously available, allow a well constrained retrieval of ice crystal size and IWC (Donovan and van Lammeren, 2001).

Future steps in remote sensing will try to investigate cirrus cloud evolution by observing heterogeneous ice formation in ice and mixed-phase clouds. This task requires high demands from all kind of available instruments and data processing. Due to the turbulent environment of cirrus clouds in which ice particles are formed, the identification of ice-formation processes becomes complicated. Especially, data from active sensors can be distorted from spectrally resolved measurements (Bühl et al., 2017). Another important questions is how cirrus properties differ with cloud dynamics and on different geographic locations. Due to the lack of missing satellite data, a field program executed in the Antarctic to monitor cirrus microphysical properties is needed urgently (Heymsfield et al., 2017).

The Inverse Problem and Cirrus Cloud Retrievals

There are some prognostic quantities, like temperature, pressure or humidity that can be measured directly by radiosondes and the comparison with the corresponding model quantities is straightforward. However, there are some cloud parameters that can not be measured directly. For example, important microphysical cloud parameters are the effective ice crystal size (effective radius R_{eff}) and the ice water content (IWC).

Fortunately, there are some remote sensing observables like *radar reflectivity* and *lidar backscatter signal* that are, at least, non-linear functions of these cloud parameters. However, this circumstance demands an additional need: *ice cloud retrieval algorithms* to translate these measurement observables back to microphysical cloud parameters to serve as a data basis for parameterisation schemes. In principle, a cloud retrieval is a physical model, that inverts the measured effect of ice clouds on radiation to gain information about the actual cloud properties (e.g. ice crystal habit). Additional information as input for the retrieval can be used from several active and passive instruments with different spectral channels to retrieve certain cloud parameters. The procedure is always the same, first the identification (Yorks et al., 2021) of the cloud and then the retrieval of its microphysical properties.

The impact an ice cloud consisting of different ice crystals will have on the radiation field can be compared with a bear leaving tracks, as illustrated in Figure 1.1. The task of a retrieval would be to reconstruct the specific bear based on its tracks. Without any additional information and a realistic physical model this would be a hopeless endeavor, because the inverse problem is strongly ill-posed. Many possible "bears" could have caused the tracks. But a realistic physical model, that includes information about typical depths and sizes of bear tracks, can constrain the possibilities to realistic bears. However, if a polar bear and

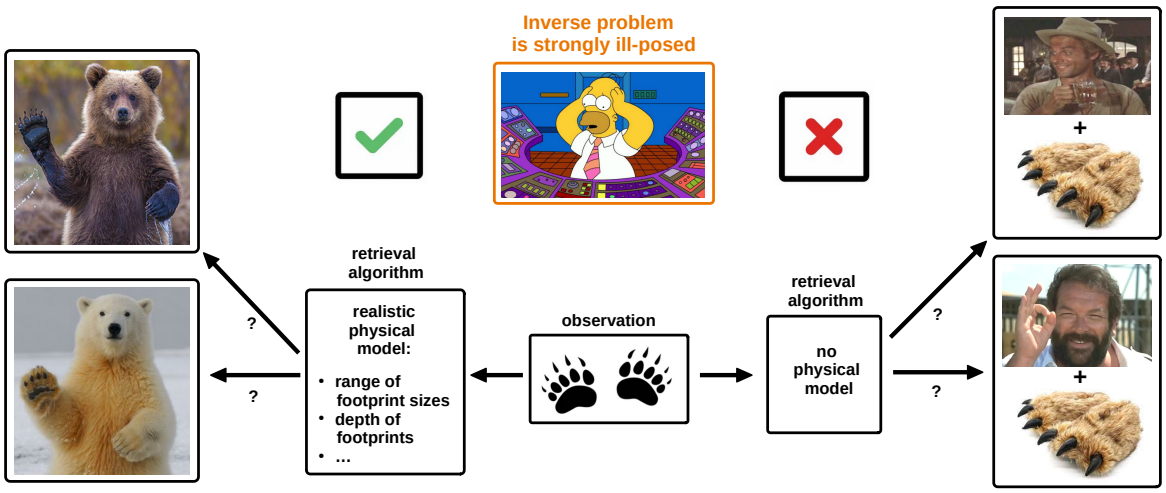

Figure 1.1.: The inverse problem in remote sensing can be compared with reconstructing a bear from its tracks. An inverse model will need additional information (e.g. more measurements) for its retrieval space and a numerical stable inversion to sample realistic physical configurations, that could have caused the tracks. If both is missing, the retrieval may tend to return very unrealistic "bears". That is the main problem in remote sensing, that multiple, in some circumstances, very different cloud properties can produce the same set of remote sensing observations. Idea is based on (Bohren and Huffman, 2008) and (Mayer, 2010).

a brown bear would have the same weight and footprint size, the physical model can not distinguish between them. Now additional information like in situ data are required to solve the retrieval unambiguously. For ice clouds, the measurable tracks would be remote sensing observations. In this case, a realistic microphysical model would add physical knowledge on scattering properties, particle size distributions, ice crystal habits and roughnesses of ice cloud particles, and their interaction with radiation.

For example, the combination of radar and lidar data into one retrieval has an advantage: because of their different wavelengths, they are sensitive to different particle size ranges and two simultaneous available profiles allow for a well constrained retrieval of two microphysical properties like IWC and R_{eff}. In contrast, retrievals only exploiting the radar signal (Hogan et al., 2006c) could retrieve misleading properties and overestimate the particle size if the lidar constraint is missing. The reason is the D^6 dependence of the radar reflectivity, which means that only a few small but large ice crystals can easily dominate the full radar signal from that range gate (Field et al., 2004).

First steps in synergistic radar and lidar retrievals were made by Intrieri et al. (1993) and extended by Donovan and van Lammeren (2001) and Tinel et al. (2005). All approaches had in common that their methods are only applicable in cloud regions where both, radar and lidar signals are available. Delanoë and Hogan (2008) overcome this specific limitation with an optimal estimate framework. In cloud regions where, e.g., only radar signals are available other information, like a temperature-dependent a-priori climatology from an in situ aircraft database is used as a constraint.

Radar-lidar retrievals can be extended by the use of passive instruments like infrared spectrometer with high-spectral-resolution for *radiance* observations (Blanchard et al., 2017; Ewald et al., 2021). The retrieved microphysical properties from the radar-lidar inversion can serve as input parameters for radiative transfer calculations. These model-computed radiances can be compared with the observed cloudy radiances by the spectrometer, to find the best match in terms of the assumed cirrus properties.

The challenge of retrieval development lies in carefully consideration of errors and uncertainties that are introduced by different technical sensitivities, by differences in sampling microphysical assumptions and the use of the method itself. This is a challenge due to the high degrees of freedom inherent in cirrus cloud nature, resulting in a large parameter space a retrieval has to sample. Ice crystal size and IWC themself are functions of other cirrus parameters like ice crystal habit, PSD or ice crystal surface roughness and all these quantities can not be measured directly. Furthermore, if in situ data from the corresponding cirrus cloud are not available, they all have to be assumed by the retrieval algorithm. This can cause large biases, as analysed by Stein et al. (2011) in retrieval intercomparison studies. Errors in the retrieved parameters, random or systematic, could be caused by several sources, like limitations of instrument performance (e.g. calibration, pulse intensity, field of view), physical assumptions in radiative transfer (e.g. ice crystal single scattering properties), as well as, uncertainties in the used retrieval inversion method (e.g. boundary value problem, lidar ratio) and all of them need a careful consideration.

Needs in Ice Cloud Research

In climate models, the cloud feedback is still the largest source of intermodel spread in climate estimations (Ceppi et al., 2017). Especially the feedback from thin cirrus clouds causes large uncertainties (Forster et al., 2021), due to the not well understood processes in modelling of ice formation and evolution (McFarquhar et al., 2017b). To tackle these obstacles, two main **research needs** can be deduced:

- Development of parameterisation schemes for shortwave and longwave radiative properties of ice clouds, including assumptions about ice crystal habit, particle size distribution (PSD) and surface roughness.

Climate models usually use ice water mixing ratio as a prognostic variable, and therefore they have to parameterize particle effective size R_{eff} in order to obtain extinction β_{ext} for radiation calculations. Ice cloud bulk optical single scattering properties can be parameterised as function of effective radius (R_{eff}) and ice water content (IWC) for different spectral ranges (Hong et al., 2009). The development of such a parameterisation requires data of spatial and temporal high-resolved profiles of R_{eff} and IWC. These parameterisations can be used in future general circulation models (GCM) for flux estimations, to gain a better estimation of the radiative cooling or warming effect of ice clouds in a future warming climate (Van Diedenhoven and Cairns, 2020; Ren et al., 2021).

- Constraining process rates in microphysical schemes, used in the dynamical core of a GCM to predict the IWC.

Microphysical parameterisation schemes in climate models try to represent the physical behavior of different hydrometeor populations and their effects on weather and climate. These

schemes consist of a set of parameterised rate equations that try to represent the microphysical processes impacting cloud and precipitation particles (Morrison et al., 2020).

The desired containment can be achieved by comparisons of climate models with spatiotemporally high-resolved microphysical profiles retrieved from observational data and will help to close fundamental gaps in knowledge of ice cloud physics. Because of the complex structure of ice crystals, especially ice-phase processes like vapor diffusional growth, melting, and aggregation cause large uncertainties. Furthermore, IWC-R_{eff} correlation analysis can improve the knowledge of ice cloud formation processes (Liou et al., 2008).

1.2. Scientific Objectives and Outline of this Work

To narrow down the mentioned gaps in the understanding of ice clouds, more temporally and vertically high resolved observational data of recorded ice clouds are required to serve as a solid data basis to develop parameterisations. The **scientific objective** of this work is:

Scientific objective: Development of a synergistic three-instrument (radar, lidar and infrared spectrometer) retrieval algorithm - *SynCirrus* - for the mapping of radar, lidar and infrared spectrometer measurements to microphysical properties (ice water content IWC and effective radius R_{eff}), including a comprehensive uncertainty consideration.

Based on existing radar-lidar retrieval approaches (Donovan and van Lammeren, 2001; Tinel et al., 2005), this includes the development of preprocessing methods like cloud masking lidar signals by a wavelet-analysis, a correction for lidar multiple scattering effects, radar signal attenuation by atmospheric gases and screening lidar signals for numerical stability in an inversion procedure. Furthermore, the identical microphysical model, including assumptions about PSD and ice crystal habit, will be incorporated consistently in the radar-lidar inversion procedure, as well as in the forward radiative transfer calculations, a part missing in older approaches.

The structure of the SynCirrus algorithm is summarised in Figure 1.2 and was used on synthetic and real data with the aim to answer the following (technical) **research questions:**

Research questions 1: What are the accuracy requirements to constrain the microphysical properties of ice clouds, based on synergistic measurements made from radar, lidar and infrared spectrometry?

This is linked to climate models. It would be very beneficial, if the used microphysical schemes, especially the involved rate equations, could be constrained by observational data gained from cloud retrievals to reduce uncertainties. For ice clouds there is a huge ambiguity because of the variety of different ice crystal habits, roughnesses and PSD parameter (type, modality and shape). Therefore, the magnitude of the different microphysical properties should be explored and compared with the occurring uncertainties, to decide if they can be retrieved unambiguously with a three-instrument retrieval.

Research questions 2: What kind of uncertainties can occur in the retrieval process, and how do these uncertainties impact the interpretation of the retrieved results?

There is a great need to incorporate a rigorous uncertainty quantification treatment related to ice density, habit, and PSD into cloud retrievals. In general, there is an outstanding need to quantify robustly the uncertainty of any observation used to inform microphysical schemes, as stressed by Morrison et al. (2020). In detail, how do quantities like instrument calibration, microphysical assumptions, retrieval techniques and atmospheric state composition influence the retrievable information content and what is the order of magnitude of the different uncertainties. Finally, this leads to the identification of necessary prerequisites (data quality, atmospheric conditions, additional instruments etc.) to retrieve microphysical properties more accurately with lower errors.

Thesis Structure

This thesis is organized as follows: Chapter 2 will give an introduction into the relevant microphysical cloud parameters, radiative transfer quantities and the basic questions governing active and passive remote sensing instruments. Chapter 3 gives an overview of the involved measurement devices. Their parameters and uncertainties will be discussed and corresponding data processing methods, like lidar cloud masking, radar signal attenuation and the exploitation of spectral microwindows will be presented. Furthermore, the different forward model solvers for lidar and radiative transfer are explained. Different methods for inverting the lidar equation will be presented and discussed. An overview of the applied corrections and their implications is giving in the end of this chapter. In the following Chapter 4, the framework to be developed will be characterised, and the uncertainties are estimated with a synthetic model. This is followed by example applications on real data: A radar-lidar retrieval intercomparison with the VarCloud retrieval algorithm (Delanoë and Hogan, 2008) on *NARVAL-I* data from the HALO aircraft research flights in the North Atlantic (Stevens et al., 2019) to test the inversion performance, the most crucial part of the retrieval. The last part of this chapter investigates the application of the full three-instrument retrieval on data from an instrumentation based at Environmental Research Station (*Umweltforschungsstation Schneefernerhaus - UFS*) on mount Zugspitze in Germany (2675 m a.s.l.). The Zugspitze is a unique site for the application of ice cloud retrievals, because it offers extraordinarily dry conditions to provide a high atmospheric transparency to observe cirrus clouds (Sussmann et al., 2016). Finally, Chapter 5 gives a discussion of the results and uncertainties. This is followed by a summary and conclusion about the findings of this thesis in Chapter 6, and ideas for future extensions are given in Chapter 7.

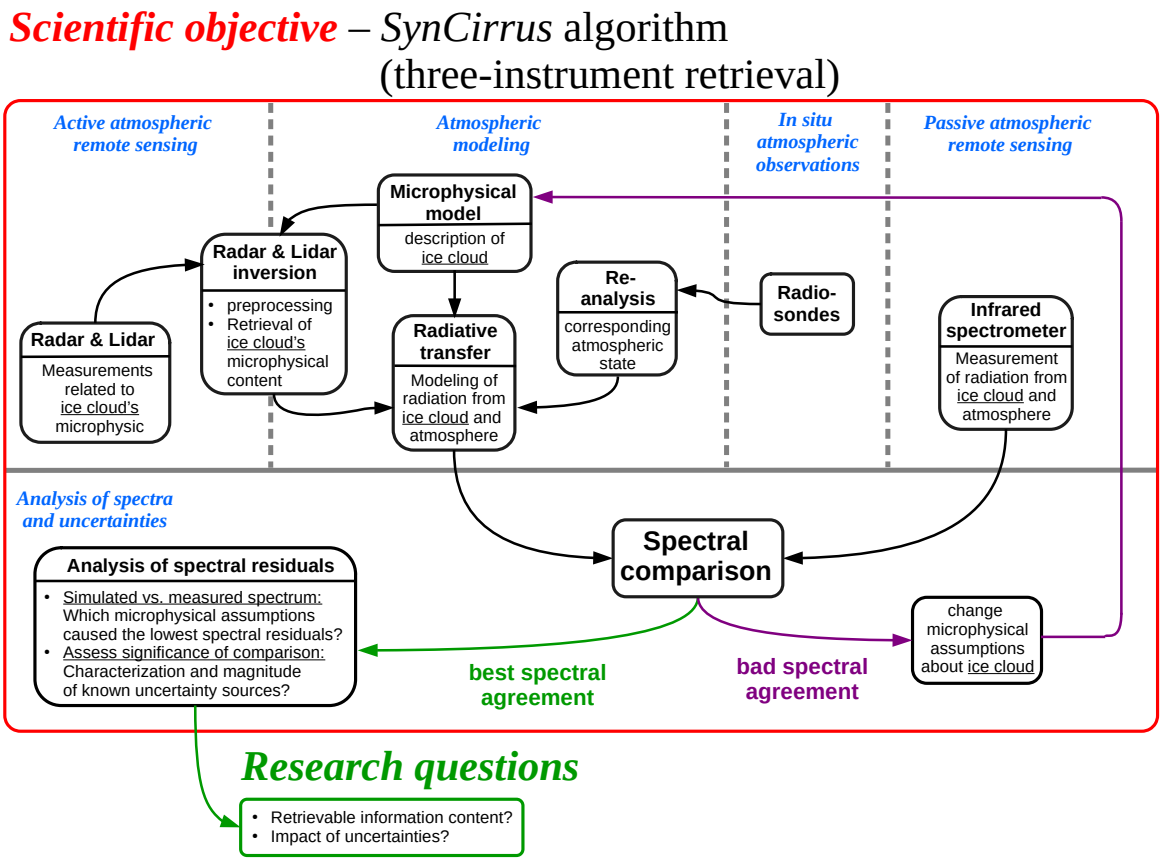

Figure 1.2.: Overview SynCirrus algorithm: Prerequisite is, that the active and passive devices are located at the same site and measuring at the same time. The combined radar and lidar measurements of a cirrus cloud are inverted to supply microphysical profiles. They will be used alongside with background profiles of the atmospheric composition, from re-analysis models, and both serve as input quantities for radiative transfer calculations of the downwelling infrared radiances at the altitude of the infrared spectrometer, which supplies measured spectra temporally consistent with the radar-lidar measurements. Now, both spectra can be compared and evaluated mainly in the mid-infrared atmospheric window, where the cloud radiative effect is observable. Minimizing the spectral residuals (measured minus simulated spectrum) via iterating the possible retrieval parameter space for microphysical assumptions will return the best match in terms of cloud properties. The significance of such a comparison would first have to undergo a careful uncertainty consideration to analyse which properties can be discriminated from each other.

2. Theory

In this chapter, the theoretical foundations for this thesis will be introduced. This work is about the retrieval of microphysical properties from ice cloud observations based on sensor synergy from active and passive remote sensing devices. Therefore, a short introduction of how to parameterise ice cloud properties is given. Furthermore, it is sketched how these properties are used as input for radiative transfer (RT) calculations of spectral radiances. The basic working principles and sensitivities of the used active and passive sensors will be mentioned and how they are linked to the microphysical cloud properties will be explained.

The chapter mainly follows Doviak and Zrnić (1993); Lynch et al. (2002); Wallace and Hobbs (2006); Weitkamp (2006); Lohmann et al. (2016); Liou and Yang (2016) and Siebesma et al. (2020).

2.1. Radiative Transfer

This section will introduce the underlying theory, how to simulate measurement observables, like downwelling thermal spectral radiances from cirrus clouds. Thermal downwelling spectral radiance is the physical observable a ground-based passive remote sensing device, like a zenith looking infrared spectrometer would record, and the SynCirrus algorithm will use such an infrared spectrometer (Knuteson et al., 2004a). Such a device would measure the radiation emitted from ice crystals within cirrus clouds, as well as radiation emitted from absorbing greenhouse gases. Therefore, following characteristics are considered:

- **Light scattering and absorption by atmospheric particles (ice crystals):** Classical description based on solving the macroscopic Maxwell equations and approximations for oscillating dipoles that are excited and then re-radiate.
- **Absorption and emission of photons by atmospheric gas molecules:** Quantum mechanical description of interacting molecules and photons via continuum transitions as well as electronic, vibrational and rotational line transitions. Based on spectroscopic laboratory measurements for absorption cross-sections.

The following description is limited to an one-dimensional geometry (1D) and 3D effects are neglected. Polarisation is neglected because the used interferometer spectra are not sensitive to polarisation, so there is no need to simulate polarisation effects (Knuteson et al., 2004a). Further details on the used approximations are summarised in Table 3.7 and Table 3.8, The goal of this section is rather to introduce the *radiative transfer equation*, which governs how the radiation field changes in space due to scattering, absorption, transmission, reflection and emission processes in planetary atmospheres.

This section mainly follows (Petty, 2006), (Lynch et al., 2002), (Stevens et al., 2019) and (Liou and Yang, 2016).

2.1.1. Basic Radiative Quantities

Radiative Properties

The energy of electromagnetic radiation, as measured by radiometry, is called radiant energy Q with unit [J]. The radiant flux or radiant power Φ is the radiant energy reflected, emitted, transmitted or received per unit time, and defined as $\Phi = \mathrm{d}Q/\mathrm{d}t$ with unit $[W]$. For applications used in this thesis, the knowledge of two radiation quantities is required. The first is the *irradiance*

$$E = \frac{\mathrm{d}Q}{\mathrm{d}A\ \mathrm{d}t} \qquad [\mathrm{W\,m^{-2}}] \ , \tag{2.1}$$

which describes the energy flux on a flat surface, e.g. specific receiver of a detector, per unit area and unit time. The second quantity is the **spectral radiance**

$$L_\lambda = \frac{\mathrm{d}Q}{\mathrm{d}A\ cos\Theta\ \mathrm{d}\Omega\ \mathrm{d}\lambda\ \mathrm{d}t} \qquad [\mathrm{W\,m^{-2}\,sr^{-1}\,nm^{-1}}] \ , \tag{2.2}$$

taking into account the direction of light propagation (Θ, ϕ). This definition quantifies radiation fully without sensor-specific information, where $\mathrm{d}\Omega = sin\Theta \mathrm{d}\phi \mathrm{d}\Theta$ is the unit solid angle and the area A is defined to be perpendicular to the propagation direction of the light beam, like described in Mayer, B. (2009, table 1).

Radiation Laws

Every material body emits thermal radiation as function of its temperature. This holds as well for atmospheric gases and particles. According to the second law of thermodynamics, where material bodies exchange energy until they are in a thermal equilibrium, the absorptivity α_λ and emissivity ϵ_λ will be equal for a material body in thermodynamic equilibrium. α_λ and ϵ_λ are defined as

$$\alpha_\lambda = \frac{\text{absorbed radiant power}}{\text{incoming radiant power}} \tag{2.3}$$

$$\epsilon_\lambda = \frac{\text{radiant power of actual material body}}{\text{radiant power of ideal black body}} \ , \tag{2.4}$$

and both can take values between 0 and 1, where $\alpha_\lambda = 1$ and $\epsilon_\lambda = 1$ describe an ideal black body.

Kirchhoff (1866) concluded for a body of any arbitrary material, that absorbs and emits thermal radiation in thermodynamic equilibrium, the emissivity is equal to the absorptivity:

$$\epsilon_\lambda = \alpha_\lambda \ . \tag{2.5}$$

This relation is known as *Kirchhoff's law of thermal radiation*. It describes, that an atmospheric gas or particles only can emit thermal radiation in spectral areas where it has absorption-lines or bands.

Planck's radiation law describes the spectral density of electromagnetic radiation emitted by a black body in thermal equilibrium (Planck, 1900)

$$B(\lambda, T) = \frac{2hc^2}{\lambda^5} \frac{1}{e^{\frac{hc}{\lambda k_B T}} - 1} \qquad [\mathrm{W\,sr^{-1}\,m^{-3}}] \ , \tag{2.6}$$

which describes the spectral radiance of a body with wavelength λ at absolute temperature T, and where $k_B = 1.380 \times 10^{-23}\ \mathrm{J\,s^{-1}}$ is the Boltzmann constant and $h = 6.626 \times 10^{-34}\ \mathrm{J\,s}$ is the Planck constant. Integrating Planck's law over half space and for all wavelength yields the irradiance emitted by a black body, and is known as *Stefan-Boltzmann's law*,

$$E = \int_0^{2\pi} \int_0^{\pi/2} \int_0^{\infty} B(\lambda, T) \cos\Theta \sin\Theta \mathrm{d}\phi \mathrm{d}\Theta \mathrm{d}\lambda = \sigma T^4 \qquad [\mathrm{W\,m^{-2}}]\ , \tag{2.7}$$

where $\sigma = 5.670 \times 10^{-8}\ \mathrm{W\,m^{-2}\,K^{-4}}$ is the Stefan-Boltzmann constant. This law describes the power radiated from a black body as function of its temperature.

The attenuation of radiation at wavelength λ, caused by absorption and scattering along a pathway s, is related to the properties of a specific material via *Beer–Lambert–Bouguer law*

$$L_\lambda(s) = L_\lambda(0) e^{-\int_0^s \beta_{\mathrm{ext},\lambda}(s')\mathrm{d}s'}\ . \tag{2.8}$$

The fraction of incident radiation, that is transmitted through the same material sample is called *transmittance* T, and is given by

$$T = \frac{L_\lambda(s)}{L_\lambda(0)} = e^{-\tau}\ , \tag{2.9}$$

where τ is the optical depth of the material.

2.1.2. Composition of Earth's Atmosphere

Solar and Terrestrial Spectrum

In dependence on their wavelength, electromagnetic radiation can be classified like shown in Table 2.1. For the most remote sensing applications it is useful to treat solar and thermal radiative transfer separately, because they only overlap in a small wavelength interval. As shown in Figure 2.1, shortwave solar irradiance arriving at Earth's surface is relevant between 0.25 µm to 4 µm, whereas longwave thermal irradiance, emitted be the surface, has a significant amount between 4 µm to 100 µm. The red area, represents the shortwave (SW) solar radifluxes a zenith-looking sensor would observe at the surface, wheres as the pink area describes the longwave (LW) thermal fluxes, emitted from the surface, a nadir-looking sensor would measure at Top Of Atmosphere (TOA). The precise position of the absorption bands in the lower panel of Figure 2.1, depends on the chemical properties of the atmospheric gases. It is clear noticeable, that water vapour is the strongest greenhouse gas, followed by carbon dioxide and various other minor greenhouse gases. Furthermore, Rayleigh scattering, responsible for the blue sky, has some effect on incoming SW radiation. In summary, up to 30% of the incoming solar radiation is captured or redistributed by the aforementioned processes. In contrary to this, greenhouse gases can capture up to 80% of the outgoing thermal radiation (Stephens et al., 2012).

Molecular Gases

Earth's atmosphere contains two types of gases, those with almost constant concentrations and those with a variable concentration. The group of constant gas concentrations include molecules from nitrogen (N_2, 78.084 %), oxygen (O_2, 20.948 %) and argon (Ar, 0.934 %) and

Table 2.1.: Classification of electromagnetic radiation according to Stamnes et al. (2017) and DIN5031 (1984)

Subregion	Range	Main Characteristics
X rays	$\lambda < 10\,\text{nm}$	Photoionizes all thermosphere species
UV	$10\,\text{nm} < \lambda < 400\,\text{nm}$	Processes like photo-ionization/dissociation
VIS	$400\,\text{nm} < \lambda < 700\,\text{nm}$	Scattered by clouds, aerosols, and molecules
Near IR	$0.7\,\mu\text{m} < \lambda < 3.0\,\mu\text{m}$	Absorbed by O_2, H_2O, CO_2 in vibrational bands
Mid IR	$3.0\,\mu\text{m} < \lambda < 50\,\mu\text{m}$	Absorbed by O_2, H_2O, CO_2 in vibrational bands. Atmospheric window (used in remote sensing)
Far IR	$50\,\mu\text{m} < \lambda < 1000\,\mu\text{m}$	Absorbed by O_2, H_2O, CO_2 in vibrational bands

in total they represent 99.96 % of the dry atmosphere by volume, and have almost constant values up to altitudes of about 60 km.

Then, there are carbon dioxide (CO_2), whose concentration is increasing by about 0.4 % per year as a consequence of fossil fuel combustion, absorption and release by the oceans and of photosynthesis. Another greenhouse gas, methane (CH_4), has been increasing by, 1 % to 2 % per year, due to a larger biogenic emission associated with rising human population.

Water vapor (H_2O), is a highly variable gas and the strongest greenhouse gas in Earth's atmosphere, as indicated in Figure 2.1. The H_2O concentration varies significantly in time and space, because it is impacted by the local hydrological cycle by evaporation, condensation, and precipitation, as well as by large-scale transport processes. Water vapor concentrations have a strong temperature dependence, and more than 50 % of the total amount is concentrated below 850 hPa.

Therefore, radiance simulations on the ground require knowledge of the vertical concentration of these gases. Due to the low variability of the dry components of the atmosphere, it is sufficient to fall back on some predefined standard atmospheres for certain latitudes (Anderson et al., 1986). In contrary to this, for water vapour as a highly variable gas and the strongest absorbing greenhouse gas, current profiles from re-analysis data or even better from radiosonde measurements are required.

2.1.3. Interaction of Light with Atmospheric Particles

Interaction of light with atmospheric particles, could for example take place via scattering with ice crystals and aerosols, or via absorption with greenhouse gases. Physically, light scattering is a process, where a particle in the pathway of an incident electromagnetic wave, will take energy from that wave and re-radiates this energy in all directions, leading to a combination of incident wave and scattering field. The exact space-time propagation of the incident and scattered wave will be obtained by solving Maxwell's equations, but analytic solutions, like *Mie-theory* (Mie, 1908), can only be obtained for specific particle geometries (such as spheres, cluster of spheres, infinite cylinders). For more complicated particle geometries, like ice crystals, only approximate solutions are available, see Table 2.2. It is useful to distinguish the different methods, via comparing the relative size of a scattering particle with the wavelength of the incident wave and with the particle dimension. Therefore, the size parameter is a helpful quantity

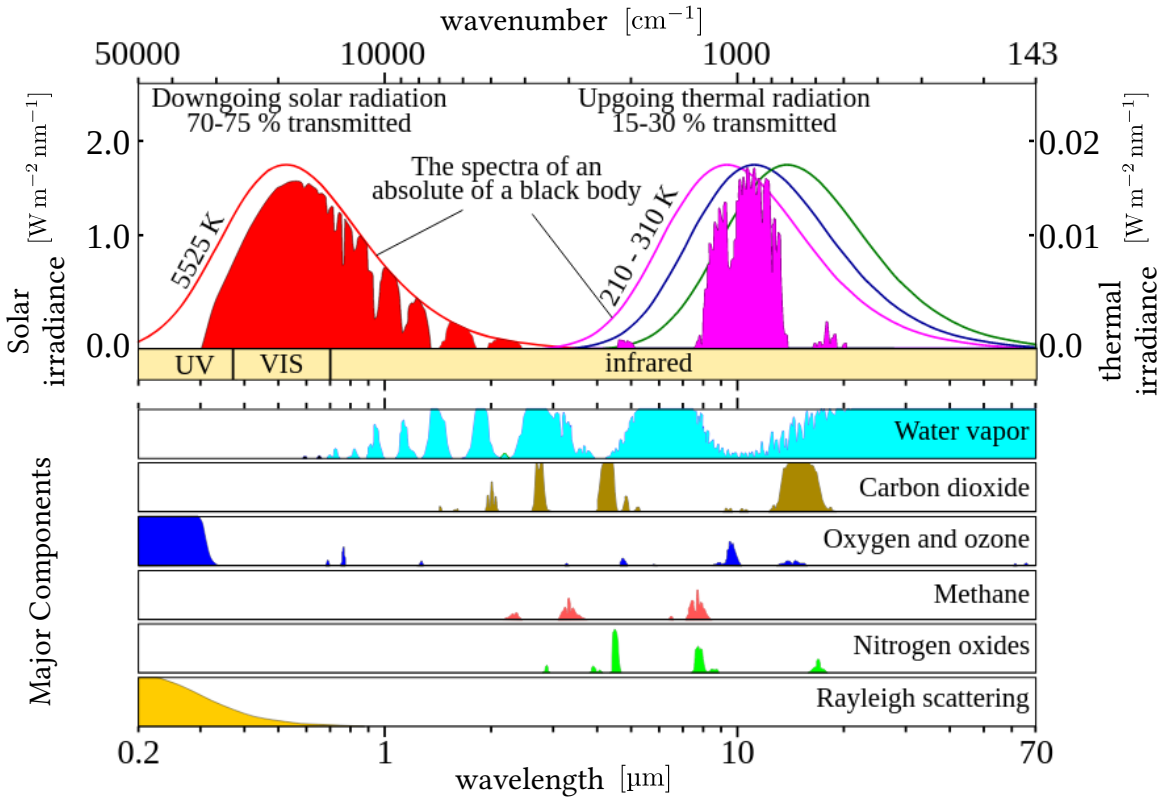

Figure 2.1.: (Top panel) Radiative transfer clear-sky simulation, that shows the effect of molecular absorption bands in Earth's atmosphere on both, incoming solar radiation and outgoing thermal radiation at the Earth's surface. Furthermore, the black body Planck curve for radiation emitted from Sun's photosphere (T≃5754 K) and three representative curves for Earth's surface temperature (T≃210 K to 310 K) are shown. The peak of the thermal spectra are normalized with reference to the solar spectral peak. (Lower panel) Individual absorption spectra for major greenhouse gases and Rayleigh scattering. Figure taken and modified from Wikipedia contributors (2022).

$$\chi = \begin{cases} \frac{2\pi r}{\lambda} & \text{spherical scatterer} \\ \frac{\pi D_{\max}}{\lambda} & \text{non-spherical scatterer} \end{cases} \tag{2.10}$$

with particle radius r and maximum particle dimension $D_{\max}$. For aspherical particles like ice crystals, the definition of a size measure is not straight forward, hence size is described as maximum dimension of an ice crystal $D_{\max}$ and for simplicity will be denoted as D in the following. Radiation which is scattered by only one localised scattering particle, is called *single scattering*. Using a radiative transfer solver like DISORT for a grid-box containing molecules, aerosols and clouds, the single scattering properties would be provided as a linear combination (Stamnes et al., 1988). In a scattering volume with many particles, light can undergo many scattering events and is called *multiple scattering*. In the following section it will be shown, how to take out multiple scattering calculations with *radiative transfer* by using *single scattering properties*, gained from methods like Mie-theory. In order to take this out, following limitations are applied, according to Hansen and Travis (1974); Liou and Yang (2016); Mishchenko (2018):

- Only *elastic scattering* processes are considered. Atmospheric scattering and absorption processes are usually considered to preserve the light frequency of the interacting wave.
- The scattering by one particle is called *independent scattering*, when the scattering process is not affected by the presence of surrounding particles. This can be assumed, because the number density of ice crystals in cirrus clouds is relatively low, and they are separated from each other by distances, much larger than their size. The independence of scattering by samples of ice crystals, leads to that a scattering event at one ice crystal does not interfere with one at another ice crystal. As a consequence, scattered intensities can be added without to regard the phases of the individual scattered waves. Thus, bulk optical properties can be obtained by a weighted mean of single particle properties.

Spherical Scatterers

Mie theory, sometimes called Lorenz-Mie theory or Lorenz-Mie-Debye theory, provides an analytic solution to the absorption and scattering of light by small spherical, circular cylindrical, and spheroidal particles of arbitrary size and refractive index (Mie, 1908). For an isotropic homogeneous sphere, the electric field of the scattered radiation $\mathbf{E}_{\text{sca}}$ at a distance R from the particle (in the far-field) can be represented by (Hansen and Travis, 1974)

$$\mathbf{E}_{\text{sca}} = \frac{e^{ik(z-R)}}{ikR} \begin{pmatrix} S_1(\Theta) & 0 \\ 0 & S_2(\Theta) \end{pmatrix} \mathbf{E}_{\text{inc}} \quad , \tag{2.11}$$

where $\mathbf{E}_{\text{inc}}$ is the incident field, which propagates into positive z direction and Θ is the scattering angle. The scattered field is an outgoing spherical wave and has an angular intensity distribution. The information about the intensity distribution is stored into the Müller Matrix elements $\mathbf{S}_{\text{i}}$. The matrix will be calculated by expanding the electromagnetic field in spherical basis functions. The key point of the Mie-theory is the computation of coefficients a_n and b_n with recursion relations. Finally, the scattering and extinction efficiency can be deduced from them (Hansen and Travis, 1974)

Table 2.2.: Computational methods to calculate single-scattering properties for atmospheric particle scattering (Petty, 2006; Wriedt, 2009; Baran, 2012).

Computation Method	Size Parameter χ	Comment
Geometric optics	> 2000	Approximate solutions to Maxwell's
Improved geometric optics method (IGOM)	> 20	equations based on ray tracing.
Mie theory	$0.2 - 2000$	Solves Maxwell's equations for elastic scattering on spherical particles (e.g. water droplets).
Finite-difference time-domain (FDTD)	< 20	Solves Maxwell's equations for elastic scattering on particles of arbitrary
Amsterdam discrete dipole approximation (ADDA)	< 50	shape (e.g. ice crystals).
T-matrix	< 20	
Rayleigh scattering	$0.002 - 0.2$	Asymptotic approximation of elastic dipole scattering (e.g. molecules).

$$Q_{\text{sca}}(\lambda, D) = \frac{2}{\chi^2} \sum_{n=1}^{\infty} (2n+1)(|a_n|^2 + |b_n|^2) \tag{2.12}$$

$$Q_{\text{ext}}(\lambda, D) = \frac{2}{\chi^2} \sum_{n=1}^{\infty} (2n+1)\Re(a_n + b_n) \ . \tag{2.13}$$

The scattering and absorption efficiencies Q_k are related to their cross-sections σ_k via

$$Q_{\text{ext/abs}}(\lambda, D) = \frac{\sigma_{\text{ext/abs}}(\lambda, D)}{\sigma_{\text{geo}}(D)} \ , \tag{2.14}$$

with the geometrical cross-section $\sigma_{\text{geo}} = \pi(D/2)^2$ and particle diameter D. Physically, the infinite series can be interpreted as a multipole expansion of the scattered light and a_n/b_n stands for electric/magnetic multipol radiation. With Q_{sca}, Q_{ext} and the single scattering properties, which can be calculated from the Müller or transition matrix elements $\mathbf{S}_{\text{i}}$, all the relevant input quantities, to take out Mie calculations, are known.

In Figure 2.2, Mie calculations for spherical ice particles are illustrated over a wide range of particle sizes.

Non-Spherical Scatterer

The aforementioned theory can only be used to calculate optical input properties for radiative transfer calculations in water clouds with spherical cloud droplets. Although, there were some approaches to treat ice crystals with various "equivalent" sphere approaches, like equivalent area spheres or equivalent volume spheres (Donovan et al., 2004; Grenfell et al., 2005). Nowadays, modern consistent data libraries for single scattering properties of ice crystals with different habits and at solar and thermal wavelengths are available (Yang et al.,

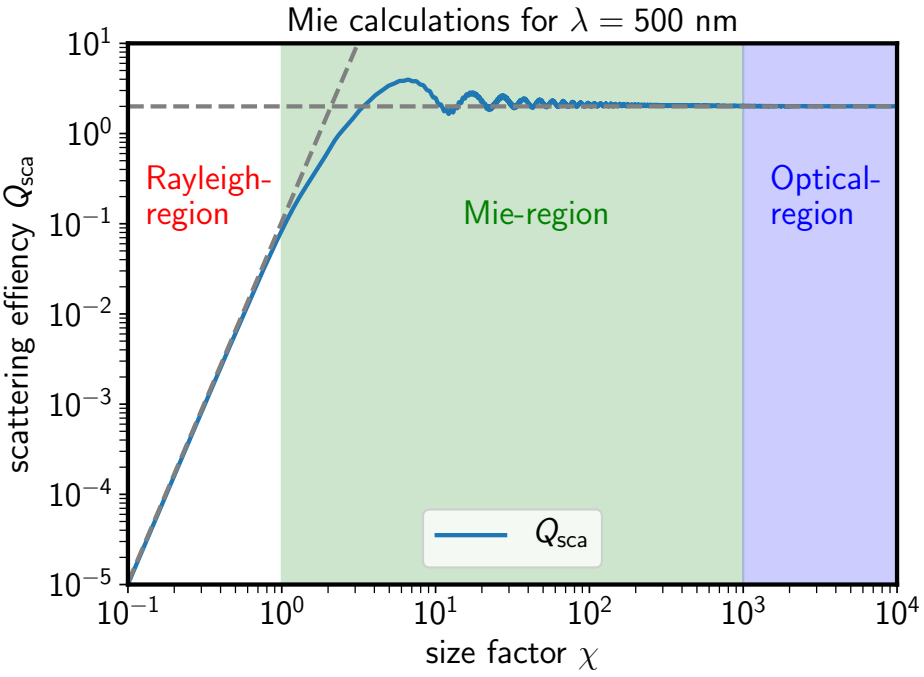

Figure 2.2.: Scattering efficiency for spherical ice crystals interacting with an electromagnetic wave of wavelength $\lambda = 500\,\text{nm}$. In the Rayleigh-region, the efficiency is $Q_{\text{sca}} \sim \chi^4$, whereas in the optical-region the behavior is constant $Q_{\text{sca}} \approx 2$, due to the extinction paradox. Calculations were taken out with libRadtran (Emde et al., 2016).

2013). Unfortunately, there is no unified theory to calculate these optical properties across all regimes of the size parameter χ. Therefore, Yang et al. (2013) used a combination of the Amsterdam discrete dipole approximation (ADDA), the T-matrix method, and the improved geometric optics method (IGOM), see Table 2.2. These methods can be distinguished on how the Maxwell equations are solved, there are volume (FDTD, ADDA) and surface-based (T-matrix) methods. Volume-based methods rely on discretisation of the volume of the scattering particle and can be applied to any arbitrary shape, but they are numerically expensive (Baran, 2012). Surface-based methods, like T-matrix, rely on the linearity property of the Maxwell equations, to relate incident and scattered field via the transition matrix, and is independent of the direction of incidence or scattered wave. Therefore, if the T-matrix is known, the single-scattering properties can be fully calculated (Mishchenko, 1991; Mishchenko and Travis, 1994).

Rayleigh Scattering

The Rayleigh scattering regime describes the scattering of light by small spherical particles, that are much smaller than the wavelength of the light. In this case, it is possible to find a simple solution by the method of asymptotic matching (Strutt, 1871, 1899). In detail, Lord Rayleigh, considered a plane wave incident on a dielectric sphere of diameter D and with dielectric factor $|K|^2$, where the probability that the spherical particle scatters light at angle

Θ is proportional to the differential scattering cross-section, $\mathrm{d}\sigma(\Theta)/\mathrm{d}\Omega$, which describes the ratio of scattered power into the solid angle $\mathrm{d}\Omega$ (Cox et al., 2002)

$$\frac{\mathrm{d}\sigma(\Theta)}{\mathrm{d}\Omega} = \frac{\pi^4}{8} |K_\lambda|^2 \left(1 + \cos^2 \Theta\right) \lambda^{-4} \; D^6 \; , \tag{2.15}$$

where $|K_\lambda|^2 = |(n_\lambda^2 - 1)/(n_\lambda^2 + 2)|$ as function of refractive index n_λ at wavelength λ, describes how radiation propagates through the scattering medium. An integration of this equation over the entire solid angle yields the total cross-section

$$\sigma_{\mathrm{sca}}(\lambda, D) = Q_{\mathrm{sca}}(\lambda, D)\sigma_{\mathrm{geo}}(D) = \frac{2\pi^5}{3} |K_\lambda|^2 \lambda^{-4} \; D^6 \; . \tag{2.16}$$

Rayleigh scattering shows a strong wavelength dependence ($\sim \lambda^{-4}$), which indicates that shorter (blue) wavelengths will be scattered more strongly than longer (red) wavelengths. The Rayleigh scattering cross-section can be used to approximate the scattering of light by cloud particles, where the light is emitted by active remote sensing devices like radars, which emit pulsed LW radiation in the microwave region.

Geometric Optics

Geometric optics describes light scattering by large particles $\chi \gg 1$ and for spherical particles, the scattering/extinction cross-section is given by

$$\sigma_{\mathrm{ext/sca}}(\lambda, D) = Q_{\mathrm{ext/sca}}(\lambda, D) \; \sigma_{\mathrm{geo}}(D) = 2 \; \sigma_{\mathrm{geo}}(D) = 2 \; \pi (D/2)^2 \; . \tag{2.17}$$

In this scattering regime, Q_{ext} can be approximated with the geometrical optics result 2 (Hulst, 1981). The extinction paradox relies on diffraction around the edges, and will be relevant in the range of visible wavelengths, where lidar sensors operate. In this shortwave region, scattering will be the dominant contribution to extinction, and absorption effects from hydrometeors are neglected.

Single-Scattering Optical Properties

The previous mentioned independent scattering assumption, allows to simplify calculations of light scattering by atmospheric particles by using *single-scattering properties*. Within an ice cloud a sufficiently small volume is considered, so that its single-scattering or *optical properties* can be defined in accordance to Maxwell's equations. The parameters that govern scattering are the wavelength of the incident radiation, the size and shape of the scattering particle and the particle's optical properties relative to the surrounding medium, described by the refractive index. Later in this section, it will be shown, how to take out *multiple scattering* (and absorption/emission) calculations with ice crystals, by using radiative transfer with single-scattering properties as input.

The **index of refraction** is part of the macroscopic Maxwell equations, and is a dimensionless number with dispersion features, that describes how fast light propagates through a certain material. Furthermore, if the considered material exhibits significant absorption

properties, refraction index is a complex number with real part n_r and imaginary part n_i and is defined as

$$n(\lambda) = n_r(\lambda) + i\ n_i(\lambda) \quad \text{and} \quad n_r(\lambda) = \frac{c_0}{c(\lambda)}, \tag{2.18}$$

where c_0 is the vaccum and $c(\lambda)$ the material dependent speed of light. The real part n_r describes the actual refraction effects, whereas the imaginary part n_i allows to determine the rate of absorption, see Figure 3.13. If an ice crystal would show no absorption, only the real-part n_r alone will be considered for the scattering process. But, when absorption is involved in the interaction process, the amount of scattered and absorbed energy, would both rely on the real and the imaginary part. For any calculations of solar or thermal radiative fluxes in an atmosphere with ice or water clouds, precise values of the real and imaginary parts, at all relevant wavelengths, are necessary to be known. Because these values will be required for the methods listed in Table 2.2 to calculate the extinction efficiencies Q_{ext} at different wavelengths (Warren and Brandt, 2008; Yang et al., 2013).

The **single-scattering albedo** ω_0 is defined as the ratio of scattering and extinction cross-section

$$\omega_0 = \frac{\sigma_{\text{sca}}}{\sigma_{\text{ext}}}\ , \tag{2.19}$$

and describes the fraction of light that would be scattered out of an incident light beam or plane wave. Further, $1-\omega_0$ represents the fraction of the light beam, that would be absorbed. In Figure 2.3 (c), ω_0 for different ice crystals as function of the wavelength is shown.

The **scattering phase matrix** $\mathbf{P}(\Theta)$ describes the angular distribution of the intensity and polarisation of the scattered radiation. Because polarisation is not relevant in the course of this work, it is sufficient to consider the first element of this matrix. This element is called **scattering phase function** $P_{11}(\Theta)$, and describes the probability of scattering of light into the direction of the scattering angle Θ. It is normalised to unity

$$\int_0^{2\pi} \int_0^{\pi} \frac{P_{11}(\Theta)}{4\pi} \sin(\Theta) \mathrm{d}\Theta \mathrm{d}\phi = 1\ . \tag{2.20}$$

For ice crystals assumed to be randomly oriented, this matrix contains six independent elements (Yang et al., 2013).

The **asymmetry parameter** g, or asymmetry factor, is the first moment of the phase function and used in radiative transfer considerations for the characterization of the degree of anisotropy of single scattering. It is defined as an intensity-weighted average of the cosine of the scattering angle

$$g = \langle \cos\Theta \rangle = \frac{1}{2} \int_0^{\pi} P_{11}(\Theta) \sin\Theta \cos\Theta\ \mathrm{d}\Theta\ , \tag{2.21}$$

where $P_{11}(\Theta)$ denotes the normalized phase function. The g-factor is directly connected to the total scattered intensity in dependence of the scattering angle, and therefore a good measure for the strength of forward scattering. It has the following value range $-1 \leq g \leq 1$, where $g = 1$ is for forward scattering, $g = -1$ describes backward scattering and $g = 0$ is

for isotropically scattering the same amount of light in all directions. In Figure 2.3 (d), g for different ice crystals as function of the wavelength is presented.

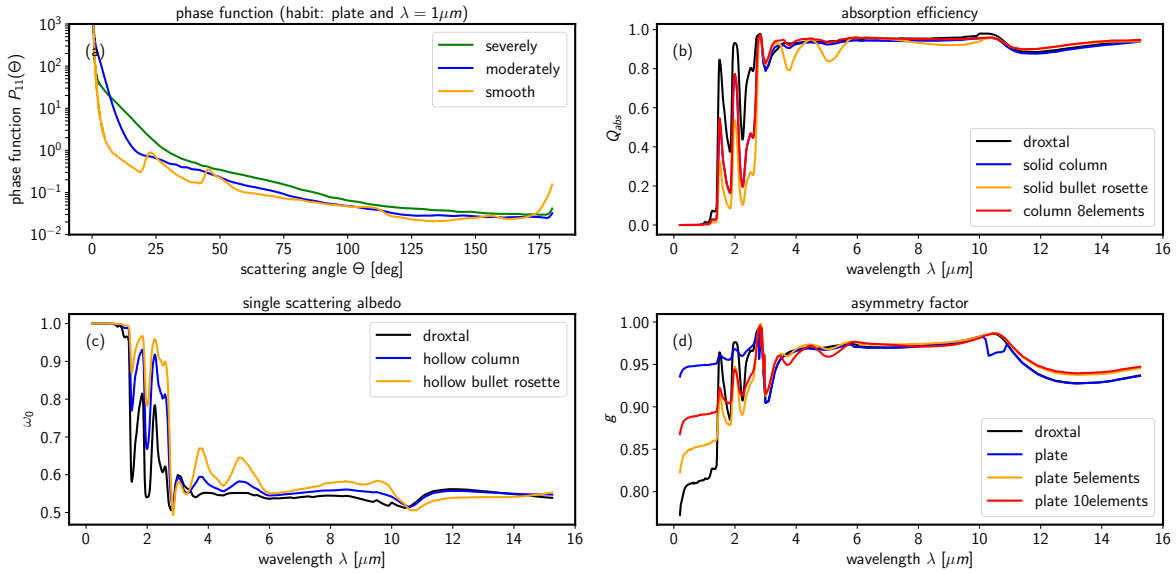

Figure 2.3.: (a) Phase functions of plates for different degrees of surface roughness, for stronger roughnesses the phase functions gets more washed out. (b) Absorption efficiency, (c) Single scattering albedo, (d) Asymmetry factor and $D_{\max} = 637.5\mu m$.

The aforementioned quantities will be the main input quantities for radiative transfer calculations with ice crystals. In Figure 2.3 an overview of the single-scattering properties of the Yang database for different ice crystal habits is given.

Molecular Absorption

Besides their kinetic energy, molecules have internal quantised energy states. There are three different types of energy states: electronic, vibrational and rotational. Electronic quantum states describe the energy of an electron in the molecule, vibrational states describes the engergy associated with bond stretching and compression, and the rotational states describe the energy due to a specific angular momentum of diatomic molecules. All of these states are specified with their own quantum number. Absorption or emission of a photon by a molecule will change its energy state in accordance with the photon's energy. Photons at short visible wavelengths have higher energies, and they participate in electronic transitions, whereas low energy photons at long infrared wavelengths participate in vibrational or rotational transitions.

To include atmospheric line absorption for various atmospheric gases into radiative transfer simulations, knowledge of the absorption coefficients for a given wavelength λ is required

$$\beta_{\text{abs},\lambda}(p,T) = \sum_{j=1}^{N} S_j(T) f_{\lambda,j}(p,T) \ , \tag{2.22}$$

where, j is the index of the absorption coefficient for the jth line, S is the line-strength

as function of temperature, and f_ν is the line shape factor. The line shape is a function of pressure and temperature, and for pressure-broadened lines it would be a Lorentz line shape, where doppler-broadened lines are characterised by a Voigt line shape. $\beta_{\text{abs},\lambda}(p,T)$ is deposited in a high-resolution transmission molecular absorption database (Rothman et al., 2005). Furthermore, current profiles of pressure and temperature from re-analysis or measurements are required.

Radiative Transfer Equation

A major goal of this thesis is to simulate the spectrum, an zenith-looking infrared spectrometer would record, when cirrus clouds are present above. The basis, to model these downwelling infrared radiances, is the 1D *radiative transfer equation* (RTE) (Chandrasekhar, 1960). This equation describes the light propagation through planetary atmospheres by incorperating the interaction with atmospheric constituents, like cloud particles, molecules and aerosols, through scattering, absorption, transmission, reflection and emission processes. The RTE can be derived based on Boltzmann's equation (Stamnes et al., 2017) or based on Maxwell's equations (Mishchenko, 2002) or just postulated like in this thesis. In a plane-parallel one-dimensional geometry, the monochromatic RTE at wavelength λ for a macroscopically isotropic medium, i.e. randomly oriented particles and molecules, could be written as (Stamnes et al., 1988)

$$\frac{\mu}{\beta_{\text{ext},\lambda}(z)}\frac{\mathrm{d}L_\lambda(z,\mu,\phi)}{\mathrm{d}z} = -\underbrace{L_\lambda(z,\mu,\phi)}_{\textbf{(a)}} + J_\lambda(z,\mu,\phi)\ , \tag{2.23}$$

where the source function J_λ is given by

$$J_\lambda(z,\mu,\phi) = \underbrace{\frac{\omega_{0,\lambda}(z)}{4\pi}\int_0^{2\pi}\mathrm{d}\phi'\int_{-1}^{1}\mathrm{d}\mu' P(z,\mu,\phi;\mu',\phi')L_\lambda(z,\mu',\phi')}_{\textbf{(b)}} + \underbrace{(1-\omega_{0,\lambda}(z))B_\lambda(T(z))}_{\textbf{(c)}}\ , \tag{2.24}$$

where $\mu = \cos(\theta)$ and $\mathrm{d}\mu = -\sin(\theta)\mathrm{d}\theta$ were introduced for the angular part. Here, L_λ describe the radiance at wavelength λ, z is the altitude, $\beta_{\text{ext},\lambda}$ is the volume extinction coefficient, $\omega_{0,\lambda}$ is the single scattering albedo and $B_\lambda(T(z))$ is the Planck emission function in dependence of the temperature T. The phase function P, depends on zenith and azimuth angle of the incoming light direction (μ',ϕ') and scattered outgoing light direction (μ,ϕ). In detail, the specific terms represent

- **(a)** the attenuation of an incoming light beam due to scattering and absorption by atmospheric particles and molecules, in accordance to Lambert-Beer's law,
- **(b)** the multiple scattering contribution from all directions. The phase function redirects the incoming radiation from (μ',ϕ') to the outgoing direction (μ,ϕ), and quantifies the probability for these processes to occur. The scattering volume is infinitesimal small, i.e. optically thin but large enough to contain many scatterer,
- **(c)** and the thermal emission from the scattering volume element in accordance to Planck's law.

In the literature, the RTE is also very often formulated in τ coordinates instead of z, via using $\mathrm{d}\tau = \beta_{\mathrm{ext},\lambda}\mathrm{d}z$. Equations like the RTE are denoted as integro-differential equation, due to the presence of term **(b)**. This term, which couples radiation from all incoming directions (μ', ϕ') to the radiation of the desired direction (μ, ϕ), requires a simultaneous solution for all directions (Mayer, B., 2009). Fortunately, for the considered one-dimensional geometry several numerical solutions exists (Stamnes et al., 1988), e.g. Section 3.3.2.

2.2. Microphysics of Cirrus Clouds

2.2.1. Optical, Micro- and Macrophysical Cloud Properties

In this section, the quantities to describe and parameterise optical, micro- and macrophysical cloud parameters, sensitive to remote sensing measurements, are introduced. It is the goal of cloud retrievals to derive these quantities from observational data to constrain microphysical schemes, used in current climate models. A very short overview of the representation of cirrus clouds in numerical weather and climate models is given. The aim is, to shortly sketch the stages until model output quantities, that can be compared with observations, are available and to identify them. This section mainly follows Liou and Yang (2016), Morrison et al. (2020) and Storch et al. (1999).

As previously indicated, climate and weather models can not resolve a growth process of an individual ice crystal and active remote sensing data can not detect the scattering amplitude of a single ice crystal. Therefore, bulk microphysical model quantities are required, that describe cloud processes on a larger scale, respectively on a certain cloud volume. In practice, a cloud volume could be a grid box in a climate model or a range gate from a radar or lidar signal return. In a cloud volume, the optical and microphysical properties of ice hydrometeors are averaged with respect to a **particle size distribution** (PSD). Cloud parameters are divided into **microphysical quantities**, parameters that are related to a moment of the PSD, **optical quantities**, parameters describing the attenuation of radiation in a cloud and **macrophysical quantities**, describing the geometry of a cloud. For aspherical particles like ice crystals, a size measure is not straight forward, therefore size is described as maximum dimension of an ice crystal $D_{\max}$ and for simplicity will be denoted as D in the following. PSDs can have one (monomodal) or more (multimodal) particle modes (Mitchell et al., 1996a; Ivanova et al., 2001) and their form can be parameterised by exponential, lognormal or gamma distributions. Due to results from in situ measurements, most commonly gamma-type distributions are used (Heymsfield et al., 2013). In this thesis the generalised gamma distribution will be used (Hu and Stamnes, 1993)

$$N(D) = \begin{cases} \frac{N_0}{D_s}\frac{1}{\Gamma(\mu)}\left(\frac{D}{D_s}\right)^{\mu-1} e^{-\frac{D}{D_s}} & \text{monomodal} \\ \\ \sum_{j=1}^{2} \frac{N_{0,j}}{D_{s,j}}\frac{1}{\Gamma(\mu_j)}\left(\frac{D}{D_{s,j}}\right)^{\mu_j-1} e^{-\frac{D}{D_{s,j}}} & \text{bimodal} \end{cases} \quad [\mathrm{m}^{-4}] \tag{2.25}$$

where $\Gamma(\mu) = (\mu - 1)!$ is the gamma function and N_0 is the total (volume) number concentration. D_s is the scale parameter, increasing the scale will increase the spread of the distribution, whereas the shape is described by μ and will turn into an exponential distribution for small values of $\mu < 1$, and broaden the distribution for large values. For further

calculations, it is helpful to know the different statistical moments of the PSD, because they can be used to describe cloud microphysical properties (Siebesma et al., 2020). The PSD k-th moment generating function for spherical particles is given by

$$M_k \coloneqq \left\langle D^k \right\rangle \coloneqq \int_{D_{\min}}^{D_{\max}} N(D) D^k \mathrm{d}D \quad , \tag{2.26}$$

where the angel brackets denote averaging over PSD and $D_{\min}$ and $D_{\max}$ are the lower and upper boundary of the maximum crystal dimension. Ice particles in cirrus clouds can have lower densities than that of solid ice $\rho_{\text{ice}} = 0.917 gcm^{-3}$, due to air intrusions of bubbles (Sato and Okamoto, 2006). To account for these variations in effective ice density and due to different particles shapes, the particle mass and projected area are often parameterised as a power-law relationship of the maximum dimension, like (Brown and Francis, 1995; Mitchell et al., 1996b; Heymsfield et al., 2010a; Ham et al., 2017)

$$m(D) = aD^b \quad [\mathrm{g}] \tag{2.27}$$

$$A(D) = \gamma D^\delta \quad [\mathrm{cm}^2] \quad , \tag{2.28}$$

with coefficients a in [g cm^{-b}], b (unitless), γ in [g $\mathrm{cm}^{2-\delta}$] and δ (unitless) to be determined in fitting routines. They require different moments of the PSD for projected area and mass

$$\left\langle [A(D)]^k \right\rangle \coloneqq \int_{D_{\min}}^{D_{\max}} N(D) \left[A(D)\right]^k \mathrm{d}D \tag{2.29}$$

$$\left\langle [m(D)]^k \right\rangle \coloneqq \int_{D_{\min}}^{D_{\max}} N(D) \left[m(D)\right]^k \mathrm{d}D \quad . \tag{2.30}$$

The dependence on the habit in the microphysical model is represented by the a, b, γ and δ coefficients and will not be mentioned explicitly in the following formulas due to clearness reasons. However, wherever $m(D)$ and $A(D)$ are mentioned, a habit dependence is present.

Another microphysical parameter to study cloud dynamics and precipitation is the **ice water content** (IWC), and approximately represents the mass of ice in a cloud volume

$$IWC = \langle m(D) \rangle = \int_{D_{\min}}^{D_{\max}} N(D) m(D) \mathrm{d}D \quad [\mathrm{gm}^{-3}] \quad , \tag{2.31}$$

where $m(D)$ is the mass of an individual ice crystal that accounts for the specific shape. For liquid water clouds the corresponding quantity, the liquid water content, is proportional to the third moment of the PSD. The integration of IWC from cloud-base to cloud-top yields the **ice water path** (IWP), which describes the total amount of ice within a cloud

$$IWP = \int_{z_{\text{cb}}}^{z_{\text{ct}}} IWC(z) \mathrm{d}z \quad [\mathrm{gm}^{-2}] \quad . \tag{2.32}$$

The **volume extinction coefficient**, defined as proportional to 2^{nd} moment $\langle D^2 \rangle$ for spherical particles, is an important parameter for determining the radiative properties of a cirrus cloud

$$\begin{aligned} \beta_{\text{ext}} &= \int_0^\infty Q_{\text{ext}}(D,\lambda) A(D) N(D) \mathrm{d}D \\ &\overset{D \gg \lambda}{=} 2 \langle A(D) \rangle \quad [\mathrm{m}^{-1}] \quad , \end{aligned} \tag{2.33}$$

where $A(D)$ is the projected or cross-sectional area of the cloud particles per unit volum and Q_{ext} is the extinction efficiency at wavelength λ. At visible wavelengths (lidar sensors), and in accordance to the geometrical optics regime, Q_{ext} can be approximated with 2, like known from the extinction paradox (Hulst, 1981). The vertical integral of β_{ext}, from cloud-base to cloud-top, yields a further important optical cloud property, the dimensionless **cloud optical thickness**

$$\tau = \int_{z_{\text{cb}}}^{z_{\text{ct}}} \beta_{\text{ext}}(z) \mathrm{d}z \quad , \tag{2.34}$$

which describes how strong radiation would be attenuated by propagating through a cloud. z_{cb} and z_{ct} are the geometrical cloud base and cloud top, but from a remote sensing perspective, the detected cloud boundaries can differ from the real geometrical boundaries. The reason is, that for optical thick ice clouds, the lidar signal, emitted from a ground-based sensor can be completely attenuated before reaching the cloud top, whereas the radar, due to the larger wavelength, will miss to detect small ice crystals.

Another parameter, to describe the radiative impact of a cloud, is the usage of an effective particle size or **effective radius** to represent the size dependence of scattering and absorption processes in radiation transfer. For spherical particles, this quantity is defined as ratio of the third $\langle D^3 \rangle$ over the second $\langle D^2 \rangle$ moment, as a weighted mean of the size distribution of cloud droplets, like described in Hansen and Travis (1974). But for non-spherical particles this definition is not usable, because the radius is not directly related to a physical or measurable quantity and the third (second) moment is not proportional to mass (area). Therefore, many other definitions are suggested, but there is no agreement on a convention yet (McFarquhar and Heymsfield, 1998). Throughout this thesis, the mean effect ice crystal size will be defined as 0.75 times the ratio of an ensemble particle volume and the particle projected area (Foot, 1988; Francis et al., 1994; Wyser and Yang, 1998; Yue et al., 2007; Hong et al., 2009)

$$R_{\text{eff}} = \frac{3}{4} \frac{\langle V(D) \rangle}{\langle A(D) \rangle} = \frac{3}{4} \frac{\int_{D_{\min}}^{D_{\max}} V(D) N(D) \mathrm{d}D}{\int_{D_{\min}}^{D_{\max}} A(D) N(D) \mathrm{d}D} \quad [\mu\mathrm{m}] \quad , \tag{2.35}$$

The integration of R_{eff} from cloud-base to cloud-top yields the **integrated effective radius** (IER), which describes the total effective particle size of the cloud

$$IER = \int_{z_{\text{cb}}}^{z_{\text{ct}}} R_{\text{eff}}(z) \, \mathrm{d}z \quad [\mu\mathrm{m \ m}^{-2}] \quad . \tag{2.36}$$

The effective radius will be important for radiative transfer (RT) calculations, because the main optical input parameters will be parameterised as function of R_{eff} and PSD. R_{eff} is used as parameter for a simplified description of cloud radiative properties, which in principle is retrievable from remote sensing measurements. Physically, its definition can be understood as a representative photon path for all cloud particles in the PSD (Mitchell, 2002). Although,

effective ice crystal size would be the proper wording, effective radius is used instead in the course of this work, because it is the common expression in literature.

The aforementioned quantities of interest are not independent of each other and can be linked for plane-parallel, homogeneous clouds in the visible spectrum (Foot, 1988)

$$R_{\text{eff}} = \frac{3IWC\Delta z}{2\rho_{\text{ice}}\beta_{\text{ext}}} \quad [\mu\text{m}] \quad , \tag{2.37}$$

where Δz is the vertical extension of a cloud layer. If one considers two clouds with the same IWC, the cloud with a smaller R_{eff} will have a bigger optical depth $\tau = \beta_{\text{ext}}\Delta z$, leading to more reflected sunlight.

The **equivalent radar reflectivity factor**, defined as to be proportional to the 6^{th} moment $\langle D^6 \rangle$ for spherical particles, is important for radar applications. In simple terms, this is just a parameter of the cloud to which the detected radar signal is sensitive. For non-spherical ice particles the volume $V(D)$ will be replaced by $m(D)/\rho_{\text{ice}}$ to obtain

$$Z_{\text{e}} = \frac{|K_{\text{ice}}(\lambda, T)|^2}{|K_{\text{w}}(\lambda, T)|^2} \frac{36}{\pi^2 \rho_{\text{ice}}^2} \left\langle [m(D)]^2 \right\rangle \quad , \tag{2.38}$$

where $|K_{\text{w}}|^2(\lambda, T)$ and $|K_{\text{ice}}|^2(\lambda, T)$ are the dielectric factors for liquid water and solid ice, respectively. Historically, the definition is based on Rayleigh scattering at radar wavelengths with spherical cloud particles, where the cross-section is $\sim D^6$. In order, to retrieve the effective radius from radar and lidar remote sensing data, it will be useful to introduce an auxiliary quantity, the **radar lidar effective radius** (Donovan and van Lammeren, 2001, 2002). For spherical particles it is defined as $R_{\text{eff}}^{\text{rali}} = 0.5 \left[\langle D^6 \rangle / \langle D^2 \rangle \right]^{1/4}$, and for non-spherical particles it is given by

$$\begin{aligned} R_{\text{eff}}^{\text{rali}} &= \left[\frac{9}{16\pi\rho_{\text{ice}}^2} \right]^{1/4} \left[\frac{\left\langle [m(D)]^2 \right\rangle}{\langle A(D) \rangle} \right]^{1/4} \\ &= \left[\frac{|K_{\text{w}}(\lambda, T)|^2}{|K_{\text{ice}}(\lambda, T)|^2} \frac{\pi}{32} \frac{Z_{\text{e}}}{\beta_{\text{ext}}} \right]^{1/4} \quad [\mu\text{m}] \quad . \end{aligned} \tag{2.39}$$

The advantage of $R_{\text{eff}}^{\text{rali}}$ is, that it is not direct dependent on habit and PSD, because Z_{e} and β_{ext} are gained from measurements without assumptions on habit and PSD. Later, the effective radius, used in RT calculations, can be retrieved based on $R_{\text{eff}}^{\text{rali}}$, with a specific function $C_{R_{\text{eff}}}$ for conversion

$$R_{\text{eff}} = C_{R_{\text{eff}}}(R_{\text{eff}}^{\text{rali}}, \text{PSD}, \text{habit}) \quad , \tag{2.40}$$

which requires assumptions of the ice crystal habit and about the type, modality and parameter of the PSD. The converting function $C_{R_{\text{eff}}}$ will be introduced in Section 3.4.2. In the literature, the radar lidar effective radius is often just denoted as primed quantity, $R_{\text{eff}}^{'}$. However, to point out more clearly, that it is a different quantity and not to be mistaken with R_{eff}, it will be denoted by $R_{\text{eff}}^{\text{rali}}$ in this thesis.

For some special retrieval techniques like Tinel et al. (2005) it will be useful to introduce the **normalized number concentration parameter** (Testud et al., 2001; Illingworth and Blackman, 2002). For ice clouds it is defined as

$$N_0^* = \left(\frac{4}{D_m}\right)^4 \frac{IWC}{\pi \rho_w} \quad , \tag{2.41}$$

where D_m is the melted-equivalent mass-weighted mean diameter and ρ_w is the density of liquid water. This quantity is useful, because analysis of aircraft data showed, that when moments of the PSD are normalized by N_0^*, precise power-law relationships exist between them (Hogan et al., 2006b).

The mentioned definitions assume only one habit per unit volume, to take a habit mixture into account, substitutions for the cloud volume $V(D) \longrightarrow \sum_{h=1}^{N_h} f_h(D) V_h(D)$, as well as the projected area $A(D) \longrightarrow \sum_{h=1}^{N_h} f_h(D) A_h(D)$ are required. Here N_h is the total number of habits and f_h is the fraction of a certain habit in the cloud volume's PSD with $\sum_{h=1}^{N_h} f_h = 1$.

Important **macrophysical cloud properties** are the phase (liquid or ice) and the altitudes of cloud base z_{cb} and top z_{ct}. For meaningful radiative transfer and climate simulations it is of course important to include the microphysical cloud properties at the correct altitude. These geometrical quantities will be obtained from active remote sensing instruments like radar and lidar. Because of the limitations due to their different wavelength sensitives, it is necessary to map cloud base and top measurements to the specific sensors. Lidars are good in detecting cloud bases $z_{\mathrm{cb,li}}$, but are limited in thick clouds, where they suffer strong extinction and the detected $z_{\mathrm{ct,li}}$ is not identic with the geometric cloud top z_{ct}. On the other side, radars do not suffer strong attenuation but detected radar cloud bases $z_{\mathrm{cb,ra}}$ and tops $z_{\mathrm{ct,ra}}$ are not identic with z_{cb} and top z_{ct} when there are small ice crystals present, that lie below the detection threshold of the radar.

The aforementioned quantities are useful, because they include the PSD. In a retrieval algorithm, these introduced microphysical properties of ice clouds will be converted to suitable spectral parameterised optical properties of ice crystals (Yang et al., 2013), to serve as input parameters to take out radiative transfer calculations with the aim of simulating the spectrum of a passive remote sensing device. Therefore, the optical single scattering properties will be parameterised as function of the effective radius and the PSD, see Section 3.3.4.

2.2.2. Representation of Cirrus Clouds in NWP and Climate Models

Need for Physical Parameterisation

To be able to give a numerical weather or climate prediction, models need to solve primitive prognostic equations. They account for conservation of momentum, mass and energy in order to approximate the global atmospheric flow. This work is done by the dynamical core of the model. In order to obtain solutions for the evolution of ice crystal size distributions (ice mixing ratios), several physical factors are involved in the governing equations like radiation, saturation ratio, air temperature, and horizontal and vertical motion. These adiabatic subgrid-scale processes to treat clouds and radiation can not be described explicitly,

and therefore have be included in parameterisations as *microphysical and radiation schemes* (Storch et al., 1999; Randall, 2000).

There are different types of hierarchy in models, concerning the scale of atmospheric motion. The hydrometeor population in turbulent clouds on scales from 1 mm to 1 m, can be explicitly represented in particle-by-particle direct numerical simulations (DNS) (Wang et al., 2009). On larger scales, individual hydrometeors can not be represented explicitly any more. Atmospheric scales ranging from 10 m to 100 km, allow to resolve clouds, but will require microphysical parameterisation schemes to represent unresolved microphysical processes and hydrometeor populations statistically in large eddy simulation models (LES) (Sölch and Kärcher, 2010). For scales larger than 100 km, both, micro- and macrophysical processes have to be paramaterised in GCMs (Kärcher et al., 2006).

Microphysical Schemes

In atmospheric science, microphysics refer to small-scale processes, that influence clouds, ice and precipitation particles, by diffusional growth from water vapor, evaporation, or melting and are a very important part in predicting Earth's weather and climate (Hofer et al., 2019).

An accurate representation of microphysical processes in models is a major challenge and leads to large uncertainties in numerical weather and climate simulations. Because of the impossibility of simulating all particles individually within a cloud it is difficult to describe the representation of the population of clouds and precipitation particles. Furthermore, due to missing knowledge of cloud physics, there are uncertainties in the underlying microphysical process rates. These uncertainties are especially large for processes in the ice phase, such as vapor diffusional growth, melting, and aggregation, which is due to the fact, that atmospheric ice particles have many complex shapes with a large variety (Morrison et al., 2020).

In models, so called, microphysical parameterisation schemes are deployed. They attempt to represent the unresolved microphysical processes and hydrometeor populations statistically. Typically, these schemes include parameterized rate equations that correspond to microphysical processes, such as diffusional growth or ice particle melting (Liou and Yang, 2016).

There are three main types of microphysical schemes: bulk, bin and particle-based Lagrangian. In bulk schemes, variables that describe bulk properties of a cloud within a grid volume, like cloud mass, are predicted. In bin schemes, the PSD is explicitly represented and predict variables like cloud mass for a specific size interval of the PSD. These schemes have more predicted variables than the bulk scheme and provide more flexibility at the cost of higher computational times. In Lagrangian based schemes, the particle population is represented by a discrete sampling of cloud and precipitation particles (Gettelman et al., 2019). In Figure 2.4, a two-moment bulk microphysics scheme is shown.

Radiation Schemes

For the temporal integration of the basic primitive equations, the heating and cooling rates in the atmosphere as well as the radiation fluxes of SW and LW at the surface and TOA are required (Roeckner et al., 2003). A radiation schemes provides profiles of the net radiation fluxes in specific spectral bands for solar and thermal radiation.

Radiative transfer with single-scattering properties require a light-scattering code and detailed ice crystal size and shape distributions. These calculations are numerical very expensive and could not be used as part of a GCM, where broadband calculations are required for every

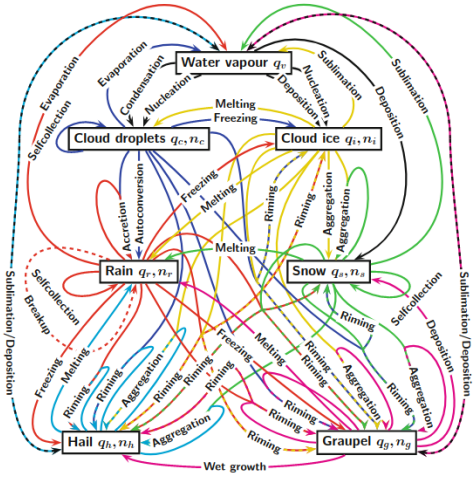

Figure 2.4.: Schematic diagram of processes in the six-class, two-moment microphysics scheme of Seifert and Beheng (2001). The rates and functional form of the different processes, indicated by arrows, have to be constrained with observational data gained from cloud retrievals. Figure taken from Gettelman et al. (2019).

time step and every grid point. Therefore, the calculation of broadband single-scattering properties of cirrus clouds should be simplified. In order to achieve this, Fu and Liou (1993) introduced parameterisation equations of broadband solar and infrared radiative properties, where they used R_{eff} to account for PSD effects and parameterised the single-scattering properties as function of IWC and R_{eff}. Now, in an evolving cloud field in a model, the parameterisation of the single-scattering properties of ice crystals will include the predicted ice water content $IWC(t, x, y, z)$ together with ice crystal size and shape information represented by $R_{\text{eff}}(t, x, y, z)$, from which the corresponding radiation field will follow. In this manner, cirrus-radiation interactions and feedbacks can be completely included in a GCM (Liou and Yang, 2016).

Comparison of Model Output with Observations

A fundamental difficulty in using parameterisation schemes in GCMs and NWP, is the underlying uncertainty in quantifying the individual microphysical process rates, particularly for ice processes, see Figure 2.4. There are two main types of uncertainty, *parametric uncertainty*, describing the uncertainty of the specific parameters used in process rate formulations, and *structural uncertainty*, associated with the functional forms of the process rates, which are both highly uncertain (Hourdin et al., 2017; Schmidt et al., 2017).

In order, to tackle these uncertainties, the microphysical schemes have to be compared with cloud measurements. The three categories of observations, laboratory, in-situ and remote sensing, have their own unique strengths and limitations. Laboratory single-particle experiments can provide physically based parameterisations of ice particle growth from vapor diffusion (Koenig, 1971) and riming (Hindman and Johnson, 1972), but care must be taken when applying results from ultra-clean vacuum-chambers to surrounding effects in turbulent atmospheric conditions. In-situ observations can provide detailed information on a particle-by-particle basis, but are usually very limited in time and space. Active and passive remote

sensing observations are only sensitive to vertical profiles of some specific moments of the PSD or to integrated quantities, but they can provide continuous long term measurement data for model comparisons in order to obtain robust and objective statistics. For this purpose, there are many measurement networks like Cloudnet (Illingworth et al., 2007a) or the Atmospheric Radiation Measurement (ARM) program (Stokes and Schwartz, 1994).

In solving a prognostic equation, a typical information available at each model layer is the relative humidity, which is then converted to cloud cover and ice water content or ice water mixing ratio by using certain parameterisation schemes. Subsequently, the main model variables to be compared with observations, based on radar and lidar data, are *cloud cover*, the fraction of the model gridbox containing clouds, and profiles of *ice water content*.

The vertical profiles of radar and lidar profiles are limited so very small space regions in comparison to model gridboxes and their temporal resolution is also much higher than the integration time of a model. To take out comparisons, the gridbox-mean's of ice water content and the observations will be averaged both on a common spatio-temporal grid, where the integration time is dependent on the wind speed (Hogan et al., 2006a). There are two approaches, in order to take out comparisons. The first, uses the model output to simulate the instrument, via using forward operators (Mech et al., 2020), effectively comparing observables. The second, converts the observations to cloud properties, via using ice cloud retrievals, effectively comparing microphysics.

2.3. Remote Sensing of Cirrus Clouds

Remote sensing is the field, responsible for metrological monitoring of cloudy and clearsky atmospheres. Due to different operating principles, it is usually separated into active and passive remote sensing. Passive remote sensing data, gained from infrared spectrometers, deliver spectral radiance measurements from an atmospheric column, containing information from both, cloud and molecular emission. In turn, active remote sensing devices, like radar and lidar, have their own light source, and monitor high range- and time-resolved vertical intensity profiles from scattering particles in clouds and atmosphere (lidar), and clouds only (radar).

Remote sensing of clouds include a huge variety of different techniques and instruments, but in this section, only techniques and instruments used in this thesis are discussed. This section mainly follows descriptions from Lynch et al. (2002); Griffiths and De Haseth (2007); Liou and Yang (2016); Yang et al. (2018) and Siebesma et al. (2020).

2.3.1. Passive Remote Sensing

Fourier Transform Infrared Spectrometry

The introduced SynCirrus algorithm relies on measurements of downwelling infrared spectrial radiances from thermal emission processes in the atmosphere. These measurements are carried out by an accurately calibrated ground-based Fourier transform spectrometer (FTS). Their working principle is based on Fourier transform infrared (FTIR) spectrometry techniques. In a Michelson-type interferometer (Michelson and Morley, 1887) adapted for FTIR measurements, light from a polychromatic infrared source is collimated and directed into the aperture. A configuration of a fixed and a movable mirror as well as a beam splitter allows

the measurement of the *interferogram* in dependence of the *optical path difference* (OPD). The OPD Δx denotes the difference in optical path length between the two arms of to the interferometer. An interferogram is recorded by varying the retardation Δx and recording the signal from a detector for various values of this retardation $L(\Delta x)$. The values Δx of the OPD are required with a very high accuracy for a proper analysis of the recorded interferogram and usually interferometer using an internal helium-neon laser aligned with the beam, where the wavelength is known. In spectrometry it is common to use wavenumbers instead of wavelengths, because this unit is proportional to energy

$$\widetilde{\nu} = \frac{1}{\lambda} \ . \tag{2.42}$$

Furthermore, it makes comparing and measuring band widths more easy, because the spectrum will be easier to read. On the linear wavelength-scale, the spectrum would be broad and spread out some feature in one region, and compressed features in another region, which makes it difficult to identify them visually. In contrary, wavenumbers will provide more symmetric peak shapes and are just more practical in usage (Griffiths and De Haseth, 2007).

The interferogram $L(\Delta x)$ can be related to the thermal radiance spectrum $L(\widetilde{\nu})$ via Fourier transform and vice versa:

$$L(\Delta x) = \int_{-\infty}^{\infty} L(\widetilde{\nu}) \cos(2\pi\widetilde{\nu}\Delta x) \mathrm{d}\widetilde{\nu} \tag{2.43}$$

$$L(\widetilde{\nu}) = \int_{-\infty}^{\infty} L(\Delta x) \cos(2\pi\widetilde{\nu}\Delta x) \mathrm{d}x \ . \tag{2.44}$$

In Equation (2.44) of the Fourier transform pair, the complete spectrum at infinitely high resolution could be measured. In theory, this is synonymous when the moving mirror of the interferometer could be varied on an infinitely long distance. But in experimental practice, the fact of measuring the signal only over a limited retardation is possible, and this will cause the effect of measuring the spectrum only at a finite resolution, depending on the finite maximum path difference $\mathrm{OPD}_{\mathrm{max}}$. The best resolution of an interferometer is obtained by (Griffiths and De Haseth, 2007)

$$\Delta\widetilde{\nu} = \frac{1}{\mathrm{OPD}_{\mathrm{max}}} \ . \tag{2.45}$$

Restricting the maximum retardation of an interferogram to $\mathrm{OPD}_{\mathrm{max}}$, results in multiplying the hole interferogram by a truncation function, called the apodization function $A(\Delta x)$, which is defined as

$$A(\Delta x) = \begin{cases} 0 \text{ if } & -\mathrm{OPD}_{\mathrm{max}} \leq \Delta x \leq \mathrm{OPD}_{\mathrm{max}} \\ 1 \text{ if } & \Delta x > |\mathrm{OPD}_{\mathrm{max}}| \ , \end{cases} \tag{2.46}$$

leading to

$$L(\widetilde{\nu}) = \int_{-\infty}^{\infty} L(\Delta x) \ A(\Delta x) \ \cos(2\pi\widetilde{\nu}\Delta x) \ \mathrm{d}x \ . \tag{2.47}$$

From a mathematical point of view, the effect of the multiplication of the interferogram with a window function, like $A(\Delta x)$, is equal to the convolution of the spectrum with a function, called *instrumental line Shape* $\mathrm{ILS}(\widetilde{\nu})$. Therefore, the observed radiance will be described by

$$\begin{aligned} L_{\mathrm{obs}}(\widetilde{\nu}) &= L(\widetilde{\nu}) \circledast \mathrm{ILS}(\widetilde{\nu}) \\ &= \int_{-\infty}^{\infty} L(\widetilde{\nu})\ \mathrm{ILS}(\widetilde{\nu}-\widetilde{\nu}')\ \mathrm{d}\widetilde{\nu}' \ . \end{aligned} \tag{2.48}$$

The ILS, in turn, is the Fourier transform of the apodization function

$$\begin{aligned} \mathrm{ILS}(\widetilde{\nu}) &= \mathrm{FT}\left[A(\Delta x)\right] \\ &= 2\mathrm{OPD}_{\max}\frac{\sin(2\pi\widetilde{\nu}\mathrm{OPD}_{\max})}{2\pi\widetilde{\nu}\mathrm{OPD}_{\max}} \ . \end{aligned} \tag{2.49}$$

Therefore, to be able to compare simulated with measured spectra, simulated spectra with a higher resolution than the device first have to be convolved with the ILS.

For the near IR, the thermal emission by the instrument is very small compared to the measured downwelling solar radiances. But in the mid and far IR, however, the spectral radiances measured from the atmospheric scene are comparable to the thermal emission by the instrument, at least for lower atmospheric layers, where the temperatures are comparable with the ambient temperature of the instrument.

An approach, introduced by Revercomb et al. (1988), uses the complex Fourier transform to represent the interferogram in an alternative form to Equation (2.43)

$$L(\Delta x) = \frac{1}{2}\int_{-\infty}^{\infty} C(\widetilde{\nu})\ e^{i\phi(\widetilde{\nu})}\ e^{i2\pi\widetilde{\nu}\Delta x}\mathrm{d}\widetilde{\nu} \ , \tag{2.50}$$

where $\phi\left(\widetilde{\nu}\right)$ is the phase response of the instrument, which characterises the optical and electrical dispersion of the instrument. For the uncalibrated magnitude spectrum $C(\widetilde{\nu})$, it is assumed, that the system has a linear response function $r(\widetilde{\nu})$ and an instrument emission offset $L^0(\widetilde{\nu})$

$$C(\widetilde{\nu}) = r_{\widetilde{\nu}}\left[L(\widetilde{\nu}) + L^0(\widetilde{\nu})\right] \ . \tag{2.51}$$

Therefore a calibration procedure would require two reference blackbodies, with known constant temperatures, to calculate the two unknowns $r(\widetilde{\nu})$ and $L^0(\widetilde{\nu})$. The emission of these blackbodies is described by the Planck function for a blackbody with a constant cold temperature $B(\widetilde{\nu}, T_{\mathrm{col}})$ and a constant hot temperature $B(\widetilde{\nu}, T_{\mathrm{hot}})$.

Revercomb et al. (1988) emphasised, that a two-point calibration for FTIR spectrometer, only including the magnitude spectrum, lead to brightness temperature errors because of a source-dependent phase response, caused by emission from the interferometer of the beam splitter. Their new analysis includes the complete complex spectra obtained from Fourier transforming the measured interferograms instead of only using the magnitudes

$$C'(\widetilde{\nu}) = FT\left[L(\Delta x)\right] = r(\widetilde{\nu})\left[L(\widetilde{\nu}) + L^0(\widetilde{\nu})e^{i\phi^0(\widetilde{\nu})}\right]e^{i\phi(\widetilde{\nu})}, \tag{2.52}$$

where ϕ^0 is the difference from the normal phase of the anomalous phase associated with the combined radiance from the many emitting components of the instrument. This leads to a new two-point blackbody calibration equation, including the differences of the full complex spectra

$$L(\tilde{\nu}) = \Re\left[\frac{C(\tilde{\nu}) - C_{\mathrm{col}}(\tilde{\nu})}{C_{\mathrm{hot}}(\tilde{\nu} - C_{\mathrm{col}}(\tilde{\nu}}\right][B(\tilde{\nu}, T_{\mathrm{hot}}) - B(\tilde{\nu}, T_{\mathrm{col}})] + B(\tilde{\nu}, T_{\mathrm{col}}) \tag{2.53}$$

to ensure, that the complex phase and the offset contribution do not bias a radiative calibration anymore. This procedure is relevant, because the measured radiance spectrum after calibration with Equation (2.53) will be compared with a simulated spectrum as part of the SynCirrus algorithm.

In this work, spectrometry data from the Atmospheric Emitted Radiance Interferometer (Knuteson et al., 2004a,b), recorded at Mount Zugspitze, are used. In Figure 2.5, an example measurement is illustrated.

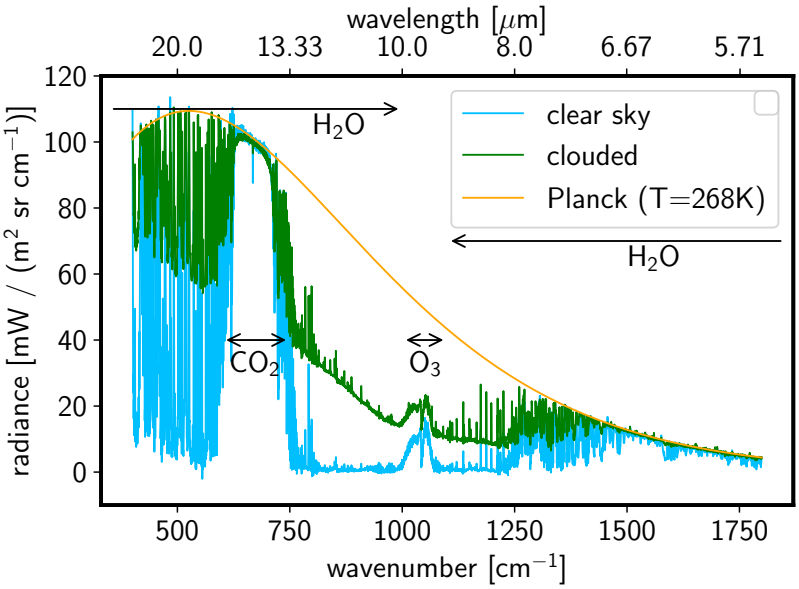

Figure 2.5.: Illustration of downwelling atmospheric radiances recorded with an AERI. Also denoted are the absorption regions for the main atmospheric constituents and the Planck function for the ambient temperature. The clear sky and clouded radiances were recorded at 2012-11-23 06:23 UTC and 16-10-06 00:17 UTC, respectively.

2.3.2. Active Remote Sensing

While passive remote sensing devices monitor radiation emitted naturally by a cloudy atmosphere, active sensors have their own source to emit pulsed radiation towards atmospheric scatterers. The detected intensity of the backscattered pulses and their time-of-flight, provides insight about the type of scatterer and its location, respectively.

An advantage of active senors is, that they can deliver vertical resolved profiles proportional to cloud properties. Passive sensors, measuring only vertically integrated measures of cloud

properties, and suffer the limitation that the observed radiances are weighted towards the values at cloud base (ground-based configuration). But passive sensor have larger field of views, where active sensors can only sample smaller portions of an atmospheric scene.

There are many different operating principles for lidars (backscatter, HSRL, Raman, DIAL) and different frequency ranges for radars (clouds, rain, wind) used for active remote sensing. In the following section the focus will be on the basics of an elastic backscatter lidar and a cloud radar.

Similarities of Radar and Lidar

Besides the wavelength of their light source, radar (microwave spectrum) and lidar (visible spectrum) devices share many properties. Both rely on scattering which is important in the microwave and the visible spectrum of radiation. For the most applications they have a narrow field of view, and therefore the detected intensity is dominated by pulses that were only scattered once by an atmospheric scatterer in backward direction. For some applications, the field of view is already large enough, that multiple scattered radiation will be detected along-side single scattered radiation. Because multiple scattered radiation takes longer to reach the detector, it will be interpreted by the detector as coming from higher altitudes. These multiple scattering effects have to be accounted for in a retrieval algorithm, when retrieving microphysical cloud properties, see Section 3.4.4.

In general, single scattering by an atmospheric target, is given by the active remote sensing equation (Lynch et al., 2002; Siebesma et al., 2020)

$$P_{\mathrm{SS}}(R,\lambda) = C_{\mathrm{sys}}\; G_{\mathrm{geo}}(R,\lambda)\; \beta_{\mathrm{sca},\pi}(R,\lambda)\; T^2(R,\lambda)\;, \tag{2.54}$$

where R is the distance from a zenith-looking active sensor to the target or just the range, λ is the wavelength of the instrument's light source, C_{sys} is the specific system constant (instrument hardware like transmitted power P_{Tx}), $G_{\mathrm{geo}}(R,\lambda)$ is the range dependent measurement geometry, $\beta_{\mathrm{sca},\pi}(R,\lambda)$ is the back scatter coefficient, describing the radiation scattered once by the targets within the pulse volume, before reaching the detector ($\theta = \pi$), $T^2(R,\lambda)$ is the two-way transmission term, describing atmospheric attenuation, and $P(R,\lambda)$ is the received power from an atmospheric scatterer at position z. In principle, Equation (2.54) is essentially the RTE in a scattering media with a single direction $P(\theta = \pi)$. The geopotential height z is related to the range R via the altitude z_{ins} of the instrument, $z = z_{\mathrm{ins}} + R$. Depending on the wavelength of the emitted pulses, Equation (2.54) will take a concrete form, due to the different scattering regimes. For scattering effects in backward direction, the term $\beta_{\mathrm{sca},\pi}(R)$, gives information about the size of the scatterer, and the extinction term $T(R,\lambda)$, provides insight about the particle number density or just the optical thickness of a cloud layer. Furthermore, it is assumed that there is an underlying PSD describing the different sizes and cross-sections $\sigma_{\mathrm{sca},\pi,i}$ of the target particles in the pulse volume. Because the wavelength is a fixed parameter by the light source of the sensor, it will not be mentioned in the following formulas. The distances between the scattering hydrometeors are very small compared to distances to the detector. Therefore, only the range R from the detector to the sample volume of the pulse is relevant.

Some radar and lidar devices can emit linear polarised radiation for target classification. If the detected radiation would retain its linear polarisation, the scatterer would have been a spherical particle. Because the SynCirrus algorithm does not exploit this information, polar-

isation will not be considered in this section.

Differences between Radar and Lidar

Lidars use laser light sources at visible wavelengths. Because visible wavelengths are much smaller than ice crystal sizes, the scattering efficiency will take a constant value $Q_{\text{ext}} \approx 2$ and the backscatter coefficient is given by $\sigma_{\text{sca},\pi} \sim D^2$, like aforementioned for the geometric optics regime as described by Equation (2.17). The signal contributions are from cloud particles, aerosols and Rayleigh scattering from atmospheric gas molecules. In optically thick ice clouds, the lidar signal would be completely attenuated before reaching the cloud top. This is a serious limitation lidars used for ice cloud remote sensing suffer from. The main microphysical quantity of interest in lidar measurements is the extinction coefficient β_{ext} ($\sim$ 2^{nd} moment of PSD), which will be obtained via the inversion of the lidar signal, making assumptions about the atmospheric scatterers in that process.

Radars on the other side, use a magnetron light source that produce pulsed microwave radiation. In this part of the spectrum, the wavelengths are much longer than typical ice crystal size and their backscatter cross section is in the Rayleigh regime $\sigma_{\text{sca},\pi} \sim D^6$, like indicated by Equation (2.16). Therefore, the detected radar signal can be dominated by only a few but very large ice crystals. A limitation of radars is, due to their large wavelengths, they are not sensitive to small ice crystals. In contrary to lidars, they can penetrate even thick ice clouds, and only suffer serious attenuation in strong precipitation clouds. The microphysical quantity of interest in radar measurements is the equivalent radar reflectivity factor Z_{e} ($\sim$ 6^{th} moment of PSD), which will be obtained directly from the returned radar signal.

Radar

Radar (RAdio Detection And Ranging) instruments are operating at long wavelengths in the microwave region, where they are able to resolve ice crystals, droplets and raindrops. Their light source emits microwave radiation at typical frequencies of around 6 GHz(C-band: precipitation), 36 GHz(Ka-band: clouds) or 95 GHz(W-band: clouds). The single-scattering radar equation for distributed meteorological targets is given by (Probert-Jones, 1962; Rinehart, 1991; Doviak and Zrnić, 1993)

$$P_{\text{SS}}(R) = C_{\text{rad}} \, \frac{1}{R^2} \, \beta_{\text{tot,sca},\pi}(R) \, T^2(R) \, , \tag{2.55}$$

where R is again the range from the sensor to the target, C_{rad} is the hardware constant (antenna properties etc.) and $P_{\text{SS}}(R)$ is the detected power by the receiver. $T^2(R)$, sometimes called loss factor L, describes the two-way atmospheric attenuation due to traces gases, but at radar wavelengths this is usually only a small effect, leading to $T^2(R) \sim 1$. The attenuation at radar wavelengths will be further investigated in Section 3.2.3.

The total backscattered radiation $\sigma_{\text{sca},\pi}$ from the pulse volume V_{pul} is a sum over the individual cross-sections per unit volume V_0 and multiplied by the pulse volume afterwards (Doviak and Zrnić, 1993)

$$\beta_{\text{tot,sca},\pi} = \left(\sum_{k \in V_0} \frac{\sigma_{\text{sca},\pi,k}}{V_0} \right) \, V_{\text{pul}} = \eta \, V_{\text{pul}} \, . \tag{2.56}$$

This introduced radar reflectivity η describes the backscatter cross-section per unit volume. Because radar wavelengths are usually much bigger than the size of atmospheric hydrometeors, the backscatter cross-section is in the Rayleigh regime, given by Equation (2.15) evaluated at $\theta = \pi$, leading to

$$\begin{aligned} \eta &\overset{D \ll \lambda}{=} \frac{\pi^5}{\lambda^4} |K(\lambda, T)|^2 \int_0^\infty N(D) D^6 \mathrm{d}D \\ &= \frac{\pi^5}{\lambda^4} |K(\lambda, T)|^2 Z \quad [\mathrm{m}^{-1}], \end{aligned} \tag{2.57}$$

where it was assumed, that all the particles in the radar beam have the same dielectric factor. If this is not true, $|K(\lambda, T)|^2$ is part of the integral. Furthermore, the sum over particles was replaced by integrating over a PSD and the radar reflectivity factor was introduced. Two radar devices with the same hardware but different wavelengths should measure the same Z. To make them comparable, it is useful to introduce a new auxiliary quantity, the equivalent radar reflectivity factor Z_e, which removes the wavelength dependence and is defined by

$$Z_\mathrm{e} = \frac{\lambda^4}{|K_\mathrm{w}(\lambda, T)|^2 \pi^5} \eta = \begin{cases} Z & \text{liquid droplets} \\ Z \frac{|K_\mathrm{ice}(\lambda,T)|^2}{|K_\mathrm{w}(\lambda,T)|^2} & \text{ice crystals .} \end{cases} \tag{2.58}$$

The convention for this definition is to become $Z_\mathrm{e} = Z$ if the targets are liquid droplets, where $|K|^2 = |K_\mathrm{w}|^2$. The final output from the radar is then given by

$$Z_\mathrm{e}(R) = P_\mathrm{SS}(R)\ R^2\ \frac{|K_\mathrm{w}(\lambda, T)|^2}{|K(\lambda, T)|^2}\ \frac{1}{C^*_\mathrm{rad}}\ \frac{1}{T^2(R)}\ , \tag{2.59}$$

with the new constant C^*_rad including the pulse volume. Considering the unit of Z_e, the diameter to the sixth power gives [mm^6], where the number of particles per unit volume has units of [m^{-3}]. The combination leads to [mm^{6}m^{-3}] and will not be further simplified to [m^3], because [mm^{6}m^{-3}] was historically the most used unit to measure raindrop diameters and [m^3] is easy to be misunderstood for volumes. Measured Z_e from meteorological targets can span a huge range of values, like 1×10^{-3} mm^{6}m^{-3} for fog up to 5×10^7 mm^{6}m^{-3} for heavy hail (Rinehart, 1991). This large dynamic range can be presented more understandable on a logarithmic dBZ-scale

$$Z_\mathrm{e}\,[\mathrm{dBZ}] = 10 \log_{10} \left(Z_\mathrm{e} \left[\mathrm{mm}^6 \mathrm{m}^{-3} \right] \right) \ . \tag{2.60}$$

For very high frequencies and in turn small wavelengths, the Rayleigh approximation is maybe not longer valid for all particles from the sampling volume. If the wavelength of the radiation will be not significantly larger than the particle sizes, but in the same order of magnitude, Mie theory should be taken into account. This can be done by including a correction factor in Z_e, the Mie-to-Rayleigh ratio $\gamma_\mathrm{M/R}$, like presented here for ice spheres (Benedetti et al., 2003; Hogan et al., 2006c)

$$Z_\mathrm{e} = \frac{|K_\mathrm{ice}(\lambda, T)|^2}{|K_\mathrm{w}(\lambda, T)|^2} \int_0^\infty \gamma_\mathrm{M/R}(D) N(D) D^6 \mathrm{d}D \ . \tag{2.61}$$

At the long radar wavelengths multiple scattering effect are usually ignored and they only become relevant at high radar frequencies, where the signal is stronger affected by extinction. Here, the transport mean-free-path will be comparable with the instrument footprint, which is determined by the antenna beam-width and the platform altitude (Battaglia et al., 2010).

Lidar

Lidar (LIght Detection And Ranging) instruments are operating at short laser wavelengths with typical values of 355 nm (near-UV: trace gases, aerosols, clouds), 532 nm (green spectrum: trace gases, aerosols, clouds) or 1064 nm(near-infrared: trace gases, aerosols, clouds). The single-scattering lidar equation for an elastic backscatter lidar in its most common form is given by (Weitkamp, 2006)

$$P_{\mathrm{SS}}(R) = C_{\mathrm{lid}} \ \frac{1}{R^2} \ \beta_{\mathrm{sca},\pi}(R) \ \exp\left[-2\int_0^R \beta_{\mathrm{ext}}(R')\mathrm{d}R'\right] \ , \tag{2.62}$$

where R is again the range or the altitude relative to a vertically pointing active sensor, C_{lid} is the system's hardware representing constant, R^{-2} is the geometric factor of the receiver area and P_{SS} is the detected backscattered power from an atmospheric scatterer, a dimensionless number of the detected photons per range-bin. The total backscatter and extinction coefficients are describing the atmospheric properties. Because the short lidar wavelengths are sensitive to many atmospheric constituents, the coefficients are composed as a sum of the molecular part (air molecules, sometimes called Rayleigh-atmosphere or Rayleigh-signal) and the particular part (ice crystals, cloud droplets, aerosol particles)

$$\beta_{\mathrm{sca},\pi}(R) = \beta_{\mathrm{sca},\pi,\mathrm{par}}(R) + \beta_{\mathrm{sca},\pi,\mathrm{mol}}(R) \tag{2.63}$$

$$\beta_{\mathrm{ext}}(R) = \beta_{\mathrm{ext,par}}(R) + \beta_{\mathrm{ext,mol}}(R) \ . \tag{2.64}$$

With the detected power $P_{\mathrm{SS}}(R)$ there is only one known measured profile, but four unknown profiles for the molecular and particular backscatter and extinction coefficients. Considering cloud applications, it is not necessary to know all these four profiles simultaneously. One is only interested in that part of the backscatter and extinction profile, which was caused by scattering of cloud particles. Within the cloud, the molecular return is negligible in comparison to the cloud return, and therefore it is possible to treat the cloud and the cloud free parts of the lidar signal as a single-component atmosphere, reducing the problem to two unknown profiles. To eliminate one of the two unknowns in Equation (2.62), it is assumed, that the ratio of β_{ext} and $\beta_{\mathrm{sca},\pi}$ can be guessed on a physical reasonable basis. This ratio is called *lidar ratio*

$$LR(R) = \frac{\beta_{\mathrm{ext}}(R)}{\beta_{\mathrm{sca},\pi}(R)} = \frac{1}{\omega_0(R) \ P(\theta=\pi)} \ , \tag{2.65}$$

with single-scattering albedo ω_0 and phase function P for 180°. This quantity can be assumed, guessed or calculated with methods introduced in Table 2.2.

The lidar equation assumes, that detected photons were only scattered once, but this assumption is only correct for a very narrow field-of-view of the instrument. For larger field-of-view configuration multiple scattering effects have to be taken into account. Simulations indicated, that only photons that have not left the field-of-view are relevant in multiple

scattering processes, once they left this area the probability is very low, that they will reach the detector after several scattering events (Hutt et al., 1994). Therefore, the main part of multiple scattered photons came from forward scattered photons, that undergo one or many forward scattering events until they got scattered back towards the detector (Bissonnette et al., 1995). Because of multiple scattering effects, the detected signal is higher, than just the part from single scattering and this signal will be interpreted incorrect by Equation (2.62) as higher transmission. Subsequently, multiple scattering will lead to an underestimation of the extinction coefficient. Therefore, the multiple scattering signal, looks like a single scattering signal with reduced optical thickness. This fact allows an easy approximation: Platt (1973) introduced an multiple scattering factor, η_{MS}, to correct the two-way transmittance for the contribution from multiple scattering

$$P_{\mathrm{MS}}(R) \approx C_{\mathrm{lid}} \; \frac{1}{R^2} \; \beta_{\mathrm{sca},\pi}(R) \; \exp\left[-2 \; \eta_{\mathrm{MS}} \int_0^R \beta_{\mathrm{ext}}(R')\mathrm{d}R'\right] \; . \tag{2.66}$$

In the single scattering approximation, η_{MS} is equal to 1 and for multiple scattering effects, η_{MS} takes values below unity. In Equation (2.66), η_{MS} is assumed to be constant throughout the hole cloud layer, but this is only true for thick liquid clouds like shown by Weinman (1976) and Platt (1981). For ice clouds, η_{MS} is in principle dependent on the range and the ice crystal scattering phase function and in turn on their particle properties (PSD, refractive index) and takes typical cirrus values of below 0.5 (Platt, 1981). There are computational algorithms for an accurate estimation of the multiple scattering lidar signal based on the instrument parameters (wavelength, field-of-view) like introduced by Eloranta (1998) and Hogan (2006, 2008); Hogan and Battaglia (2008).
The different methods of how to retrieve β_{ext} by inverting the lidar signal will be discussed in Section 3.4.3.

2.3.3. Benefit of Sensor Synergies

Like aforementioned, different remote sensing devices are sensitive to different cloud properties. Radars are more sensitive to size and therefore useful to retrieve R_{eff}-profiles, where lidar in turn are more sensitive to particle concentration and useful to retrieve β_{ext}-profiles. Passive imager or spectrometer have many different wavelength channels to retrieve information about atmospheric constituents, where especially the spectral bands in the atmospheric window between 8 µm to 14 µm can provide valuable information about integrated cloud properties (Chang et al., 2017).

Retrieval algorithms that are based on the data from only one instrument suffer serious limitations. Retrievals based on multi-channel passive remote sensing data can only provide integrated information about optical thickness τ and particle size R_{eff} (Nakajima and King, 1990). Radar-only based retrievals can derive IWC only with large errors up to 200 %, due to the fact of the high moment of the PSD in Z_{e} measurements, where the signal is dominated by large particles (Brown et al., 1995). In detail, these radar-only retrievals use power-law relationships like $Z_{\mathrm{e}} = gIWC^h$ with coefficient g and h to be determined. Because no other constraints are availabe, these coefficients can only be determined on a climatologial scale, e.g. from in-situ measurements with aircrafts, which can introduce a large bias on the retrieval results (Hogan et al., 2006b). Due to the lack of size information, the same principle is used in lidar-only retrievals, which use $IWC = c(\beta_{\mathrm{ext}})^d$ empirical relationships to retrieve IWC

(Heymsfield et al., 2014). But these lidar-only retrievals suffer as well on large errors (Avery et al., 2012).

In turn, radar-lidar retrievals would avoid these large spread of possible values and offer the possibility for a well constrained size retrieval. Like defined in Equation (2.35) and Equation (2.39) for R_{eff} and $R_{\text{eff}}^{\text{rali}}$ respectively, size quantities require two moments to the PSD. Therefore, with two measured observables, sensitive on two PSD moments, it is possible to retrieve the two unknown microphysical properties β_{ext} and $R_{\text{eff}}^{\text{rali}}$, which in turn can be converted to IWC and R_{eff} as input for RT calculations via assuming PSD and ice crystal habit. In order to retrieve cloud properties from combined radar and lidar measurments it is necessary, that the cloud signals from both devices show a large vertival overlap. Due to their different wavelength sensitives, lidars can miss detecting cloud top due to strong attenuation in thick clouds, whereas radars could miss small ice crystals around cloud top and base, if they are below their detection threshold. With a large overlap from both cloud signals, it is ensured, that they have detected the same cloud vertically, and a meaningful retrieval of the microphysical cloud profiles is possible (Stein et al., 2011). The still remaining uncertainties, due to the lack of information about PSD and ice crystal habit, can be reduced via including data from a passive imager to the sensor synergy approach. Here, different variations of PSD and ice crystal habit configuration for the IWC and R_{eff} profile can be used in RT simulations to obtain different spectra and compare them with recordings of the passive imager. The configuration causing the lowest spectral residuals can be a indicator for good assumptions of PSD and ice crystal habit.

3. Methods

In this chapter, the main idea of the retrieval algorithm will be presented. The developed ice cloud retrieval relies on data from radar, lidar and infrared spectrometry. Therefore, the involved instruments, their parameters and data proceeding procedures will be introduced. Furthermore, the details of the two branches of the retrieval algorithm will explained: A radar-lidar inversion and forward radiative transfer calculations of the spectrometer. Finally, a categorised overview of the used methods and codes, a flowchart of the hole algorithm and all the assumptions used in the algorithm are presented.

3.1. Basic Idea

The main idea of the proposed retrieval algorithm is based on a comparison of a measurement with a modeling scenario as sketched in Figure 3.1. The first step will be to develop a radar-lidar inversion procedure to derive microphysical profiles from co-located radar and lidar observations. They are suitable instruments for cloud observations, because they operate at different wavelengths, and therefore they are sensitive to different sizes of ice cloud particles and subsequently to different moments of the cloud's particle size distribution (PSD). These two independent measurements allow a well-constrained retrieval of ice water content IWC and effective radius R_{eff}. The second step will be to use a three-instrument retrieval framework to validate the radar-lidar inversion results with other observations. It is helpful to use an instrument working at other wavelengths as the active sensors, to evaluate the radar-lidar retrieval performance. The derived profiles of IWC and R_{eff} will be used alongside profiles of traces gases and prognostic variables from re-analysis models (Dee et al., 2011) and different microphysical assumptions to simulate the spectrum of the infrared spectrometer. Now, it is possible to minimise the spectral residuals between measured and simulated spectrum by iterating the possible microphysical assumptions.

Concerning the used terminology, SynCirrus describes a three-instrument retrieval based on radar, lidar and infrared spectrometry data. The radar-lidar inversion is a sub-retrieval of SynCirrus and is only responsible for deriving IWC and R_{eff} for given set of ice crystal assumptions. SynCirrus will then use the derived microphysical profiles for forward radiative transfer calculations to minimise the spectral residuals with measurements from the co-located infrared spectrometer. In the literature, such a spectral comparison between multiple different measurements or simulation techniques is often denoted as radiative closure study or closure experiment (Sussmann et al., 2016). A radiative clousure experiment is a tool, that allows to evaluate retrieved microphysical properties (Comstock et al., 2007), or to validate and improve the spectroscopic parameters (absorption models and spectral line parameters) used in line-by-line radiative transfer models (Turner et al., 2004). However, the SynCirrus algorithm minimises the spectral residuals for different assumptions and tries to retrieve the best matching microphysical assumptions. Therefore, it is more appropriate to describe SynCirrus as three-instrument retrieval instead of a closure study, because the spectrometer is not an independent measurement anymore but rather a part in the retrieval procedure.

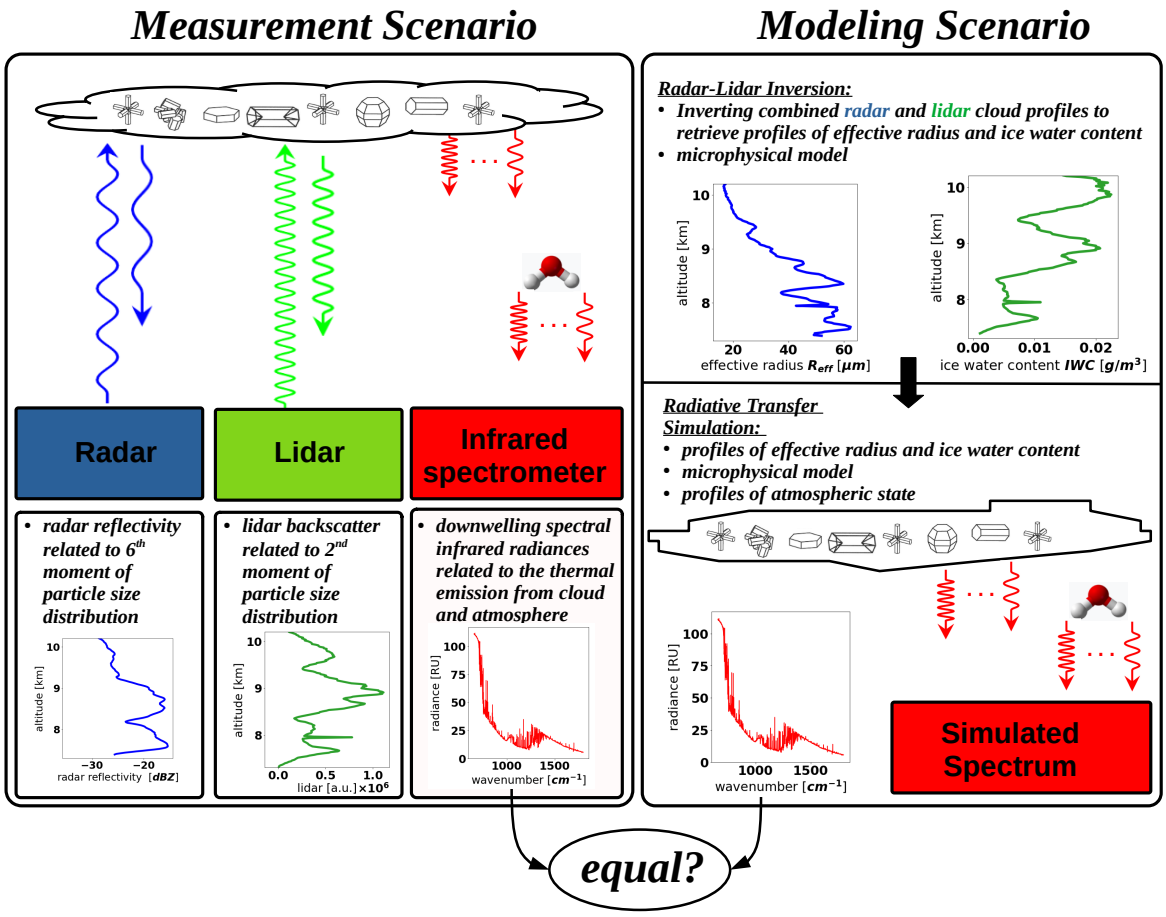

Figure 3.1.: Overview of the proposed measurement and modelling scenarios for co-located measurements based on radar, lidar and infrared spectrometry as input for a synergistic retrieval algorithm to derive microphysical profiles from ice clouds with examples of typical measured cloud signals. The radar signal is more sensitive to particle size (R_{eff}) and the lidar signal is more sensitive to the ice water content, due to their wavelength influenced sensitivity on different moments of the PSD. The hydrogen molecule is representative for the absorption by all atmospheric traces gases.

3.2. Instruments and Data Processing

3.2.1. Setups and Instrumentations

For this work, two types of data were used. The first data were recorded during the NARVAL-I aircraft field campaign (Konow et al., 2018). This campaign had the aim to validate various remote sensing measurements on board of the HALO aircraft with satellite measurements. The High-Altitude LOng-endurance (HALO) aircraft instrumental payload includes a microwave radiometer, a lidar, a cloud radar and dropsondes, and is operated by the German Aerospace Center (Deutsches Zentrum für Luft- und Raumfahrt, DLR). These data were interesting, because the results of the developed radar-lidar ice cloud retrieval could be compared with results from a well established method, that uses a different approach (VarCloud, Delanoë and Hogan (2008)). It is helpful to check, where the radar-lidar inversion is performing well, and if all the included corrections like for lidar multiple scattering and numerical stability are working correctly. In this campaign, the used radar was working on a frequency of 35.5 GHz (8.45 mm) and lidar used the 532 nm wavelength channel. The data from the instruments used during NARVAL-I are summarised in Table 3.1.

The second dataset was recorded at two measurement sites at Mount Zugspitze (summit station and research station UFS). The instrumentations on both sites are operated by the Institute of Meteorology and Climate Research Atmospheric Environmental Research (Institut für Meteorologie und Klimaforschung Atmosphärische Umweltforschung, IMK-IFU). This place offers very dry atmospheric conditions at high altitudes with no saturated spectral regions of the AERI instrument, and is therefore a formidable place to exploit spectrometer data for a cloud retrieval or for a radiative closure study (Sussmann et al., 2016). Radiative comparisons between simulated and measured infrared radiances are helpful to analyse the retrieved microphysical content from an ice cloud by exploiting radar and lidar signals. The main idea is to use the retrieved microphysical profiles as input for a radiative transfer solver to compute a radiance spectrum. Iterating over the retrieval assumptions (ice properties and retrieval technique) in order to minimize the spectral residuals between simulation and observations, will help to find the best matching microphysical assumptions. On the two Zugspitze sites, the used radar was working on a frequency of 36.0 GHz (8.33 mm), the ceilometer used the 1064 nm wavelength channel and the AERI spectrometer was detecting radiances in the thermal infrared spectral range from 550 cm^{-1} to 3000 cm^{-1} (3.3 µm to 18.2 µm). The instrument specifications used at Zugspitze sites are given in Table 3.2. VarCloud could not be used to evaluate the data from Mount Zugspitze, because it requires calibrated lidar signals and only ceilometer data were available for cloud measurements.

In Figure 3.2, the mentioned ground-based (Mount Zugspitze summit station and UFS) and aircraft (HALO during NARVAL-I) instrumental setups are illustrated.

3.2.2. Lidar Signal Processing

Difference between detected Cloud Boundaries by Radar or Lidar

Radar-lidar cloud retrievals are only applicable to parts of the signal, where both, radar and lidar have detected a cloud simultaneously in the corresponding range gates. Due to their different sensitivities, cloud base and top detected by a lidar does not have to be identic with their radar counter-parts. Where a radar could miss small ice crystals in a cloud, a lidar would suffer strong attenuation in optical thick clouds, unable to detect cloud top properly

(Wang and Sassen, 2001) in ground-based configuration. Therefore, the signals of radar and lidar have to be preprocessed separately to detect clouds and find possible vertical high signal overlap regions, suitable for usages in cloud retrievals, afterwards. Due to the large wavelength emitted by radars pulses, there will be no significant return from hydrometeors smaller than cloud particles. But lidars are able to record various atmospheric targets. Here, a main differentiation is required between cloud and aerosol layers, and subsequently a more detailed signal analysis have to be used. There are different established methods for detecting the planetary boundary layer (PBL), based on gradient (Wang and Sassen, 2001) or wavelet analysis (Brooks, 2003; Baars et al., 2008). All of them, try to separate significant signal features, from the noise background. In the following, a cloud detection algorithm will be introduced. The existing methods for PBL detection, based on the wavelet covariance transform, will be extended to detect cloud boundaries.

Signal to Noise Ratio

All lidar measurements, especially from ceilometers, are influenced by noise. To distinguish, usable signal parts from noise dominated parts, the signal-to-noise ratio (SNR) should be considered. SNR values of 1 or higher are usually considered to be trustworthy, depending on the concrete meteorological application. The photons detected by a lidar obey a Poisson distribution, where the noise is denoted by the square root of the signal (Elbaum and Diament, 1976). To estimate the SNR, the background signal P_{bg}, and the number of laser pulses n during the average time for a recorded measurement should be known (Heese et al., 2010; Mattis and Clough, 2014). If these quantities are not provided, the noise can be estimated, via calculating the standard deviation σ of the lidar signal in the far range of the lidar signal,

Table 3.1.: Technical specifications of the active remote sensing sensors on the HALO aircraft during the NARVAL-I campaign, which will be used in the retrieval algorithm.

	Radar	Lidar
name	HAMP MIRA	WALES
type	pulsed Ka-band, polarimetric Doppler millimeter-wavelength radar	high-power/performance airborne water vapor differential absorption lidar
wavelength/frequency	8.45 mm/35.5 GHz	532 nm/563.5 THz + two other channels
field of view (receiver)	-	1.6 mrad
beam divergence (emitter)	0.56° (6 dB two-way attenuation angle)	1.0 mrad
calibration offset	+7.6 dBZ	-
references	Görsdorf et al. (2015); Ewald et al. (2019)	Wirth et al. (2009)

Table 3.2.: Technical specifications of the active and passive remote sensing sensors at UFS and on summit platform of Mt. Zugspitze, which will be used in the retrieval algorithm.

	Radar	Lidar
name	MIRA-36	JenOptik CHM15k "NIMBUS"
type	vertical pointing pulsed Ka-band, polarimetric Doppler millimeter-wavelength radar	low-power elastic backscatter lidar (ceilometer)
location	UFS, 2671 m a.s.l.	UFS, 2668 m a.s.l.
wave-length/frequency	8.33 mm/36.0 GHz	1064 nm/281.8 THz
field of view (receiver)	-	0.45 mrad
beam divergence (emitter)	0.56° (6 dB two-way attenuation angle)	0.3 mrad
magnetron pulse power	27 kW	-
pump laser pulse energy	-	7 µJ
time resolution	10 s	15 s
range resolution	30 m	5 m to 15 m
calibration uncertainty	1.3 dBZ	-
calibration offset	+4.2 dBZ	-
references	Görsdorf et al. (2015); Ewald et al. (2019); DLR (2022)	Wiegner et al. (2014); Wiegner (2018); Luf (2022)

	Infrared Spectrometer
name	ER-AERI
type	ground-based Fourier transform spectrometer for the measurement of downwelling infrared thermal emission at the Earth's surface
location	Zugspitze Summit station, 2961 m a.s.l.
zenith field of view	46 mrad
time resolution	∼8 min (including data transfer and Interferometer scan period)
viewing modes	• ambient blackbody calibration reference (ABB, 113 s) • hot blackbody calibration reference (HBB, 113 s) • zenith atmospheric view (SKY, 214 s)
measurement sequences	..., HBB, ABB, SKY | ABB, HBB, SKY | HBB, ABB, SKY, ...
spectral coverage	550 cm^{-1} to 3000 cm^{-1} (3.3 µm to 18.2 µm)
spectral resolution	0.5 cm^{-1} (max OPD of 1 cm)
radiometeric calibration	Absolute accuracy: < 1 % of ambient blackbody radiance Reproducibility: < 0.2 % of ambient blackbody radiance
noise	< 0.4 $mWm^{-2}sr^{-1}cm^{-1}$ for 670 cm^{-1} to 1400 cm^{-1}
references	DeSlover et al. (1999); Knuteson et al. (2004a,b); Rettinger (2019)

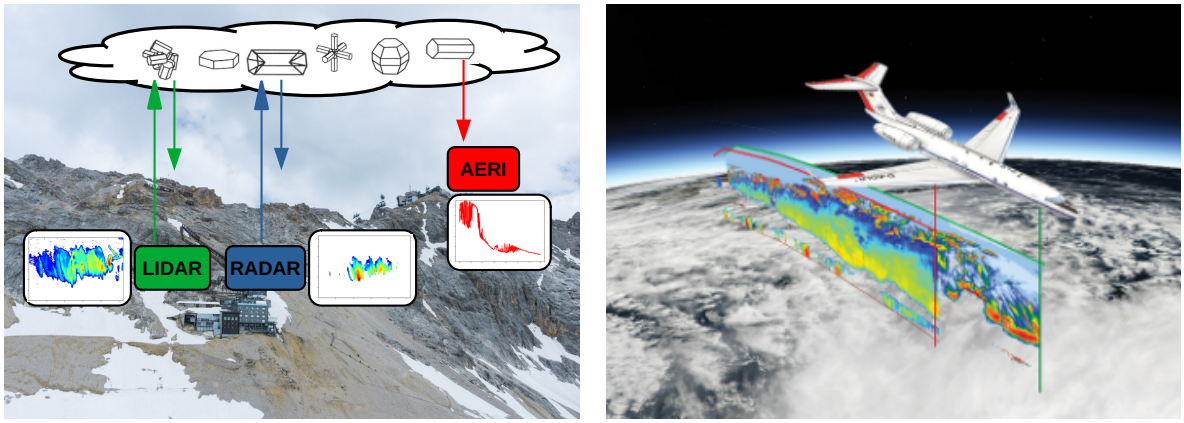

Figure 3.2.: (left) Instrumental setup for a three-instrument retrieval framework at Mount Zugspitze. The derived microphysical profiles from radar (MIRA) and lidar (ceilometer) measurements, located at UFS, will be used as input for RT calculations (libRadtran). The simulated spectrum will be compared with the measured spectrum from the AERI instrument, located at the summit platform. (right) Combination of lidar (WALES) and radar (HAMP MIRA) measurements from the HALO Aircraft. Lidar (green) and radar (red) provide vertical profiles along the flight-track while overflying ice clouds. Pictures are taken, modified and combined from `www.auf-den-berg.de`, Yang et al. (2005b) and Schäfler et al. (2018).

usually the last 100 range gates, where only noise is present (Durieux and Fiorani, 1998). In summary, the SNR is given by

$$SNR(R) = \begin{cases} \frac{nP(R)}{\sqrt{nP(R)+nP_{\mathrm{bg}}}} & n \text{ and } P_{\mathrm{bg}} \text{ provided} \\ \\ \frac{P(R)}{\sigma} & \text{else.} \end{cases} \tag{3.1}$$

In part (a2) of Figure 3.3, an example SNR profile, measured at UFS is shown.

Wavelet Covariance Transform

In lidar signals, detected cloud boundaries and PBL show a sharpe increase of the signal. These signatures have to be identified with signal processing routines. Recent studies, showed that wavelet based techniques are less affected by signal noise than the variance and gradient method (Baars et al., 2008). Wavelet based transformations are “local” transformations, suitable to detects sharp signal transitions, caused by clouds or aerosol layers. The localised transform $W_f(d,t)$ of a function $f(R)$ is

$$W_f(d,t) = \frac{1}{d^p} \int_{R_{\mathrm{min}}}^{R_{\mathrm{max}}} f(R)\; h\left(\frac{R-t}{d}\right) \mathrm{d}R \;, \tag{3.2}$$

where d is the dilation and t is the translation parameter. The function $f(R)$ is the range-corrected lidar signal $P(R)R^2$ and the lower and upper limits of the profile are denoted as $R_{\min}$ and $R_{\max}$, respectively. The step function $h(^{R-t}/_{d})$ is called the Haar function, sometimes Haar wavelet, and is defined as

$$h\left(\frac{R-t}{d}\right) = \begin{cases} +1 & t - \frac{d}{2} \leq R \leq t \\ -1 & t \leq R \leq t + \frac{d}{2} \\ 0 & \text{elsewhere} \end{cases}, \tag{3.3}$$

and has to fulfill some criteria like zero mean and an adequate decay in frequency space (Gamage and Hagelberg, 1993). $W_f(d,t)$ is denoted as *wavelet transform* for $p = {}^1/_2$ (Daubechies, 1988; Grossman, 1989; Meyer, 1989) and as *wavelet covariance transform* (WCT) for $p = 1$ (Gamage and Hagelberg, 1993). In contrary to the wavelet transform, the WCT is not a norm preserving transformation. In the course of this thesis, p is always assumed to be 1. For the Haar wavelet, like shown by Gamage and Hagelberg (1993), the WCT can be rewritten as

$$W_f(d,t) = cov_{f,h}(d,t) \tag{3.4}$$

$$= r_{f,h}(d,t)\left[cov_{f,f}(d,t)\right]^{1/2} , \tag{3.5}$$

$$\tag{3.6}$$

where $r_{f,h}(d,t)$ is the correlation between the functions f and h, and $cov_{f,f}(d,t)$ is the covariance of f with itself. $r_{f,h}(d,t)$ is a measure to describe the similarity in shape between f and h in a close area around t, and will equally weight signals f of arbitrary amplitude but of similar shape. Therefore, $r_{f,h}(d,t)$ can not distinguish noise from desired signal parts. But $cov_{f,f}(d,t)$ is a measure of the variance of the signal f in an area around translation t, and provides a mean of distinguishing of noise and desired signal. Hence, $W_f(d,t)$ is measure for the similarity of f and h, and the form of h is chosen to locate sharp transitions in f, like caused by cloud boundaries and the PBL in lidar signals. In part (b2) and (c2) of Figure 3.3, an example of the Haar wavelet's shape to detect sharp signal transitions is illustrated.

Detection of Alpine PBL

Brooks (2003), showed the utility to use thresholds to separate noise from desired signal and identify the PBL altitude based on WCT analysis. The Haar wavelet has a maximum amplitude of 1, and therefore the range-corrected lidar signal first has to be normalised by the maximum of the PBL, to be usable in a WCT analysis. Because the PBL is temporal much less variable than cloud boundaries, it is useful for the signal normalisation. The extent of the Haar function, the dilation d, is chosen a priori, so the WCT becomes a function of the translation t only, which is mainly the location of the step in h. The dilation is an important parameter for the edge detection and its size should cover the transition zone. A good value of d was found to be 490 m. For much smaller values of d, the noise will dominate the WCT profile of $P(R)R^2$, and much larger values can lead to a cut-off of the lower and upper parts of the profile, but they are critical for the detection of a shallow PBL. Hence, $W_f(d,t)$ is a similarity measure of $P(R)R^2$ and Haar function h, $W_f(d,t)$ will take a local maximum at the top height of the PBL (see (b3) of Figure 3.3). The first guess for detection of the the

PBL top requires the WCT to pass a wavelet threshold $TH_{\mathrm{WCT,PBL}} = 0.06$ (green line in (b3) of Figure 3.3) and the height of local maximum of the WCT above $TH_{\mathrm{WCT,PBL}}$ will be identified as the PBL top height.

Detection of Cloud Base

The signatures of cloud boundaries in the $P(R)R^2$ signal, always show a steep increase at cloud base and a subsequent strong decrease of the signal, due to the Lambert-Beer term in the lidar equation, until cloud top or the signal will become fully attenuated before reaching it. Because of these characteristic signatures, the WCT can be used for cloud detection as well. Like illustrated in (c3) of Figure 3.3, the WCT first becomes negative at cloud base until it reaches a local minimum, and then becomes positive until reaching the local maximum. Hence, the first guess for cloud top can be identified at the height where the WCT falls between a negative wavelet threshold value of $TH_{\mathrm{WCT,base}} = 0.3$, see green line in (c3) of Figure 3.3. Because of the noise presence two criteria have to be added to establish a more robust cloud base detection: (i) the WCT has to fall below the threshold $TH_{\mathrm{WCT,base}}$ for at least $N = 15$ consecutive range gates, to ensure that the identified cloud base was not caused by a noisy signal part. (ii) The vertical moving average of the $SNR(R)$ profile, with 4 range gates filter length, has to exceed a SNR threshold $TH_{\mathrm{SNR,base}} = 2.5$ for a certain number of consecutive range gates again. The WCT threshold is very good to estimate a first guess of the cloud base and the criteria (i) and (ii) will move the detected cloud base a little bit up if necessary, to have numerically more robust results.

Detection of Cloud Top

The detection of cloud top is similar to the base detection. A wavelet criteria will provide the first guess for cloud top and two following signal criteria (i) and (ii) will investigate the signal quality and lower the detected cloud top if necessary. The wavelet criteria to identify cloud top relies on calculating the cumulative WCT (CWCT)

$$\mathrm{Cum}(W_f(d,t)) \coloneqq \int_{\mathrm{cb}}^{t} W_f(d,t')\mathrm{d}t' \ , \tag{3.7}$$

where cb is the already detected cloud base. As indicated in (d3) of Figure 3.3, the cumulative WCT, starting from detected cloud base is negative and becomes smaller until reaching a local minimum. Now, the CWCT, increases until it reaches positive values around cloud top. The first guess for detecting cloud top is, where CWCT first exceeds the wavelet threshold of $TH_{\mathrm{WCT,base}}$. As for cloud base, the signal quality criteria (i) and (ii) are applied and would lower the detected cloud top a little bit, if necessary.

Application to Datasets

Depending on the wind speed and the structure of the cloud, the lidar signals could be temporal averaged to reduce noise, before using them in a WCT analysis. The used thresholds were found to deliver good results but have to be chosen a priori and they would differ for a different lidar system. To have a fully consistent procedure, one could use a machine learning based preprocessing, to be independent of specific lidar system parameters (Wang et al., 2020;

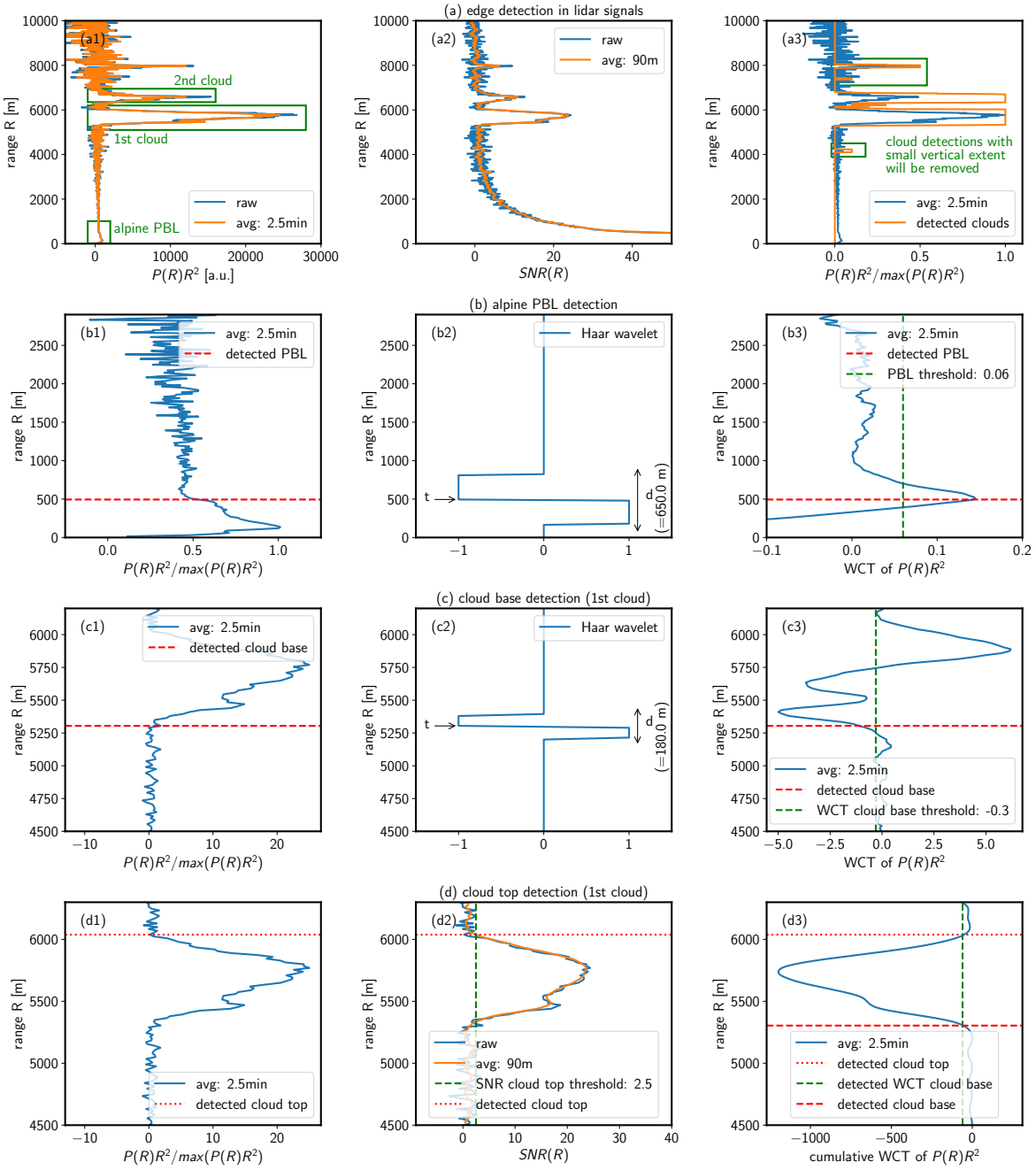

Figure 3.3.: Schematic illustration of the steps in the cloud detection algorithm for a ceilometer backscatter profile recorded at UFS (2017-05-10 23:52:10 UTC). Due to the high altitude of the ceilometer location, it is recording an alpine PBL, a PBL associated with mountain regions. Its signal is much weaker and temporal more variable than the ordinary PBL. The negative signal parts of the range-corrected ceilometer signal $P(R)R^2$ are caused by background subtraction. The temporal filter length of the signals is 2.5 min.

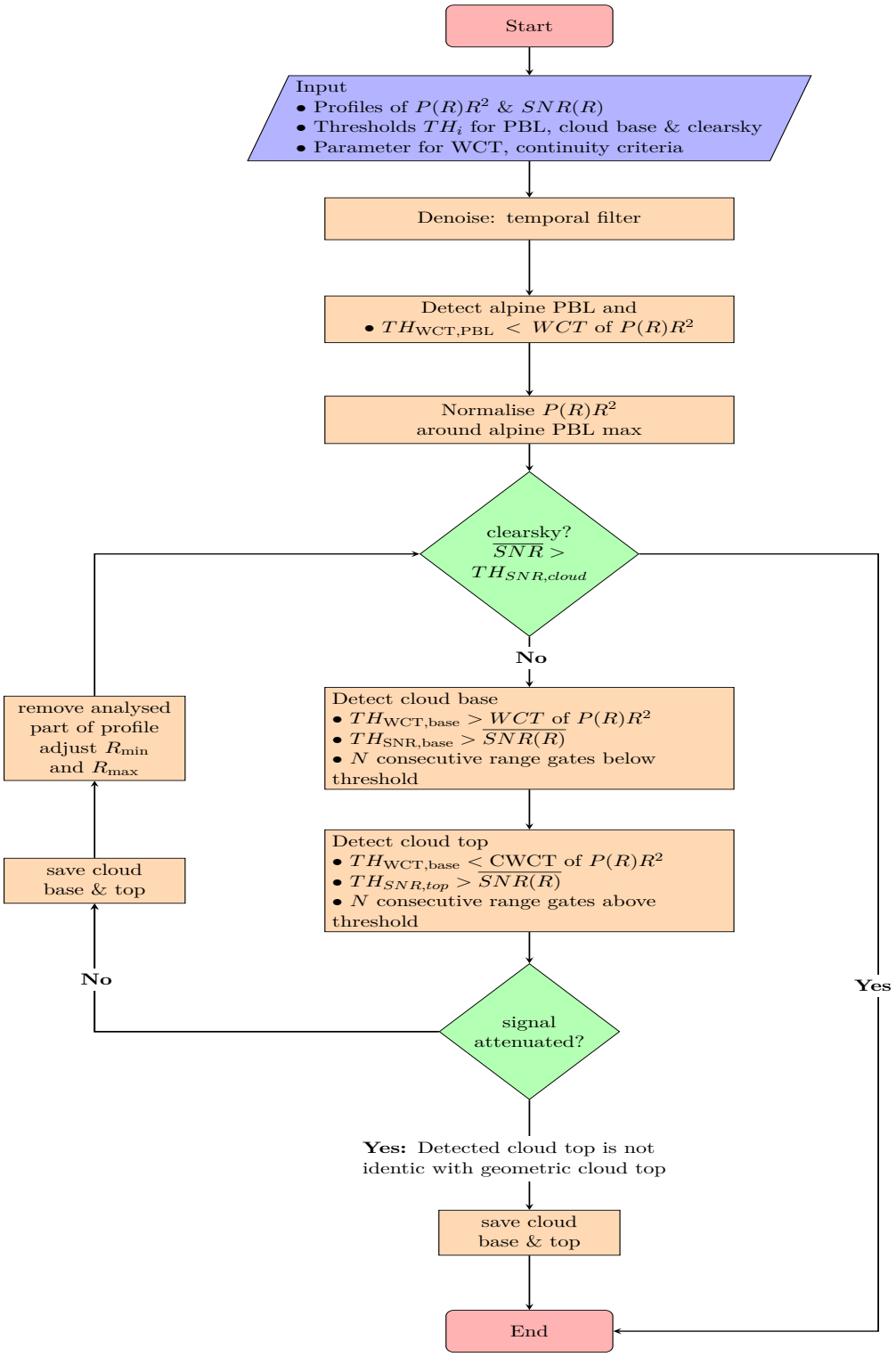

Figure 3.4.: Flowchart to illustrate the steps involved in the cloud detection algorithm.

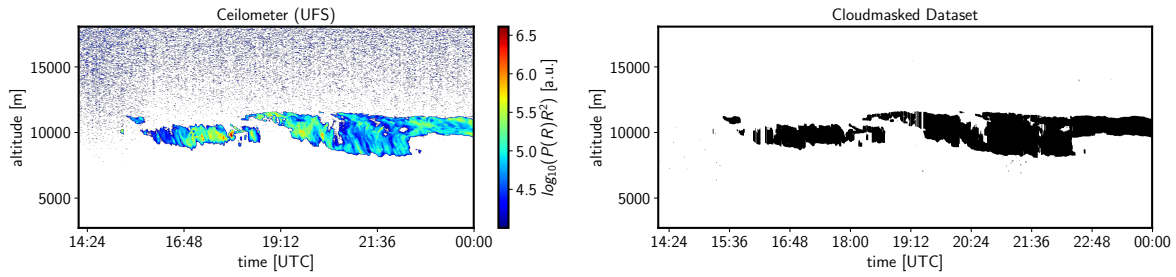

Figure 3.5.: (left) Range-corrected lidar signal $P(R)R^2$, measurement recorded from a Ceilometer at UFS at 17th November, 2012. (right) Corresponding cloud masked dataset after WCT analysis. For very low signal values, the SNR threshold is not exceeded and therefore no clouds will be detectable.

Yorks et al., 2021). In Figure 3.5, an example of a cloud masked dataset, recorded from a ceilometer at UFS, is shown.

3.2.3. Radar Signal Processing

Ewald et al. (2019) explored, that measured radar reflectivities from HAMP MIRA had to be corrected for an offset of +7.7 dB. Because the MIRA radar used at UFS is similar constructed, its data have to be corrected as well, but there are some differences between aircraft and ground-based instrumentation (Ewald, 2019), lowering the offset to +4.2 dB, like shown in Table 3.3.

Correction of Radar Signal Attenuation

The observations made by molecular spectroscopy showed, that there are electronic, vibrational, or rotational transitions of quantised states of molecules in the gas phase. Electronic transitions have energies in the optical and UV range, vibrational transitions occur between different vibrational levels of the same electronic state and have energies in the IR range, and rotational transitions occurring mostly between rotational levels of the same vibrational state and have energies in the microwave region (Demtröder, 2010). Therefore, when dealing with radar waves, only rotational transitions are important, and under atmospheric circumstances, these transitions are broadened proportional to the air pressure and due to the Doppler effect (Maryott and Birnbaum, 1962). Radars with frequencies higher than 94 GHz are generally considered to be unsuitable for ground-based observations of ice clouds, due to the strong water vapour and oxygen absorption in the boundary layer (Hogan et al., 2006c). Below frequencies of 100 GHz, the gaseous attenuation of a radar beam is dominated by oxygen and water vapour, as illustrated in Figure 3.6 (a). For high ice clouds in altitudes of 10 km the two-way gaseous attenuation of a radar beam at 36 GHz, can amount up to 1.5 dB and lies in the same order of magnitude as the calibration uncertainty, as shown in Figure 3.6 (b). Therefore, a correction on the radar reflectivity must be applied for the attenuation by intervening atmospheric gases

$$Z_{\mathrm{e,corr}}(z) = Z_{\mathrm{e}}(z) + 2\int_0^z K_f\left[P(z'), T(z'), RH(z')\right] \mathrm{d}z' \quad , \tag{3.8}$$

Table 3.3.: Overview of the different contributions to the radar calibration offset, relevant for NARVAL-I and UFS data. The parameters are according to Ewald et al. (2019, Table. 2) and (Ewald, 2019).

Parameter	Original	Ewald Study	Offset HAMP-MIRA	Offset UFS-MIRA
receiver and transmitter waveguides	-	1.5 dB	+1.5 dB	-
finite receiver bandwidth	-	1.2 dB	+1.2 dB	+1.2 dB
belly pod radome	1.0 dB	3.0 dB	+2.0 dB	-
peak antenna gain	49.75 dBi	50.0 dBi	-0.5 dB	-0.5 dB
antenna half-power beamwidth	0.6°	0.56°	+0.6 dB	+0.6 dB
RF front-end noise figure	8.8 dB	9.9 dB	+1.1 dB	+1.1 dB
RF noise bandwidth	5 MHz	7.5 MHz	+1.8 dB	+1.8 dB
total offset			+7.7 dBZ	+4.2 dBZ

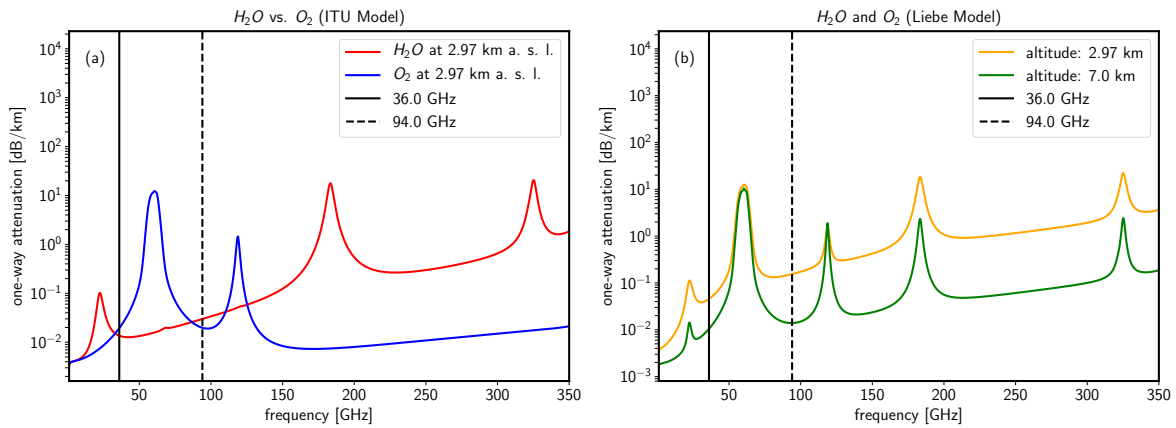

Figure 3.6.: Theoretical values for signal attenuation of radio waves by atmospheric gases using re-analysis data from 22nd October, 2013 for the gridbox including Mt. Zugspitze at two different altitudes. (a) Attenuation caused by H_2O or O_2 alone, and (b) Attenuation caused by H_2O and O_2 for two different altitudes. The meteorologic parameters at 2.96 km a. s. l are 52 % relative humidity, 277 K, 714 hPa and water vapour mass density of 3.24 g m^{-3}, and at 7.0 km a. s. l are 29 % relative humidity, 249 K, 423 hPa and water vapour mass density of 0.22 g m^{-3}.

where Z_e, P, T and RH denote the measured attenuated radar reflectivity factor (dBZ), the air pressure, the temperature and the relative humidity, respectively. The coefficient K_f is the one-way specific attenuation from atmospheric gases (dB km^{-1}) for frequency f and is calculated based on ITU (2013) or with the pyMPM code based on the model presented in (Liebe et al., 1993). In Equation (3.8), the assumption was used, that the radar attenuation by ice clouds can generally be considered to be negligible up to 94 GHz (Hogan and Illingworth, 1999), and hence it is sufficient to only calculate the attenuation up to the ice cloud base. For the inclusion of liquid water clouds and melting ice, there would be a significantly higher attenuation and the two-way gaseous attenuation factor has to include liquid water content additionally (Lhermitte, 1990; Hogan et al., 2005).

3.2.4. Interferometer Spectra Processing

Uncertainty from Spectral Radiance Measurements

AERI measurements provide absolute downwelling atmospheric emitted infrared radiances with high spectral accuracy (0.4821 cm^{-1},Knuteson et al. (2004b)). To give a meaningful comparison of them with RT simulations, the uncertainties for recording spectral radiances should be investigated. Following Knuteson et al. (2004a,b), there are three main sources of uncertainty. First, there is the AERI measurement noise, an estimate of this radiance measurement noise is automatically generated by the AERI software within the radiometric calibration procedure according to the method established by Revercomb et al. (1988); Sussmann et al. (2016). A noise reduction of about 50 % can be achieved by applying a principal component analysis filter (PCA, Turner et al. (2006)) to the spectra. The other two radiance uncertainties are associated with the radiometric calibration errors. The calibration uncertainty is estimated to be less than 0.67 % (2 σ), and the repeatability (precision) is assumed to be 0.13 % (2 σ) of the ambient blackbody radiance, like shown by Knuteson et al. (2004b). The resulting radiance uncertainties are shown in Figure 3.7 for a clear sky and a clouded scene. The dominant part of the uncertainties is caused by the radiometric calibration. For clear sky closure experiments, the AERI uncertainty should be considered, but for spectra recorded from clouded scenes the radiometric calibration error is negligible in comparison to uncertainties caused by the retrieval method (Blanchard et al., 2017). Hence, due to the high spectral and absolute accuracy, AERI measurements are considered to be suitable for spectral comparison with RT simulations of clouded scenes.

Selection of Spectral Microwindows in Atmospheric Spectroscopy

Spectrometer measurements include mainly contributions from line absorption (typically from water vapour), continuum absorption (the sum of the contributions of absorption in the far wings of the line), and cloud absorption. Due to the spectral resolution of the AERI of 0.4821 cm^{-1}, it is possible to find spectral *microwindows* of cloud absorption between gaseous absorption lines. Therefore, microwindows are the least-absorbing regions within the spectral bandpass of the instrument and offer the possibility to evaluate spectral comparisons in the least "contaminated" regions, which relieves the analysis of cloud microphysics by separating the uncertainty in the strength and width of the individual absorption lines (DeSlover et al., 1999; Yang et al., 2005a; Guo et al., 2005; Turner, 2005). In Table 3.4, a number of low-absorption regions, that will be used for analysing the impact of clouds on a spectrum, are listed and illustrated in Figure 3.8.

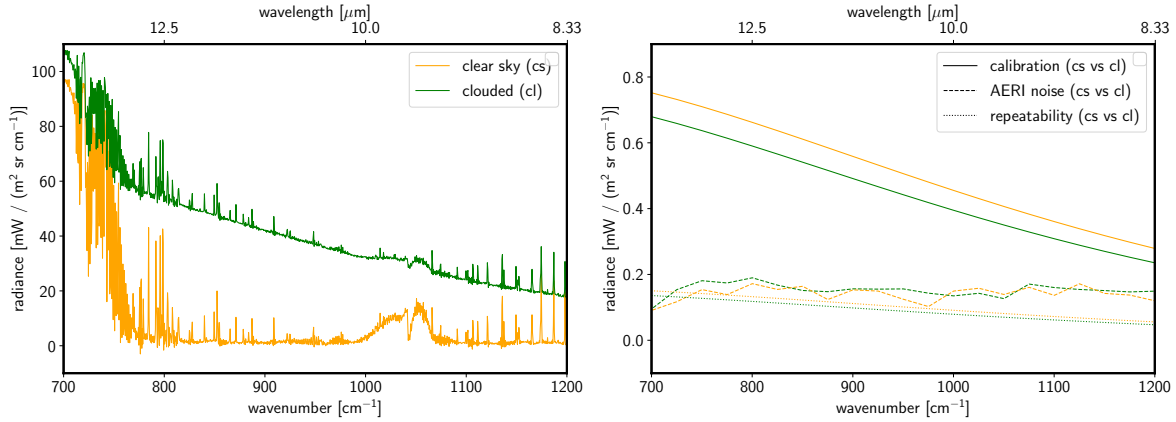

Figure 3.7.: Contributions to uncertainty budget in AERI measurements from 18th October, 2013 with radiance spectra recorded from a clouded (23:39:17 UTC) and a clear sky scene (03:52:48 UTC).

There are different strategies possible, to exploit the information content represented by the recorded spectral radiances in the microwindows. In retrievals, the spectral residuals (measured spectrum minus best-fitting simulated spectrum) could be calculated by simple formations of means in the microwindows or by using optimal estimation methods (von Clarmann and Echle, 1998). The number and location of microwindows is somehow arbitrary, as long as they are chosen in the atmospheric infrared window, similar results can be obtained with different sets of microwindows (Turner, 2005).

In contrary to single or multi-channel broadband thermal radiometers, high resolution spectrometer and the propositioning exploitation of consecutive spectral grid points in microwindows offers several advantages. For example, distortions in the shapes of spectral lines, can cause an overestimation of the measured radiances at some spectral grid points, but can also cause an underestimation of the measured radiances at some others points, consequently the usage of well-chosen microwindows allows for a partly compensation of these effects. Furthermore, systematic errors in retrievals typically translate into typical structures of the residual spectrum, an information that would be lost with only using a single spectral grid point (von Clarmann and Echle, 1998; Blanchard et al., 2017).

3.2.5. Target Classification

Before the cloud-masked data can be evaluated, it is important to determine the nature of the target in each observed pixel on the interpolated common radar-lidar grid. Currently, the SynCirrus algorithm can only retrieve ice cloud properties, but liquid water and mixed-phase clouds could be included in the future. The cloud phase information is also very important for radiative transfer calculations, see Figure 3.13. The presence of liquid water layers in the measured profile, can lead to a significant reduction of the detected infrared radiances compared to, when only ice is present. Therefore, simulated infrared radiances would be overestimated, if they do not account for the liquid part of the profile. Hence, the algorithm searches for cloud areas, where the temperature is below -38 °C, because for these temperatures clouds consist almost exclusively of ice crystals (Korolev et al., 2017).

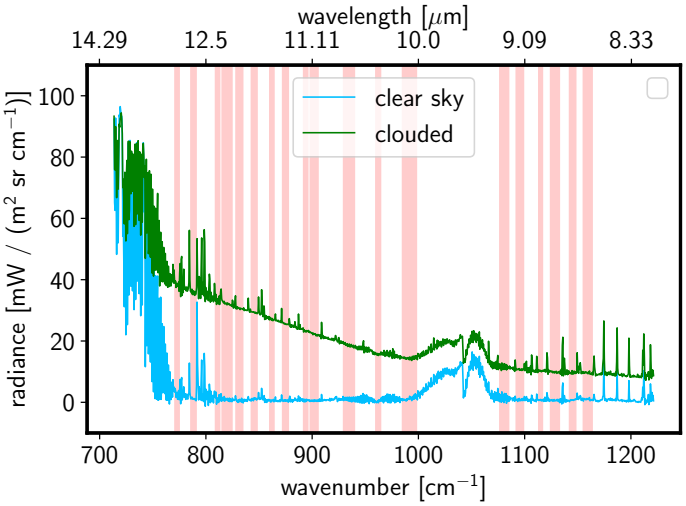

Figure 3.8.: Used microwindows between strong absorption lines. AERI measurement from 23rd November, 2012 with radiance spectra for clouded (00:16:59 UTC) and a clear sky scene (06:23:17 UTC).

Table 3.4.: Selection of microwindows regions, according to (DeSlover et al., 1999; Turner, 2005).

Window	**Region** [cm^{-1}]	**Region** [μm]
1	770.900 to 774.800	12.972 to 12.907
2	785.917 to 790.739	12.724 to 12.646
3	809.061 to 812.919	12.360 to 12.301
4	815.330 to 824.491	12.265 to 12.129
5	828.348 to 834.617	12.072 to 11.982
6	842.814 to 848.118	11.865 to 11.791
7	860.172 to 864.030	11.626 to 11.574
8	872.227 to 877.531	11.465 to 11.396
9	891.996 to 895.853	11.211 to 11.163
10	898.264 to 905.497	11.133 to 11.044
11	929.606 to 939.731	10.757 to 10.641
12	959.982 to 964.323	10.417 to 10.370
13	985.056 to 998.075	10.152 to 10.019
14	1076.670 to 1084.867	9.288 to 9.218
15	1092.100 to 1098.850	9.157 to 9.100
16	1113.316 to 1116.691	8.982 to 8.955
17	1124.406 to 1132.603	8.894 to 8.829
18	1142.246 to 1148.032	8.755 to 8.711
19	1155.265 to 1163.462	8.656 to 8.595

The results were compared and cross-checked with the target categorization used in Cloudnet (Hogan and O'Connor, 2004a; Hogan et al., 2006a; Illingworth et al., 2007b; Delanoë and Hogan, 2010).

3.2.6. Meteorological Re-Analysis

Among the variable greenhouse gases in Earth's atmosphere, the strongest contribution is from water vapour, as mentioned in Section 2.1.2. To be able to undertake reasonable radiative transfer calculations, at least, current profiles of temperature, pressure and the water vapor concentration need to be known. If close-by radiosonde data are not available, these profiles can be obtained by meteorological re-analysis, at the cost of a higher uncertainty. Re-analysis data are based on the assimilation of quality-checked observational data into calculations based on weather and climate models. These data offer global fields at different altitude model levels of various parameters and are calculated backwards over a long period of time using all suitable observational data available, with the aim to provide a temporally and spatially highly resolved homogeneous dataset. In this thesis, meteorological data from the European Center for Medium-Range Weather Forecasts (ECMWF) ERA-Interim re-analysis (Dee et al., 2011; Hoffmann et al., 2019) were used. ERA-Interim data offer a horizontal resolution of approximately 80 km on 60 vertical model levels and 37 vertical pressure levels, from the surface up to a pressure of 0.1 hPa. The temporal grid provides these profiles in steps of 6 h at 0, 6, 12 and 18 UTC every day. The used ERA-Interim quantities are temperature, relative and specific humidity, surface geopotential, surface pressure, surface temperature, surface dew point and model levels. The suitable ECMWF grid box is for the geographical location of Mount Zugspitze is chosen by applying the Haversine formula which determines the shortest distance between two points on the surface of a sphere given their longitudes and latitudes (Chopde and Nichat, 2013). With the pressure level coefficients and the surface pressure, the air pressure on model levels can be calculated. The specific humidity at surface can be calculated using surface temperature, surface pressure and surface dew point temperature by using the Clausius-Clapeyron equation. With these quantities and the virtual temperature, using the hydrostatic equation, the pressure differences can be converted to height differences. Finally, the water vapour number density can be calculated with the ideal gas equation using air pressure, specific humidity and temperature. All the used and mentioned conversion formulas can be found in Berrisford et al. (2011) and Stull (2015).

3.3. Radiative Transfer Simulations

3.3.1. Library for Radiative Transfer - libRadtran

Radiative transfer (RT) calculations to simulate the AERI spectrum were taken out by using the *libRadtran* software package (Mayer and Kylling, 2005; Emde et al., 2016). Besides RT radiance calculations, libRadtran was also used for Mie calculations. The main tool of this software library is *uvspec* which contains several solvers for the RT equation. As input, uvspec requires a description of the atmospheric state, e.g. atmospheric profiles of trace gases and cloud profiles of ice water content and effective radius. Several parameterisations can be chosen, to convert the atmospheric state into single-scattering or optical properties,

see Section 2.1.3, and then they will be passed to the RTE solver to take out calculations monochromatically or in desired wavelength bands.

In the thermal infrared region, there are thousands of narrow absorption lines, due to several vibrational or rotational transitions in molecules from atmospheric gases. To handle spectral regions, that are affected by molecular absorption, libRadtran offers different parameterisations. Among others, there is the *reptran* parameterisation, where integrals over spectral intervals are parameterized as weighted means over representative wavelengths (Gasteiger et al., 2014). For "exact" spectral calculations, it is possible to rely on Line-By-Line (LBL) models, where libRadtran offers the possibility to use predefined spectrally resolved absorption cross-section profiles from LBL models like ARTS (Eriksson et al., 2011; Buehler et al., 2018), which in turn are using spectroscopic databases like HITRAN as input (Rothman et al., 2005, 2009).

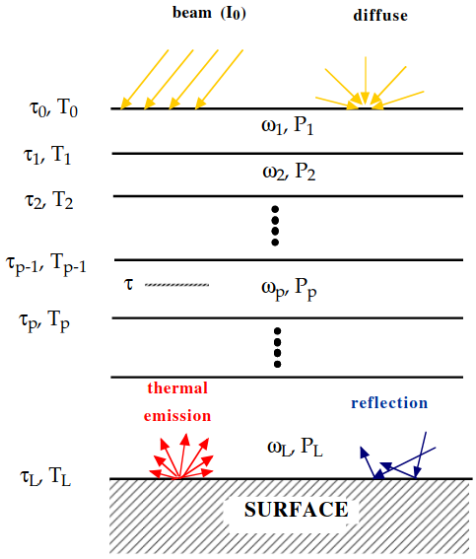

Figure 3.9.: Schematic illustration of a multilayered plane-parallel horizontally homogeneous medium. The optical properties of a layer is characterized by its optical thickness τ_p, the single-scattering albedo $\omega_{0,p}$, and the scattering phase function P_p. They are constant within each layer, but allowed to vary from layer to layer. Figure taken from Stamnes et al. (2000).

3.3.2. 1D Radiative Transfer Solver - DISORT

The DIScrete ORdinate Radiative Transfer procedure (DISORT), proposed by Chandrasekhar (1960) and implemented by Stamnes et al. (1988), is a numerical method to approximately solve the RT equation for a multi-layered plane-parallel atmosphere in one-dimensional geometry, see Figure 3.9. The main idea is, to apply three types of discretisations to the RTE and transform the pairs of coupled integral-differential equations into a simpler system of linear coupled ordinary differential equations. These equations are finally converted into a high-dimensional linear algebra system, which is solved like an eigenvalue problem (Stamnes et al., 2000; Liang, 2004).

The purpose of the first two discretisations, is to factor out the azimuthal dependence. The

scattering particles in an atmospheric layer are assumed to have random orientations and therefore ω_0 does not explicitly depend on the direction of the incident beam and the phase function P only depends on the angle between incident and scattered beam, $P(\tau, \mu, \phi; \mu', \phi') = P(\tau, \cos\Theta)$. Due to this restriction, it is possible to expand the phase function into a series of Legendre polynomials P_l

$$P\left(\tau, \cos\Theta\right) = \sum_{l=0}^{2N-1} \left(2l+1\right) g_l P_l\left(\cos\Theta\right) \ , \tag{3.9}$$

where g_l are expansion coefficients. Applying the addition theorem for spherical harmonics, allows to transform the Legendre polynomials P_l into a Fourier cosine series (Stamnes et al., 2000; Kokhanovsky, 2021) of ϕ (Kokhanovsky, 2021). Because of this, it is useful to use the second discretisation to similarly expand the radiance into a Fourier cosine series as well

$$L(\tau, \mu, \phi) = \sum_{m=0}^{2N-1} L^m(\tau, \mu) \cos\left[m\left(\phi_0 - \phi\right)\right] \ . \tag{3.10}$$

These two discretisations will split the RTE into a set of $2N$ independent integro-differential equations, one for each azimuthal radiance component L^m, it uncouples the Fourier components, and they do not depend on azimuth angle any more.

The final discretisation uses the method of discrete ordinates, to sample μ for the zenith angle distribution. Therefore, the angular integrals of the RTE will be approximated via the Gaussian quadrature rule (Stamnes et al., 2000)

$$\int_{-1}^{1} L(\tau, \mu)\mathrm{d}\mu \ \approx \ \sum_{j=-N}^{N} w_j L(\tau, \mu_j) \ , \tag{3.11}$$

where w_j is the quadrature weight and μ_j is called discrete ordinate. The quadrature weights are orthogonal polynomials, that can be integrated, but the quadrature rule will only be an accurate approximation to the integral above, if $L(\tau, \mu)$ is well-approximated by a smooth Legendre polynomial of degree $2N-1$ or less on $[-1, 1]$. The use of Gaussian quadrature guarantees that the phase function will be normalized, implying that energy is conserved for the computations. The number of streams is given by $2N$ and libRadtran uses 16 streams as default.

These three discretisations allow for a compact matrix formulation of the RTE for every layer in Figure 3.9. Because the resulting form of the RTE is linear in radiance, its general solution is given by the sum of two separate solutions, the homogeneous (no thermal source) and particular solution. The required boundary conditions are given by solving linear algebraic equations for the arbitrary constants of the homogeneous solution (Kokhanovsky, 2021).

The most important feature of DISORT is, its unconditionally stability for an arbitrarily large number of quadrature angles (streams) and arbitrarily large optical depths (Stamnes et al., 1988).

3.3.3. Treatment of Molecular Absorption

The passive atmospheric sounder AERI is able to record the downwelling infrared radiances with a high spectral resolution (0.5 cm^{-1}) and is therefore formidable to be used in so-called

clearsky *radiative closure experiments* (Turner et al., 2004; Sussmann et al., 2016). The idea is, to compare measured radiance spectra with simulations (high spectral accuracy) of the spectra driven by coincident-state measurements. When the radiative closure of measured minus simulated spectral radiances will show spectral residuals, they can be minimised by adjusting the atmospheric state input parameters of the model. Hence, a closure study is a quality measurement experiment for the downwelling infrared radiance and helps to validate and improve the absorption models and spectral line parameters used in spectral high resolved radiative transfer models. For comparisons, the RT model should be calculated on a higher spectral resolution than the AERI and the synthetic radiance spectra have to be convolved with a sinc-type instrumental line shape accounting for the maximum OPD (Knuteson et al., 2004b).

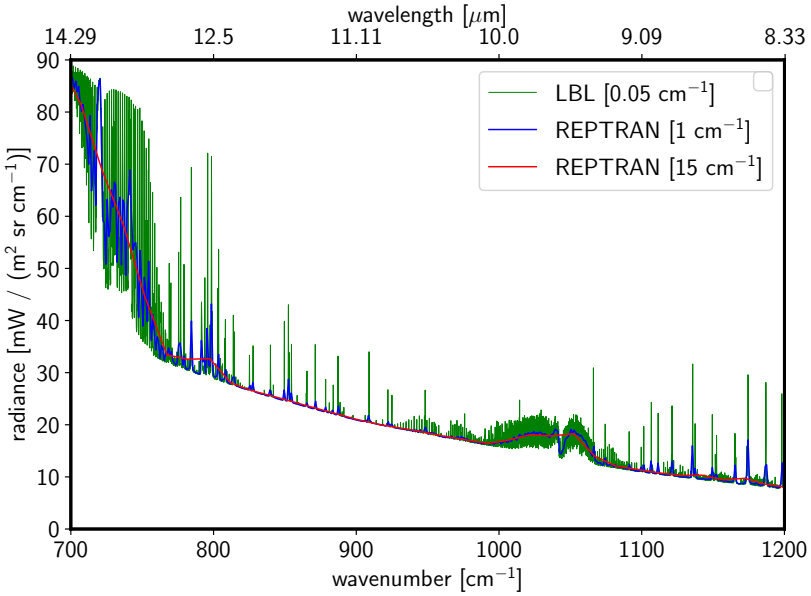

Figure 3.10.: Simulated spectra for a cloud with $\tau = 2.25$, using different molecular parameterisation schemes.

Therefore, clearsky closure comparisons require modeling the radiative impact of molecules and to include radiative processes such as pure rotational absorption/emission in the far infrared (FIR) and vibration-rotation absorption/emission in the mid-infrared (MIR) and the near infrared (NIR). Quantum mechanical selection rules for absorption and emission lead to atmospheric band-type spectra with thousands of individual spectral lines. The most accurate, but very time-consuming, method of simulating these processes is a fully resolved Line-By-Line approach (Eriksson et al., 2011).

Clearsky radiative closure studies for the full infrared spectrum are helpful to gain insight about uncertainties related to the spectroscopic line parameters (e.g., line strength and pressure-broadened half width), but for retrieving ice cloud properties, it is more useful to rely on the analysis of radiances in microwindows, like indicated in section 3.2.4. The uncertainties introduced by the assumptions in a cloud retrieval are probably much larger than the uncertainties in spectroscopic line parameters. Furthermore, if the spectral residuals between an exact method (LBL) and a parameterisation of molecular absorption (e.g. REPTRAN,

max resolution of 1.0 cm^{-1}) are much smaller, than spectral residuals caused by retrieval assumptions, it is possible to compare the AERI spectrum with a simulated spectrum on a coarser grid than 0.5 cm^{-1}, like shown in Section 4.1.1.

Line-By-Line

The LBL method is considered to be an "exact" computation of radiative transfer in the gaseous absorbing/emitting inhomogeneous atmosphere and it includes all (known) gas absorption lines in the wavenumber range from 0 to 17.900 cm^{-1} (Rothman et al., 2005). In order, to be able to resolve individual lines, the absorption coefficient must be computed at wavenumber intervals, that are smaller than the line half-width. The HITRAN database includes more than 1 million line parameters and includes the species H_2O, CO_2, O_3, N_2O, CO, CH_4 and O_2.

REPTRAN

To speed up the costly calculations of spectral ranges affected by fine-structured absorption features of gases, different parameterisation approaches are used. The most prominent, is the *correlated k-distribution* (CKD) method (Fu and Liou, 1992). In this method, the frequency grid will be sorted according to the absorption coefficient at different frequencies. The result is a re-ordered frequency grid, where the spectrum is smooth and monotonic, and therefore it can be approximated with only a few frequency grid points and linear interpolation between them. The disadvantage of the CKD method is that the exact sorting depends on pressure, temperature, and trace gas concentration, and it is thus not straightforward to determine the optimal compromise for a frequency grid sorting (Gasteiger et al., 2014).

An alternative parameterisation to the CKD method, is to approximate spectrally integrated radiances by weighted means of radiances at so-called representative frequencies or wavelengths (Buehler et al., 2010). This method was extended to cloud parameters by Gasteiger et al. (2014). The underlying assumption of this method is that the radiance at a single frequency will be representative for the radiance at some other frequencies, where atmospheric optical properties are considered as similar. Thus, the integrated radiances for a broad instrument channel can be approximated as (Gasteiger et al., 2014)

$$L_{\text{int}} = \int_{\lambda_{\min}}^{\lambda_{\max}} L(\lambda) R(\lambda) \mathrm{d}\lambda \approx \left[\int_{\lambda_{\min}}^{\lambda_{\max}} R(\lambda) \mathrm{d}\lambda \right] \left[\sum_{i_{rep}=1}^{N_{\text{rep}}} L(\lambda_{i_{\text{rep}}}) w_{i_{\text{rep}}} \right] \quad , \tag{3.12}$$

where $R(\lambda)$ is the spectral weighting function of the spectral interval. The selection of an optimum set of representative wavelengths is based on accurate LBL simulations for Top-Of-Atmosphere radiances of a highly variable set of atmospheric states (Emde et al., 2016).

In Figure 3.10, high resolution line-by-line calculations are compared with coarser REPTRAN calculations for the infrared window range.

3.3.4. Ice Crystal Optical Properties

To take out RT calculations with ice crystals in cirrus clouds, the single-scattering properties given by Yang et al. (2013) were used in this thesis. Yang et al. (2013) provides an extensive database of ice crystal optical properties for 11 different ice crystal habits assuming

three-dimensional random orientations. In detail, it contains the extinction efficiency, single-scattering albedo, asymmetry parameter, six independent non-zero elements of the phase matrix, and all given in the spectral range from 0.2 µm to 100 µm. The included ice crystal habits are droxtals, prolate spheroids, oblate spheroids, solid and hollow columns, compact aggregates composed of eight solid columns, hexagonal plates, small spatial aggregates composed of 5 plates, large spatial aggregates composed of 10 plates, and solid and hollow bullet rosettes. For each habit, particle projected area and particle volume is given, and the maximum dimension of each habit ranges from 2 µm to 10 000 µm. Furthermore each ice crystal habit is given at three different surface roughness conditions (smooth, moderately roughened, and severely roughened).

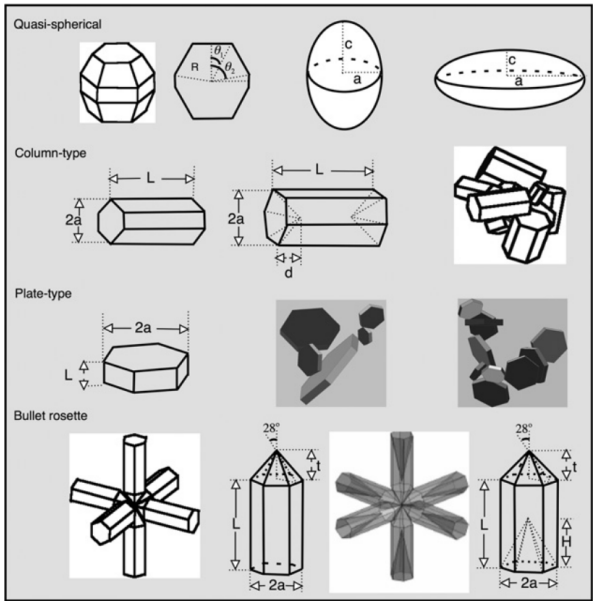

Figure 3.11.: Ice crystal habits given in Yang database. Figure taken from Yang et al. (2013).

The spatial orientation of non-spherical ice crystals in cirrus clouds is a significant factor for RT calculations in the atmosphere (Yang et al., 2000). Models usually distinguish between horizontally (e.g. plates) and randomly oriented ice crystals (e.g. aggregates) in non-turbid atmospheres. Yang et al. (2018) showed, that it is quite reasonable to assume ice particles to be randomly oriented for passive remote sensing applications. In that case, the single-scattering properties for a sample of non-spherical ice crystals have to be averaged over Euler angles (α, γ), that specify the orientation

$$P(\cos\Theta, \Delta\phi) = \frac{1}{2\pi\sigma_{\text{sca}}} \int_0^{2\pi} \int_0^{\pi/2} P(\alpha', \gamma'; \cos\Theta, \Delta\phi)\sigma_{\text{sca}}(\alpha', \gamma') \sin\alpha' \mathrm{d}\alpha' \mathrm{d}\gamma' \quad (3.13)$$

$$\sigma_{\text{ext,sca}} = \frac{1}{2\pi} \int_0^{2\pi} \int_0^{\pi/2} \sigma_{\text{ext,sca}}(\alpha', \gamma') \sin\alpha' \mathrm{d}\alpha' \mathrm{d}\gamma' \quad , \quad (3.14)$$

where (α,α') are zenith angles with respect to the orientation of the ice particle, and (γ,γ') correspond to the azimuthal angles (Liou and Yang, 2016). In case, all non-spherical ice particles would have rotational symmetry (e.g., circular cylinders), then the phase function is independent of the azimuthal angle $\Delta\phi = (\phi - \phi')$.

For surface roughness, the normal distribution of the surface slope of an ice crystal's surface is described by

$$P(Z_x, Z_y) = \frac{1}{\sigma_{\text{sur}}^2 \pi} \exp\left(-\frac{Z_x^2 + Z_y^2}{\sigma_{\text{sur}}^2}\right) \quad , \tag{3.15}$$

following the approach from Cox and Munk (1954), where Z_x and Z_y denote the local slope variations of the particle's surface along the two orthogonal directions x and y. The parameter σ_{sur} is used to quantify the degree of surface roughness: smooth surface ($\sigma_{\text{sur}} = 0$), moderate surface roughness ($\sigma_{\text{sur}} = 0.03$), and severe surface roughness ($\sigma_{\text{sur}} = 0.5$).

3.3.5. Microphysical Model and Single Scattering Properties

In order, to be able to retrieve useful microphysical ice cloud properties, it is necessary, that the two branches of the thee-instrument retrieval (SynCirrus), see Figure 1.2, make consistent assumptions about the underlying microphysical model. The first branch, the radar-lidar inversion procedure, mainly uses assumptions about habit geometry and PSD. The second branch, the RT calculations, extends this to single-scattering properties. The different ice crystal databases available in the scientific community (Yang et al., 2005b; Baum et al., 2005; Yue et al., 2007; Baran, 2009; Baum et al., 2011; Yang et al., 2013), have significant differences concerning their assumptions about ice habits etc., and therefore it is necessary to use the same database consistent in both retrieval branches.

As described in section Section 2.2.1, bulk microphysical properties are required to parameterise ice cloud properties to be used by a RTE solver. Thus, and for operational retrieval usage, the single-scattering properties have to be averaged over various particle size distributions with an assumed ice crystal habit, and have to be tabulated in lookup tables (LUTs) for use in RT calculations.

Assuming, a monomodal generalised gamma distribution, there are two independent parameters, the scale D_s and the shape μ, that have to be fixed. To build up a LUT, it is useful, to calculate the bulk-optical properties on an equidistant effective radius grid, including values from 5 µm to 160 µm in steps of 5 µm, and on an equidistant shape parameter grid, ranging from -1 to 11 in steps of 1 (Heymsfield et al., 2013). Thus, for a given R_{eff}, habit and μ, the scale parameter D_s will be determined by solving the equation

$$R_{\text{eff}} \stackrel{!}{=} \frac{3}{4} \frac{\langle V(D, D_s, \mu) \rangle}{\langle A(D, D_s, \mu) \rangle} \quad , \tag{3.16}$$

for all the LUT grid points. Therefore, the ice crystal optical bulk properties will be calculated via integrating the Yang database according to

$$\langle \beta_{\text{ext}}(R_{\text{eff}}, \mu) \rangle = \frac{\int_{D_{\min}}^{D_{\max}} N(D, \mu) Q_{\text{ext}}(D) A(D) \mathrm{d}D}{\rho_{\text{ice}} \int_{D_{\min}}^{D_{\max}} N(D, \mu) V(D) \mathrm{d}D} \tag{3.17}$$

$$\langle \omega_0(R_{\text{eff}}, \mu) \rangle = \frac{\int_{D_{\min}}^{D_{\max}} N(D, \mu) \omega_0(D) Q_{\text{ext}}(D) A(D) \mathrm{d}D}{\int_{D_{\min}}^{D_{\max}} N(D, \mu) Q_{\text{ext}}(D) A(D) \mathrm{d}D} \tag{3.18}$$

$$\langle P_{ij}(R_{\text{eff}}, \mu, \theta) \rangle = \frac{\int_{D_{\min}}^{D_{\max}} N(D, \mu) P_{ij}(D, \theta) \omega_0 A(D) Q_{\text{ext}}(D) \mathrm{d}D}{\int_{D_{\min}}^{D_{\max}} N(D, \mu) A(D) Q_{\text{ext}}(D) \omega_0(D) \mathrm{d}D} \quad , \tag{3.19}$$

for every ice crystal habit and surface roughness included in the database, where ρ_{ice} is the density of ice, P_{ij} denotes the six independent phase matrix elements and Q_{ext} is the extinction efficiency coefficient.

In Figure 3.12, the absorption and scattering efficiency spectra are shown in order to illustrate the spectral sensitivity of these important radiative transfer parameters. It can be seen, that the thermal IR channels of the absorption efficiency become increasingly less sensitive to particles larger than about 100 µm.

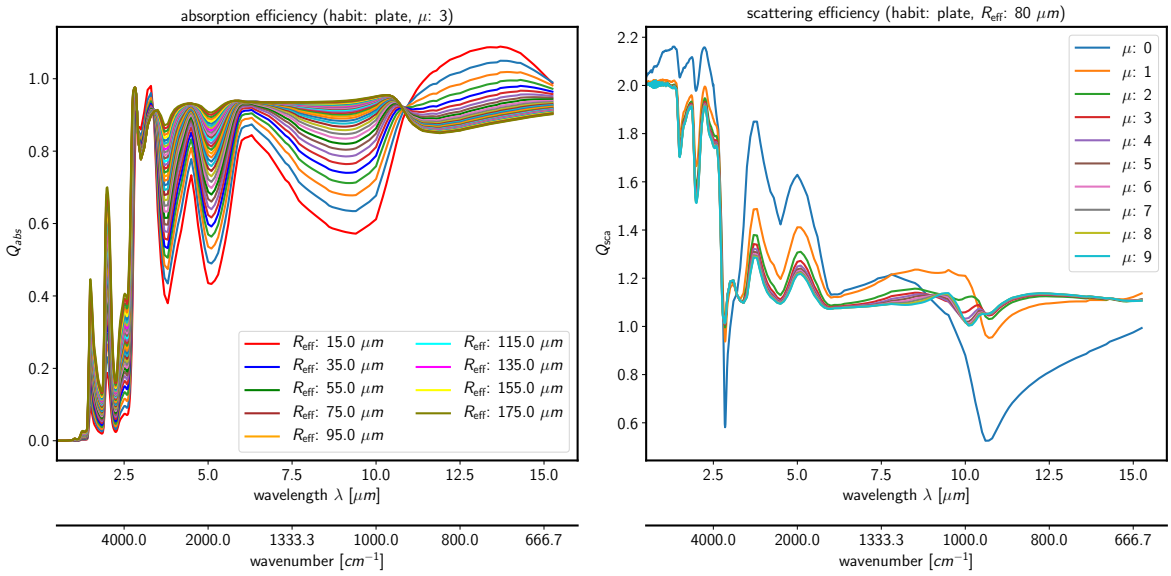

Figure 3.12.: (left) Absorption efficiency spectra for ice crystals across a range of R_{eff} values. (right) Scattering efficiency spectra for a range of different PSD shape parameters μ. Both spectra are for plate like ice crystals with smooth surface roughnesses, obtained by integrating the Yang database.

3.3.6. Magnitude of Processes Contributing in Thermal Infrared Spectrum

The AERI detects downwelling radiation from 3.3 µm to 18.2 µm in the Mid-wavelength infrared region. As shown in Figure 2.1, the most of the radiative energy emitted by the Earth and atmosphere is found in the thermal infrared band from 4 µm to 100 µm. It is apparent, that a wavelength of approximately 4 µm clearly separates the bands containing 99 % of the solar radiation from that containing 99 % of the terrestrial emission. Only for a narrow range of wavelengths in the environment of 4 µm, both terrestrial and solar radiation have to be considered because they are in a similar order of magnitude.

In both spectral regions, the dominant particle-radiation interaction process is different. Scattering by cloud particles or gas molecules, is much less important when the gains of the intensity field due to scattering along a particular viewing direction are negligible compared to losses caused by extinction and gains because of thermal emission. These conditions are usually fulfilled for atmospheric radiation in the thermal IR band. Here, the longer wavelengths would require larger particles than molecules and cloud particles to be capable of undergoing scattering events appreciably. But for precipitation particles like raindrops,

snowflakes and hailstones scattering can not be neglected. These findings are summarised in Figure 3.13 (a) and (b). Knowing, that absorption is the most dominant process contributing to the measured AERI spectrum, the question arises which set of microwindows would be beneficial to explore the radiative impact of ice crystals from cirrus clouds. In Figure 3.13 (c) it is demonstrated, that the set of microwindows from Table 3.4 is suitable for the mentioned task, because it exploits regions where the absorption of ice is greater than that of liquid water.

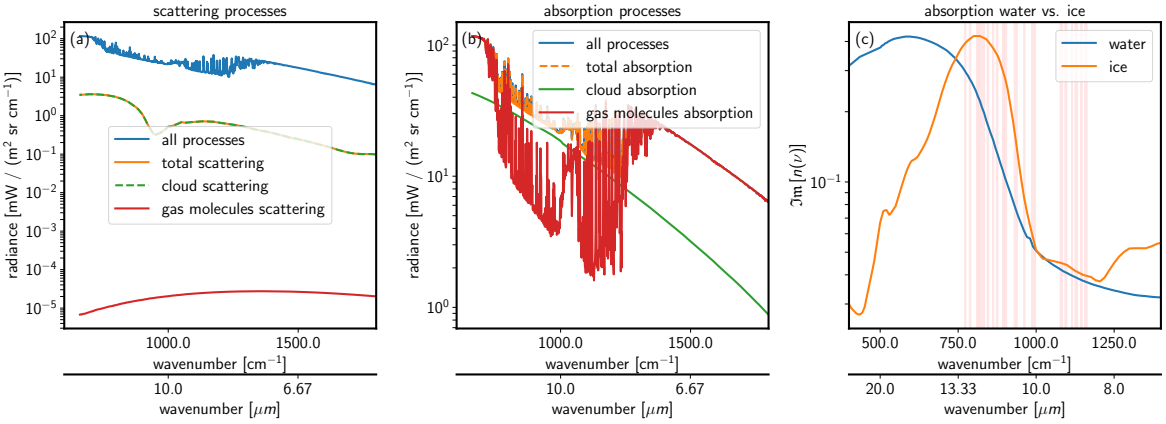

Figure 3.13.: Mid IR radiance spectrum divided into (a) scattering and (b) absorption processes by the respective atmospheric constituents, showing the dominance of absorption. (c) Using microwindows, where the imaginary party of the refractive index for water and ice is different in the Mid IR spectrum. Used MIE-TOOL from libradtran (Emde et al., 2016).

3.3.7. Reduction of the Radiance Spectrum to a Scalar Quantity using Microwindows

As described in section 3.2.4, passive remote sensing instruments such as the AERI provide broad spectral content and sufficient spectral resolution to discriminate between gaseous emitters (e.g. carbon dioxide, water vapor) and suspended matter (e.g. aerosols, water droplets and ice crystals in clouds). To analyse the downwelling infrared spectral signatures of clouds it is better to exploit the radiances in microwindows, see Table 3.4. In these spectral regions they are least-contaminated by line absorption and the cloud properties in these microwindows are essentially unchanged. This allows the radiances to be averaged from higher spectral resolution to that of the width of the microwindow.

There are different possibilities to use the microwindows in a retrieval algorithm. Turner (2005) used them in the framework of an iterative optimal estimation approach, where they calculated a retrieval state vector and its covariance in microwindows, after looping over all the microwindows, the cloud emissivity was computed and compared to the observed emissivity spectrum. Chang et al. (2017) made an entropy based information content analysis, designed to select optimal channels for ice cloud retrievals. The analysis is for satellite-based hyperspectral instruments such as the Atmospheric Infrared Sounder (AIRS).

For the purpose of simplicity, a scalar quantity associated with every spectrum will be defined in this thesis, and is used to investigate the radiative impact on several parameters in upcoming parameter studies

$$E_{\text{win,obs/sim}} = \frac{1}{N_{\text{sp}}} \sum_{k=1}^{N_{\text{win}}} \sum_{l=1}^{N_{\text{lin},k}} L_{AERI/DISORT}[\widetilde{\nu}_l] \quad , \tag{3.20}$$

where the normalisation factor $N_{\text{sp}} = \sum_{k=1}^{N_{\text{win}}} \sum_{l=1}^{N_{\text{lin},k}} l$ is given by the number of spectral sampling points, N_{win} is the number of used spectral windows and $N_{\text{lin},k}$ is the number of spectral grid points for the k-th microwindow. The corresponding spectral residuals between observed and simulated spectrum are defined as the absolute value of their difference

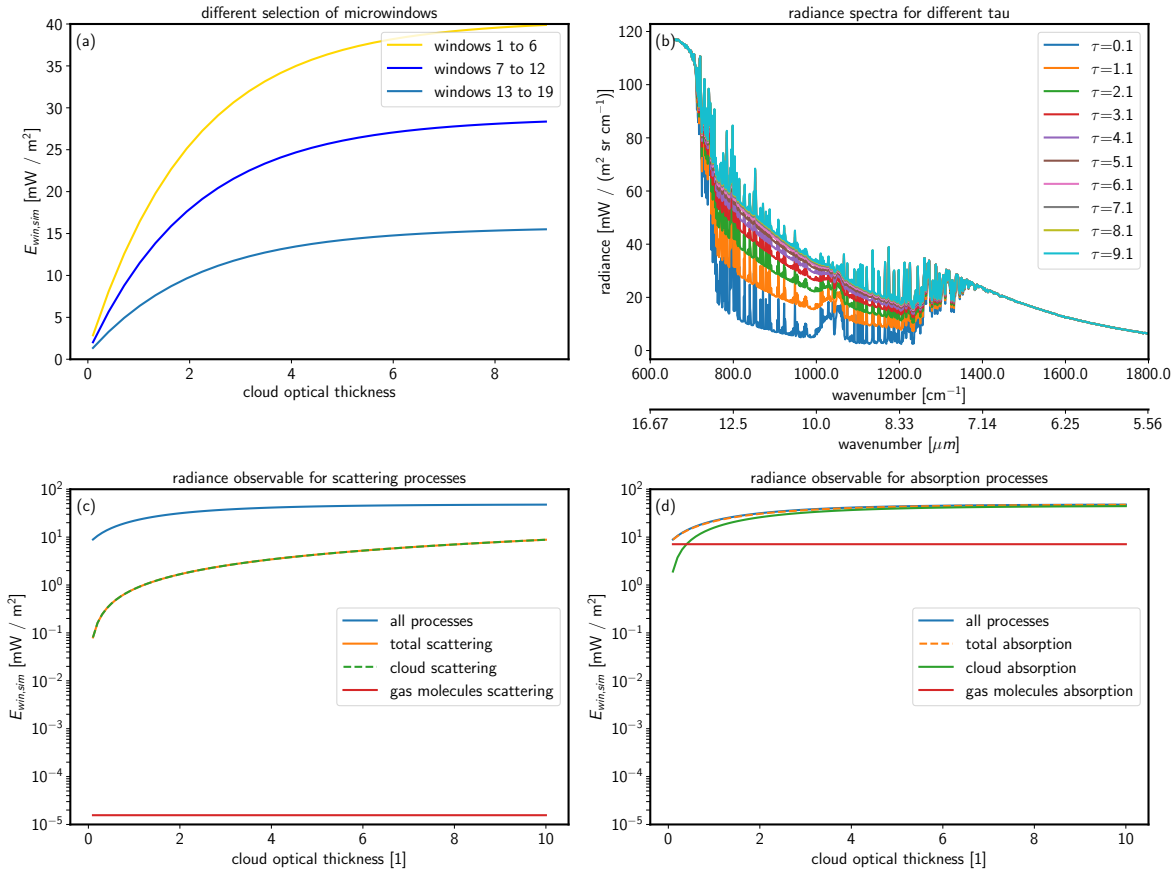

Figure 3.14.: (a) Different microwindow sets used for reducing the hole spectrum to a scalar quantity. (b) Simulated AERI radiances at UFS using DISORT in combination with REPTRAN for different COT ranging from 0.1 w to 9.1 with constant effective radius $R_{\text{eff}} = 50\mu m$ and droxtal as ice crystal habit. Spectrum averaged in microwindows, defined by $E_{win,sim}$, as function of COT for scattering (c) and absorption (d) processes.

$$\Delta E_{\text{win}} = \frac{1}{N_{\text{sp}}} \sum_{k=1}^{N_{\text{win}}} \sum_{l=1}^{N_{\text{lin},k}} |L_{\text{AERI}}[\widetilde{\nu}_l] - L_{\text{DISORT}}[\widetilde{\nu}_l]| \quad . \tag{3.21}$$

The number and location of the used microwindows in the retrieval algorithm is somehow arbitrary, but should lie in the primary spectral regions of 8 µm to 10 µm and 10 µm to 13 µm. A consequence of this choice, is that similar results can be obtained with different sets of microwindows. This is illustrated in Figure 3.14 (a), where the values of E_{sim} as a function of cloud optical thickness values are shown for different sets of microwindows, based on Table 3.4. So, to reproduce the results, the same microwindows have to be used. The average quantities $E_{\text{win,sim}}$, $E_{\text{win,obs}}$ and ΔE_{win} have the same unit as the irradiance E. Figure 3.14 (b) shows simulated AERI spectra for increasing values of cloud optical thickness, and illustrates a saturation effect for higher COT values. In Figure 3.14 (c) and (d), $E_{\text{win,sim}}$ is shown as function of COT and for different interaction processes. Comparing the results, exhibits that the dominant contribution of $E_{\text{win,sim}}$ is given by absorption of cloud particles.

3.4. Radar-Lidar Cloud Retrieval

3.4.1. Possibility to use Combinations of Radar and Lidar in Cloud Retrievals

Ice cloud microphysical properties (i.e. effective radius, IWC) can be retrieved by different methodologies based on radar-only (Hogan et al., 2006c), lidar-only (Heymsfield et al., 2013), radar-lidar-combination (Donovan and van Lammeren, 2001; Tinel et al., 2005) or a combination of more remote sensing instruments (Boers et al., 2000; Donovan et al., 2005; Delanoë and Hogan, 2008). All approaches have considerable uncertainties, especially if they only rely on one instrument. Dual wavelength approaches are another possibility to increase the information content (Matrosov et al., 2005).

Radar-Only Retrievals

Derivations of liquid water content from only radar reflectivity measurements have been suggested by Atlas (1954). In detail, he suggested to use empirical power law relationships, that relate radar reflectivity to liquid water content. In a similar fashion, ice water content can be retrieved from radar measurements as well. Because radar reflectivity factor depends on a much higher moment of the PSD than IWC (6^{th} vs. 3^{rd} moment), the retrieved results of IWC show errors up to a factor of 2 (Brown and Francis, 1995). Hogan et al. (2006c) developed empirical relationships for a 35 GHz by comparing coordinated aircraft in situ measurements and scans by a 3 GHz radar and added atmospheric temperature, which essentially contains size information

$$\log_{10}(IWC) = (0.000242) Z_{\text{e}} T + 0.0699 Z - 0.0186 T - 1.63 \tag{3.22}$$

$$\log_{10}(\beta_{\text{ext}}) = (0.000337) Z_{\text{e}} T + 0.0683 Z - 0.0171 T - 3.11 \quad , \tag{3.23}$$

where T is the temperature and Z_{e} is the equivalent radar reflectivity factor. Their results indicated a lowering of the uncertainty for temperatures from −30 °C to −10 °C, but still underestimate the IWC by a factor of 2 at colder temperatures. Please note, that in this approach, the ice crystal habit and the PSD type and parameter are fixed and not free parameters.

Lidar-Only Retrievals

Lidar-only retrievals are especially necessary for measurements below radar's detection threshold. Here, the extinction is first retrieved by inverting the lidar equation (Klett, 1985), and similar to radar-only retrievals, the retrieved extinction can then be related to the IWC by using empirical power low relationships. Heymsfield et al. (2013) introduced relationships, that can be used to derive IWC and effective diameter D_{eff} from extinction β_{ext}

$$IWC = \beta_{\text{ext}} \frac{0.91}{3} D_{\text{eff}} \tag{3.24}$$

$$D_{\text{eff}} = \alpha e^{\beta T} \quad , \tag{3.25}$$

where T is the temperature, α and β are temperature depended coefficients. Again, like in the radar-only approach, the ice crystal habit and the PSD type and parameter are not included as free parameters in these retrievals.

Combined Radar-Lidar Retrievals

Combined radar-lidar retrievals have the advantage, that they are well-defined because they can fall back on measurements sensitive to two different PSD moments, enabling them to derive particles size directly. Donovan and van Lammeren (2001) and Tinel et al. (2005) have developed a technique where they obtain an auxiliary quantity, the radar-lidar effective radius, from the ratio of equivalent radar reflectivity factor and attenuation-corrected lidar extinction coefficient. With assumptions about ice crystal habit and PSD type and shape parameter, the radar-lidar effective radius

$$R_{\text{eff}}^{\text{rali}} = \begin{cases} \frac{1}{2}\left[\frac{\langle D^6\rangle}{\langle D^2\rangle}\right]^{1/4} & \text{spherical ice crystal} \\ \left[\frac{9}{16\pi\rho_{\text{ice}}^2}\right]^{1/4}\left[\frac{\langle [m(D)]^2\rangle}{\langle A(D)\rangle}\right]^{1/4} & \text{non-spherical ice crystal} \end{cases} \tag{3.26}$$

can be converted to the microphysical effective radius R_{eff}. Here, the extinction coefficient β_{ext} will be obtained via inverting the lidar equation (Klett, 1985), and the radar reflectivity factor Z_{e} is a direct measurement quantity. The radar-lidar ratio $Q_{sca,\pi}(35.5GHz)/Q_{\text{ext}}(532nm)$ is a well-defined unique quantity, for ice crystals sizes D much bigger than the lidar wavelength λ_{lid} (optical scatterer: $\beta_{\text{ext}} \propto \langle D^2\rangle$), and much smaller than the radar wavelength λ_{rad} (Rayleigh scatterer: $Z_{\text{e}} \propto \langle D^6\rangle$).

The utility of this auxiliary quantity is illustrated in Figure 3.15. In the left plot, the radar-lidar ratio is a function of the microphysical effective radius R_{eff} and depends also on the PSD parameter μ, but using the ratio as a function of $R_{\text{eff}}^{\text{rali}}$, see right plot, removes the PSD parameter dependence for a wide range of $R_{\text{eff}}^{\text{rali}}$ values. In both plots, the limits of the methods are indicated. For large $R_{\text{eff}}^{\text{rali}}, R_{\text{eff}}$ values of about 200 µm, the ratio loses its well-defined $R_{\text{eff}}^{\text{rali}4}$ dependence, because at the frequency of 35 GHz, the ice crystals can no longer be considered as Rayleigh scatterer. For small $R_{\text{eff}}^{\text{rali}}$ and R_{eff} values, in turn, the ice crystals can no longer be considered as optical scatterer with respect to the lidar wavelength. But, the wide range of $R_{\text{eff}}^{\text{rali}}$ and R_{eff} values with a well-defined $R_{\text{eff}}^{\text{rali}4}$ dependence is sufficient

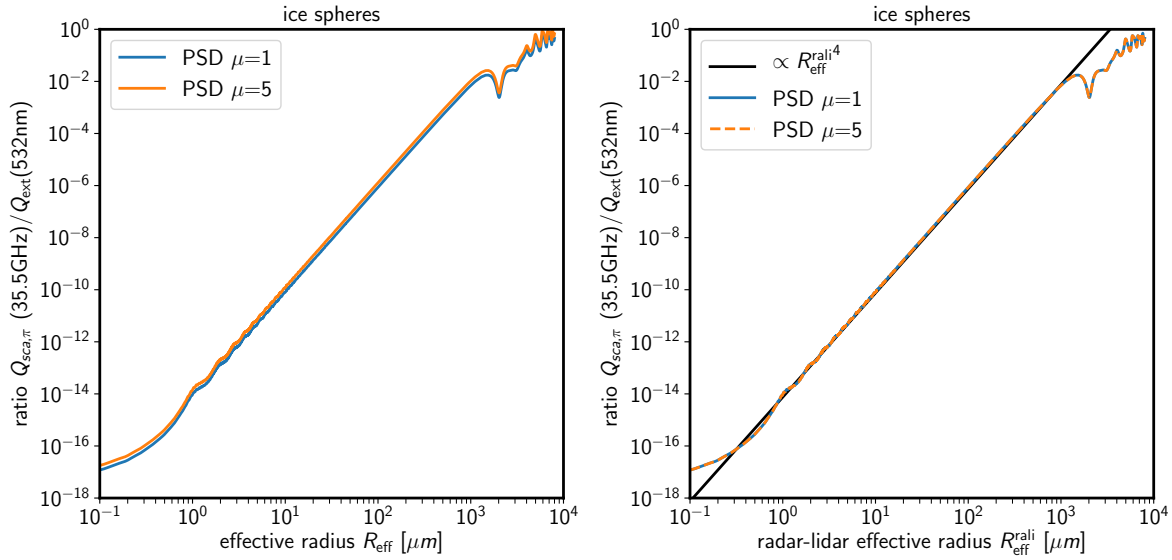

Figure 3.15.: Ratio of 35.5 GHz radar reflectivity backscatter to 532 nm lidar extinction efficiency for ice spheres for two PSD (mono-modal gamma type) shape parameters of μ (1 and 5) as a function of (left) microphysical effective radius R_{eff}, (right) and radar-lidar effective radius $R_{\text{eff}}^{\text{rali}}$. For simplicity, the calculations were performed using Mie theory and assuming ice spheres, but could be repeated with the methods mentioned in Table 2.2, assuming irregular ice crystal shapes.

enough to cover the most ice crystal sizes occurring in nature (Donovan and van Lammeren, 2001; Donovan et al., 2001).

Other retrieval methods, like Okamoto et al. (2003) or Delanoë and Hogan (2008), use forward algorithms instead of inverting the lidar equation. Here, they iterate over different microphysical input profiles to simulate radar and lidar measurements, and minimise the difference between observations and forward simulations to obtain the best matching microphysical profiles.

3.4.2. Microphysical Model and Radar-Lidar Inversion

Power Law Relationships for Non-Spherical Ice Crystals

As mentioned in Equation (2.28), the mass and projected area of non-spherical ice crystals can be described with power law relationships like $m(D) = aD^b$ and $A(D) = \gamma D^\delta$. This approach is similar to earlier studies from Donovan and van Lammeren (2001); Fontaine et al. (2014); Ham et al. (2017), and allows to take into account variations of the density of ice crystals due to their different crystal habits. In Table 3.5, the coefficients used in this thesis and their root-mean-square-errors (RMSEs) are summarised. The coefficients γ and δ are obtained via linear regression between $\log(D)$ and $\log[m(D)]$, the a and b coefficients are gained similarly. The mass $m(D)$ and area $A(D)$ are, besides optical properties, included in the Yang database as well. Some habits have a constant ice crystal aspect ratio for all maximum dimensions from 2 µm to 10 000 µm, and some habits have piecewise defined aspect

Table 3.5.: Power law fit coefficients derived from linear regression for mass a, b and area γ, δ. The correlation coefficients is > 0.99. For changing aspect ratios of the ice crystals the root mean square error (RMSE) increased.

habit	a $\left[\mathrm{g\ m}^{-b}\right]$	b [1]	RMSE mass	γ $\left[\mathrm{g\ m}^{2-\delta}\right]$	δ [1]	RMSE area
constant aspect ratios:						
droxtal	347 664.232	3.000	1.188×10^{-12}	0.673	2.000	9.054×10^{-15}
plate aggregates (10 elements)	20 844.151	3.000	8.139×10^{-15}	0.261	2.000	2.320×10^{-16}
plate aggregates (5 elements)	32 843.488	3.000	1.414×10^{-14}	0.234	2.000	1.977×10^{-16}
column aggregates (8 elements)	65 545.423	3.000	1.582×10^{-14}	0.356	2.000	1.761×10^{-22}
changing aspect ratios:						
solid column	15 877.266	2.730	1.277×10^{-6}	0.121	1.840	7.436×10^{-9}
hollow column	13 231.055	2.730	1.064×10^{-6}	0.121	1.840	7.436×10^{-9}
plate	738.526	2.472	2.608×10^{-10}	0.073	1.801	1.993×10^{-9}
solid bullet rosette	2209.362	2.653	1.072×10^{-7}	0.074	1.830	1.164×10^{-9}
hollow bullet rosette	2339.869	2.686	9.533×10^{-8}	0.074	1.830	1.164×10^{-9}
reference:						
sphere	480 663.676	3.000		0.785	2.000	

ratios. Therefore, using power laws with a single fit coeffiencient and exponent for the hole range of the maximum dimension D, will create a larger RMS error. The different ice crystal aspect ratios are summarised in Yang et al. (2013, Table 1).

Besides using habit dependent power law coefficients, it also possible to use temperature dependent coefficients, obtained from in situ observations, like in Heymsfield et al. (2013). In earlier studies, like Brown and Francis (1995) and Francis et al. (1998), they had to use fixed $m - D$ and $A - D$ relationships, regardless of temperature and habit, due to the lack of suitable additional data.

Conversion $R_{\mathrm{eff}}^{\mathrm{rali}} \rightarrow R_{\mathrm{eff}}$

To be able to calculate cloudy radiance spectra, one requires cloud optical properties like R_{eff} and IWC derived from ice cloud retrieval algorithms based on observations from radar and lidar. Generally, these properties depend on many parameters, like PSD type, PSD modality, PSD shape parameter and ice crystal habit, that are unknown and have to be assumed by the retrieval algorithm, because from radar and lidar measurements only two equations are available to fix parameters. Therefore, it is important to relate the microphysical effective radius R_{eff} with the help of the auxiliary quantity $R_{\mathrm{eff}}^{\mathrm{rali}}$ to the observations from radar (Z_{e}) and lidar (β_{ext}) as function of the mentioned free parameters, the retrieval have to assume.

These relations can be derived by using Equation (2.38) (Z_{e}), Equation (2.33) (β_{ext}), Equation (2.35) (R_{eff}), Equation (3.26) ($R_{\mathrm{eff}}^{\mathrm{rali}}$) and a generalised monomodal gamma distribution

as PSD. The next step is to integrate the maximum crystal dimension D from 0 to ∞ in the given PSD moments $\langle M_i(D)\rangle$. For spherical particles the relation between microphysical effective radius and radar-lidar effective radius is given by

$$R_{\text{eff}} = \left[\frac{(2+\mu)^3}{(3+\mu)(4+\mu)(5+\mu)}\right]^{1/4} R_{\text{eff}}^{\text{rali}} \quad , \tag{3.27}$$

and the relationship of R_{eff} as a direct function of measurement quantities is specified by

$$R_{\text{eff}} = \left[\frac{(2+\mu)^3}{(3+\mu)(4+\mu)(5+\mu)}\right]^{1/4} \left[\frac{|K_{\text{w}}|^2}{|K_{\text{ice}}|^2}\frac{\pi}{32}\frac{Z_{\text{e}}}{\beta_{\text{ext}}}\right]^{1/4} \quad . \tag{3.28}$$

The extension to non-spherical ice crystals via $m-D$ and $A-D$ power law relationships requires the inclusion of the corresponding prefactor and exponents like

$$R_{\text{eff}} = \left[\frac{3a\Gamma(b+\mu)}{4\gamma\rho_{\text{ice}}\Gamma(\delta+\mu)}\right]\left[\frac{16\pi\rho_{\text{ice}}^2\gamma\Gamma(\delta+\mu)R_{\text{eff}}^{\text{rali}\,4}}{9a^2\Gamma(2b+\mu)}\right]^{\frac{b-\delta}{2b-\delta}} \tag{3.29}$$

$$R_{\text{eff}} = \left[\frac{3a\Gamma(b+\mu)}{4\gamma\rho_{\text{ice}}\Gamma(\delta+\mu)}\right]\left[\frac{|K_{\text{w}}|^2\,\pi^2\rho_{\text{ice}}^2\gamma\Gamma(\delta+\mu)Z_{\text{e}}}{|K_{\text{ice}}|^2\,18a^2\Gamma(2b+\mu)\beta_{\text{ext}}}\right]^{\frac{b-\delta}{2b-\delta}} \quad , \tag{3.30}$$

where $\Gamma(n) = (n-1)!$ denotes the Gamma function. Again, Equation (3.30) summarises, that R_{eff} is a function of ice crystal habit and PSD settings (type, modality and shape paramater). Equation (3.30) is a generalised form of Equation (3.28). The specific relations for spherical particles can be restored by inserting the assumptions about spherical ice crystals ($a = \rho_{\text{ice}}\pi/6$, $b = 3$, $\gamma = \pi/4$ and $\delta = 2$). For bimodal gamma distributions it is not possible to derive analytical expressions and numerical methods have to be used instead.

In Figure 3.16 the dependence of the ratio $R_{\text{eff}}^{\text{rali}}$ and R_{eff} is illustrated for different ice crystal habits and PSD shape parameters. Especially for habits, where the ice crystal aspect ratio is piecewise defined, the ratio will not be a constant function of $R_{\text{eff}}^{\text{rali}}$ anymore. $R_{\text{eff}}^{\text{rali}}$ is used as independent variable, because it is not dependent on ice crystal habit and PSD shape parameters.

Corrections due to Changing Ice Crystal Aspect Ratios

As indicated in Section 3.4.2, some ice crystal habits have constant or piecewise defined aspect ratios. This may cause deviations in the retrieval procedure and should be estimated. In Figure 3.17, the results of a synthetic parameter study are illustrated. Here, cloud input parameter R_{eff} is varied and if the habit and the PSD shape parameter are known, the deviation $\Delta R_{\text{eff}} = R_{\text{eff}}(\text{input}) - R_{\text{eff}}(\text{retrieved})$ should be zero. But for ice crystal habits with piecewise defined aspect ratio, deviations ΔR_{eff} up the the order of 10 µm can occure. This is an artefact of using only single fit coefficients a and γ, and single exponents b and δ over the hole range of the maximum ice crystal dimension D from 2 µm to 10 000 µm. These deviations can be corrected by adding a correction function f_{corr} to compensate the deviation. The corrected microphysical effective radius is then given by

$$R_{\text{eff,corr}} = R_{\text{eff,uncorr}} + f_{\text{corr}}(R_{\text{eff,uncorr}}, \text{PSD}, \text{habit}) \quad . \tag{3.31}$$

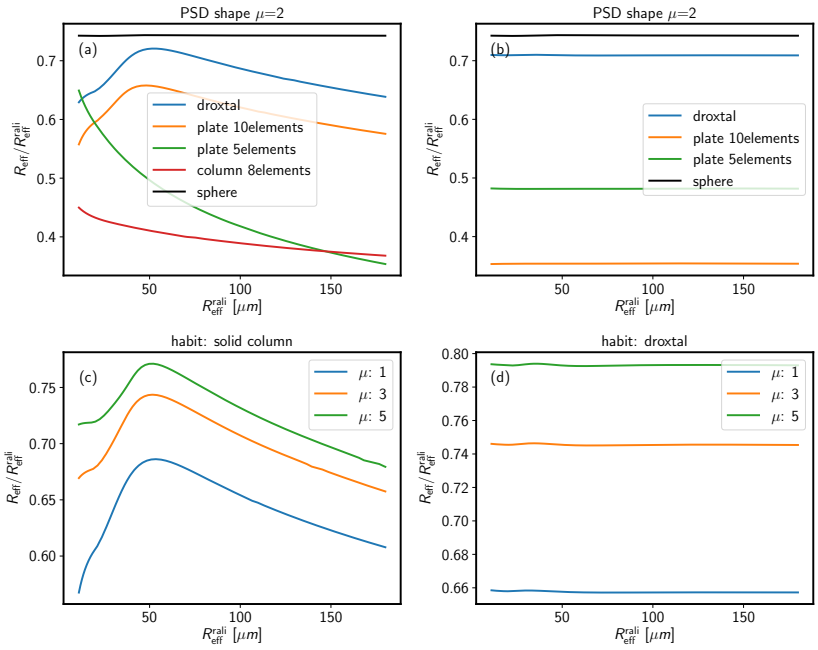

Figure 3.16.: Dependence of the ratio $R_{\mathrm{eff}}/R_{\mathrm{eff}}^{\mathrm{rali}}$ as a function of $R_{\mathrm{eff}}^{\mathrm{rali}}$ on habit and PSD shape parameter of a mono-modal gamma distribution. The ratio shows a significant dependence for a variation of habits (top left) and a variation of the PSD shapes (bottom left). For these habits, the ice crystal aspect ratio is piecewise defined in certain ice crystal size intervals. For other habits, where ice crystal aspect ratio stays constant, the variation of habits (top right) and the variations of the PSD shape (bottom right), is constant for changing $R_{\mathrm{eff}}^{\mathrm{rali}}$ values.

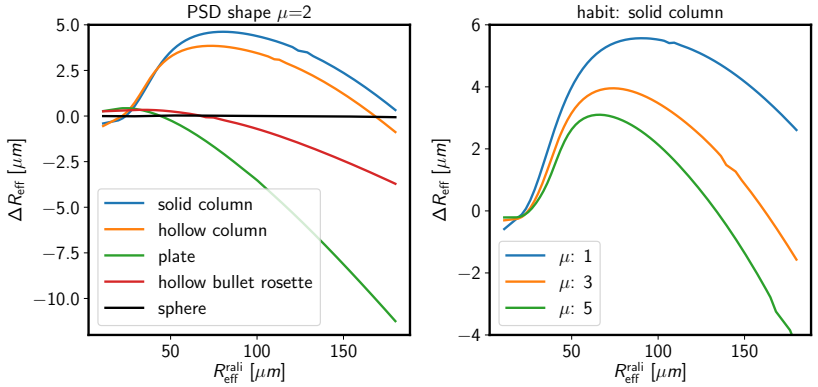

Figure 3.17.: Dependence of effective radius deviation ΔR_{eff} as a function of $R_{\mathrm{eff}}^{\mathrm{rali}}$ on (left) habit and (right) PSD shape parameter of a mono-modal gamma distribution. Due to piecewise defined ice crystal aspect ratios and only using a single $A-D$ and $m-D$ relationships for all D, the occurring deviations ΔR_{eff} have to be compensated by a function $f_{\mathrm{corr}}(R_{\mathrm{eff,uncorr}}, \mathrm{PSD}, \mathrm{habit})$. For all other habits, there is no deviation.

The usage of piecewise defined versions of the conversion formula Equation (3.30) would require a numerical implementation, because an analytical form can only be derived for integration limits of D from 0 to ∞.

3.4.3. Solutions of the Lidar Equation

There are different procedures to solve the lidar Equation (2.62). The majority of them are based on signal inversion to extract the backscatter $\beta_{\mathrm{sca},\pi}(R)$ and extinction $\beta_{\mathrm{ext}}(R)$ coefficient profiles from the detected power $P_{\mathrm{SS}}(R)$. These methods are separated into one-component atmospheres with two unknowns profiles (Klett, 1981), or two-component atmospheres with four unknowns profiles (Fernald et al., 1972; Fernald, 1984; Sasano et al., 1985). The first one is called Klett inversion/algorithm, whereas the second is called Klett-Fernald-Sasano algorithm. As already mentioned, the developed retrieval algorithm uses the radar and lidar cloud signal profiles themselves as main source of information. Considering the cloud part of the lidar signal, the scattered part from molecules is much weaker than that of ice crystals, and can therefore be neglected, leading to one-component solution methods.

A more convenient and easier way to handle lidar signal, is to use the range-corrected power

$$S(R) = P_{\mathrm{SS}}(R)R^2 \quad . \tag{3.32}$$

Using $S(R)$ and assuming a constant, the so-called lidar ratio as liner law for all ranges

$$LR = \frac{\beta_{\mathrm{ext}}}{\beta_{\mathrm{sca},\pi}} \quad , \tag{3.33}$$

between backscatter and extinction coefficient, the corresponding differential equation to the integral Equation (2.62) is given by

$$\frac{\mathrm{d}\log[S(R)]}{\mathrm{d}R} = \frac{1}{\beta_{\mathrm{ext}}(R)}\frac{\mathrm{d}\beta_{\mathrm{ext}}(R)}{\mathrm{d}R} - 2\beta_{\mathrm{ext}}(R) \quad . \tag{3.34}$$

In general the lidar ratio LR depends on particle size, shape, and orientation, and assuming LR the to be constant through the hole profile, is identic with assuming to have the same type of particles along the lidar beam.

Klett (1981) found out, that this type of a ordinary non-linear differential equation has the same structure as the Bernoulli (Bernoulli, 1695) or homogeneous Riccati equation (Riccati, 1724) and a general solution in terms of a boundary value $\beta_{\mathrm{ext}}(R_{\mathrm{far}})$ can be obtained

$$\beta_{\mathrm{ext}}(R) = \frac{S(R)}{\frac{S(R_{\mathrm{far}})}{\beta_{\mathrm{ext}}(R_{\mathrm{far}})} + 2\int_R^{R_{\mathrm{far}}} S(R')\mathrm{d}R'} \quad , \tag{3.35}$$

where R_{far} is the far-end measurement distance from a zenith looking lidar sensor. With other words, R_{far} denotes the last range gate, where the lidar has detected a cloud signal. The solution form of Equation (3.35) allows to retrieve the extinction profile via inversion of the lidar signal and is called "backward solution", because in the denominator is a plus sign and the integration direction is "backwards" from R_{far} (cloud top) to R_{near} (cloud base). The corresponding "forward solution", includes a minus sign in the denominator and the integration direction is from R_{near} to R_{far}. However, this solution will not be numerical stable, and even small deviations from the boundary value $\beta_{\mathrm{ext}}(R_{\mathrm{near}})$ can not assure convergence for $R > R_{\mathrm{near}}$, whereas the forward solution starting at $\beta_{\mathrm{ext}}(R_{\mathrm{far}})$ will quickly converge to

the "true" extinction profile for $R < R_{\mathrm{far}}$, if the error in the specified extinction boundary value is not unreasonably large. The disadvantage of the "backward solution" is, that the lidar signal quality is often worse at inversion start R_{far}, especially for optically thick clouds. If the boundary value $\beta_{\mathrm{ext}}(R_{\mathrm{far}})$ can be estimated without large errors, the extinction cloud profile can be retrieved via Equation (3.35) (Klett, 1981).

Estimation of the Boundary Value via $R_{\mathrm{eff}}^{\mathrm{rali}}$-Gradient and C_{lid}-Constant Method

To have a self-consistent inversion method, that only relies on the cloud part of the lidar signal, Donovan and van Lammeren (2001) developed an iterative procedure, that estimates the extinction boundary value at the far-end of the measurement distance $\beta_{\mathrm{ext}}(R_{\mathrm{far}})$ with the help of the radar signal at R_{far}. They showed, that it is much easier to estimate $R_{\mathrm{eff}}^{\mathrm{rali}}(R_{\mathrm{far}})$ instead of $\beta_{\mathrm{ext}}(R_{\mathrm{far}})$, because the extinction at R_{far} (cloud top) is difficult to specify since cloud extinction values at a single point can vary by several orders of magnitude, whereas the range of $R_{\mathrm{eff}}^{\mathrm{rali}}(R_{\mathrm{far}})$ values is smaller. In detail, they estimated $R_{\mathrm{eff}}^{\mathrm{rali}}$ in a realistic range from 1 µm to 1000 µm, and via Equation (2.39), one obtains the corresponding $\beta_{\mathrm{ext}}(R_{\mathrm{far}})$ for the signal inversion. They defined two cost functions J_{RD} and J_{LC}, both depend on the boundary value $R_{\mathrm{eff}}^{\mathrm{rali}}(R_{\mathrm{far}})$, and are given by

$$J_{\mathrm{RD}}[R_{\mathrm{eff}}^{\mathrm{rali}}(R_{\mathrm{far}})] = \sum_{i=N_{\mathrm{far}}-N_{\mathrm{RG}}}^{N_{\mathrm{far}}} \left[\frac{\mathrm{d}}{\mathrm{d}R}\log\left(R_{\mathrm{eff}}^{\mathrm{rali}}(R_i)\right)\right]^2 \quad , \tag{3.36}$$

$$J_{\mathrm{LC}}[R_{\mathrm{eff}}^{\mathrm{rali}}(R_{\mathrm{far}})] = \frac{S(R_{\mathrm{far}})}{\beta_{\mathrm{ext}}(R_{\mathrm{far}}, R_{\mathrm{eff}}^{\mathrm{rali}}(R_{\mathrm{far}}))} e^{2\tau_{\mathrm{cld}}(R_{\mathrm{eff}}^{\mathrm{rali}}(R_{\mathrm{far}}))} \quad , \tag{3.37}$$

where J_{LC} is defined slightly different in this thesis, and use their product as function of $R_{\mathrm{eff}}^{\mathrm{rali}}(R_{\mathrm{far}})$ to estimate a boundary value

$$\underset{R_{\mathrm{eff}}^{\mathrm{rali}}(R_{\mathrm{far}})}{\text{minimize}}\ J_{\mathrm{tot}}[R_{\mathrm{eff}}^{\mathrm{rali}}(R_{\mathrm{far}})] = J_{\mathrm{RD}}[R_{\mathrm{eff}}^{\mathrm{rali}}(R_{\mathrm{far}})]\ J_{\mathrm{LC}}[R_{\mathrm{eff}}^{\mathrm{rali}}(R_{\mathrm{far}})] \quad . \tag{3.38}$$

The first cost function J_{RD} penalises gradients of $\log(R_{\mathrm{eff}}^{\mathrm{rali}})$ in the N_{RG} farthest range gates ($N_{\mathrm{RG}} \approx 20$) of the cloud signal. The subscript RD is for radius derivatives. Because the natural logarithm of $R_{\mathrm{eff}}^{\mathrm{rali}}$ is used, the exponent 1/4 will have no impact on the retrieved results. The minimum of this cost function will return a reasonable estimate for the boundary value and inserting this into Equation (3.35) will allow to retrieve the extinction profile. The term $S(R_{\mathrm{far}})/\beta_{\mathrm{ext}}(R_{\mathrm{far}})$ in the denominator of Equation (3.35) is inverse proportional to the lidar ratio LR, and the minimising procedure effectively returns those values of the LR, that produce a plausible $\beta_{\mathrm{ext}}(R)$ profile and are in accordance with the information available from the radar.
But, this method has limitations for large $R_{\mathrm{eff}}^{\mathrm{rali}}(R_{\mathrm{far}})$, where the cost function J_{RD} becomes insensitive and stays constant (see Figure 3.18 (c) and (d)). To overcome this limitation, Donovan and van Lammeren (2001) introduced a second cost function J_{LC}, a rearrangement of Equation (2.62) for the lidar constant and evaluated it at R_{far}. This cost function helps to restrict the estimation of the boundary value for large $R_{\mathrm{eff}}^{\mathrm{rali}}(R_{\mathrm{far}})$, where J_{LC} will increase and serves as an additional consistency check for unrealistic values of the lidar constant. Here, τ_{cld} denotes the guessed optical cloud thickness for values of $R_{\mathrm{eff}}^{\mathrm{rali}}(R_{\mathrm{far}})$ in a realistic range from 1 µm to 1000 µm, and the subscript LC stands for lidar constant.

In summary, J_{RD} will give a good estimation of the boundary value, especially for small guessed values of $R_{\mathrm{eff}}^{\mathrm{rali}}(R_{\mathrm{far}})$ and J_{LC} will discriminate unrealistic high values of $R_{\mathrm{eff}}^{\mathrm{rali}}(R_{\mathrm{far}})$, if J_{RD} did not find a minimum. So, putting them together will give a robust estimation of the boundary value via minimising their product cost function J_{tot}.

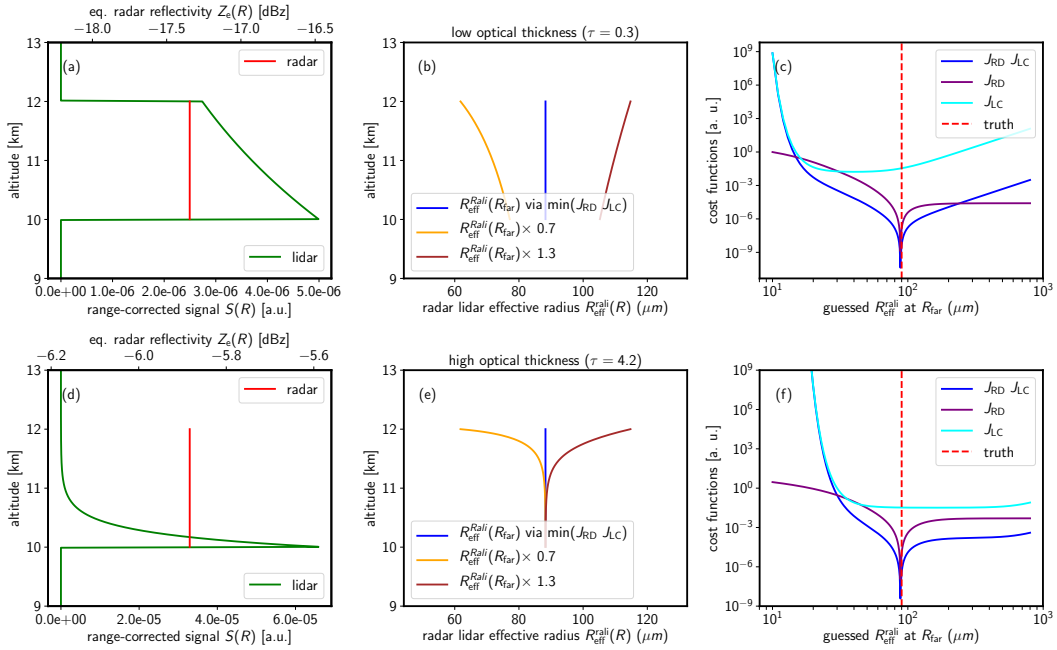

Figure 3.18.: Simulated radar and lidar signals (a) and (d). Result of the retrieved $R_{\mathrm{eff}}^{\mathrm{rali}}(R)$ profiles (b) and (e). Estimation of the boundary value $R_{\mathrm{eff}}^{\mathrm{rali}}(R_{\mathrm{far}})$ via different costfunctions (c) and (f). (a) - (c) is for low optical thickness and (d) - (f) is for high optical thickness.

In Figure 3.18 the usage of the cost function estimation method is illustrated for synthetic radar and lidar data, generated from constant microphysical profiles with $R_{\mathrm{eff}}^{\mathrm{rali}} = 90\mu m$. Two cases are considered for a cirrus cloud with a low ($\tau = 0.3$) and a high ($\tau = 4.2$) optical thickness, and both located at an altitude between 10 km to 12 km. In Figure 3.18 (a) and (d) the synthetic radar and lidar signals are illustrated, for low and high COTs, respectively. For a low cloud optical thickness, the lidar signal is able to fully penetrate the cloud and only loses about 45 % of its signal in the course of the attenuation process. However, for the case with a high cloud optical thickness, the lidar signal is strongly affected by attenuation, and only has 2 % left after interacting with the cloud particles. Here, attenuation caused by atmospheric gases is neglected and the radar attenuation by ice clouds can generally be considered to be negligible (Hogan et al., 2006c). In Figure 3.18 (b) and (e) the retrieved $R_{\mathrm{eff}}^{\mathrm{rali}}(R)$ profiles based on the $J_{\mathrm{tot}} = J_{\mathrm{RD}}J_{\mathrm{LC}}$ estimation are shown, the cost function found the correct boundary value to start the inversion (blue curve). Furthermore, the effect of errors in underestimating (orange curve) and overestimating (brown curve) of the boundary value are shown. Here, the boundary value was intentionally guessed with a deviation of ± 30 % from the true boundary value. Even with a wrong guessed boundary value, the Klett inversion will force the $R_{\mathrm{eff}}^{\mathrm{rali}}(R)$ profile to converge towards the true profile, but this will need some range gates, and this distance will increase for larger deviations of the boundary value.

In detail, the distance required until convergence is accomplished, is dependent on the cloud optical thickness, the thicker the cloud, the shorter the distance until convergence. There is also a difference between under- and overestimating the boundary value, because of the proportionality $R_{\mathrm{eff}}^{\mathrm{rali}} \propto \beta_{\mathrm{ext}}^{-1/4}$, an underestimation of $R_{\mathrm{eff}}^{\mathrm{rali}}(R_{\mathrm{far}})$ corresponds to an overestimation of $\beta_{\mathrm{ext}}(R_{\mathrm{far}})$. Therefore, convergence is reached after a shorter distance when overestimating $\beta_{\mathrm{ext}}(R_{\mathrm{far}})$ or underestimating $R_{\mathrm{eff}}^{\mathrm{rali}}(R_{\mathrm{far}})$, because this is associated with a higher optical thickness. As seen in the Figure 3.18 (c) and (f), the product cost function $J_{\mathrm{RD}}J_{\mathrm{LC}}$ has a clear minimum, where the true value of $R_{\mathrm{eff}}^{\mathrm{rali}}(R_{\mathrm{far}})$ is located (blue curve). J_{RD} has limitations for large $R_{\mathrm{eff}}^{\mathrm{rali}}(R_{\mathrm{far}})$, here the cost function only takes constant values and is not able to discriminate unrealistic boundary values (purple curve). Therefore, J_{LC} is required as an additional consistency check for large $R_{\mathrm{eff}}^{\mathrm{rali}}(R_{\mathrm{far}})$ values. On its own, J_{LC} can not give a precise estimation of the boundary value, but it can discriminate unrealistic large $R_{\mathrm{eff}}^{\mathrm{rali}}(R_{\mathrm{far}})$ values (cyan curve).

Estimation of the Boundary Value via N_0^*-Iteration Method

Tinel (2002) and Tinel et al. (2005) developed a different method to estimate the boundary value for the lidar inversion. They used the complete radar and lidar cloud signal to constrain both measurements in relation to each other. The used integral constrain is given by

$$\int_{R_{\mathrm{near}}}^{R_{\mathrm{far}}} \beta_{\mathrm{ext}}(R)\mathrm{d}R = m \int_{R_{\mathrm{near}}}^{R_{\mathrm{far}}} [N_0^*(R)]^{(1-n)} K^n \mathrm{d}R \quad , \tag{3.39}$$

where, R_{near} and R_{far} correspond to cloud base and top, respectively. The left side is the cloud optical thickness based on lidar quantities, and the right side is based on radar quantities, m and n are coefficients gained from aircraft in situ measurements with a 94 GHz radar (Tinel et al., 2005, Table 1). N_0^* is the normalised number concentration, an auxiliary quantity, and K is the specific radar attenuation, based on the Hitschfeld-Bordan equation (Hitschfeld and Bordan, 1954). Based on this integral relation, they derived an implicit equation in $\beta_{\mathrm{ext}}(R_{\mathrm{far}})$, which is given by

$$\begin{aligned}\beta_{\mathrm{ext}}(R_{\mathrm{far}}) = & \frac{\beta_{\mathrm{att}}(R_{\mathrm{far}})}{2\int_{R_{\mathrm{far}}}^{R_{\mathrm{near}}} \beta_{\mathrm{att}}(R')\mathrm{d}R'} \left\{ \exp\left(\frac{2\beta_{\mathrm{ext}}(R_{\mathrm{far}})}{[f(R_{\mathrm{far}})]^{1-n}} \int_{R_{\mathrm{far}}}^{R_{\mathrm{near}}} [f(R)]^{1-n} \right.\right. \\ & \left.\left. \left[\frac{[f(R)]^{1-b} Z_a^b(R)}{[f(R)]^{1-b} Z_a^b(R_{\mathrm{far}}) + \left[\frac{\beta_{\mathrm{ext}}(R_{\mathrm{far}})}{m[f(R_{\mathrm{far}})\overline{N_0^*}]^{1-n}}\right]^{1/n} I(R, R_{\mathrm{far}})} \right]^n \mathrm{d}R \right) - 1 \right\} \quad ,\end{aligned} \tag{3.40}$$

where

$$I(R, R_{\mathrm{far}}) = 0.46b \int_R^{R_{\mathrm{far}}} [f(R')]^{1-b} Z_a^b(R')\mathrm{d}R' \quad , \tag{3.41}$$

and the attenuated backscatter is denoted by

$$\beta_{\mathrm{att}}(R) = \beta_{\mathrm{sca},\pi}(R) \exp\left[-2 \int_0^R \beta_{\mathrm{ext}}(R')\mathrm{d}R' \right] \quad , \tag{3.42}$$

the coefficients a, b, m and n, are again given by Tinel et al. (2005, Table 1), and $f(R)$ is a function introduced to stabilize the numerical process. This implicit equation is solved by an

iterative numerical procedure, which is initialised by $N_0^* = 10^{10}$ and $f(R) = 1$. The hypothesis of this procedure is, that the best found $\beta_{\text{ext}}(R)$ profile will have the least fluctuation of the normalised particle number concentration with height. The physical foundation behind this is, that ice particle growth by vapor deposition and riming will lead to a change in particle size, but not affecting the number of particles (Tinel et al., 2005). Please note, although only data from 36 GHz radars are used in this thesis, the numerical method was originally developed with coefficients gained from a 94 GHz radar. Therefore, testing the implemented numerical procedure in this work, is achieved by the evaluation of so-called "blind tests".

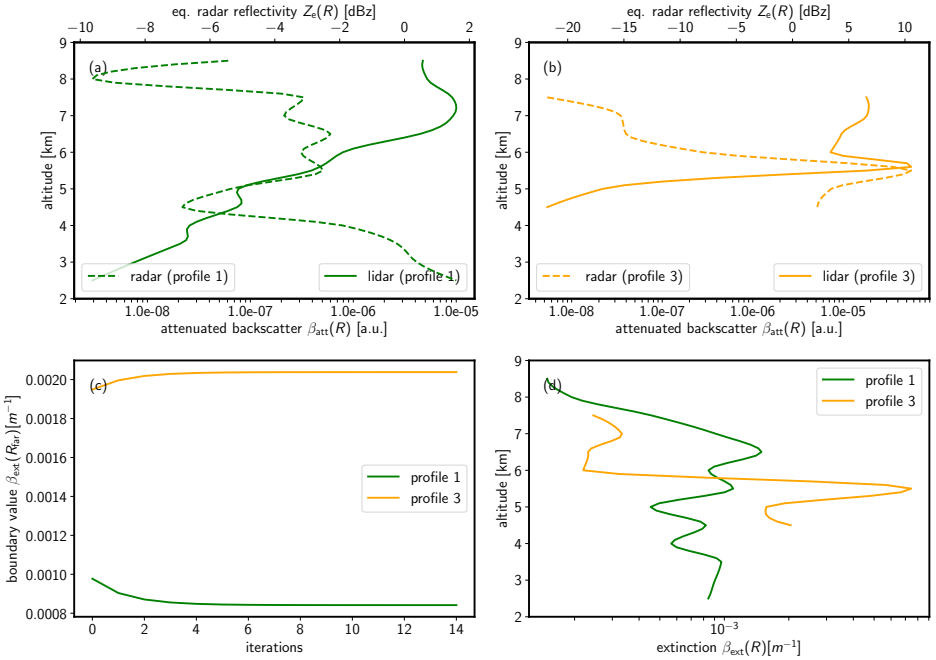

Figure 3.19.: Evaluation of blind-profile 1 and 3 from Hogan et al. (2006b). (a) Simulated radar and lidar signals for *profile* 1. (b) Simulated radar and lidar signals for *profile* 3. (c) Estimating of boundary value via Equation (3.40). (d) Retrieved extinction profiles for both blind-profiles.

Here, Hogan et al. (2006b) used ice size distributions measured during an aircraft campaign, with a 94 GHz radar and a 355 nm lidar, to simulate radar and lidar profiles measured from space. The data and complete descriptions of the blind-test scenarios can be found at Hogan, R. J. (2003) and Hogan et al. (2006b), respectively. In Figure 3.19, the results of evaluating *profile* 1 (variable LR, $\tau_{\text{cld}} = 4.7$) and *profile* 3 (constant LR, $\tau_{\text{cld}} = 5.0$) are illustrated. As indicated in Figure 3.19 (c), the algorithm converges for both profiles in less than 6 iterations. The retrieved extinction profiles in Figure 3.19 (d), are in good agreement with the results given in Hogan, R. J. (2003, Fig. 3). Please note, due to the aircraft-geometry, the boundary value $\beta_{\text{ext}}(R_{\text{far}})$ is located at cloud base and not at cloud top, like for the aforementioned ground-based-geometry.

Estimation of the Boundary Value via Rayleigh Calibration Method

The aforementioned methods, relied on the radar signal for determining the extinction boundary value. But, it is also possible to determine the boundary value based on the lidar signal with additional information about the atmospheric composition. This so-called Rayleigh-calibration uses the lidar signal attenuation, caused by the cloud, to estimate the cloud optical thickness. Then, different $\beta_{\text{ext}}(R_{\text{far}})$ are guessed, until a value converges with the retrieved optical thickness from the signal loss. The applicability of this method make some demands on the lidar signal quality. In detail, the method requires the lidar signal to be free of aerosol at some range before and after penetrating the cloud. Then, the atmosphere in these parts, only consists of molecules and is therefore sometimes called Rayleigh-atmosphere.

The advantage is, that the extinction of a molecular or Rayleigh-atmosphere can be described theoretically by (Fröhlich and Shaw, 1980)

$$\beta_{\text{ext,mol}}(z) = \frac{8\pi^3}{3\lambda^4} \cdot \frac{1}{N_s(z)} \left[\frac{n_a^2 - 1}{n_a^2 + 1}\right]^2 \frac{6 + 3\delta}{6 - 7\delta} \cdot \frac{T_0}{p_0} \cdot \frac{p(z)}{T(z)} \quad , \tag{3.43}$$

where N_s is the number of molecules, n_a is dimensionless refractive index of air, δ is the depolarisation factor, λ is the lidar wavelength in [µm], $p(z)$ is the air pressure in [hPa] and $T(z)$ is the air temperature in [K]. Using reasonable values, like described in (Wiegner, 2017; Freudenthaler et al., 2018) the equation can be simplified to

$$\beta_{\text{ext,mol}}(z) = 2.795 \cdot 10^{-4} \cdot \frac{p(z)}{T(z)} \cdot \lambda^{-4.08} \quad . \tag{3.44}$$

Hence, with the knowledge of well measured temperature and pressure profiles from close radiosondes or re-analysis data, the molecular extinction can be determined. Because the molecular lidar ratio is a constant and given by $LR_{\text{mol}} = \frac{8\pi}{3}$, the molecular lidar signal can be completely calculated. In detail, considering a two-component atmosphere, that is free of clouds and aerosol for $R > R_{\text{mol,start}}$

$$\begin{aligned} P_{\text{SS}}(R)R^2 &= \beta_{\text{sca},\pi,\text{mol}}(R)\ C_{\text{lid}}\ \exp\left[-2\int_0^{R_{\text{mol,start}}} \{\beta_{\text{ext,mol}}(R') + \beta_{\text{ext,par}}(R')\}\mathrm{d}R'\right] \\ &\quad \exp\left[-2\int_{R_{\text{mol,start}}}^{R} \beta_{\text{ext,mol}}(R')\mathrm{d}R'\right] \qquad (3.45) \\ &= B_{\text{mol}}(R_{\text{mol,start}}, R)\beta_{\text{sca},\pi,\text{mol}}(R)\exp\left[-2\int_{R_{\text{mol,start}}}^{R} \beta_{\text{ext,mol}}(R')\mathrm{d}R'\right] \quad , \end{aligned}$$

where the fit coefficient B_{mol} was introduced. For a pure molecular atmosphere, B_{mol} represents the slope of the Rayleigh signal and is calculated by

$$B_{\text{mol}}(R_{\text{mol,start}}, R) \coloneqq \frac{P_{\text{SS}}(R)R^2}{\beta_{\text{sca},\pi,\text{mol}}(R)\exp\left[-2\int_{R_{\text{mol,start}}}^{R} \beta_{\text{ext,mol}}(R')\mathrm{d}R'\right]} \quad . \tag{3.46}$$

So, the lidar signal can be calibrated via comparison of the slope of the actual measured lidar signal with the calculated molecular signal. The quality of the molecular fit in an interval

$(R_{\mathrm{mol,start}}, R_{\mathrm{mol,end}})$ can be characterised by its percentage error

$$\Delta B_{\mathrm{mol}}(R_{\mathrm{mol,start}}, R_{\mathrm{mol,end}}) = \frac{\sigma_{B_{\mathrm{mol}}}}{\overline{B_{\mathrm{mol}}}} \quad , \tag{3.47}$$

where especially after penetrating the cloud, the lidar signal and therefore the fit quality will decline. If there are two molecular regions before (R_1, R_2) and after (R_3, R_4) interaction of the lidar beam with the cloud, the cloud optical thickness can be calculated from the signal attenuation via

$$\tau_{\mathrm{cld}} = \frac{1}{2} \log \left[\frac{B_{\mathrm{mol}}(R_1, R_2)}{B_{\mathrm{mol}}(R_3, R_4)} \right] \quad . \tag{3.48}$$

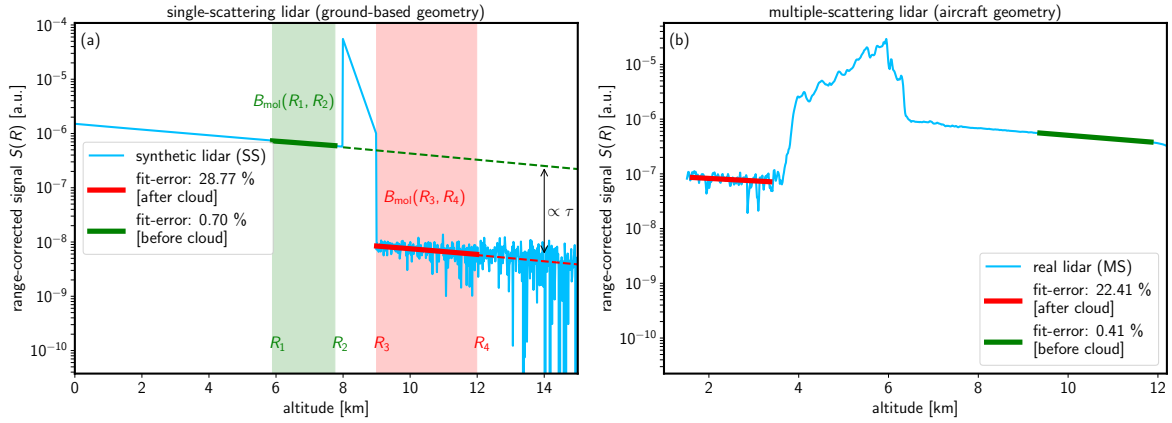

Figure 3.20.: Rayleigh fit method to calculate cloud-optical thickness for (a) synthetic single-scattering lidar data, and for (b) a real multiple scattering lidar (WALES, Wirth et al. (2009)). The calculation of lidar signals based on different FOVs was taken out with a lidar multiple scattering model developed by Hogan (2006, 2008); Hogan and Battaglia (2008).

The hole procedure works as follows: First the cloud masks identifies the signal parts before and after the cloud, then several molecular fit coefficient B_{mol} are calculated. Here, the length of the fit intervals $(R_{1/3}, R_{2/4})$ can lie between 1.5 km to 3.5 km, the altitude of these intervals will be increased in steps of 100 m and for all steps, B_{mol} coefficients are calculated. In the end, the value of B_{mol} with the lowest error, before and after the cloud, will be used as final value to calculate the cloud optical thickness. In Figure 3.20 the procedure is illustrated for (a) a synthetic lidar signal with noise, and (b) for a real lidar signal, recorded at the NARVAL-I campaign. Please note, that Equation (3.4.3) is based on the single-scattering lidar equation. Therefore, if a lidar with a larger FOV is used, multiple-scattering effects have to be included. The procedure will estimate τ_{MS}, which is lower than the desired τ_{SS}, because the corresponding lidar signal was increased by multiple scattered photons, leading to lower cloud attenuation. τ_{SS} can be either be retrieved, via dividing τ_{MS} with a multiple-scattering factor η_{MS} or with an procedure, like described in Wandinger (1998).

Other Approaches for the Estimation of the Boundary Value

In the course of this thesis, other approaches have been developed and will be mentioned here for completeness:

- **Backward vs. forward Klett-inversion:** Here, the boundary values will be guessed for the forward Klett-inversion (start integration at cloud top $R_{\text{eff}}^{\text{rali}}(R_{\text{far}})$), like described in Section 3.4.3, and additional for the backward Klett-inversion (start integration at cloud base $R_{\text{eff}}^{\text{rali}}(R_{\text{near}})$). The guessed boundary value, which minimises the difference of these two extinction profiles was used as retrieved boundary value.

- **Characterise similarities between $P_{\mathbf{obs}}(R)$ and $P_{\mathbf{sim}}(R)$ and minimize deviation:** Here, a optimisation algorithm (e.g. truncated Newton method) is used to minimise the RMSE between the measured and a forward simulated lidar signal, based on retrieved microphysical profiles. The algorithm needs initial conditions for the boundary value ($R_{\text{eff}}^{\text{rali}}(R_{\text{far}})$) and the cloud lidar ratio LR.

- **Characterise and minimize vertical fluctuation:** This method calculates the left- and right-handed envelopes (via Hilbert transformation) of the retrieved microphysical profiles for different guessed $R_{\text{eff}}^{\text{rali}}(R_{\text{far}})$. Then, a fit function is used to characterise the fluctuation of the profiles with height. Finally, the profile which caused the lowest vertical fluctuation returns the used boundary value.

- **Characterise similarities between $P(R)$ and $IWC(R)$ and minimize deviation:** As shown in Figure 4.20 (b) and (c), the retrieved ice water content and extinction resembles the range-corrected lidar signal $S(R)$. This similarity can be characterised, after normalising the value ranges, for different $R_{\text{eff}}^{\text{rali}}(R_{\text{far}})$, like described in the previous methods. Minimizing the cost function J_{tot}, should retrieve the best matching microphysical profile to the given lidar signal:

$$\underset{R_{\text{eff}}^{\text{rali}}(R_{\text{far}})}{\text{minimize}}\ J[R_{\text{eff}}^{\text{rali}}(R_{\text{far}})] = \sqrt{\frac{1}{N}\sum_{i}^{N}\left[\frac{S(R_i)}{\|S(R_i)\|_{\max}} - \frac{\beta_{\text{ext}}(R_i, R_{\text{far}})}{\|\beta_{\text{ext}}(R_i)\|_{\max}}\right]^2}\ , \tag{3.49}$$

  where N is the number of range gates inside the detected cloud. This method is more independent from the gradient of $R_{\text{eff}}^{\text{rali}}$.

The aim was, to have additional criteria, that are not dependent on the $R_{\text{eff}}^{\text{rali}}(R)$ gradient, because that would be a limiting condition for considering real data. For the used synthetic test data, the aforementioned methods were not sensitive enough to be an improvement and could only reproduce some former results.

3.4.4. Multiple Scattering Correction

As mentioned in the previous section, lidar cloud measurements are affected by multiple-scattering (MS) effects, especially for optically thicker clouds and/or for large receiver FOVs. The single-scattering (SS) lidar equation assumes, that the detected photons were only scattered once, and interprets detected MS photons mistakenly as a higher transmission leading to a lower optical thickness. Therefore, the contribution of photons to the lidar signal, that have undergone more than one scattering event cannot be ignored. In contrary, millimeter-wave

radar measurements are typically only affected by MS effects, when observing deep convective clouds from space, and can be neglected for observing ice clouds.
MS effects are only relevant when MS photons have not left the receiver's FOV. Then, the probability that they re-enter the FOV and are scattered toward the receiver is very low, like indicated by simulations (Wandinger, 1998). Because the receiver FOVs are usually very small, only scattering processes in forward or backward direction will be detected. Forward scattering has the much higher probability and therefore MS processes are mainly the consequence of one or more forward scattering events, after a backward scattering event. Therefore, the amount of photons detected that are from multiple scattering events depend mainly on the width of the FOV, the covered volume and the width and intensity of the diffraction peak. Especially in cloud measurements, where particles are large in relation to the wavelength of the laser, MS effects are intense.

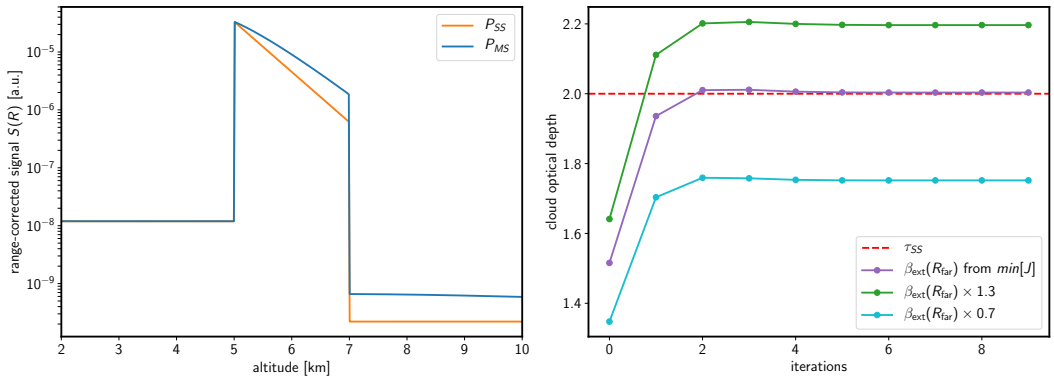

Figure 3.21.: (left) Simulated multiple scattering lidar signal for following parameters: FOV of 1.6 mrad, wavelength of 532 nm, R_{eff} of 60 µm and LR of 30. (right) Iterative correction of the cloud optical thickness for a retrieval with a multiple scattering procedure like sketched in Figure 3.22.

Because, not considering the effects of multiple scattering in a cloud retrieval would lead to a considerable underestimation of the extinction coefficient and cloud optical thickness, an iterative correction procedure was developed like sketched in Figure 3.22. The approach is similar to previous methods like described in Donovan and van Lammeren (2001) and Gouveia et al. (2018). An accurate forward model (Hogan, 2006, 2008; Hogan and Battaglia, 2008) is used, that allows the calculation of the intensity of multiple scattered photons by clouds in lidar signals. The method's focus is to obtain the best estimate of the SS lidar signal, and to use it for the retrieval of the SS microphysical profiles. In detail, a lidar forward model for the treatment of multiple-scattering effects has been incorporated into the inversion process. To account for MS effects, the first inversion is performed on the observed lidar signal P_{obs}, then the retrieved extinction profile and effective radius profiles are used in the MS model to estimate the ratio $R_{\text{MS/SS}}$ of MS signal to SS signal (Weitkamp, 2006)

$$P_{\text{MS}}(R,\Theta) = P_{\text{SS}}(R) R_{\text{MS}}(R,\Theta) = P_{\text{SS}}(R)\left[1 + F_d(R,\Theta) + F_g(R,\Theta)\right] \quad , \tag{3.50}$$

where Θ is the half-angle receiver field of view and F_d and F_g are diffraction scattering alone and all other scattering processes, respectively. Based on the results, the multiple-scattering ratio $R_{\text{MS/SS}}$ is then re-calculated and used to update the estimation of the SS lidar profile.

The process is repeated until the retrieved cloud optical thickness has converged.

An example of the correction procedure is given in Figure 3.21, for a cloud optical thickness of $\tau_{\mathrm{SS}} = 2$. In the left plot, the MS lidar signal looks like a SS lidar signal with reduced optical thickness. In the right plot, the correction results are represented, usually within a few iterations, the retrieved cloud optical thickness will converge (purple curve). The method also has some limitations, if for example the radar signal would have a calibration offset. Because the radar signal is used to estimate the boundary value $\beta_{\mathrm{ext}}(R_{\mathrm{far}})$ for the inversion start, an under- (cyan curve) or overestimation of $\beta_{\mathrm{ext}}(R_{\mathrm{far}})$ will lead to constant bias. Therefore, the correction procedure is dependent on calibrated radar data.

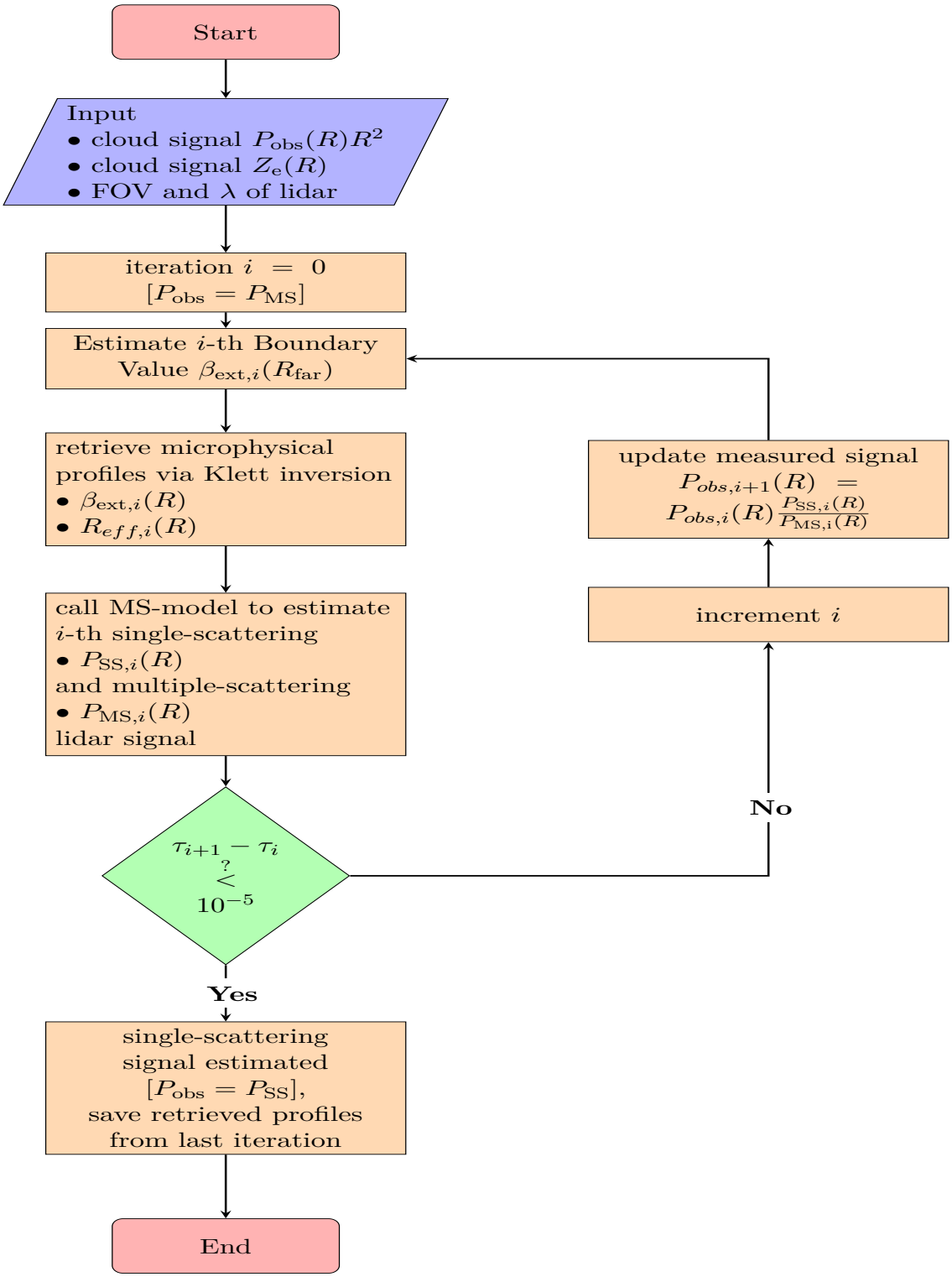

Figure 3.22.: Flowchart to illustrate the certain steps involved in the multiple scattering correction algorithm.

3.5. Synergy Thee-Instrument Retrieval - *SynCirrus*

The SynCirrus algorithm was mainly implemented in Python and uses the external scientific computational codes for radiative transfer (DISORT, libRadtran (Mayer and Kylling, 2005; Emde et al., 2016)), lidar multiple scattering (MULTISCATTER, (Hogan, 2006)) and gas attenuation at radar wavelengths (Liebe-Model, (Liebe et al., 1993)) within functions calls when they are required. A flow-chart diagram is given in Figure 3.23. The used retrieval methods, computational codes, campaign data and references included in the framework are categorised and listed in Table 3.6. The physical assumptions used in the development of the three instrument algorithm are summarised in Table 3.7 and Table 3.7.

At the beginning, the measured radar and lidar signals, as well as the temperature, pressure and water vapour profiles from re-analysis are interpolated on a common grid. Then, both signals are cloud-masked and overlap regions are identified, as described in Section 3.2.2. The AERI and radar-lidar data are temporally mapped, according to the instrument's sky-phase, the measuring interval between the calibration intervals. Furthermore, the radar and lidar signals have to be corrected for gas attenuation (see Section 3.2.3) and numerical stability (see Section 4.2.3), respectively. The single lidar profiles are inverted using three different methods, as explained in Section 3.4.3. The retrieved extinction profile is corrected for multiple scattering effects (see Section 3.4.4) and according to the assumptions about ice crystal habit and PSD (see Section 3.4.2), the profiles of R_{eff} and IWC are subsequently derived. The different habits are assumed in form of different mass-diameter and area-diameter relationships, based on an effective ice particle density. The used power law coefficients are given in Table 3.5. To quantity the uncertainty, these calculations are repeated 5 to 10 times within the uncertainty intervals for the radar calibration uncertainty ΔZ_{e}, PSD shape parameter μ and boundary value estimation error $\Delta R_{\mathrm{eff}}^{\mathrm{rali}}$. The estimation of $\Delta R_{\mathrm{eff}}^{\mathrm{rali}}$ is based on took-up tables for different COTs and normalised gradients of $R_{\mathrm{eff}}^{\mathrm{rali}}$, as presented in Figure 4.9. The retrieved profiles of R_{eff} and IWC are used as input for RT calculations, to simulate a spectrum at the location of the AERI. The RT calculations are based on a microphysical model (see Section 3.3.5), according to the same assumptions as in the inversion procedure. Therefore, the used single scattering properties based on Yang et al. (2013), were pre-calculated for different ice crystal habits and PSD parameter. Finally, the measured and simulated spectra are compared exploiting spectral microwindows, as explained in Section 3.3.7, to find the best matching assumptions in minimizing the spectral residuals.

Table 3.6.: A categorised overview of the used computational codes, models, instruments and the associated retrieved quantities within the SynCirrus retrieval.

sounding	*active*		*passive*	*in-situ*
type	Radar	Lidar	IR spectrometer	weather-balloon
device (campaign/ location, parameter)	MIRA-36 (UFS & NARVAL1, $\lambda = 8.6\,\mathrm{mm}$)	Jenoptik CHM15k (UFS, $\lambda = 1064\,\mathrm{nm}$, FOV=0.45 mrad) WALES (NARVAL1, $\lambda = 532\,\mathrm{nm}$, FOV=1.6 mrad)	AERI-ER (Summit St. Zugspitze $400\,\mathrm{cm}^{-1}$ to $3000\,\mathrm{cm}^{-1}$)	Vaisala RS41/RS92 radiosondes (Oberschleissheim) Vaisala RD-94 dropsondes (NARVAL1)
observed quantity [unit] (dimensions)	equivalent reflectivity factor Z_e $[dBZ]$, $\left[\frac{mm^6}{m^3}\right]$ (time, height)	lidar power P_MS $[\#photons]$ (time, height)	spectral radiance L_λ $\left[\frac{mW}{m^2\ sr\ cm^{-1}}\right]$ (time, wavenumber)	temperature [K], pressure [hPa], mixing ratio $[g/kg]$, relative humidity [%], all (time, height)
uncertainty/ specification	$\Delta Z_\mathrm{e} = 1.3\ \ dBZ$	calib. not relevant when using Klett inversion	resolution: $0.5\,\mathrm{cm}^{-1}$ calib. bias $< 0.66\%$ calib. precision $< 0.13\%$ of ambient BB radiance	$0.3\,°\mathrm{C} < 16\,\mathrm{km}$ 4 % RH $0.3 < 100\,\mathrm{hPa}$
references	Görsdorf et al. (2015)	Wiegner et al. (2014) Wirth et al. (2009)	Knuteson et al. (2004a) Knuteson et al. (2004b)	Jensen et al. (2016) Stevens et al. (2019)
modelling	-	-	-	-
forward and re-analysis models	analytic expression Equation (2.38) (Rayleigh regime for 8.6 mm radar), attenuation by gases with Liebe-model using pyMPM *version 0.1.0*	multiscatter *version 1.2.11*	libRadtran *version 2.0.4* RT-solver: Disort (16 streams) molecular parameterisation: Line-By-Line $< 1\,\mathrm{cm}^{-1}$ REPTRAN $\geq 1\,\mathrm{cm}^{-1}$	ECMWF ERA-Interim
references	Liebe et al. (1993)	Hogan (2006)	Emde et al. (2016)	Dee et al. (2011)
ice microphysic model (exchange-able)	ice bulk density is described by mass-diameter $m(D)$ and area-diameter $A(D)$ relationships and integrated over PSD, $m(D)$ and $A(D)$ from Yang et al. (2013)		look-up table: bulk optical properties were integrated for different PSD-types, PSD-modalities, PSD-shapes, crystal roughnesses and R_eff, single-scattering data from Yang et al. (2013)	PSD-shape $\mu(T)$ from temperature relation derived from in-situ data, Heymsfield et al. (2013) uncertainty: $\Delta\mu(T) = \pm 2$
lidar inversion technique	combination of methods from Klett (1981), Donovan and van Lammeren (2001), Tinel et al. (2005) and Rayleigh calibration e.g. described in Cadet et al. (2005)		-	temperature [K] and pressure [hPa] for Rayleigh calibration
retrieved and calculated quantities [unit] (dimension)	effective radius R_eff $[\mu m]$ ice water conent IWC $[g/m^3]$ extinction β_ext $[1/m]$ all in (time, height)		spectral radiance L_λ, $\left[\frac{mW}{m^2\ sr\ cm^{-1}}\right]$, (time, wavenumber)	water vapour, $[molecules/cm^{-3}]$ (time, height)

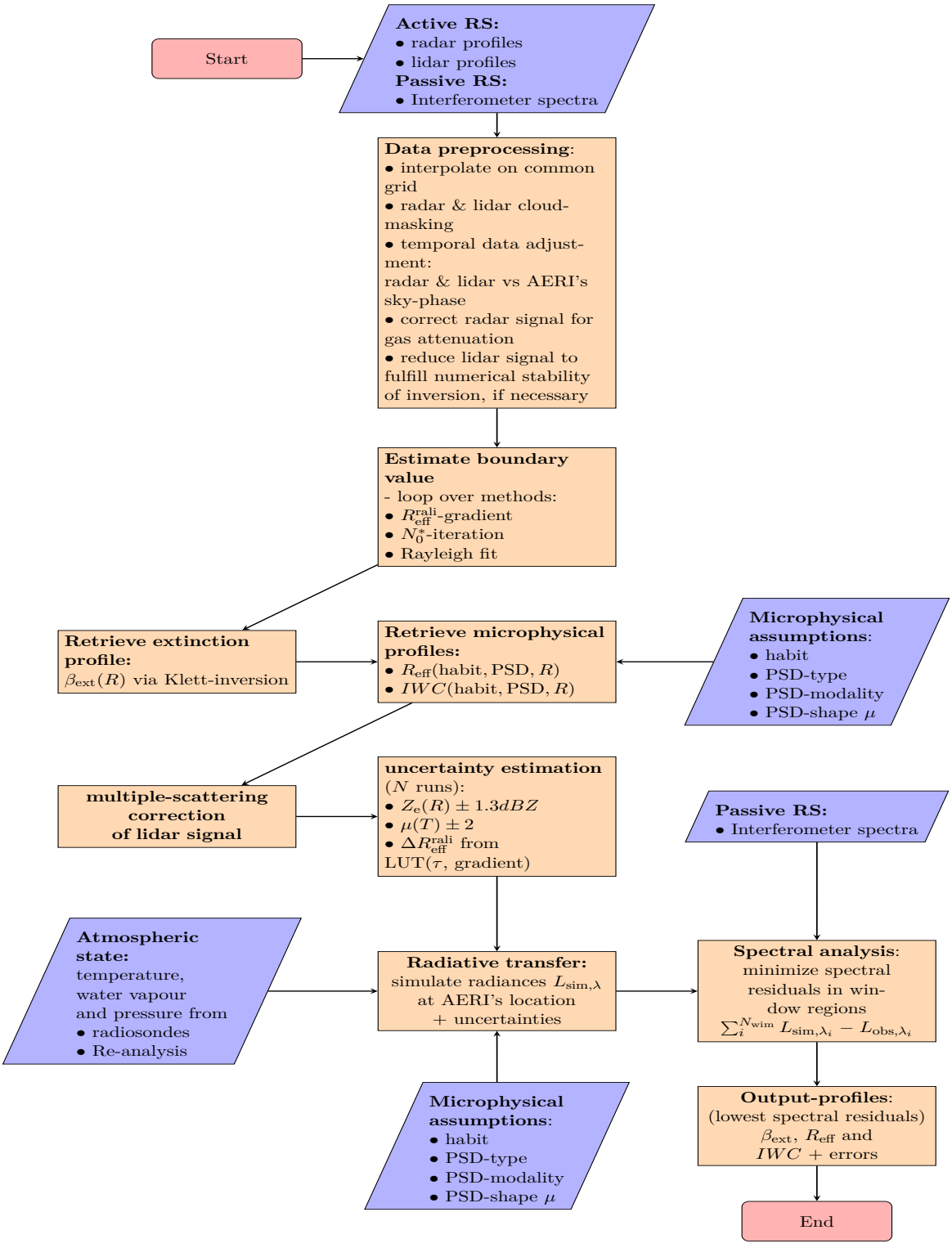

Figure 3.23.: Flowchart of the SynCirrus algorithm for the retrieval of R_{eff}, IWC and β_{ext} by using, 35 GHz radar and lidar signals and IR-spectrometer data.

Table 3.7.: Part I - Overview of used assumptions in the SynCirrus retrieval algorithm.

Assumption	**Explanation/Implication**
Retrieval Technique	
Single habit approximation (SHA): Lidar ratio LR is assumed to be vertically constant in order to use single-component Klett-inversion.	LR depends on particle size, shape, and orientation and therefore, assuming a constant LR implies to have the same type of particles along the beam. Therefore, the retrieval has to assume a single habit for a cloud (Klett, 1981; Zhou et al., 2018).
Microphysics	
PSD parameters (type, modality and shape) are assumed to be vertically constant for a cloud.	PSD-shape parameter is approximated by a temperature relation $\mu(T)$ found via in-situ measurement and the uncertainty for typical cloud measurements is covered assuming $\mu \pm 2$ (Heymsfield et al., 2013).
The ice bulk density ρ_b is assumed to be equal to the density of solid ice ρ_{ice} (=0.917 g cm^{-3}).	Ice particles in clouds can have a smaller density than the solid ice particle due to air bubbles. Therefore, Sato and Okamoto (2006) defined the ice bulk density ρ_b as the ratio of ice mass to exterior volume of ice particles including air bubbles, and $\rho_b = \rho_{\text{ice}}$ if there are no air bubbles. Because a maximal change of ρ_b ranging from 0.60 g cm^{-3} to 0.917 g cm^{-3} would only cause a difference lower than 1 dBZ in Z_{e} (Sato and Okamoto, 2006), (Ham et al., 2017).
Size and Orientation Aspects	
Cloud ice particles are assumed to be randomly oriented	The fraction of oriented ice particles is very low at cold cloud temperatures (Liou and Yang, 2016, Fig. 7, Fig. 6a). In that case, the single- scattering properties for a sample of non-spherical ice crystals can be averaged over Euler angles.
At a radar wavelength of 8.6 mm, ice crystals are considered as Rayleigh scatterer	For ice crystals scattered at a radar wavelength of 8.6 mm and $R_{\text{eff}} < 200$ µm, Mie effects can be neglected and the Z_{e} can be described with Equation (2.38) instead of T-matrix radar scattering model (Benedetti et al., 2003, Fig. 2)
At lidar wavelength < 1064 nm, ice crystals are considered as optical scatterer	The accuracy of the optical scatterer-approximation depends on the ratio of the lidar wavelength to the size and shape of the ice crystal. For hexagonal crystals, the approximation is accurate for values of $2\pi D_{\max}/\lambda > 100$ (Donovan et al., 2004).
Radar Signal	
Multiple-scattering effects at radar wavelength of 8.6 mm are negligible for ice clouds	In general, multiple-scattering of the radar signal by cloud particles can be neglected for non-precipitating clouds (Battaglia et al., 2010).
Attenuation of the radar signal is only accounted for gases and can be neglected in ice clouds	At higher frequencies a correction of the radar signal must be made for attenuation by intervening atmospheric gases (specifically water vapor and molecular oxygen). But, radar attenuation by ice clouds can generally be considered to be negligible up to 94 GHz (Hogan and Illingworth, 1999).
Instrument Parameter	
Difference in radar and lidar footprints are < 0.363 dBZ. The effect of this error is equivalent to a variation of Z_{e} around the order of the radar calibration uncertainty.	The difference in the pulse volume of an ice cloud sampled will have an impact on the retrieved results, due to cloud inhomogeneity, especially from satellites (European-Space-Agency, 2001; Hogan et al., 2006b). But, for ground based instruments this difference should be $< 1.5dBZ$ (Hogan, 2001a,b,c).

Table 3.8.: Part II - Overview of used assumptions in the SynCirrus retrieval algorithm.

Assumption	**Explanation/Implication**
Radiative transfer	
Only elastic scattering is considered	Atmospheric scattering and absorption processes are usually considered to preserve the light frequency of the interacting wave.
Independent scattering approximation (ISA): A single ice crystal in a cloud scatters light in exactly the same way if there would be no surrounding ice crystals	Can be assumed, because the number density of ice crystals in cirrus clouds is relatively low, and they are separated from each other by distances, much larger than their sizes. Therefore scattering events at different ice crystals do not interfere with each other and phases can be neglected. This concept allows the usage of energy quantities instead of the electromagnetic field, which allows using simplifications like taking out radiative transfer calculations with bulk single scattering properties.
Neglecting to simulate polarisation	The AERI uses a gold-coated mirror to switch between the zenith sky viewing mode and the calibration reference sources. The polarisation insensitivity of bare gold to the angular rotation of the scene mirror is used to avoid a polarisation sensitivity of the interferometer, because this would lead to a calibration error, since the reference sources are located at $\pm 60°$ from the vertical sky view. (Knuteson et al., 2004a)
Plane-parallel approximation (PPA): Atmospheric and ice cloud layers are considered to vary much more rapidly in the vertical than the horizontal	These assumptions are used because in plane-parallel atmospheres it is possible to solve the radiative transfer equation (Petty, 2006). However, ice cloud inhomogeneity can introduce errors, called plane-parallel bias.
Independent pixel approximation (IPA): A cloudy pixel (or column) is considered to be radiatively independent of its neighboring pixels	This assumption allows no horizontal transport of radiation and tries to avoid the plane-parallel bias, by not averaging the ice cloud properties. However, the non-consideration of the horizontal transport of radiation causes errors, because so-called 3D effects like enhanced cloud top cooling and additional cloud side cooling are not included (Mayer, B., 2009). On small spatial scales around 100 m, like the cloud-base footprints of the instruments, the errors for neglecting 3D RT effects and ice cloud inhomogeneity can lead to a COT-error of below 30 % and a R_{eff}-error below 5 % Fauchez et al. (2018). The critical error is the COT-error, because the COT has the biggest impact on the infrared spectrum. However, 5 % is below the typical error of the other retrieval uncertainties.

4. Results

This chapter summarises the results for the application of the *SynCirrus* retrieval. In the first part, the resolution of the framework concerning determination of ice crystal habits is investigated by evaluating the spectral residuals in sensitivity studies with synthetic data, based on a 1D model adjusted for the location Mount Zugspitze. The explored findings will help to develop data quality criteria, needed for retrieval results with low errors. The second part focuses on the radar-lidar retrieval-part of the algorithm and compares the results with other retrievals by evaluating real data from the NARVAL-I field aircraft campaign. The chapter closes with showing the full three-Instrument retrieval applied on remote sensing data obtained from radar, lidar and infrared spectrometer synergy at Mt. Zugspitze.

4.1. Parameter Studies with Synthetic Model

To be able to retrieve microphysical cloud properties like ice crystal habits from the *SynCirrus* algorithm, the uncertainties of the algorithm should be quantified at different stages. The last step of the algorithm is to simulate a radiance spectrum with the retrieved R_{eff} and IWC profiles from radar and lidar cloud measurements. This spectrum will then be compared with the measured spectrum from the infrared spectrometer. For the spectral comparison, a scalar quantity to assess the spectral residuals is used, and the magnitude of the spectral residuals caused by different origins will be analysed. This is necessary, because it is important to know, if spectral residuals caused by instrument uncertainties are smaller or larger as residuals caused by microphysical assumptions like the ice crystal habit. To execute this task, the different known origins for spectral perturbation will be divided into:

- **Radiative transfer settings:** Is related to the spectral resolution of RT calculations (Line-By-Line vs. REPTRAN).
- **Ice cloud microphysics:** This includes all states of the retrieval space like the choice of the ice crystal habit, the roughness of the ice crystals, the type of the PSD, the modality of the PSD and the PSD shape parameter μ.
- **Instrument parameters:** Intended are instrument footprints, the radar calibration uncertainty ΔZ_{e}, the lidar SNR and the cloud detection differences caused by the different scattering regimes of the emitted electromagnetic pulses characterised by the radar-lidar vertical cloud signal overlap. Concerning the infrared spectrometer, the calibration uncertainty and reproducibility will be investigated.
- **Atmospheric state:** Meant are, how perturbations in cloud base height and the atmospheric profiles of traces gases and prognostic variables will impact the radiative transfer part of the algorithm.
- **Radar-lidar retrieval technique:** Here, the different methods for evaluating the boundary value for the lidar inversion, the assumptions of a constant cloud lidar ratio

in the Klett algorithm and the effects of lidar multiple scattering correction have to be investigated.

The analysis of the spectral residuals will help to develop criteria on the data quality and the meteorological situation, needed to gain useful retrieval results with low uncertainties. For this purpose a 1D model was developed to create synthetic measurement data as input for the *SynCirrus* algorithm based on a microphysical ice cloud model in accordance with the Yang database. In these studies, two parameters will be varied. The cloud optical thickness, because it has the biggest impact on the radiance spectrum, and always a parameter from the above mentioned categories. The default settings of the model are summarised in Table 4.1. The parameters to be varied will be mentioned in the certain sections. Of course, such a 1D model has limitations compared to a 3D model, but it includes the main sensitivities, important in the retrieval procedure, like the sensitivities on D^6 (radar), D^2 (lidar), water vapour (infrared spectrometer), ice microphysical model (RT and inversion) and retrieval technique assumptions.

Table 4.1.: Default parameter settings for microphysical and geographical parameter used in synthetic model.

Microphysical cloud parameter		Geographical parameter	
effective radius R_{eff}	50 µm	passive sensor altitude	2961 m.a.s.l.
lidar ratio LR	30 sr^{-1}	cloud base height	8000 m.a.s.l.
ice crystal habit	droxtal	cloud top height	9000 m.a.s.l.
PSD type	gamma distribution	vertical resolution	15 m
PSD modality	monomodal	profiles of water	ECMWF
PSD shape μ	2	vapour, ozone,	5th October, 2013
		temperature	(18h - 24h)
		and pressure	at grid box:
			47.5 latitude
			10.75 longitude
		profiles of carbon	AFGL - midlatitude
		dioxide, nitrogen,	winter
		air and oxygen	

4.1.1. Sensitivity on Absorption Parameterisation: Line-By-Line vs. REPTRAN

For a retrieval to be used operational, it would be desirable, if it is based on fast numerical calculations, because sampling the full retrieval space will take some time. Concerning the *SynCirrus* algorithm, the computational bottleneck is the calculation of the radiance spectrum based on Line-By-Line calculations. A possible speed up is to use REPTRAN instead of Line-By-Line calculations, because they require less amounts of memory, can include more vertical sampling points and are generally much faster, but at the expense of a lower spectral resolution.

REPTRAN offers spectral resolutions between 15 cm^{-1} (*coarse*) and 1 cm^{-1} (*fine*), but the AERI measures with a higher resolution of 0.5 cm^{-1}. Therefore, the LBL calculations are

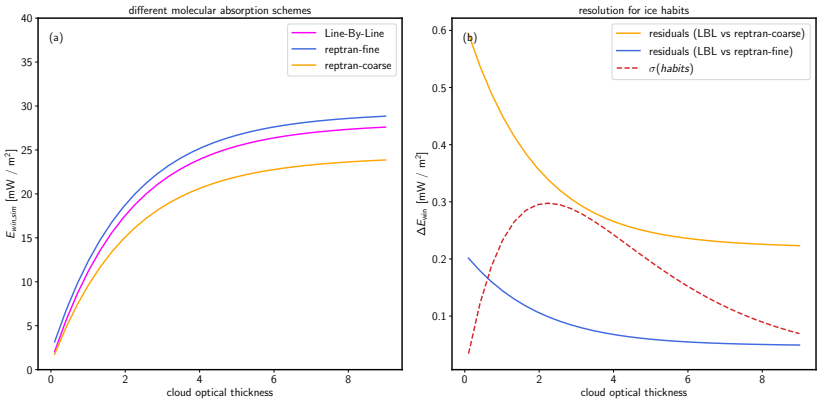

Figure 4.1.: (a) Scalar quantity E_{sim} for different absorption parameterisations. (b) Spectral residuals among different absorption parameterisation in comparison with amount of variation caused by different ice crystals habits.

taken out at a resolution of $0.05\,\text{cm}^{-1}$ and are then convolved with the ILS afterwards. The question that arises is, if the spectral residuals, exploited in microwindows, between LBL and REPTRAN absorption parameterisations are larger than the differences between important microphysical properties like the ice crystal habits. In Figure 4.1 (a), the quantity $E_{\text{win,sim}}$ is shown as function of cloud optical thickness values for different absorption parameterisation schemes and indicates, that the difference between LBL and REPTRAN-fine is much smaller than the difference between LBL and REPTRAN-coarse. In Figure 4.1 (b), the residuals ΔE_{win} between LBL and REPTRAN-fine/coarse are shown for different cloud optical thickness values and compared with the standard deviation, caused by the different ice crystals habits. The plot basically shows, that for cloud optical thickness values larger than 0.5 it is sufficient to use REPTRAN-fine because the differences between the habits can still be resolved, but for very thin cirrus clouds, radiative transfer calculations should be taken out based on LBL absorption parameterisations.

4.1.2. Sensitivity on Microphysical Model Assumptions

Ice Crystal Habits and Surface Roughnesses

As introduced in Chapter 3.4, radar-lidar cloud retrievals allow a well-defined retrieval of two microphysical properties (IWC and R_{eff}) from two measurement quantities. However, for ice clouds, IWC and R_{eff} are in turn functions of microphysical ice crystal properties themselves. Because, no further measurements are available to fix them, they have to be assumed by the retrieval. The same happens with the PSD. In Section 3.4.2, the impact of ice crystal habit and PSD shape on particle size was investigated. It was shown, that the choice of a wrong ice crystal habit has the bigger impact and can lead to a conversion of R_{eff} being off by a factor of about 2.5, whereas wrong choices of PSD shapes μ only lead the conversion to be off by a factor of about 1.2.

The interesting questions is, how these choices will impact the radiative transfer. Therefore, simulations are taken out, where the standard deviation of the radiance quantity, defined in Equation (3.3.7), is calculated for a set of habits, roughnesses and PSD shapes μ given by the integrated Yang database. This quantity will be calculated for different cloud optical thickness

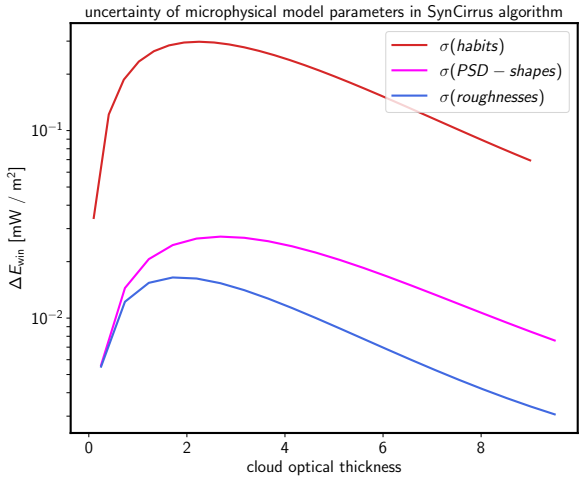

Figure 4.2.: Analysis of the variation of the residuals ΔE_{win} for different microphysical properties as function of cloud optical thickness.

values and will give insights about the magnitude of variation to be expected in the radiance spectra. This will help to figure out which are the dominant microphysical contributions and so finally which are the important assumptions, the retrieval space should iterate over. In Figure 4.2 the results are summarised and show, that the standard deviation of the set of ice crystal habits has the largest variation, whereas the standard deviation of the ice crystal roughnesses have the smallest variation. Because, there is one order of magnitude between them, it is appropriate to reduce the microphysical assumptions to ice crystals habits only as the dominant contribution, and fix the ice crystal roughness to be smooth and describe the PSD shape parameter by a temperature relation found by in situ aircrafts measurements (Heymsfield et al., 2013)

$$\begin{aligned} \mu(T) &= 1 - 0.84 - 0.0915\ T - 2.936 \times 10^{-3}\ T^2 \\ &\quad -3.653 \times 10^{-5}\ T^3 - 2.157 \times 10^{-8}\ T^4 \quad . \end{aligned} \tag{4.1}$$

In the following parameter studies, the impact of the certain parameters will be investigated by comparing their spectral residuals with the standard deviation of the set of ice crystal habits. This will show how large the variation of the parameters are allowed to be. Unless their residuals are smaller than the standard deviation of the set of ice crystal habits, the ice crystal habit variation will be the dominant contribution and in principle could be resolved by the retrieval algorithm. Please note, that the former findings are only valid in the infrared spectral region where absorption by cloud particles is the dominant interaction process, see Section 3.3.6. In the solar spectral region, the ice crystal roughness has a significant impact on the phase function, especially for scattering in forward directions, and therefore has to be incorporated by retrieval algorithms (Yang et al., 2018).

Monomodal vs. Bimodal PSD Model

As mentioned in Section 2.2.1, there are various approaches for using different PSDs in remote sensing applications, but most commonly gamma-type distributions are used (Hu and Stamnes, 1993; Heymsfield et al., 2013). Besides the certain type of distribution, their modality is a further unknown quantity and will complicate the relationship between R_{eff} and $R_{\text{eff}}^{\text{rali}}$ in that sense, that analytic relationships, like in Equation (3.30), can no longer be derived. But, results from in situ measurements showed, that mid-latitude cirrus often recorded bimodal size spectra with a large particle population in the small particle mode and a weaker population in the large particle mode (Mitchell et al., 1996a; Ivanova et al., 2001). Also remote sensing applications showed sometimes better results with assumed bimodal PSDs (Donovan and van Lammeren, 2001, Fig. 19). The questions is, how big is the retrieval error when falsely assuming a monomodal instead of a bimodal PSD. Therefore, the ratio of the particle population of the small versus the large particle mode $N_{0,1}/N_{0,2}$ will be varied. The parameters are chosen to be similar to measured by in situ instruments (Ivanova et al., 2001). The results are summarised in Figure 4.3 and basically show, that the second large particle mode can be neglected for $N_{0,1}/N_{0,2} > 10^3$ for the chosen parameters. The large diversity of different approaches for PSDs reflect the complexity of the various particle growth mechanisms in ice clouds and also the challenges of recording PSDs with in situ aircrafts (Baumgardner et al., 2012, 2017). For the following parameter studies, a ratio of $N_{0,1}/N_{0,2} > 10^3$ is assumed and only monomodal PSD are used.

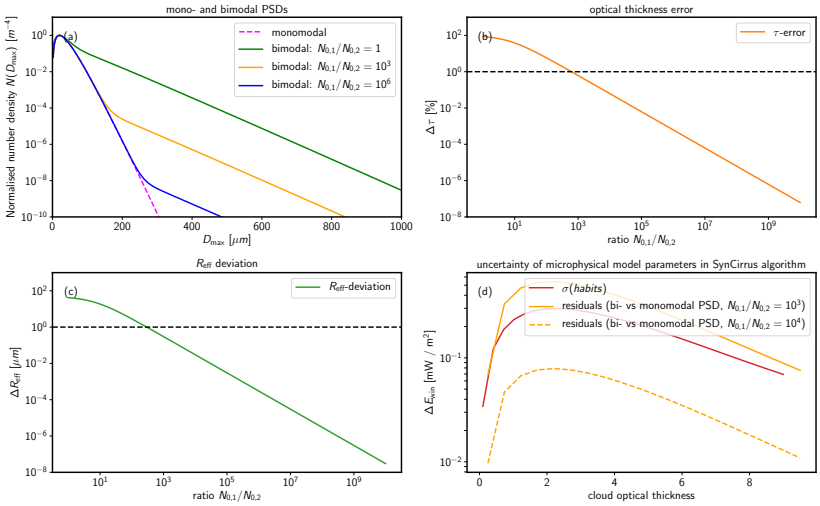

Figure 4.3.: (a) Examples for monomodal and bimodal PSDs. For simplicity, the PSDs are normalised to $N_{0,1} = 1$. The parameters for the larger occupied mode are: shape $\mu_1 = 3$ and scale diameter $D_{s,1} = 10\mu m$. The parameters for the smaller occupied mode are shape $\mu_2 = 1$ and scale diameter $D_{s,2} = 50\mu m$. (b) Error of retrieved optical thickness (given $\tau = 2$), and (c) deviation of retrieved effective radius R_{eff}, when assuming a monomodal instead of a true bimodal normalised gamma PSD for different ratios of the two occupation numbers $N_{0,1}/N_{0,2}$. (d) Comparison of spectral residuals.

4.1.3. Impact of R_{eff} and τ on Infrared Radiance Spectrum

The two main microphysical input quantities for RT calculations are profiles of IWC or β_{ext} and R_{eff}. To investigate the impact both quantities have on the infrared radiance spectrum, averaged in spectral microwindows, one of the quantities is varied while the other was held constant. In Figure 4.4 (a), the cloud optical thickness was held constant and the wide range of different R_{eff} only have a small impact on the radiance spectrum. This is because, cloud scattering does not have a big impact in the infrared region, as shown in Figure 3.13 (a). In contrary to this, in Figure 4.4 (b), R_{eff} was held constant, and the cloud optical thickness was varied, identifying the cloud optical thickness as the main impact parameter, because cloud absorption is the dominant interaction process within the atmospheric window region, see Figure 3.13 (b). Figure 4.4 (c) and (d) shows the percentual deviations on the infrared radiance spectrum, averaged in spectral microwindows, caused by R_{eff} and τ deviations. The implication from Figure 4.4 (c) and (d) is, that in the thermal infrared spectrum it is really important to retrieve IWC or β_{ext} accurately. Because the lidar signal is the basis to retrieve β_{ext}, real good lidar measurements should be available.

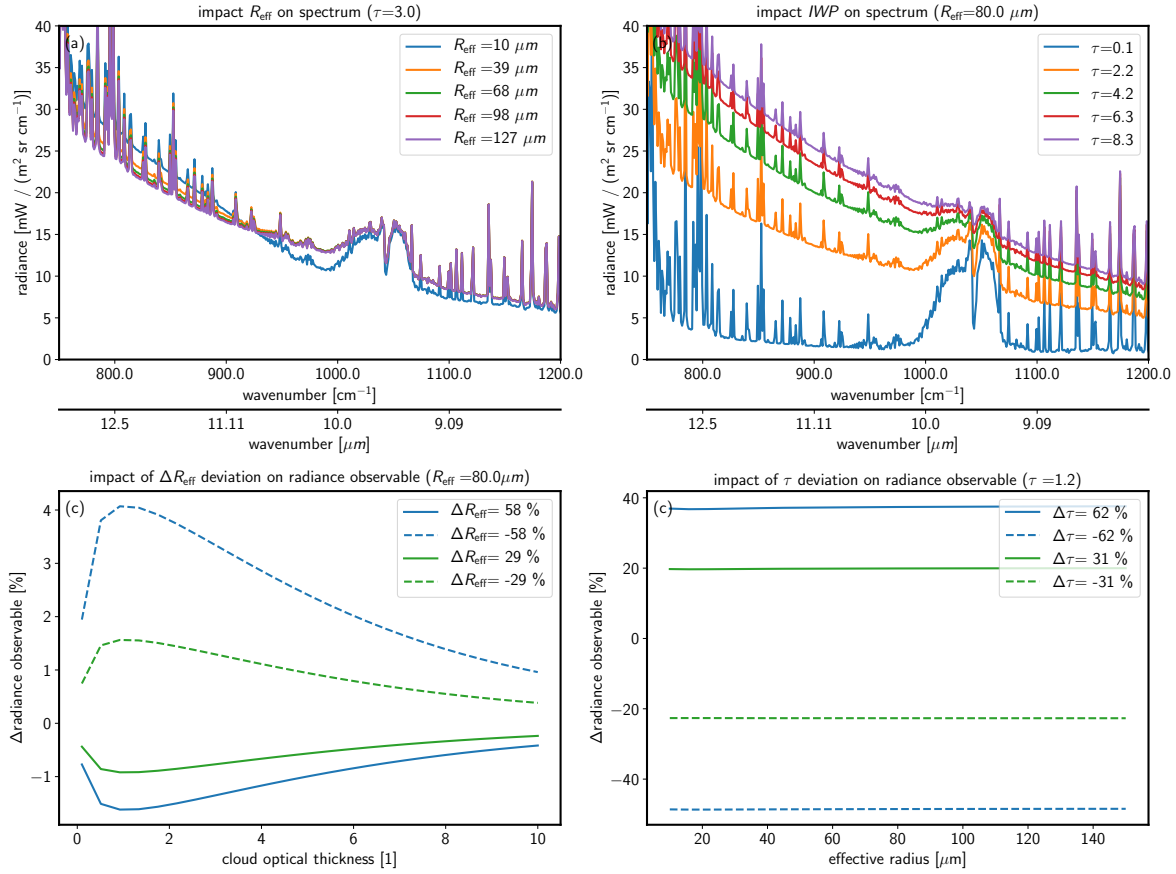

Figure 4.4.: (a) Variation of R_{eff} for constant COT and (b) variation of COT for constant R_{eff}. (c) Impact of deviations in R_{eff} on the radiance observable for different COT. (d) Deviations in COT for different R_{eff} have a bigger impact on the radiance observable.

4.1.4. Sensitivity on Instrument Parameters

Up to the present, the included instruments were assumed to be noise free, nearly infinitely sensitive and perfectly calibrated. The following section will consider the errors on the retrieved parameters caused by instrument noise and calibration uncertainty, and estimates the magnitude of the spectral residuals from these perturbations.

The most important quantity for the radar is the calibration uncertainty ΔZ_e. The radar instrument noise is negligible compared to the lidar noise, and its specific effect on the retrieved profiles is insignificant (Hogan et al., 2006b). However, the calibration uncertainty ΔZ_e will not only appear as fluctuation on the retrieved R_eff and β_ext profiles, like shown in Figure 4.5 (c1) to (c3), it will also impact the determination of the boundary value $\beta_\mathrm{ext}(R_\mathrm{far})$ by the cost function J_tot, which relies on radar measurements around the far end of the measurement distance at cloud top. In Figure 4.6 (a1) to (a4), the results are summarised. Especially, for thin clouds, the wrong estimation of the boundary value caused by radar calibration uncertainty will cause large errors, because the Klett algorithm can not converge to the real extinction for low optical thickness values. For $\tau > 1$, the errors in the microphysical profiles caused by ΔZ_e are negligible, and also the spectral residuals will lie below the variation caused by different ice crystals habits like shown in Figure 4.6 (a4). The given calibration uncertainty ΔZ_e of the Mira-36 radar is estimated to be 1.3 dBZ (Görsdorf et al., 2015).

For the lidar, the most important parameter will be the SNR. Because the Klett inversion is used within the retrieval algorithm, only relative changes in the lidar signal are relevant and the absolute calibrated value is not important. The boundary value for the inversion start will be determined by the help of the radar signal around cloud top, making lidar calibration obsolete for the J_tot-method. To understand the impact of the lidar SNR, it is useful to distinguish the cases for low and high cloud optical thickness. For low τ, the lidar beam can fully penetrate the cloud, as shown in Figure 4.5 (a1) to (a3). The smaller the SNR, the bigger the fluctuations in the retrieved R_eff and β_ext profiles. Here, the SNR is defined as $SNR(R) = P(R)/\sigma$, like described in Section 3.2.2. The quantity SNR_max describes the ratio of the maximal $SNR(R)$ value inside the cloud in relation to the noise floor, characterised by σ in the last signal range gates. For high τ, the lidar signal will be strongly attenuated by the cloud particles, like illustrated in Figure 4.5 (b1) to (b3). Now, the error changes drastically, because the lidar signal at the inversion start is in the same order of magnitude like the instrument noise. Especially, around the inversion start, large errors will be the consequence for small SNR values, unless the lidar signal grows out of the noise floor, the inversion will be numerical unstable. In Figure 4.6 (b1) to (b4), the error on the integrated microphysical quantities caused by the lidar SNR is illustrated. The bigger the SNR, the smaller the errors, until a certain optical thickness is reached where the signal at inversion start is so strongly attenuated, that it will be in the order of magnitude of the noise floor. The residuals in Figure 4.6 (b4) exhibit a minimum, because we are considering the absolute values of the residuals. Typical values for the SNR within a cirrus cloud ($\tau < 2$) are around 30 for a ceilometer and 3000 for the WALES lidar.

The impact of radar calibration uncertainty ΔZ_e and lidar SNR are contrary to each other, where ΔZ_e is causing errors mainly for low optical thickness values, the lidar SNR tends to cause errors for high optical thickness values.

A further important parameter is the radar-lidar vertical signal overlap, because the retrieval can only be applied in regions where signals from both sensors are available. Due to their different wavelengths, the instruments have different sensitivities and will not detect the

same cloud boundaries.

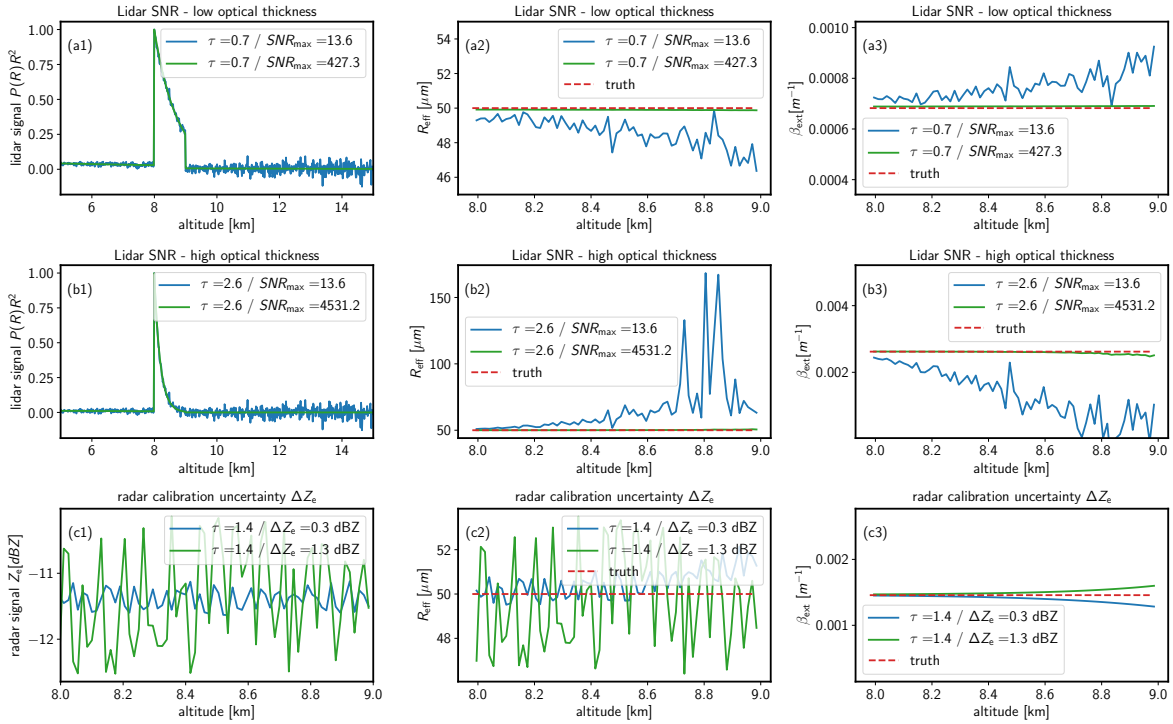

Figure 4.5.: (a1) - (a3) Range-corrected lidar signal, retrieved R_{eff} and β_{ext} profiles for low, and (b1) - (b3) high optical cloud thickness values showing the impact of different used SNR. (c1) - (c3) Radar signal, retrieved R_{eff} and β_{ext} profiles showing the impact of different radar calibration uncertainties ΔZ_{e}.

The lidar will in addition of it, suffer strong signal attenuation inside the cloud, making it difficult to detect cloud tops in optically thick clouds. For simplicity, we only consider the case, that the missing radar and lidar signal part will be taken away at the cloud top region. This corresponds with the more frequent situation, that the lidar signal suffers from attenuation towards cloud top in ground-based instrument configuration, and we neglect the case where the radar is missing to detect small ice crystals at cloud base and top below the radar sensitivity threshold. In Figure 4.6 (c1) to (c4), the results of different radar-lidar signal overlaps are illustrated. Especially in Figure 4.6 (c4) it becomes obvious, how important it is, that there will be a large signal overlap. For signal overlaps of 80 % and smaller, the residuals will be already bigger than the variation of the ice crystal habits.

For the infrared spectrometer, the possible calibration bias of $< 0.67\,\%$ of the ambient black body radiance, is the biggest part in the uncertainty budget, but more important is the calibration precision (reproducibility) of $< 0.13\,\%$ of the ambient black body radiance, see Section 3.2.4. For an assumed ambient black body temperature of $-10\,^{\circ}\text{C}$, the calibration bias is shown in Figure 4.6 (b4) and the calibration precision is shown in Figure 4.6 (c4). Due to the high calibration precision it is possible to differentiate between ice crystal habits.

The estimation of the effect of differences in radar and lidar footprints is beyond the scope of this work, and would require simulations with two-dimensional cloud fields. An estimation

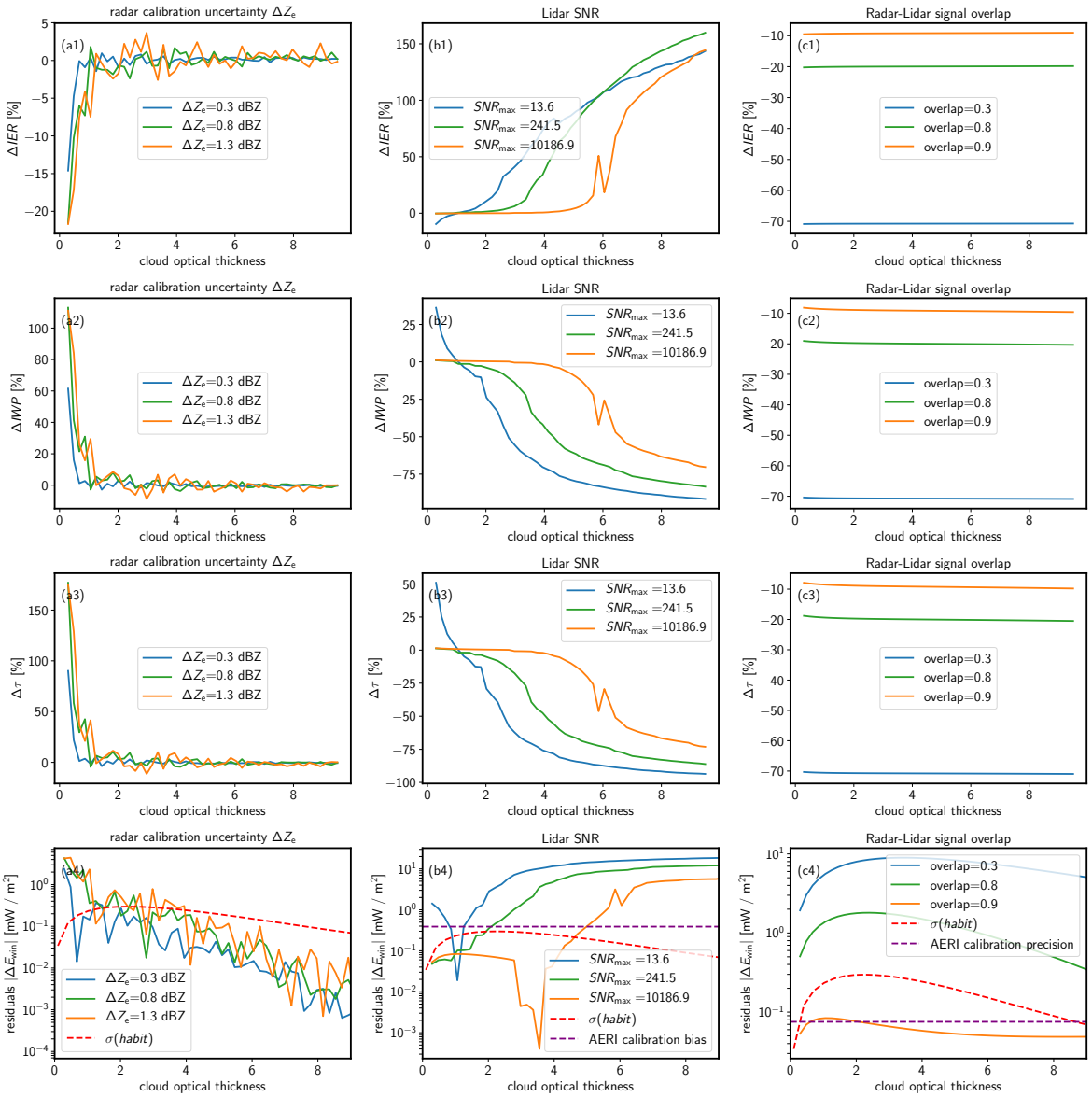

Figure 4.6.: (a1) - (a4) Mean error of retrieved R_{eff}, error of retrieved IWP, error of retrieved τ and spectral residuals as function of cloud optical thickness for different radar calibration uncertainties ΔZ_e. (b1) - (b4) Same, but for different lidar SNRs, and (c1) - (c4) for different radar-lidar signal overlaps.

was taken out by the European Space Agency, with the result, that the RMS difference in mean radar reflectivity or mean lidar backscatter, would be less than 8 % for a typical cirrus cloud (European-Space-Agency, 2001; Hogan et al., 2006b). This was confirmed by further spectral analysis of airborne lidar data, that are very similar to results from a ground-based lidar, based on two-dimensional cloud fields, and showed deviations of 0.363 dB (8 %) (Hogan, 2001a,b,c). Errors of this magnitude will be smaller than the expected uncertainty in radar calibration and errors in the used radar-lidar synergy retrieval techniques.

4.1.5. Sensitivity to Atmospheric Composition

While the microphysical profiles of ice clouds are gained from radar and lidar measurements, the atmospheric profiles of traces gases and prognostic variables are obtained from in situ measurements or from meteorological re-analysis models. These atmospheric profiles are required as input for RT calculations and will have a substantial effect on the radiance spectrum. Therefore, their uncertainties will be investigated in this section.

As mentioned in Section 2.1.2, the current atmosphere of the Earth is composed of two groups of gases, one with almost permanent concentrations and the other with variable concentrations. In this study, the relevant permanent constituents for RT simulations like nitrogen (N_2), oxygen (O_2), argon (Ar), carbon dioxide (CO_2), nitrous oxide (N_2O) and ozone (O_3) are denoted as "permanent gases" and all of them will be varied simultaneously. Although ozone varies significantly with space and time it is assigned to this group, because its variability is much lower than the variability of water vapour (H_2O), the main variable gas under consideration.

In Figure 4.7 the impact of the variation of the different parameters is summarised. For estimating the water vapour profiles with an error less than 9.5 %, the different ice crystal habits could be distinguished by a residual analysis, because the variations of the ice crystal habits are significant bigger than the residuals caused by perturbing the water vapour profiles, see Figure 4.7 (a). For the simultaneous variation of the permanent gases, the different ice crystal habits could be distinguished even for perturbations of the profile concentration up to 22.5 % like shown in Figure 4.7 (c). Therefore, water vapour profiles should be used from radiosonde measurements or at least from meteorological re-analysis. Re-analysis offers water vapor mixing ratios at a temporal resolution of 6 h with a precision of better than 9.4 % for the location UFS, like shown by Sussmann et al. (2016). The profile concentrations of the other gases, in turn, does not have to be that precise in time and space too, and can be taken from climatological data for middle latitudes. Figure 4.7 (d) illustrates, that perturbations of the temperature profile at the maximum of 1 K for cloud optical thickness values lower than 5 will still allow a spectral separation of ice crystal habits. Here, an improvement can be achieved by iterative combining the spectrometer and re-analysis data in a boundary layer temperature inversion like described in Esposito et al. (2007). Furthermore, it is also interesting to study the impact, a wrong "placement" of the cloud would have on the radiance spectrum. This could occur, if radar and lidar would not be able to accurately detect the same cloud boundaries because of their different sensitivities. In Figure 4.7 (b), it is shown, that displacements bigger than 100 m will have a large impact, especially for large optical thickness values. This indicates, that in the thermal spectral region it is important to use data, where the cloud boundaries detected by radar and lidar are not differing much.

4.1.6. Sensitivity to Retrieval Technique

Effect of Non-Constant LR

As explained in Section 3.4.3, the solutions of the lidar equations are based on the assumption of a constant profile of the lidar ratio LR. But in situ field campaigns showed, that the LR actually varies with altitude and temperature and can span values of 29 ± 12 sr for temperatures from -75 to -48 °C (Chen et al., 2002). Therefore, this section will assume the LR to vary through the cloud profile and investigate the impact on the retrieval results. Like for understanding the impact of the lidar SNR, it is again useful to distinguish the cases for low

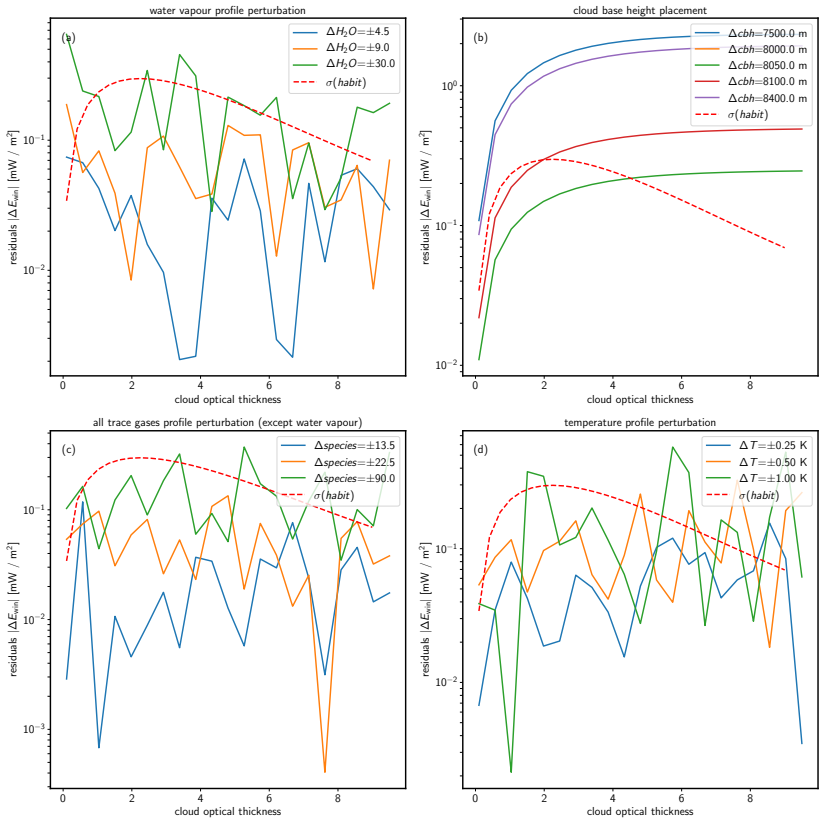

Figure 4.7.: Analysis of the spectral residuals for perturbations caused by (a) variation of the water vapour profile, (b) different placements of the cloud base height, (c) variations of the permanents gases and (d) variations of the temperature profile.

and high cloud optical thickness.

In Figure 4.8 (a) the lidar signals for a low optical thickness ($\tau = 1$) and different varying LR profiles are presented. Because the extinction profile is constant, the backscatter coefficient carries the modulation of the LR with an attenuation caused by the optical depth of the cloud. In Figure 4.8 (b), the retrieved extinction profiles are shown for using the truth boundary value (dashed line) and for using the boundary values estimated by the cost function J_{tot} (solid line). Because the Klett inversion assumes a constant LR, the variation of the backscatter coefficient can not be compensated and the retrieved extinction profile shows a variation similar to the lidar ratio LR, which can cause an overestimation up to 150 % at inversion start. Same behavior is shown for the retrieved R_{eff} profile in Figure 4.8 (c) with errors up to $-13\,\mu\text{m}$ at inversion start.

For a high optical thickness ($\tau = 9$), the variations of LR will not have a significant impact on the lidar signal, due to the strong attenuation, like presented in Figure 4.8 (d). For the retrieved extinction (Figure 4.8 (e)) and effective radius profiles (Figure 4.8 (f)) the errors went down to 26 % and $-3\,\mu\text{m}$ at inversion start. The differences between truth and estimated boundary value are marginal.

In summary, even for varying the LR the lidar inversion will stay numerical stable, but where the current LR value is higher than the mean value of the profile will lead to an

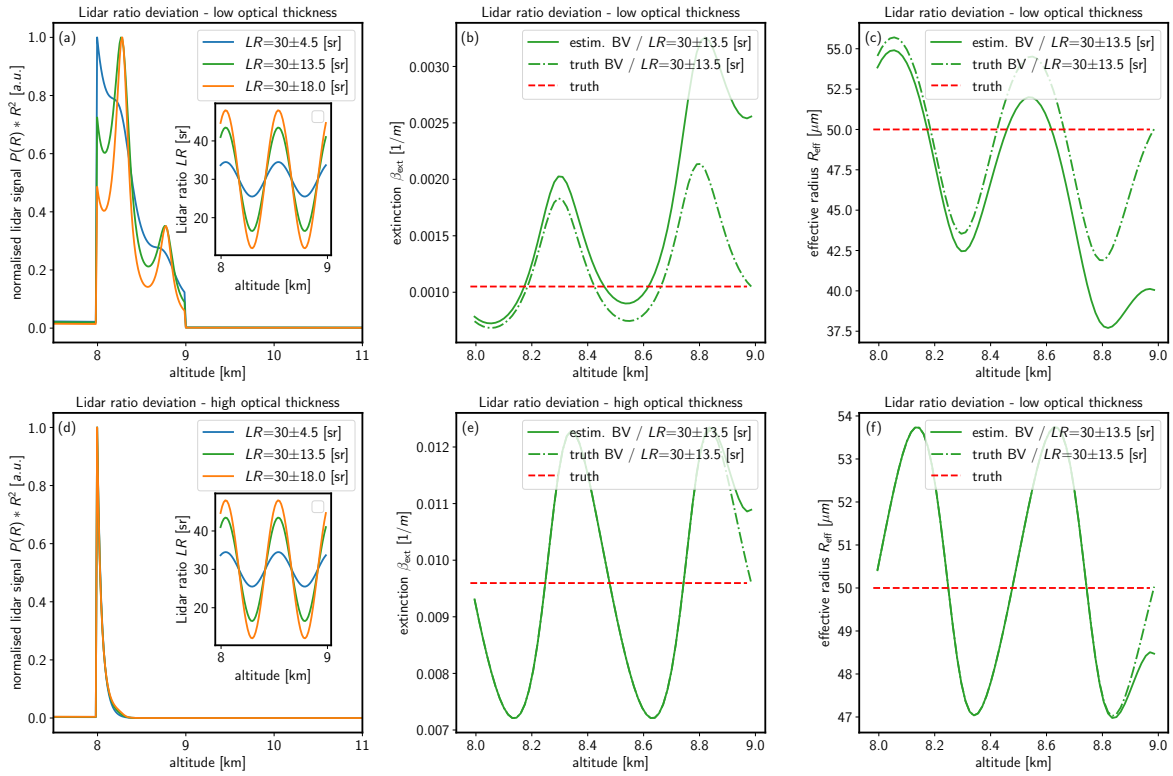

Figure 4.8.: (a) - (c) Impact of non-constant lidar ratios on the lidar signals, the retrieved extinction and effective radius profiles for low optical thickness of $\tau = 1$. (d) - (f) The same like above but for high cloud optical thickness of $\tau = 9$.

underestimation of the extinction, and conversely when the current LR value is lower than the mean value. The lower deviations in retrieved particle size showed, that this quantity is not so sensitive to LR variations. In this parameter study the extreme case was studied, where the LR differs at inversion start from the mean LR. Depending on the concrete profile of the LR, and for considering vertically integrated quantities (τ, IWP), there will be a certain cancellation in the errors caused by a variable LR.

Boundary Value Estimation (J_{tot}) - Effect of Non-Constant $R_{\mathrm{eff}}^{\mathrm{rali}}$ Profile

So far, the examples, like given in Figure 3.18, only included cases, where the true microphysical profiles were constant with height, but this can not be assumed for all clouds. To investigate the effect of non-constant microphysical profiles, synthetic data were generated, were the optical cloud thickness is varied between 0.1 to 5 and the mean normalised gradient of the radar-lidar effective radius $[1/\overline{R_{\mathrm{eff}}^{\mathrm{rali}}}][\mathrm{d}\overline{R_{\mathrm{eff}}^{\mathrm{rali}}}/\mathrm{d}R]$ is varied between $-0.5\,\mathrm{km}^{-1}$ to $0.5\,\mathrm{km}^{-1}$. Then the deviation between the "true" and the retrieved boundary value is characterised. It is assumed, that the clouds have a linear decreasing (negative slope) or increasing (positive slope) microphysical profile of $R_{\mathrm{eff}}^{\mathrm{rali}}(R)$, and that the lidar ratio is constant with height at $LR = 30$. The number of farthest range gates is assumed to be $N_{\mathrm{RG}} = 30$ and the normalised gradient of $R_{\mathrm{eff}}^{\mathrm{rali}}(R)$ is averaged along this distance.

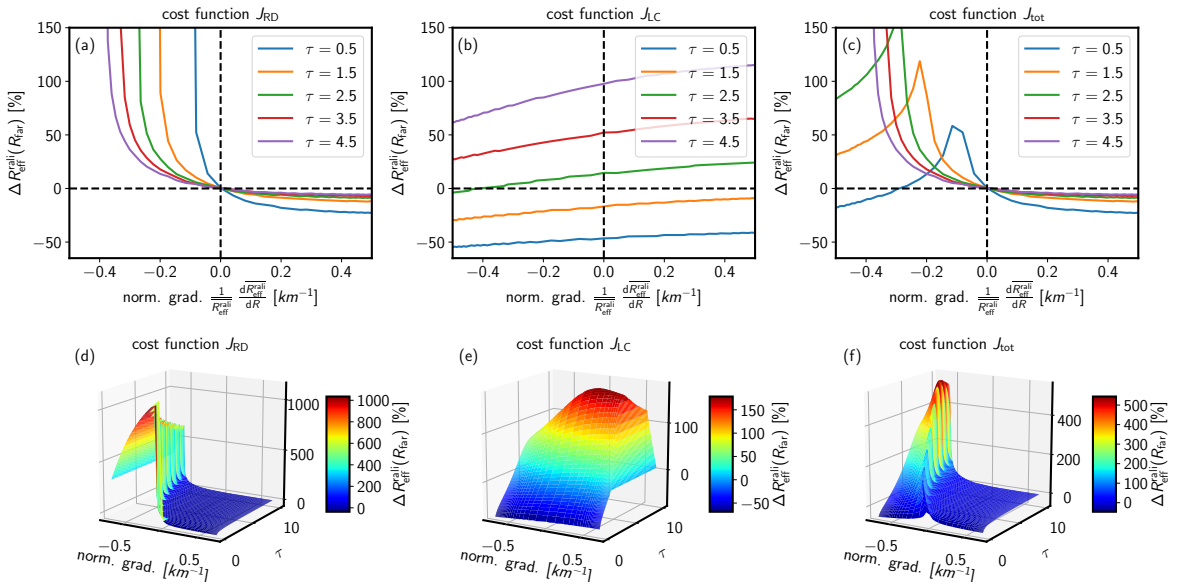

Figure 4.9.: Sensitivity study for the error in the boundary value estimation $\Delta R_{\text{eff}}^{\text{rali}}(R_{\text{far}})$ as function of the normalised gradient $[1/\overline{R_{\text{eff}}^{\text{rali}}}][\mathrm{d}\overline{R_{\text{eff}}^{\text{rali}}}/\mathrm{d}R]$. Different cloud optical thickness values are shown for cost functions based on radius derivatives J_{RD} (a), based on lidar constants J_{LC} (b) and based on their product $J_{\text{tot}} = J_{\text{RD}} J_{\text{LC}}$ (c). (d) - (f) like above, but as three-dimensional surface plot.

In Figure 4.9 the results are summarised and indicate, that the precision of the estimation depends in a complex fashion on the cloud optical thickness, the normalised gradient of $R_{\text{eff}}^{\text{rali}}(R)$ and its sign, confirming previous results from (Donovan and van Lammeren, 2001). Figure 4.9 (a) and (c) indicate, that the error will be very high for low optical thickness values and negative slopes of $R_{\text{eff}}^{\text{rali}}(R)$ around cloud top. For positive gradients, the error will be below 30 %, even for low cloud optical thickness values. These result can serve as a LUT to give a rough error estimation on the retrieved profiles. Please note, that the presence of noise will increase these errors, because the usable lidar signal will be reduced until the SNR will be high enough to evaluate the signal.

Boundary Value Estimation (J_{tot}-cost function) - Effect of Few Very Large Particles in Radar Pulse Volume

Due to the D^6 dependence of the radar reflectivity, the detected radar signal from a cloud volume can be dominated by a few but very large particles. This can have an effect on the inversion procedure, because the J_{tot}-method uses the radar signal to estimate the boundary value, like illustrated in Figure 4.10. Here, the difference ΔD_{max} between two PSD-modes was varied, see Figure 4.10 (a). The first PSD mode has a usual width ($\mu = 4$), where the second mode, including a few but very large particles, has a very narrow width ($\mu = 20$). In Figure 4.10 (b), the difference for calculating the boundary value $R_{\text{eff}}^{\text{rali}}(R_{\text{far}})$, with and without a large particle PSD mode, are compared with each other. Depending on the amount of big particles in the narrow particle mode, substantial deviations will arise for much smaller

$\Delta D_{\max}$. This indicates, that it is better to use a boundary estimation method, that relies on a lower moment of the PSD, like the Rayleigh calibration method, if possible.

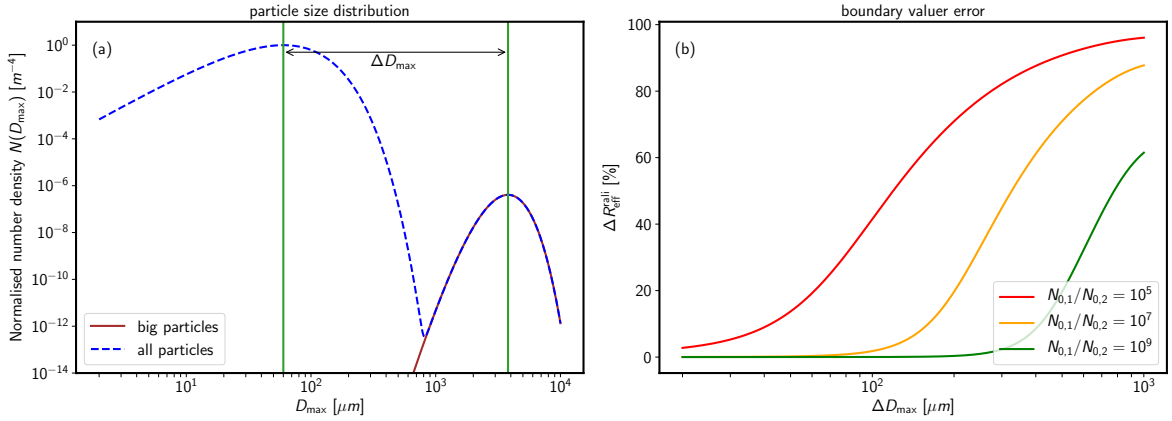

Figure 4.10.: Impact of a few but large particles in the radar signal on the range gate used for inverting the lidar equation. (a) PSDs for all particles and for big particles only. (b) Iteration of the distance $\Delta D_{\max}$ between the two PSD modes.

Boundary Value Estimation (Rayleigh Calibration) - Effect of Different Footprints and Wavelengths

As mentioned in Section 3.4.3, for lidars with a large FOV, multiple-scattering effects have to be included. The method will estimate τ_{MS}, a lower value than the wanted τ_{SS}.

In Figure 4.11 (a) the impact of the lidar wavelength on the fit result is shown. Here, typical parameter for a low-power lidar (ceilometer) are compared with parameter from a high-power lidar (WALES, Wirth et al. (2009)). The larger wavelength of the ceilometer causes a much weaker Rayleigh signal, due to the $\lambda^{-4.08}$ dependence, and in turn a larger fit error. The fit error increases for larger optical thickness values, due to the higher signal losses after passing the cloud. In Figure 4.11 (b), the impact of multiple-scattering effects due to large detector FOVs on the error of the retrieved cloud optical thickness is presented. Here, the larger FOV of the WALES shows especially for τ values between 0 , to 1 , a strong underestimation of the cloud's optical thickness. This underlines, that especially for larger FOVs, a multiple-scattering correction is necessary.

Retrieval Errors

In Figure 4.12 the errors caused by the retrieval techniques and its assumptions are summarised.

In Figure 4.12 (a1) - (a4), the effect of ignoring multiple scattering effects in lidar signals in the retrieval procedure are illustrated for parameters similar to a high power lidar with a FOV of 1.6 mrad and a wavelength of 532 nm (Wirth et al., 2009) and a ceilometer with a FOV of 0.45 mrad and a wavelength of 1000 nm (Wiegner et al., 2014). The plots show, that neglecting the effects of multiple scattering in a cloud retrieval would lead to a considerable underestimation of integrated ice water path, Figure 4.12 (a2), and cloud optical thickness,

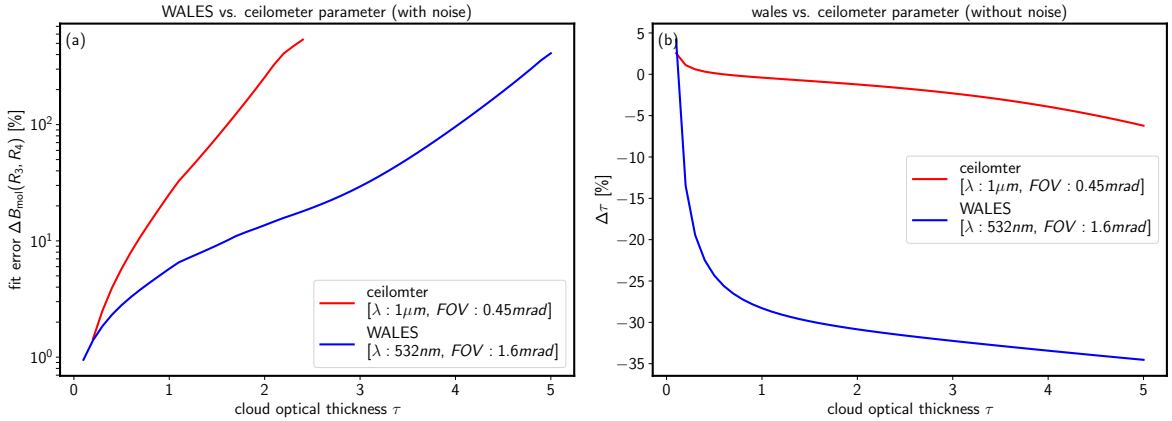

Figure 4.11.: The uncertainty of the Rayleigh fit method dependent on the lidar beam wavelength and the detector FOV are shown in (a) and (b), respectively. The calculation of lidar signals based on different FOVs was taken out with a lidar multiple scattering model developed by Hogan (2006, 2008); Hogan and Battaglia (2008).

Figure 4.12 (a3). The curves are similar to Figure 4.11 (b), but show a large error, because here the J_{tot}-cost function was used for the estimation of the boundary value. For the retrieval of particle size, the deviations are not very large. The spectral residuals for not including MS effects are bigger than the variation caused by different ice crystal habits, indicating that MS have to be included for separating ice crystal habits, see Figure 4.12 (a4).

In Figure 4.12 (b1) - (b4), the errors caused by different deviations of the lidar ratio profile as function of the cloud optical thickness are shown. The deviations in retrieved particle size (ΔIER), are smaller than the errors in optical thickness ($\Delta\tau$) and ice water path (ΔIWP). The impact on integrated quantities is only significant for low optical thickness values, for high optical thickness values the effect can be ignored, see Figure 4.12 (b2) and (b3), respectively. The reason is again, that there will be a quick convergence of the Klett inversion for high τ, even for large errors of the boundary value. The permanent underestimation of $\Delta\tau$ and ΔIWP is caused by the fact, that the lidar ratio profile was chosen to have the biggest overestimation over the mean value of 30 sr at inversion start, like sketched in Figure 4.8. For an underestimation of the mean value of the lidar ratio at inversion start, the behavior would be vice versa and for an exact matching of the mean value, the effect of a varying sinus lidar ratio profile would be cancelled out by integration. For small deviations of the lidar ratio profile, spectral residuals will be smaller than the variation of the ice crystal habits, see Figure 4.12 (b4). There is a minimum, because the absolute value is used for the log plot of the residuals.

The most relevant parameter is the estimation of the boundary value. The comparison with real data will show that there can be deviations up to 40 %, like described in Section 4.2.4. Especially for low optical cloud thickness values, there can be huge deviations in the retrieved integrated quantities τ and IWP, see Figure 4.12 (c2) and (c3), respectively. To have the spectral residuals below the variation of the different ice crystals, the boundary value error $\Delta\beta_{\text{ext}}(R_{\text{far}})$ should be around 1 %, which is hardly feasible in reality. Even in aerosol lidar remote sensing an error of 1 % would require a smoothing of the data for around two hours

(Freudenthaler et al., 2018). But cirrus clouds with their typical inhomogeneous structure allow only integration times of below a few minutes depending on the wind speed. Therefore, for low optical thickness values, it is highly recommendable to determine the boundary value with the Rayleigh calibration method, like introduced in Section 3.4.3.

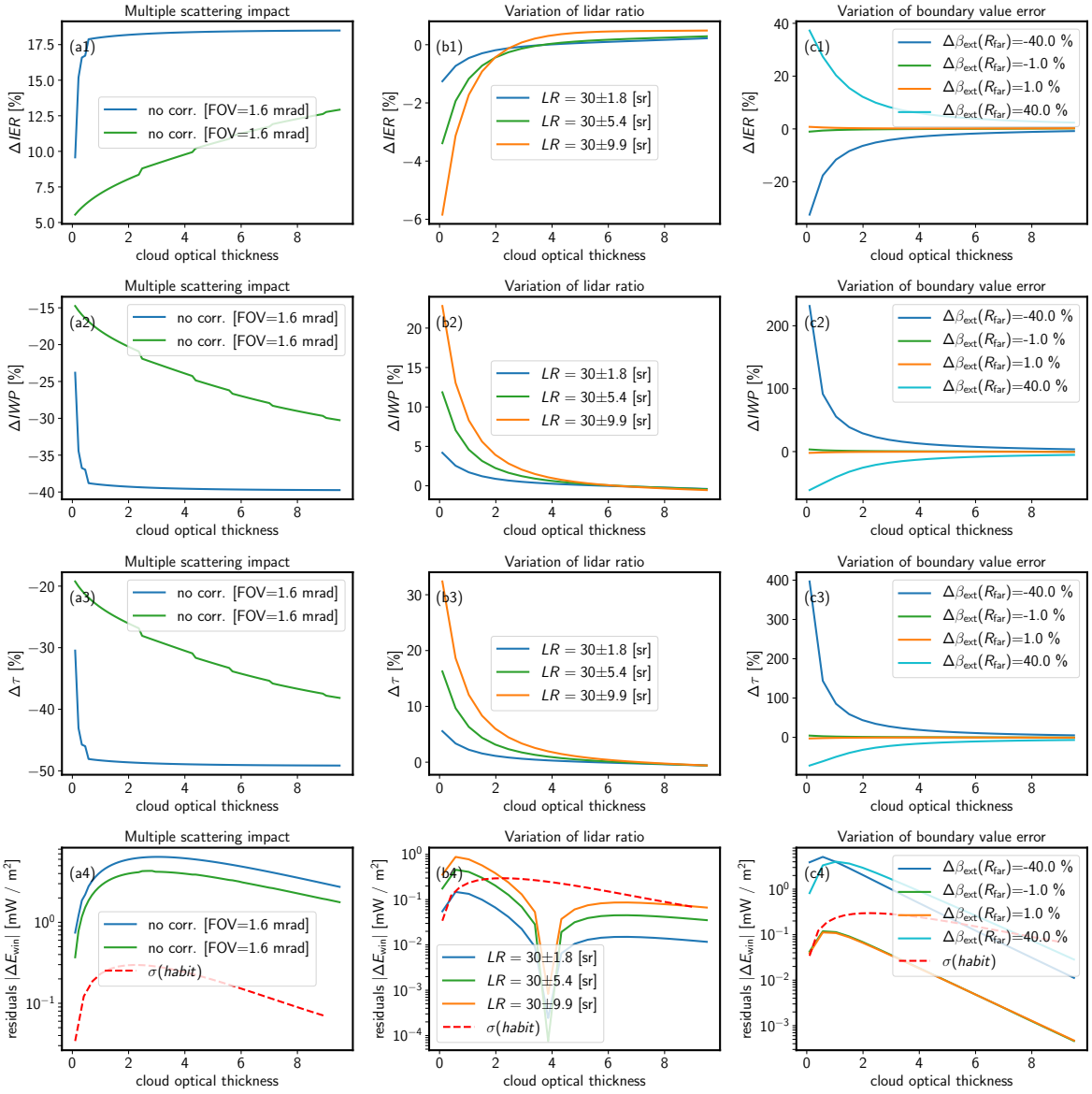

Figure 4.12.: (a1) - (a4) Error of retrieved integrated R_{eff} (ΔIER), error of retrieved IWP, error of retrieved τ and spectral residuals as function of cloud optical thickness for different errors of the boundary value at inversion start. (b1) - (b4) Same like above, but for different variations of the lidar ratio profile, and (c1) - (c4) for lidar single vs. multiple scattering.

4.2. Radar-Lidar Cloud-Retrieval Intercomparison using NARVAL-I Data

4.2.1. The NARVAL-I Field Campaign

The two Next-Generation Aircraft Remote Sensing for Validation (NARVAL-I/II) field campaigns had the aim to validate the various remote sensing measurements on board of the HALO aircraft with satellite measurements, and perform an intercomparison between them. The High-Altitude LOng-endurance (HALO) aircraft provides measurements of microwave radiometer brightness temperatures, lidar backscatter, radar reflectivity and linear depolarisation ratio, and dropsonde atmospheric profiles from aircraft campaign over mid-latitude Atlantic out of Iceland (Konow et al., 2018). The gained data were combined with in situ measurements from dropsondes, because these sensors enable a characterization of the thermodynamic (temperature and water vapor), dynamic (large-scale winds and vertical velocity), and particulate (hydrometeors, clouds, and aerosols) state of the atmosphere over the area of the flight tracks. The HALO is used as an airborne cloud observatory with the goal to capture cloud structures, cloud development and the surrounding environment in order to generate test cases to validate climate models (Stevens et al., 2019).

4.2.2. Case Study - NARVAL-I Research Flight - 18th January, 2014

In this section, three different cloud-retrievals methods will be compared with each other to evaluate the performance of the different retrievals on real data. The remote sensing payload of HALO during NARVAL-I did not include an interferometer, so only the radar-lidar retrieval part of SynCirrus can be compared with the other methods. They are listed in Table 4.2.

Table 4.2.: Different retrieval methods to be tested on NARVAL-1 data.

retrieval name	**SynCirrus**	**VarCloud**	**Radar-Only**
assumptions on microphysical model:	• different habits can be assumed according to Yang et al. (2013)	• ice particle mass follows the relations from Brown and Francis (1995) • area-size relationship is taken from Francis et al. (1998)	• ice particle mass follows the relations from Brown and Francis (1995) • area-size relationship is taken from Francis et al. (1998)
solution methodology:	• costfunction J_{tot} that penalises gradients in $R_{\text{eff}}^{\text{rali}}$ and C_{lid}, Donovan et al. (2000) • N_0^*-inverse model, Tinel et al. (2005) • Rayleigh calibration to retrieve cloud optical thickness	• optimal estimation method, that minimizes the difference between observations and forward models, Delanoë and Hogan (2008)	• based on empirical formulas for IWC and β_{ext} as function of Z_{e} and T, Hogan et al. (2006c), see Equation (3.22) and Equation (3.23)

This comparison has two aims: First, to investigate the impact of the different retrieval techniques on the retrieved microphysical profiles. Second, to quantify the bias between using radar and lidar or only radar data. The NARVAL-I data were used, because they were evaluated with the VarCloud-algorithm, and this method is very interesting because it uses a total different retrieval-approach: forward instead of inverse modelling. Another advantage is,

that NARVAL-I data provide measurements with a high-power lidar (WALES), which allows to use the Rayleigh calibration, presented in Section 3.4.3, for guessing the boundary value.

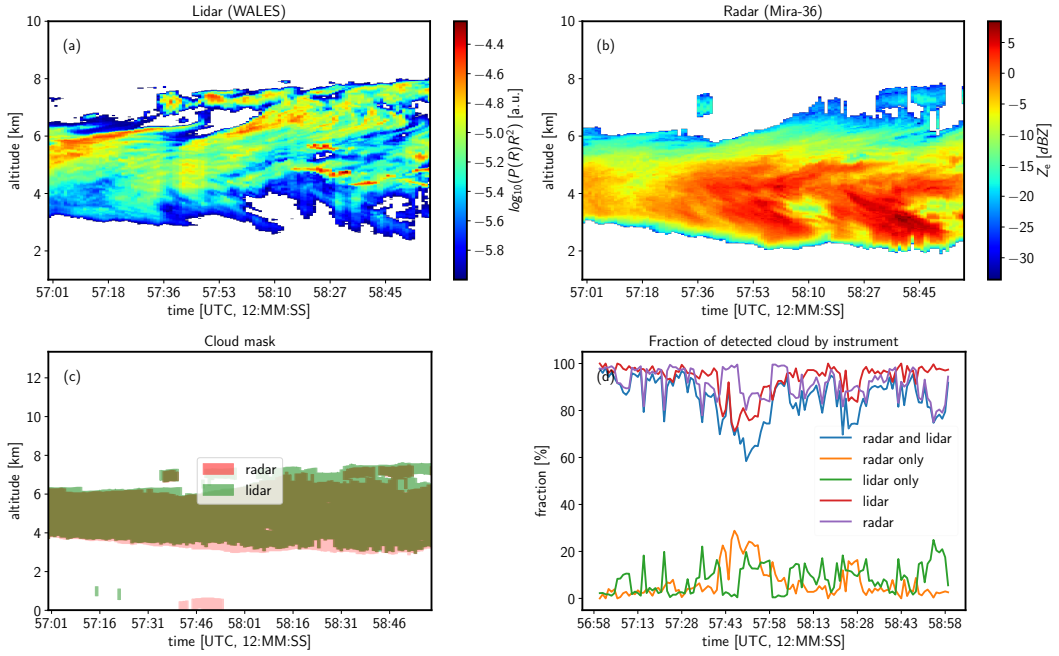

Figure 4.13.: NARVAL-I data from research flight on 18th January, 2014. Recorded (a) Lidar and (b) radar data. Data after Cloud masking (c), and separated after which instrument detected how much of the measured cloud (d)

.

In Figure 4.13, a part of the research flight, which recorded 120 radar and lidar profiles during a cloud measurements is presented. Due to the high speed of the HALO aircraft the data have to be recorded with a high temporal sampling rate of 1 s. In Figure 4.13 (d), the cloud masked data are separated into which instrument did record a certain fraction of the total measured cloud by radar and/or lidar. Of course, it would be desirable, when both instruments would "see" the same cloud, but as indicated by Figure 4.13 (c), the radar missed small ice particles on cloud top (green area, lidar only), whereas the lidar is not able to detect ice cloud particles at cloud base (red area, radar only) due to signal attenuation.

4.2.3. Numerical Accuracy and Stability - Erroneous Extinction Spikes

The backward Klett-inversion is accurate for retrieving the extinction profile, but not perfectly stable for cases, where the lidar runs out of signal (Hogan et al., 2006c, profile 6). When the lidar runs out of steam at the far end of the measurements distance, the lidar signal becomes unreliable at inversion start, and this can produce an erroneous spike in the retrieved extinction profile. In Figure 4.14 (a) this unstable behavior is illustrated, here the lidar signal loses signal with a high rate of change in the farthest range gates of the cloud signal, caused by an optically denser part around the cloud base. Without correction, this behavior will lead to an unrealistic high extinction at inversion start, see dashed line Figure 4.14 (d), where the retrieved extinction is compared with the result from the VarCloud retrieval.

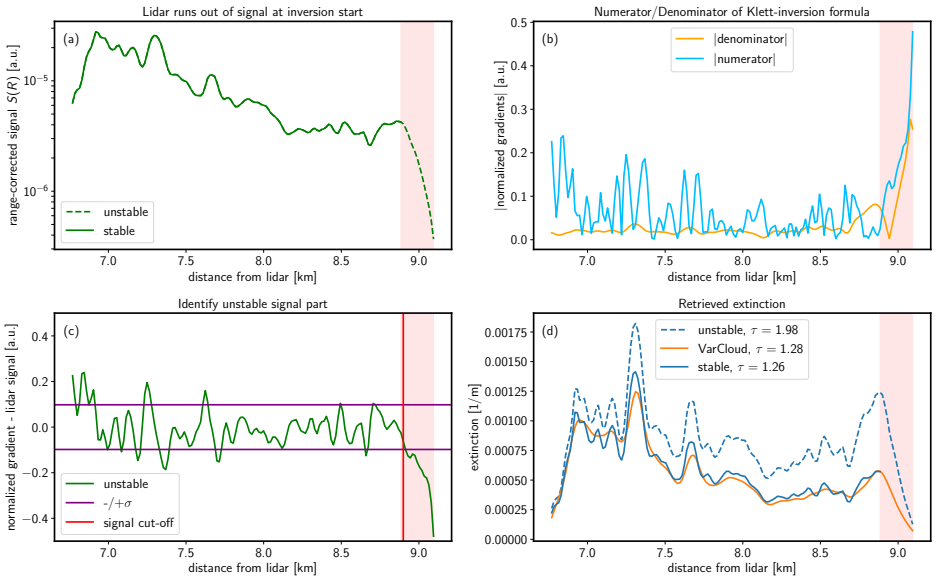

Figure 4.14.: NARVAL-I data from research flight at 12:57:09 on 18th January, 2014. (a) Lidar looses signal power with a high rate at the far end of the measurements distance. (b) Magnitude of change rate of the numerator and denominator parts of the Klett-inversion formula. (c) Method to identify unstable signal part. (d) Retrieved extinction profiles with and without correction compared with result from VarCloud retrieval.

The reason for this spike can be understood, when considering the numerator and denominator of the Klett-inversion formula separately (Equation (3.35)). Therefore, in Figure 4.14 (b) the magnitudes of the normalised gradients of the numerator (simply the range-corrected lidar signal) and denominator of the Klett-inversion formula are compared. Here, due to the high rate of change of the signal loss, the numerator has a much higher rate of change than the denominator, leading to unrealistic high extinction profiles around the inversion start. To avoid this behavior, the lidar signal will be analysed and the part with the high rate of change of the signal loss will be identified and removed from the usable lidar signal. For this purpose, like shown in Figure 4.14 (c), the normalised gradient of the range-corrected lidar signal is used, then its standard deviation is calculated and finally that part of the signal will be removed after the signal exceeds the lower boarder of σ for five consecutive range gates (75 m). The number of consecutive range gates is arbitrary and depends on the noise of the lidar signal. Now, performing the Klett-inversion on the reduced lidar signal returns a much lower extinction which is in accordance with the results from VarCloud, see Figure 4.14 (d). Although, reducing the lidar signal means reducing the extinction, it will produce a smaller error than using the full signal ($\tau = 1.26$ vs. $\tau = 1.98$) with an erroneous spike at inversion start. This method does not always find the unstable signal part perfectly, but good enough to improve the retrieved extinction profiles and avoid erroneous spikes.

4.2.4. Comparison of Cloud Optical Thickness

In Figure 4.15, the retrieved cloud optical thickness values (COT) by different retrieval methods are compared with each other. Here, the VarCloud algorithm, a well tested retrieval (Stein et al., 2011) and mainly used for data gained by aircrafts or satellites, is used as comparison reference (purple dashed line).

In Figure 4.15 (a) to (d), the results for the COT retrieved by the Rayleigh calibration method (Section 3.4.3) are presented. The lidar signal quality is assessed via searching for high lidar SNR areas (Figure 4.15 (a)) and marked by the shaded area. The lidar SNR can be increased by temporal averaging, but due to the high speed of the aircraft it is only possible to use integration times up to 5 s. For areas with high lidar SNR, the fit error of the Rayleigh calibration is low (Figure 4.15 (c)) and therefore a very reliable region to apply the retrieval method, like shown in Figure 4.15 (d). Here, the VarCloud and the Rayleigh calibration method are in accordance for the area with high lidar SNR, for the other regions the lidar signal was already attenuated and therefore missed substantial parts near cloud top. The multiple scattering correction factor η_{MS} was estimated by the *MULTISCATTER* code to be 0.7 for WALES instrument parameter.

In Figure 4.15 (e) to (g), the impact of the correction method to avoid erroneous extinction spikes is investigated. In Figure 4.15 (g), the error of the boundary value is estimated with a LUT, see Figure 4.9. The input parameters of the LUT are the mean normalised gradient of $R_{\mathrm{eff}}^{\mathrm{rali}}$ around inversion start and the retrieved COT. The correction method reduces the mean estimated error for overestimating $R_{\mathrm{eff}}^{\mathrm{rali}}(R_{\mathrm{far}})$ from +40% to +8.1% and for underestimating from −5.1% to −3.8%, in the shaded area. The very high spikes in the retrieved COT that are still present, are caused by situations with multiple clouds detected in a profile, and especially the thin clouds at higher altitudes can cause large errors when using the J_{tot} cost function, see findings in Section 4.1.6. In Figure 4.15 (e) and (f) the retrieved COT via the J_{tot} costfunction and the N_0^* inverse model, are compared with the VarCloud results. After the correction, the J_{tot}-method and N_0^*-method produce comparable τ values like VarCloud, in the shaded area.

In Figure 4.15 (h), the τ results from VarCloud are compared with the empirical Radar-Only retrieval. In the shaded area, where both instruments have a high overlap, using radar data only will lead to an overestimation of τ, due to the strong D^6 dependence of Z_{e}. At 12:57:58 or at 12:58:40, where the lidar signal is already strongly attenuated around the inversion start, see fit-error in Figure 4.15 (b), the results of VarCloud and Radar-Only are in accordance with each other, because the empirical relations from Radar-Only are used as prior within the VarCloud algorithm, when the lidar is lacking data. In Figure 4.15 (i) and (j) the importance of including multiple scattering effects is shown. Without multiple scattering correction the COT is underestimated up to 50 % in the shaded area by the J_{tot} and N_0^*-method. A comparison of the retrieved COT in the shaded area, between VarCloud and the four methods radar-only, J_{tot}, N_0^* inverse model and Rayleigh calibration, showed that they have mean deviations of 128 %, 19 %, 22 % and 14 %, respectively.

In conclusion, two data criteria should be fulfilled to apply radar-lidar retrievals (shaded areas). First, both instruments should have a very high vertical signal overlap about 90 %, but a complete overlap is very rare, because in thin ice clouds, the radar will probably miss to detect the small ice crystals at cloud base. Secondly, the lidar signal should not be strongly attenuated after interacting with the cloud and still have a high SNR at inversion start. This can be evaluated by considering the fit-error of the Rayleigh signal at the far end of the

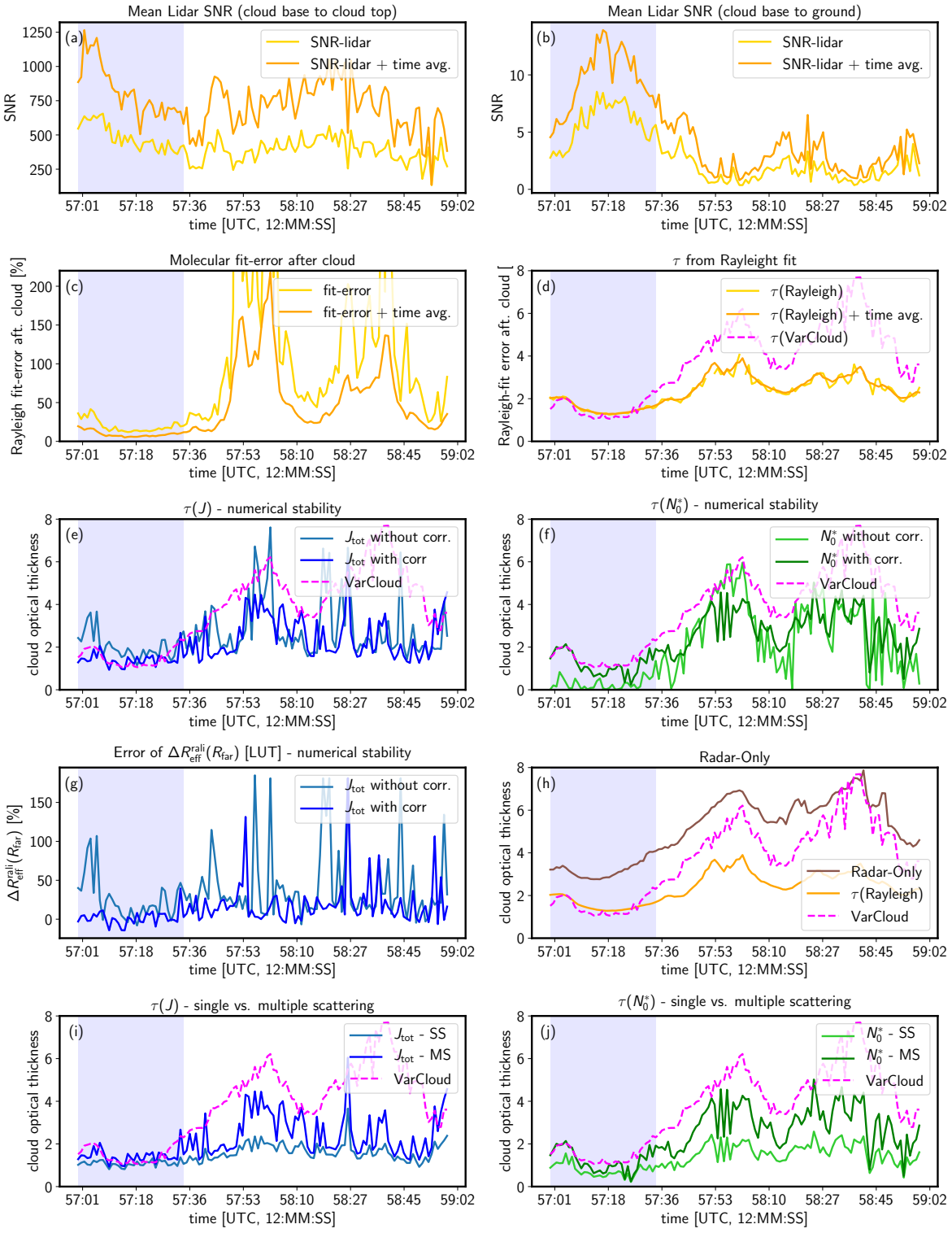

Figure 4.15.: Optical thickness retrieved with different retrievals on NARVAL-I data from research flight at 18th January, 2014. (a) - (d) Aspects of Rayleigh calibration method. (e) - (g) Impact of correction for numerical stability. (h) Comparison with Radar-Only retrieval. Multiple vs. single scattering results are shown in (i) and (j).

inversion.

4.2.5. Comparison of Extinction and Radar-Lidar Effective Radius Profiles

To assess the skill of the algorithms in retrieving vertical profiles of β_{ext} and $R_{\text{eff}}^{\text{rali}}$, the value ranges will be compared with the VarCloud results. Optical thickness is an vertically integrated quantity and errors in the retrieval procedure of the extinction coefficient fluctuate around the true value, and so they may largely cancel in some way. Therefore, the retrieved values will be compared directly value by value. The retrieval algorithms assume different ice microphysical models and therefore, the comparison uses $R_{\text{eff}}^{\text{rali}}$ instead of R_{eff}, because this quantity is, like β_{ext}, independent of habit and PSD assumptions. The comparison uses 35 profiles for times between 12:57:00 and 12:57:34, shaded areas in Figure 4.15, where the data quality is good enough to ensure a meaningful comparison, and the results are shown in Figure 4.16. The highest bias is caused by the Radar-Only retrieval, because it only exploits data from the radar. The lowest $R_{\text{eff}}^{\text{rali}}$-bias is given by the J_{tot}-method, here the values are in good accordance with the VarCloud results. Considering extinction, the lowest bias is returned by the N_0^*-method, but the bias given by J_{tot}-method is only hardly bigger. It is interesting to mention, that although, the N_0^*-method has the lowest extinction bias, the $R_{\text{eff}}^{\text{rali}}$-bias is quite large. This is an artifact of the inverse model coefficients, which were derived for a 94 GHz radar, but the HALO payload included a 35 GHz radar. Whereas lidar data are sensitive to β_{ext} ($\sim D^2$), the radar data are sensitive to Z_{e} ($\sim D^6$) and using "wrong" coefficients will show to have a bigger impact on particle size measures like $R_{\text{eff}}^{\text{rali}}$. So, deriving coefficients for an inverse model with a 35 GHz will lower the $R_{\text{eff}}^{\text{rali}}$-bias.

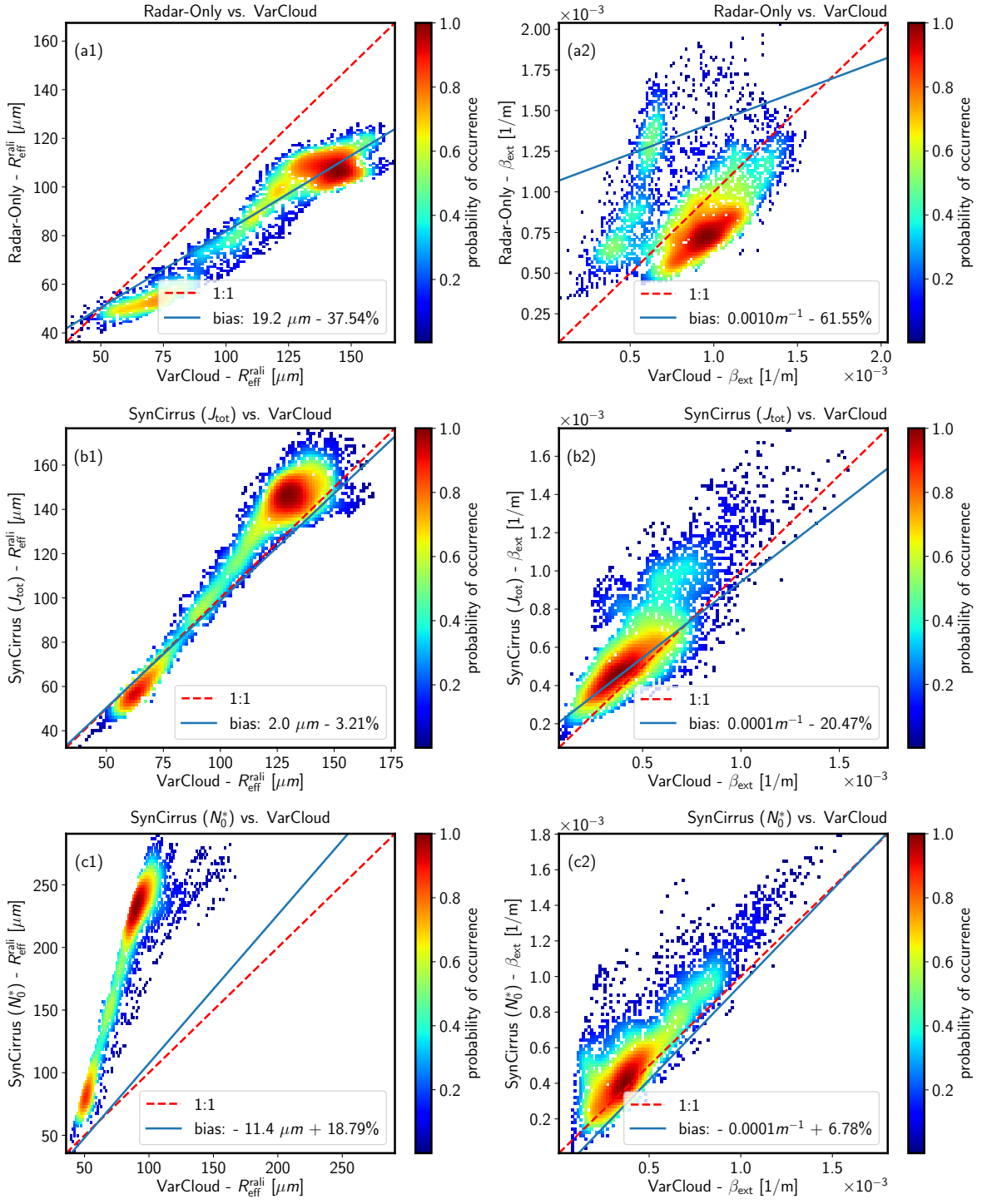

Figure 4.16.: Comparison of retrieved values for $R_{\text{eff}}^{\text{rali}}$ and β_{ext} for different retrieval methods. Radar-Only vs. VarCloud is shown in (a1) and (a2). SynCirrus with J_{tot}-method vs. VarCloud is presented in (b1) and (b2). SynCirrus with N_0^*-method vs. VarCloud is illustrated in (c1) and (c2)

.

4.3. Three-Instrument Study with *SynCirrus* using UFS Data

4.3.1. The Location at Mount Zugspitze

The measurement sites at Mt. Zugspitze, the Schneefernerhaus (UFS, 2656 m a.s.l., radar and lidar) and the platform at the summit station (2961 m a.s.l., infrared spectrometer) offer unique conditions to use spectrometer data in a three-instrument cloud retrieval or for radiative closure studies. Both sites are not remote and accessible by cable cars and offer extraordinary dry conditions and low aerosol loads. The aerosol optical depth will be a factor of 10 lower than at typical lowland midlatitude sites. These conditions are particularly helpful, because lidar signals will not be weakened by aerosol layers and the recorded downwelling radiances will benefit from the high atmospheric transparency because the used spectral microwindows will become more transparent, especially in the strong pure rotational band of water vapor, making it more reliable to compare measured radiance spectra with simulations of the spectra driven by sensor synergy. Furthermore, the easy access allows to maintain long term studies (multi-annual) with the benefit of attaining improved data statistics compared to field campaigns, which would be helpful to develop radiative ice cloud parameterisations usable in GCMs (Tobin et al., 1999; Sussmann et al., 2016).

4.3.2. Data Quality and Data Correction

The operators of the differential absorption lidar (DIAL) and the AERI at Mt. Zugspitze, the IMK-IFU, were mainly focused in recording data for clear sky radiative closure studies (Sussmann et al., 2016; Reichert et al., 2016; Reichert and Sussmann, 2016). Therefore, there were not so many data including clouds, that could be used in this study. Furthermore, the DIAL was out of service for a larger part of the observation period, making it necessary to use low power ceilometer data instead of high power DIAL data. As pointed out by Ewald et al. (2019), Mira-36 radar data should be corrected for a reflectivity calibration offset.

Lidar - Evaluating Ceilometer Signal Quality

Due to the aforementioned reasons, low power ceilometer data were used instead of high power DIAL data. In general, ceilometers have some disadvantages when using their data in cloud retrievals: they use weaker laser pulses, which lowers their ability to penetrate clouds, their larger wavelength will reduce the quality of the Rayleigh-fit (Equation (3.4.3)), and their detectors are prone to resort in saturation from cloud signal returns (Wiegner, 2018). The question is, to which extent ceilometer data can be used for a Rayleigh calibration to invert the lidar equation. In Figure 4.17 (a) - (c), the quality of the Rayleigh calibration is investigated for a daytime measurement, using a cloud signal, and in Figure 4.17 (d) - (f), the same analysis is repeated for a nightly recorded clear sky signal. Since the lidar SNR depends on background radiation, nighttime measurements without recording radiation from the sun are preferable. To have usable lidar signals for a Rayleigh calibration, the fit error after penetrating the cloud should be below 50 %, like shown in Figure 4.15 (c). But, as shown in Figure 4.17 (c), even for large temporal average times up to 80 min, the fit error of the Rayleigh calibration after penetrating the cloud is still in the order of 100 %, and in the first minutes even two orders of magnitude higher. Even for the best conditions during nighttime, and without signal attenuation caused by a cloud, a Rayleigh calibration in the upper atmosphere were cirrus clouds reside is not trustworthy, see Figure 4.17 (f). Because of

ice cloud horizontal inhomogeneity, it is necessary to have short sampling times of maximally a few minutes, depending on the wind speed (Fu et al., 2000; Hogan and Illingworth, 2003).

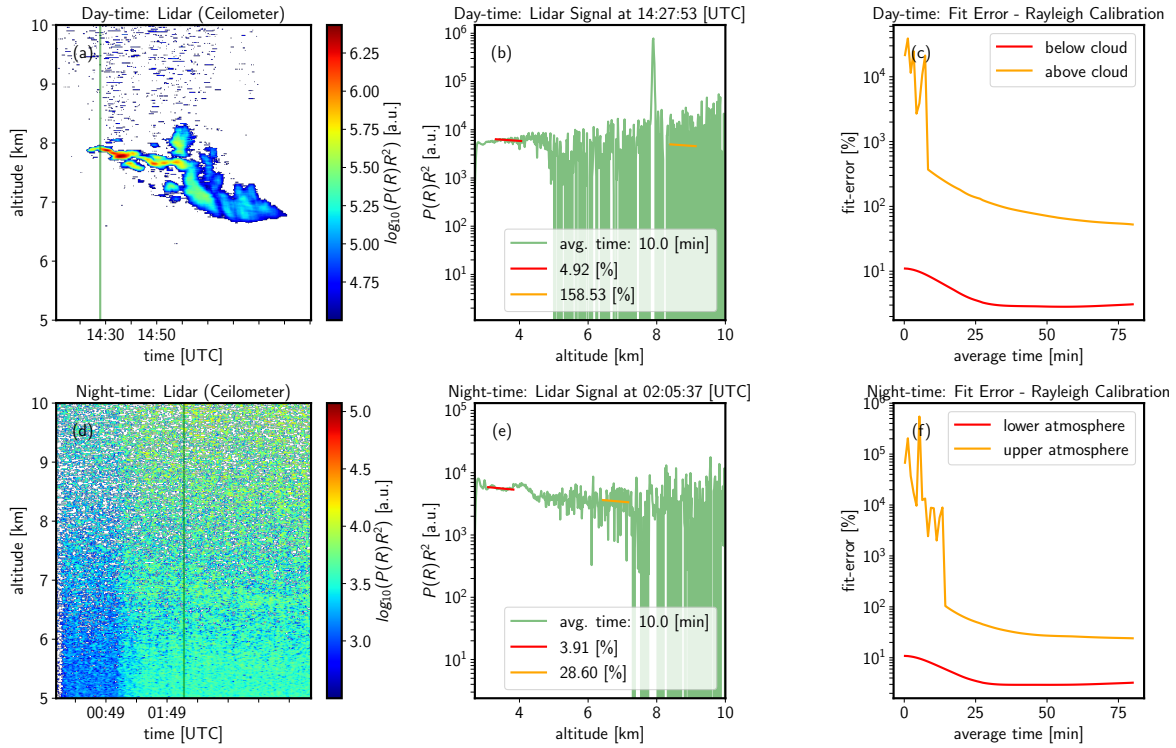

Figure 4.17.: Analysis of the ceilometer signal for its usability of a Rayleigh calibration for daytime (a) - (c), and nighttime (d) - (f) measurements

Therefore, the Rayleigh calibration method can not be used with ceilometer data to solve the lidar equation. Furthermore, as shown in Figure 4.16 (c1), the N_0^*-iteration method can not be used as well, because this method requires either data from a 94 GHz radar, or the derivation of new coefficients for a 36 GHz radar, based on in situ aircraft data. In conclusion, the only working method to solve the lidar equation with data recorded at UFS, is the combined $R_{\text{eff}}^{\text{rali}}$-gradient and C_{lid}-constant J_{tot}-cost function method.

Radar - Problems with Vertical Upwinds

The mountain location of the radar has the effect, that the assumption used for devices at non-alpine regions, that upward or downward motion at the altitude of the device is zero and consequently the cloud particle fall velocities are in equilibrium is not valid anymore, because winds with vertical velocity components can come up the slope from the valley. These strong vertical movements over mountains will lead to a broadening of the velocity doppler spectrum. Because of these strong vertical movements the equilibrium falling speed will be reduced and the velocity doppler spectrum is broadened. The consequence is, that the doppler spectrum can not be used as trustworthy retrieval input quantity to derive particle size and ice water content (Häring, 2016), based on methods like described in (Matrosov et al., 2002).

These findings are relevant for the retrieval of cloud properties based on radar measurements only. At the cost of higher uncertainties, one can overcome this limitation in using the empirical relationships in Equation (3.23) and Equation (3.22), like described in Section 3.4.1.

Radar - Correction of Reflectivity Calibration Offset

Ewald et al. (2019), presented in their study, that effective reflectivities measured by HAMP-MIRA during previous HALO aircraft campaigns had to be corrected by +7.7 dB, see Table 3.3. In detail, they characterized the internal calibration of the instrument via analysing the individual instrument components in the laboratory, and these findings were cross-checked with external reference sources like the ocean surface backscatter and different air- and spaceborne cloud radar instruments.

Because the HAMP-MIRA and the UFS-MIRA are similar constructed, suggests that UFS-MIRA data have to be corrected as well. In contrary, to the aircraft-configuration of HAMP-MIRA, the UFS-MIRA is used in ground-based-configuration and therefore the offset components of the two-way attenuation by additional waveguides and the belly pod radome, both specific airplane installations, can be taken out of consideration Ewald (2019), resulting in a likely calibration offset of +4.2 dB.

The applied radar reflectivity calibration offset can be approximately validated by a two-instrument retrieval framework based on radar and AERI measurements only. Extinction coefficient and ice water content, neglecting ice crystal habits, can be retrieved via the empirical relationships Equation (3.23) and Equation (3.22), respectively. Based on these relationships, they only require radar reflectivity Z_e and temperature to retrieve microphysical profiles, then radiance spectra at the location of the AERI instrument can be simulated. These calculations will be repeated after applying different radar calibration offsets between 0.0 dB and 10.0 dB, and minimizing the spectral residuals of simulated vs. measured spectra will return the best matching calibration offset for every profile. In Figure 4.18, the results were presented for radar and AERI data recorded on 22nd October, 2013 between 01:48:12 and 03:45:29. In Figure 4.18 (a), paired data of the retrieved reflectivity offsets which caused the lowest spectral residuals and retrieved cloud optical thickness values are presented. Here, only data were shown, were it was possible to determine a minimum between offsets ranging from 0.0 dB to 10.0 dB, excluding the two boundary values. The histogram in Figure 4.18 (b), shows the counts for the different reflectivity offsets. The database for the empirical $Z_e - T$ relationships showed large scatter for small extinction values and lower scatter for bigger extinction values (Hogan et al., 2006c). Therefore, reducing the data to cases with higher retrieved optical cloud thickness values ($\tau > 1$), will help to lower the uncertainties of the results. Furthermore, it is helpful to restrict the data to cases, where the radar alone was able to detect a large proportion of the cloud, at least more than 90 % of the detected common radar-lidar cloud profile. The data reduction causes a lowering of the mean reflectivty offset from 5.23 dB to 4.09 dB, which is closer to the assumed offset of 4.2 dB. For trustworthier results, more data and better statistics are required, and temperature profiles from local radiosondes instead of re-analysis data could also help to reduce the uncertainties, but it seems reasonable to correct the UFS radar data by +4.2 dB.

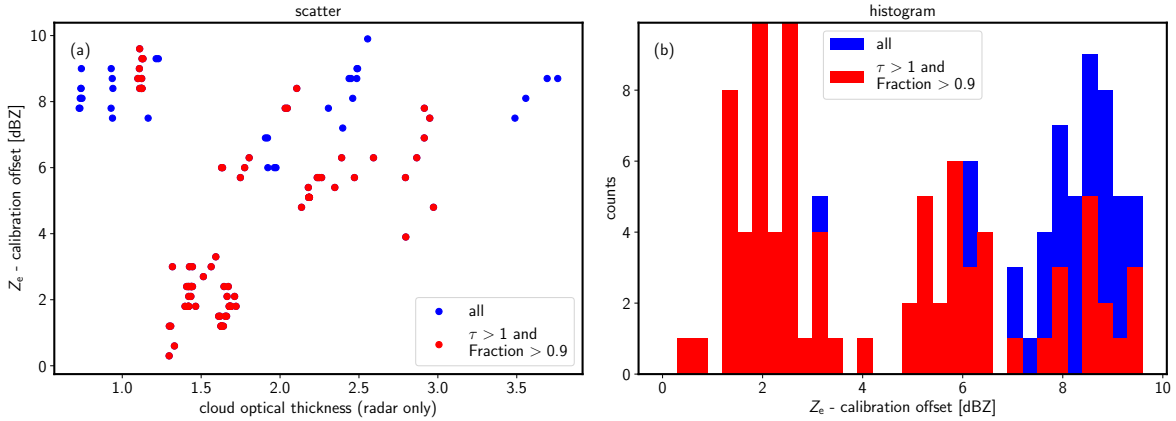

Figure 4.18.: (a) Illustration of retrieved minimal reflectivity offset vs. retrieved cloud optical thickness, based on radar and AERI data recorded on 22nd October, 2013 between 01:48:12 and 03:45:29 at Mt. Zugspitze. (b) Ocurrence of the retrieved minimal reflectivity offsets.

4.3.3. Case Study - 22nd October 2013

Potential measurement candidates for an ice cloud study should provide regions with high radar-lidar vertical signal overlap of the detected cloud profile, see Figure 4.6 (c4). Furthermore, a certain amount of temporal homogeneity, due to the large temporal integration time of the AERI instrument compared to the sampling times of the radar and lidar devices, should be given. The case study, recorded at 22nd October, 2013 from 01:48:12 to 03:45:29, offers both high and low radar-lidar overlap regions and is therefore a good candidate to see, where the SynCirrus algorithm could produce useful results and where not.

Radar-Lidar Inversion

In Figure 4.19 (a) and (b), the used radar reflectivities and range corrected lidar signals are shown for data acquired for 22nd October, 2013 by a MIRA-36 radar and a Jentoptik ceilometer. The temperature were lying mainly below $-38\,°C$, indicating that the observed cloud is in the ice phase. Exploiting measurement data from a co-located microwave radiometer at UFS, the Cloudnet target categorization determines that the observed cloud was composed of ice as well (Hogan and O'Connor, 2004b).

The comparison of the detected cloud boundaries shows, that the lidar signal usually penetrates the entire cloud layers, whereas the radar is only be able to detect similar cloud bases, missing only the very small ice crystals directly at the cloud base, but fails to detect the cloud tops around an altitude of 12 km. Between altitudes ranging from 10.2 km to 12 km it is assumed that the particles in this area are too small to give rise to an usable radar signal, indicating that the ice crystals in that layer have probably an effective radius below a few microns. Only between 02:08:00 and 02:22:00, both instrument have a large overlap of the detected cloud regions, as presented in (c) and (d).

The results of the radar-lidar inversion procedure, using the J_{tot}-cost function, are presented in Figure 4.19 (e) - (h). The retrieved profiles of β_{ext} (e) and $R_{\text{eff}}^{\text{rali}}$ (f), will be converted

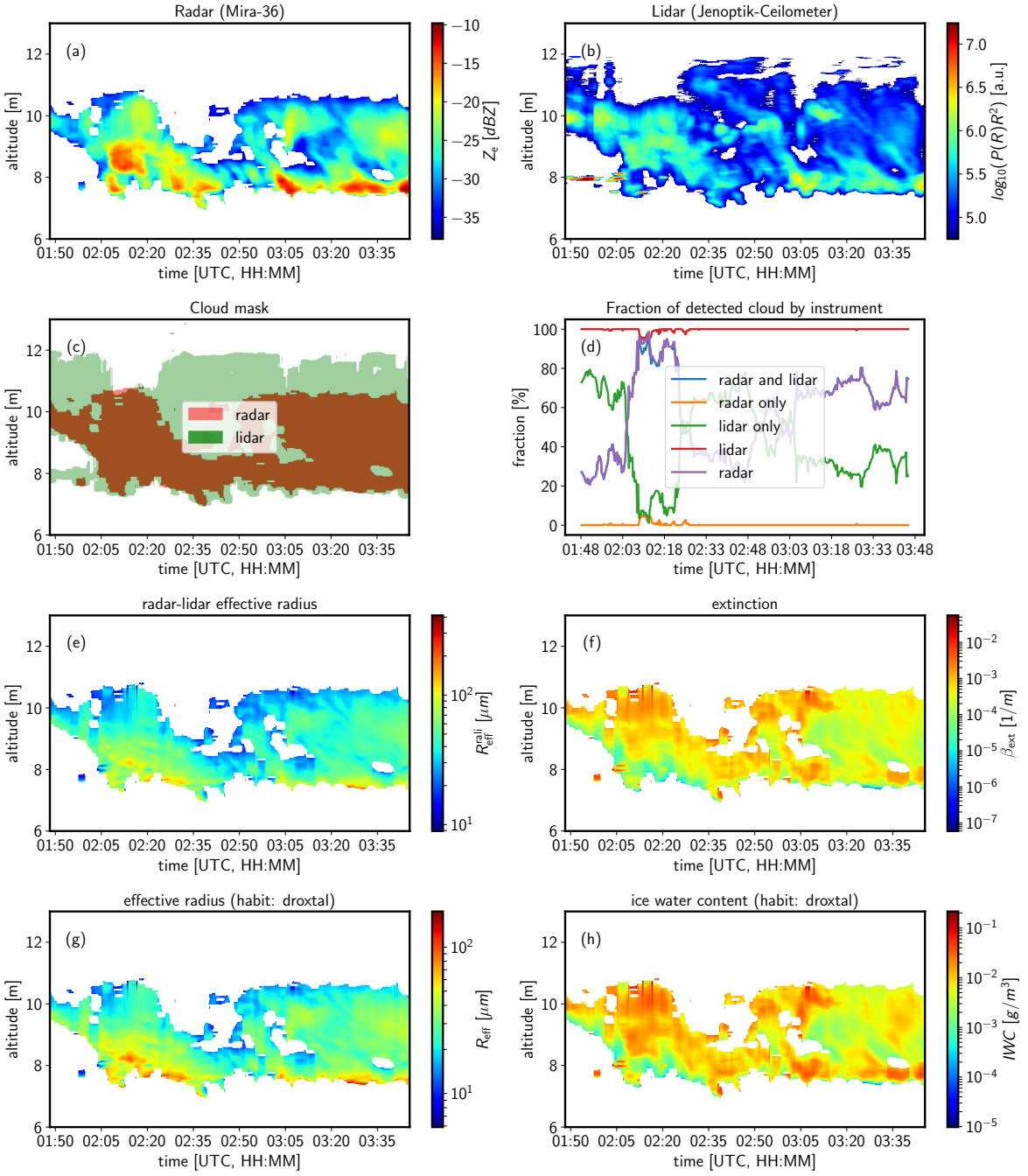

Figure 4.19.: Observed radar (a) and lidar (b) data at UFS for 22nd October, 2013. Detected cloud boundaries (c) and fractions separated by instrument (d). Inversion results for $R_{\text{eff}}^{\text{rali}}$ (e), β_{ext} (f), and for the RT input quantities R_{eff} (g) and IWC (f), assuming droxtal as ice crystal habit.

to profiles of R_{eff} (g) and IWC (h), using assumptions on PSD and ice crystal habit, like described in Chapter 3.4. The retrieved values for IWC, mainly ranging from $1 \times 10^{-4}\,\text{g}\,\text{m}^{-3}$ to $1 \times 10^{-2}\,\text{g}\,\text{m}^{-3}$, and R_{eff}, mainly ranging from 30 µm to 100 µm, are in accordance with what is usually observed in ice clouds (Stein et al., 2011).

From 453 profiles in total, 9 profiles located around 01:56:00 and 02:14:00, were excluded from the evaluation, because the presence of noise, attenuation of the lidar signal, or the absence of a strong enough radar return made a representative and numerical stable inversion impossible.

Comparison with AERI Results

In Figure 4.20, the full procedure for the SynCirrus retrieval is illustrated. First, the mean temperature of the cloud is used with Equation (4.1.2), to determine the shape parameter μ for the assumed monomodal gamma PSD, see Figure 4.20 (a). This parameter has to be consistent in the radar-lidar inversion as well as in radiative transfer calculations. In Figure 4.20 (b) and (c), it is shown that the retrieved effective radius profile resembles the measured radar reflectivity profile, whereas the retrieved ice water content profile resembles the measured lidar backscatter signal. This is an artifact of the different sensitivities of the instruments concerning the PSD moments of the microphysical properties. In Figure 4.20 (d), the observed zenith downwelling radiance spectrum is compared with the simulated spectrum based on the above mentioned microphysical profiles as input quantities at 02:08:44. Finally, Figure 4.20 (e) compares the radiance observables evaluated in the different spectral microwindow regions for every time step from AERI with simulations assuming droxtals or solid columns as ice crystal habit. The step size structure results from the large AERI sampling time of approximately 8 min. In Figure 4.20 (f) compares the spectral residuals of observation minus simulation with the variation given by the standard deviation of the set of all assumed ice crystal habits. It is seen, that only in three AERI sampling intervals the residuals are below the variation of the ice crystal habits. This, in turn, indicates that the failing to retrieve cloud microphysics within uncertainties in the other intervals, can not arise from assuming the wrong ice crystal habit, rather pointing to other errors in the retrieval procedure, that have to be investigated.

4.3.4. Analysis of Retrieval Quality

The presented ice cloud study in Figure 4.20 (e) and (f) showed large deviations between observation and simulation, making it impossible to retrieve ice crystal habits. Therefore, the numerical stability of the retrieval procedure and the data quality has to be further investigated.

Increasement of SNR at Inversion Start

Due to the low power of the ceilometer, the signal quality at cloud top is very poor and the signal is strong oscillating between negative and positive values. Negative values occur due to an applied dark current correction (Wiegner, 2018). Therefore, removing signal parts with the method presented in Section 4.2.3 is not enough and more parts of the lidar signal and consequently of the radar signal can not be used in the inversion. Whereas for the WALES data only a few range gates had to be removed, the poor ceilometer data quality required the removal of up to 50 signal range gates. In Figure 4.21 (a) the lidar SNR before and after removing the poor quality oscillating signal parts is illustrated. Especially, the boundary value

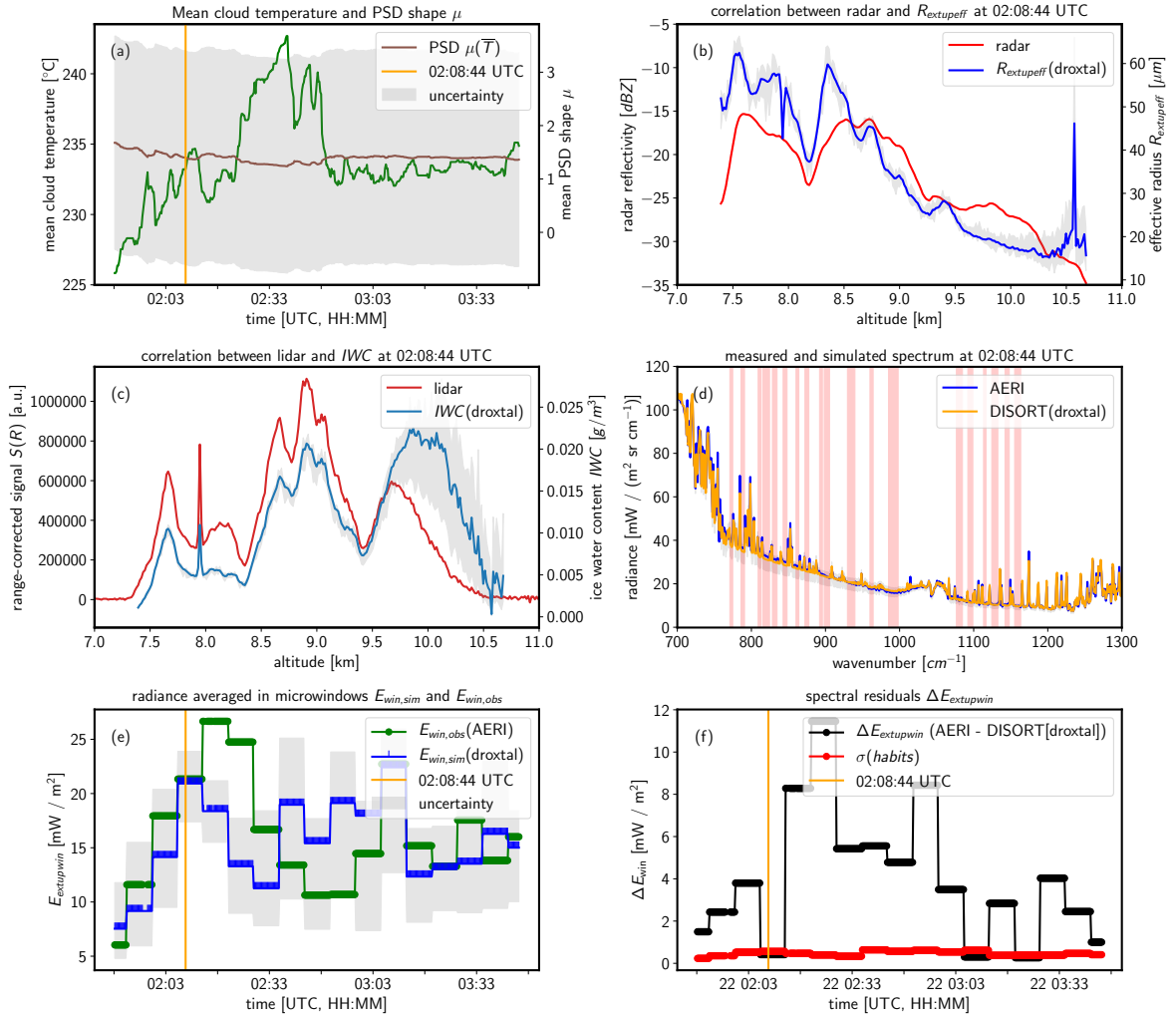

Figure 4.20.: Steps within the SynCirrus retrieval procedure, observed at 22nd October, 2013. Estimation of the shape parameter for the gamma PSD (a). The certain intermediate results of the ice cloud study, the retrieved R_{eff} (b), the retrieved IWC (c) and the calculated radiance spectrum based on these profile (d), for a representative point at 02:08:44 and assuming droxtals as ice crystal habit. The radiance observable, averaged over the given microwindows, for the AERI observations and the RT simulation assuming droxtals (e). The spectral residuals between observation minus simulation, assuming droxtals, in relation to the habit variation (f). The step size behavior of in (e) and (f) is caused by the used long AERI calibration intervals.

error decreases for higher SNR, like illustrated in Figure 4.21 (b), and the mean estimated error of $R_{\text{eff}}^{\text{rali}}(R_{\text{far}})$ was lowered from $+138\%/-3\%$ to $+36\%/-14\%$.

Temporal Alignment of Radar and Lidar Data on AERI Sky-Phase

The AERI systems alternates between three different viewing modes: the ambient blackbody calibration reference (2.0 min), the hot blackbody calibration reference (2.0 min), and the zenith atmospheric view (3.5 min). With additional data transfer time, the temporal sampling rate is 7.5 min (Knuteson et al., 2004a). Hence, for spectral comparisons with RT calculations, based on input from radar and lidar synergy, it will be beneficial to temporally restrict the radar and lidar profiles to the corresponding zenith atmospheric view of the AERI. In Figure 4.21 (c) and (d) the results are presented. However, the temporal data restriction to use only sky-phase AERI data leads to an increasement of mean residuals from 4.07 mW m^{-2} to 4.18 mW m^{-2}. The reason for this unexpected deviation is caused by the fact, that the instruments are located at positions further away from each other, than the footprint sizes of the individual instruments and will be discussed in the following section.

Separate Locations of Active and Passive Sensors

All sensors are ground-based and near-zenith viewing instruments, observing a vertical atmospheric column. The upcoming question is, under which circumstances the active and passive sensors are detecting the same cloud volume, when they have different field of views and are placed on different locations.

Therefore, the cloud volumes, sampled by radar pulses or the lidar laser beam have to be compared with the field of view of the infrared spectrometer. As mentioned in Table 3.2, the radar beam divergence α_{rad} is 9.8 mrad, the lidar beam divergence α_{lid} is 0.3 mrad and the AERI full-angle field of view γ is 46 mrad. For a cirrus with a cloud base at an altitude of 8 km, observed with the configuration like presented in Figure 4.22, the radar, lidar and AERI would have footprint diameters of 52 m, 1.5 m and 245 m at cloud base, respectively. Thus, an AERI observed scene's footprint at 8 km is up to 150 times larger than the lidar or up to 5 times larger than the radar. There are several situations imaginable, where these differences could cause a bias. Examples are, when active sensors detecting the edge of a cloud that is completely within the AERI-FOV, or active sensors have little breaks in cloud covers, but the AERI detects a cloud radiative signature anyway of the breaks, because of its large FOV, or the active sensor's FOV is completely cloud free, but a small part of a cloud is entering the large AERI FOV causing a cloud radiative signature as well. In all cases, the measured radiance would be larger than from simulations based on radar and lidar measurements.

A further complexity arises, when the instruments are not placed together. The used radar and lidar instruments are located at UFS, whereas the AERI is placed 290 m higher and 670 m away on a platform at the summit station of Mt. Zugspitze. Therefore, the minimum distance R_i, relative to UFS, before the different field of views began to overlap will increase. According to the geometric considerations from Figure 4.22, this distance can be estimated via

$$R_i = \frac{D_{\overline{US}} + Z_{\overline{US}} \tan(\gamma/2)}{\sin(\alpha_i/2) + \tan(\gamma/2)} \quad , \tag{4.2}$$

where R_i stands for the distance R_{rad} or R_{lid}, and α_i stands for the angle α_{rad} or α_{lid}. For

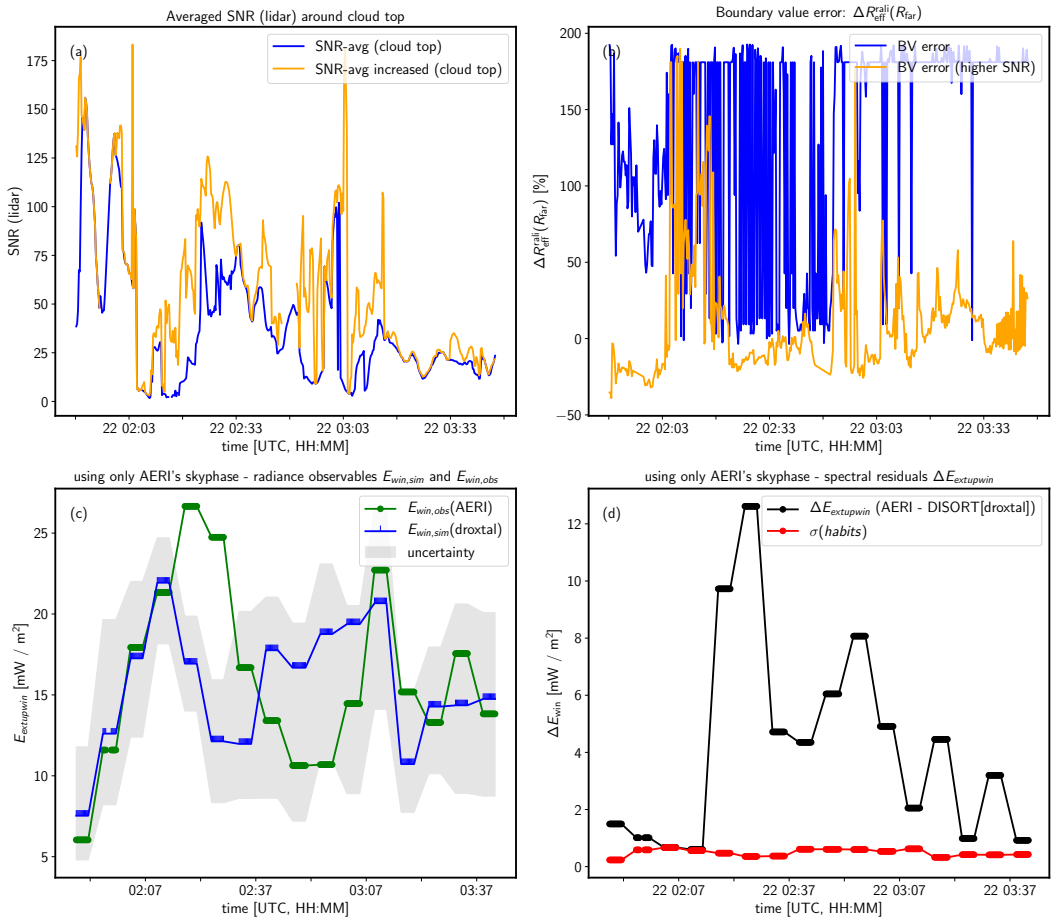

Figure 4.21.: (a) Increasement of lidar SNR by the removal of the most upper signal range gates around cloud top, and (b) its effect on the estimation of the boundary value error. Temporal alignment of radar and lidar data on AERI sky-phase for the radiances averaged in microwindows (c) and (d) residuals.

the radar, there will be no footprint overlap before the emitted pulse propagated for a distance of 21.8 km and for the lidar a distance of 24.8 km. Theses distances are far beyond the range of the instruments, and where cirrus clouds occure. Thus, for all detected cloud volumes there will be an additional spatial offset between radar/lidar and AERI observations, see Figure 4.22 (b). For the case study, there was an average zonal wind of around $15.5 \pm 0.3\,\mathrm{m\,s^{-1}}$ in east direction and an averaged meridional wind of around $0.6 \pm 0.2\,\mathrm{m\,s^{-1}}$ in south direction, according to re-analysis data and averaged from 00:00:00 to 04:00:00 UTC for altitudes between 8 km to 10 km, where the cloud did reside. Because the ratio of the magnitude of the wind components do not match the ratio of the geographic distances between Zugspitze and UFS, it is not possible to match the cloud pixel in the data between radar-lidar and AERI by applying a temporal offset on the radar-lidar data. In Figure 4.23 temporal sequences of the recorded data from the three instruments are illustrated. The sequence is constrained to cases, where the COT is first increasing and then decreasing in the interval from 01:57:00 to 02:27:00. Where radar and lidar record a maximum signal at the same time (green signal at 02:17:00), the AERI records its maximum spectrum 5 min later (blue spectrum at 02:22:00).

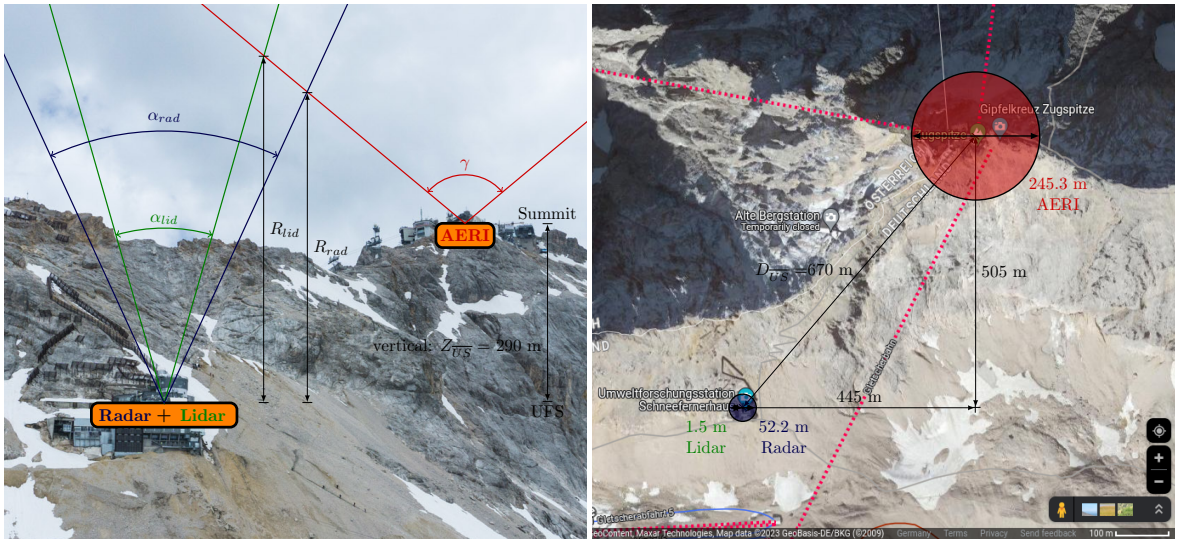

Figure 4.22.: (left) Comparison of the characteristics for radar and lidar beam divergence in relation to the AERI field of view. The active sensors are located at UFS, whereas the AERI is located on the summit station of Mt. Zugspitze. According to Table 3.2, the used radar beam divergence α_{rad} is 9.8 mrad, the lidar beam divergence α_{lid} is 0.3 mrad and the AERI field of view γ is 46 mrad. Figure not true to scales. (right) Different footprint diameters of the instruments (1.5 m for lidar, 52.2 m for radar and 245.3 m for AERI) for a cloud with a cloud base altitude of 8 km, similar to the case study from 22nd October, 2013. Pictures are taken and modified from `www.auf-den-berg.de` and Google Maps (2023).

This underlines the aforementioned spatial offset.

Depending on horizontal cloud inhomogeneity and horizontal cloud extent, this offset can cause a large bias between the simulated and measured spectrum. But a precise analysis of the magnitude of the bias caused by not overlapping FOV's, would require 3D radiative transfer simulations with at least 2D cloud fields, and is beyond the scope of this work.

The mentioned differences would be definitely smaller for instruments located together and for atmospheric scenes with slowly varying or uniform cloud scenes instead of broken cloud cover conditions, or cirrus inhomogeneity temporally on bigger scales than the AERI's sky phase, but they are rare to observe (DeSlover et al., 1999).

The original idea for this thesis was, to use the same data, that were measured in a previous multiannual campaign focusing on clear sky cases for a water vapour closure experiment (Sussmann et al., 2016; Reichert et al., 2016; Reichert and Sussmann, 2016). For this campaign it was necessary to place the AERI on the summit station and not at the lower UFS, where the radar and lidar are located. In all regarded cases within the observational period from 2013 to 2018, there was no case, where the magnitude and direction of the meridional and zonal wind components matched the spatial distances, see Figure 4.22, that would have allowed the application of a temporal offset.

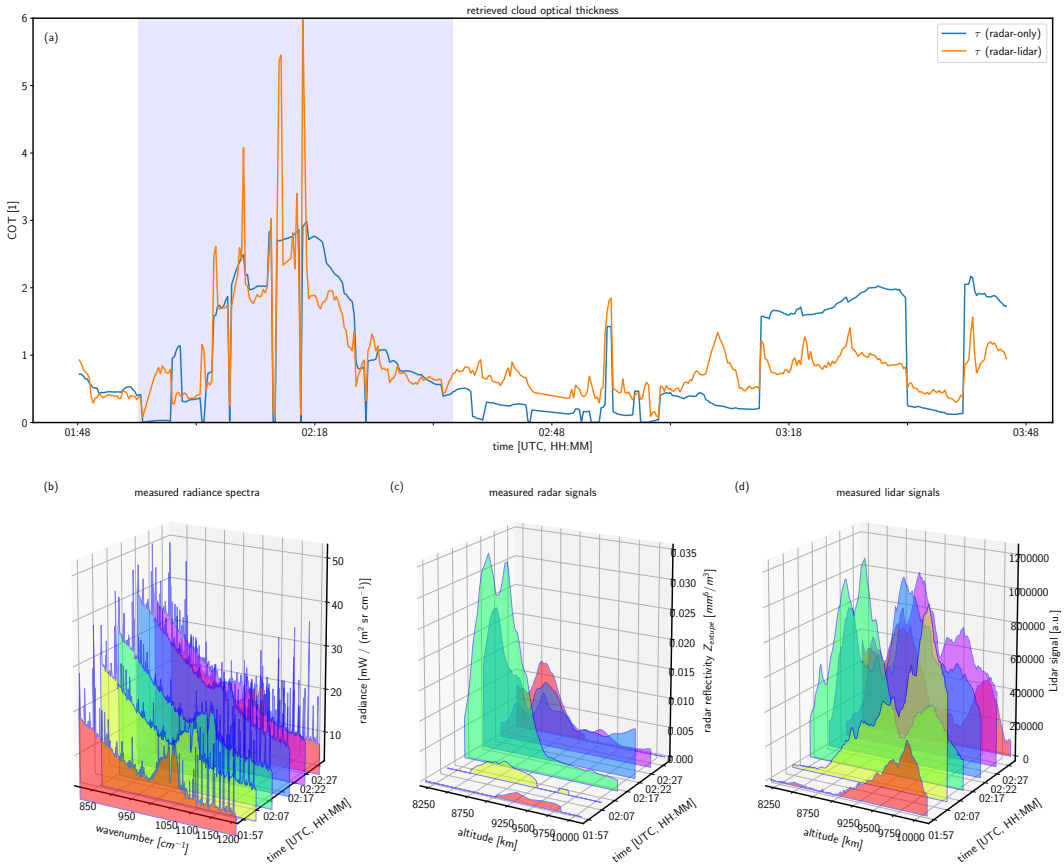

Figure 4.23.: (a) Retrieved cloud optical thickness based on radar-lidar and radar-only measuements. Recorded AERI spectra (b), recorded radar (c) and lidar signals (d) show maxima at different times: radar-lidar at 02:17:00 (green signal) and AERI at 02:22:00 (blue spectrum) indicating that the instruments are not able to detect the same cloud scene simultaneously, because the spatial separation of the instruments is considerably bigger than the footprint of each instrument.

5. Discussion

In the following chapter, the findings from Chapter 4 are discussed and compared to previous results from current literature. Identified strengths and shortcomings of the used methods are mentioned, data quality criteria are summarised, and suggestions for future work are mentioned.

5.1. Used Retrieval Techniques

Ice cloud retrieval algorithms are required to translate remote sensing observations to microphysical properties. The retrieved microphysical profiles are required to parameterise radiation schemes and to constrain microphysical schemes in General Circulation Models (GCMs). Retrieval algorithms differ mainly in their assumptions, used instruments and their methodical complexity. In the case of radar and lidar measurements of ice clouds, there are two measured quantities (lidar backscatter signal $\beta_{\mathrm{sca},\pi}$ and radar reflectivity Z_{e}) but six unknowns microphysical properties (ice water content IWC, effective radius R_{eff}, particle size distribution (PSD) knowledge, like PSD-type and PSD-shape parameter μ, ice crystal habit and lidar ratio LR) resulting in an under-constrained problem, where the radar-lidar retrieval has to assume the missing information by iterating over a realistic retrieval space. It was demonstrated in Section 4.1.6 that among these assumptions by far the biggest uncertainty comes from the estimation of a constant lidar ratio LR. This is synonymous with estimating the boundary value for inverting the lidar equation by using the Klett algorithm (Donovan and van Lammeren, 2001; Tinel et al., 2005; Hogan et al., 2006b).

Demanding the lidar ratio LR to be constant with height, is a prerequisite of the Klett algorithm. It effectively means that only one type of scatterer can be assumed along the measured profile (Klett, 1981). It was demonstrated that this limitation has no effect on the numerical stability of the radar-lidar retrieval, when the true LR profiles are variable with height. Strongly variable LR profiles (value range $\Delta LR > 12$) can have a substantial effect on low optical thickness values on the retrieved IWC profile, but only a small effect on the retrieved R_{eff} profile.

Because the boundary value estimation is the most dominant uncertainty contribution, the three-instrument retrieval includes three different estimation methods from previous studies, shortened as J_{tot}, J_{ray} and $I_{N_0^*}$. The letter J describes methods based on minimizing a cost function, whereas the letter I describes an iterative method by solving an implicit equation. They all have specific strengths and weaknesses, as discussed in Table 5.1. The J_{ray}-method is causing the lowest errors, but requires very good lidar signals and a cloud optical thickness (COT) below 2. The method is based on evaluating the signal attenuation loss of the lidar signal by calculating a Rayleigh fit before and after interaction of the lidar beam with the ice cloud. The biggest advantages are that this method is neither prone to erroneous extinction spikes nor to biases caused by a few big particles in the evaluated pulse volume, when using radar signals. The J_{tot}-method is based on penalising unrealistic gradients of $\log(R_{\mathrm{eff}}^{\mathrm{rali}})$ and is always applicable when radar and lidar signals are available, it only requires a calibrated

radar signal. But, strong negative gradients of $R_{\text{eff}}^{\text{rali}}$ at inversion start or a few large particles in the evaluated radar range gates can cause large errors. A wrong estimation of the boundary value is especially a problem for ice clouds with low COT (< 1), because the Klett inversion formula can not force the retrieved extinction profile to converge with the true profile fast enough. For high COT (> 3), even large estimation errors of $\pm 30\,\%$, will only have an impact on the upper third of the profile after inversion start, for lower range gates a convergence with the true profile is achieved. This is in accordance to previous studies (Hogan et al., 2006b). The $I_{N_0^*}$-iteration method assumes to return the best results in case of the least fluctuation of particle number concentration with height. The underlying physical principle is, that ice particle growth by vapor deposition and riming leads to a change of particle size, but not in the number of particles (Tinel, 2002). Evaluated real data, showed a lower mean bias ($< 7\,\%$) for retrieved extinction values, when using the $I_{N_0^*}$ method. This could be an evidence, that it is physical more reasonable to assume N_0^* constant near cloud top instead of $R_{\text{eff}}^{\text{rali}}$. But this method requires an inverse model based on in situ data, developed for a certain radar frequency, and the inverse model for a 36 GHz radar is missing. This caused a large bias (19 %) for retrieved particle size. Both, the J_{tot} and $I_{N_0^*}$ method suffer from the same contradictory behaviour, that on one side a high COT will help to achieve a convergence between the true and the retrieved profile faster, but on the other side a high COT will make it very difficult to estimate the boundary value with a low error, because there will be no usable lidar signal with high SNR at inversion start.

It was pointed out in the literature, although it is a big challenge, that there is an outstanding need to include coherent uncertainty estimations in any retrieval algorithm (Morrison et al., 2020). That is of fundamental importance, because the retrieved results are required for comparisons with model simulations, model parameterisation development, and understanding ice cloud processes (Comstock et al., 2007). The approach, used in the SynCirrus algorithm, is to focus on the main uncertainty contributions, coming from the radar calibration and the estimation of the boundary value. The radar calibration is varied within its uncertainty range, whereas the boundary value uncertainty is estimated with the help of a look-up table. This 1D approach has its limitations, a 3D simulation would be more accurate, but the main sensitivities (COT, gradient of $R_{\text{eff}}^{\text{rali}}$), are included and the order of magnitude for the error can be estimated.

At the moment, optimal estimation methods are the most promising retrieval approaches to tackle inverse problems in remote sensing of ice clouds (Stein et al., 2011; Ewald et al., 2021). Their main advantage is, that the underlying mathematical formalism automatically provides a consistent and rigorous treatment of estimating errors caused by uncertainties from measurements and assumptions (Delanoë and Hogan, 2008). Furthermore, additional instruments can easier be incorporated in the retrieval framework, by an extension of the input state vector. But, there is a need to better understand the errors' order of magnitude in cases where the information content is low. This refers to cases, where the retrieval can not exploit the lidar signal and mainly relies on the radar signal. In such cases, the information is completed with the prior from empirical relations, like $Z_{\text{e}} - IWC - T$ from Hogan et al. (2006c), and the retrieval results tend to converge to these climatological results. Although, the empirical relations have reported very high errors, the optimal estimation framework, returns error estimations in the same order of magnitude, as when both, radar and lidar signals, are available. Another obstacle is, that it is not easy to include different ice crystal assumptions in the forward scattering models used by optimal estimation frameworks, because

Table 5.1.: Overview of advantages and disadvantages of the different methods for estimating the boundary value, for inverting the lidar equation in cloud retrievals.

solution methodology	**advantages**	**disadvantages**
$R_{\mathbf{eff}}^{\mathbf{rali}}$-Gradient ($J_{\mathbf{tot}}$): • uses Klett-inversion for a single component atmosphere to retrieve β_{ext} and R_{eff} profiles • boundary value was constrained with support of radar signal by finding the minimum of an cost function which penalises gradients of $\log(R_{\text{eff}}^{\text{rali}})$ • used in: Donovan and van Lammeren (2001)	• self-consistent, only requires lidar and radar signal • does not require signal parts outside of cloud (e.g. molecular signal) • no calibration of lidar signal required • microphysical assumptions (habit, PSD) can be incorporated consistently in inversion and RT path • uncertainty estimation with LUT	• prone to erroneous extinction spikes when lidar runs out of signal at inversion start • uses only signal parts at the start of the inversion for boundary value estimation (weaker constraint) • few large particles at inversion start can dominate the radar signal and lead to wrong boundary values • large errors for low optical cloud thickness values and negative gradients • can only use constant LR $\rightarrow$ has to assume a single habit for a cloud profile • needs signals from both, radar and lidar and a high signal overlap to yield reliable results
$\dot{N}_0^*$-Iteration ($I_{N_0^*}$): • uses Klett-inversion and Hitschfeld-Bordan equation • boundary value will be constrained by estimation of cloud optical thickness with an implicit equation based on an inverse model • used in: Tinel et al. (2005)	• uses all signal range gates within cloud for boundary value estimation (stronger constraint) • does not require signal parts outside of cloud (e.g. molecular signal) • microphysical assumptions (habit, PSD) can be incorporated consistently in inversion and RT path	• prone to erroneous extinction spikes when lidar runs out of signal at inversion start • requires microphysical inverse model based on aircraft in-situ data for used radar frequecy • can only use constant LR $\rightarrow$ has to assume a single habit for a cloud profile • needs signals from both, radar and lidar and a high signal overlap to yield reliable results • uncertainty estimation is hardly feasible
Rayleigh calibration ($J_{\mathbf{ray}}$): • based on a fit of the lidar signal to the molecular atmosphere before and after cloud • boundary value was constrained by estimation of cloud optical thickness due to signal loss • used in: Cadet et al. (2005)	• avoids erroneous extinction spikes at inversion start • can give a good estimation of the boundary value for low cloud optical thickness values • fit error can be used as data quality criteria	• requires high lidar SNR especially after penetration of cloud • for large lidar FOVs, the derived optical cloud thickness must be corrected for multiple scattering effects and correction requires size information from LUT or radar • can not be used with ceilometers (low power and too weak molecular signal) • can only be used for low optical cloud thickness values ($\lesssim 2$) • can not be used with ceilometer wavelengths
Optimal estimation (VarCloud): • optimal estimation scheme based on fast forward models for included instruments • a cost function for the obervation vector was minimized • used in: Delanoë and Hogan (2008)	• can also be used when only radar or only lidar signals are available • avoids erroneous extinction spikes at inversion start • numerical stable even when lidar runs out of signal • additional instruments can easy be incorporated in optimal estimation framework • lidar ratio LR can be variable $\rightarrow$ different habits can be assumed for a cloud profile • mathematically consistent error propagation is included in formalism automatically	• minimization procedure can lead to a local instead of a global minimum • for profiles e.g. with large radar only part, the result can tend to climatology relationships • microphysical information content is difficult to be separate from optimal estimation framework • lidar signal must be calibrated • cost function requires good uncertainty estimations • inconsistency between RT and radar-lidar forward model, concerning microphysical model

the included look-up tables first must be extended on ice crystal habit, roughness and PSD, to be consistent with the RT assumptions, like demanded by McFarquhar and Heymsfield (1998). Therefore, a better understanding of how the measured information content is exploited by an optimal estimation framework is required. This knowledge can be gained, by further comparisons with inversion approaches, like used in this thesis.

5.2. Radar-Lidar Retrieval Intercomparison

The aim of the retrieval intercomparison, was to test the radar-lidar retrieval part of the three-instrument retrieval framework. In particular, the different boundary value estimation methods (J_{tot}, J_{ray} and $I_{N_0^*}$) as well as the multiple scattering correction should be tested with high quality lidar data from WALES. The data were taken during the NARVAL-I aircraft field campaign. The results were compared with totally different retrieval approaches based on optimal estimation (VarCloud - Delanoë and Hogan (2008)) and empirical relations (Radar-Only - Hogan et al. (2006c)). Currently, VarCloud is the most promising retrieval approach in remote sensing of ice clouds (Stein et al., 2011; Delanoë et al., 2013; Ewald et al., 2021). For high-quality flagged data (COT < 2, Rayleigh fit error $< 10\,\%$ and radar-lidar vertical signal overlap $> 90\,\%$), the Rayleigh calibration method showed good agreement (bias $< 20\,\%$) with the VarCloud results. After correction of the lidar signals, to avoid erroneous spikes in the retrieved extinction profile, good agreement between VarCloud and the two methods (J_{tot} and $I_{N_0^*}$) could be achieved as well. The methods evaluating radar and lidar signals, had a lower bias with VarCloud than the empirical relations method, using the radar signal alone. The low bias result could only be achieved when including a multiple scattering correction.

5.3. Three-Instrument Retrieval with Zugspitze Data

The developed SynCirrus retrieval algorithm was applied on data from the two sites at Mount Zugspitze, where passive and active remote sensing data were available, in contrary to the NARVAL-I campaign, were only radar and lidar data from clouds were available. The Zugspitze offers extraordinarily dry conditions and provides a high atmospheric transparency to observe cirrus clouds. The radar and lidar instruments are located at UFS, while the infrared spectrometer AERI is located at the summit observatory. Because cloud measurements were only available from a ceilometer, it was not possible to use the Rayleigh calibration for the estimation of the boundary value for radar-lidar inversion, because the laser wavelength of the ceilometer only generates a weak Rayleigh signal, which in turn causes large fit errors. The $I_{N_0^*}$ could not be used, because there is no inverse model for a 36 GHz radar. Such an inverse model provides coefficients of the power-law relationships corresponding to different particle size range (Tinel et al., 2005). Only the J_{tot} is applicable, but this method is prone to erroneous extinction spikes or large particle biases at inversion start. The UFS cloud radar data were corrected before usage, following Ewald et al. (2019).

In Section 4.3.3 the result of the ice cloud case study showed that for the main part of the evaluated data the SynCirrus algorithm could find a microphysical state, based on radar and lidar data, to explain the AERI spectrum within their uncertainties. But, a discrimination between different ice crystal habits was not possible due to large mean boundary value errors of $+36\%/-14\%$, caused by poor ceilometer signal quality (WALES caused only an error of $+8.1\%/-3.8\%$). As described in Section 4.3.4, the biggest obstacle in the ice cloud study

was the fact, that the measurement devices are separated from each other at distances much larger than the cloud base footprint sizes of the individual instruments. Because of these non-overlapping FOVs, the data to be used require a higher degree of horizontal homogeneity, which is especially for cirrus clouds hard to observe.

5.4. Retrieval of Ice Cloud Properties and Requirements on Data Quality

In order to be able to make a statement, which microphysical properties can be retrieved from the synergy of active and passive remote sensing, the order of magnitude of the thermal spectral residuals, caused by different uncertainty sources, should be known. The spectral residuals are defined as difference between radiative transfer simulations towards spectral infrared measurements. However, for the synthetic parameter studies, the spectral residuals were used to investigate the impact of certain parameters on the spectrum. To assess these residuals, a synthetic 1D model was used in Section 4.1, and based on a microphysical cloud state, the different measurements for radar, lidar and infrared spectrometer were simulated. Using the simulated radar and lidar data, the retrieval returns different microphysical cloud states, depending on the retrieval assumptions. The measurements were perturbed by instrument noise and the retrieval results were iterated for different microphysical assumptions. Based on the retrieved microphysical profile, a spectrum is calculated and compared with the "true" one, by exploiting spectral microwindows between absorption lines. Such a 1D model is not as accurate as a 3D model and assumptions have to be applied, summarised in Table 3.7 and Table 3.8, but the important sensitivities (radar - D^6, lidar - D^2, radiative transfer simulation - water vapour, microphysical assumptions) can be included and their effects on the retrievable information content can be investigated. The error for neglecting radiative 3D effects in the thermal spectral range is below 30 % for effective ice crystal sizes and below 5 % for the cloud optical thickness, and both errors are below the typical errors caused by the retrieval technique Fauchez et al. (2018).

The different sources of uncertainties were identified and categorised into radiative transfer settings (Line-By-Line vs. reptran), ice cloud microphysical assumptions (ice crystal habit and roughness, the type of the PSD, the modality of the PSD, PSD shape parameter), instrument parameters (radar calibration uncertainty, lidar SNR), atmospheric state knowledge (temperature and water vapour uncertainty) and retrieval technique (constant lidar ratio assumption, uncertainty in estimation of the boundary value). Based on the executed parameter studies a set of parameters could be identified that will cause low retrieval errors making it possible to distinguish different ice crystal habits, and they are summarised in Table 5.2. Based on the application on synthetic and real data, criteria for high quality data, to retrieve reliable microphysical profiles, can be identified: low Rayleigh fit error of the lidar signal after cloud-lidar beam-interaction, high radar-lidar vertical signal overlap and low spectral residuals between AERI and simulated retrieved spectrum. Among the microphysical parameters for a monomodal gamma PSD, the ice crystal habit has the biggest impact on the thermal spectral residuals. But even with high quality data it is not possible to discriminate between the different habits, because the boundary value estimation error is only allowed to be below ±1 %. But, realistic values are between ±36 % (ceilometer) and ±8 % (WALES). An error in the order ±1 % can only be achieved after integration times of around 2 h, like done in aerosol remote sensing (Freudenthaler et al., 2018; Freudenthaler, 2019). But in contrary to aerosol

Table 5.2.: Required knowledge on specific parameters and their accuracy for successful retrievals of ice crystals habits, when only using remote sensing data from radar, lidar and infrared spectrometer.

Parameter	Value	Comment
Microphysical Model Assumptions		
Ice Crystal Surface Roughnesses:	not relevant	In the used longwave thermal spectral range of $700\,\mathrm{cm}^{-1}$ to $1200\,\mathrm{cm}^{-1}$ the surface roughness can be neglected but for shortwave radiation it can have a substantial impact
PSD-Shape (Monomodal):	not relevant	Does only have a minor effect on the spectral residuals and can be approximated by PSD shape $\mu(T)$ from Heymsfield et al. (2013)
Occupation of Modes (Bimodal):	$N_{0,1}/N_{0,2}$ $> 10^3$	If there is a certain occupation in the large particle mode, the retrieval formulas based on a monomodal PSD will return wrong results. With in situ measurements the PSD could be determined.
Radar-Lidar Retrieval Technique		
Boundary Value Error:	$\Delta R_{\mathrm{eff}}^{\mathrm{rali}}(R_{\mathrm{far}})$ $\lesssim 1\,\%$	Small errors are hardly to achieve, because retrievals tend to overestimate the boundary value $\Delta R_{\mathrm{eff}}^{\mathrm{rali}}(R_{\mathrm{far}})$ up to 40 %. An error reduction can be achieved when using the Rayleigh calibration for low τ, and the J_{tot} and N_0^* cost function for high optical thickness values. Attention should be paid on extinction spikes at inversion start, like described in Section 4.2.3.
Lidar Ratio Variation:	ΔLR $\lesssim 2\,\mathrm{sr}$	The lidar ratio can vary within a cloud profile, depending on temperature and scatterer composition. Magnitude could be estimated with lidar ratio-temperature relations (Cazenave et al., 2019)
Multiple Scattering:	include	For real lidars with a large FOV like WALES (1.6 mrad), there will be a substantial signal part from multiple scattering, which the retrieval should account for
Radar-Lidar Signal Overlap:	$\gtrsim 90\,\%$	To achieve such a high radar-lidar signal overlap, cloud optical thickness values should be below 2. 100 % will never be reached, because radar has a limited sensitivity. Thus small ice crystals at cloud base can not be detected by radar.
Rayleigh-fit error	$\lesssim 10\,\%$	A low Rayleigh-fit error of the lidar signal after cloud penetration is an indication, that the retrieved boundary value has a small error and that the lidar signal was not attenuated critically. This enables a numerical stable inversion of the lidar signal. Low fit errors only occure for a COT below 2 and lidars with a suitable wavelength and high pulse power.
Instrument Parameters		
Radar Calibration Uncertainty:	ΔZ_{e} $\lesssim 0.3$ dBZ	The Mira-36 has a ΔZ_{e} of 1.3 dBZ (Görsdorf et al., 2015), a typical value for radar calibration uncertainties and smaller uncertainties are difficult to achieve.
Lidar Cloud SNR:	SNR $\gtrsim 1000$	For cloud optical thickness values below 2, typical SNR values are around 30 for a ceilometer and around 3000 for a high power lidar.
Knowledge of Atmospheric Composition and Meteorological Conditions		
Water Vapour Uncertainty:	$\lesssim 10\,\%$	Sussmann et al. (2016) showed, that deviations between re-analysis and radiosondes are below 10 % for UFS. ERA-Interim data are precise enough but improvements can be achieved with using radiosondes.
Trace Gases Uncertainty:	$\lesssim 50\,\%$	No TCCON data are required, all permanent traces can be estimated with data from standard atmospheres for midlatitudes.
Temperature Uncertainty:	ΔT $\lesssim 1\,\mathrm{K}$	For cloud optical thickness values below 5, it is sufficient to use temperature data from meteorological re-analysis.
Type of Cloudiness:	different instrument FOVs	Preferential atmospheric conditions would provide slowly varying or uniform cloud scenes, unbroken cloud cover. To temporally resolve cirrus inhomogeneity, AERI's sky observing phase should be in the order of <30 seconds, to avoid biased-scenarios like described in Section 4.3.4.

processes, the important cloud dynamics happens on time scales of below a few minutes. Furthermore, the unawareness about the PSD can create large errors, when the retrieval assumes, for example, a monomodal instead of a bimodal distribution. Hence, mulitfrequency-radar and multiwavelength-lidar or in situ data are required to have a meaningful constraint of the PSD.

5.5. Suggestions for Future Work

Based on the results of this thesis and the state of the art in current literature, the following seems to be the way forward towards better retrievals.

A necessary improvement for retrievals at Mt. Zugspitze would be the placement of all active and passive sensors at the same location to have a maximal overlapping footprint. Instruments not seeing the same part of the cloud, can cause large biases, especially for horizontal inhomogeneous cloud properties.

Further important improvements and extensions are:

1. Instead of a ceilometer, a high power lidar at a wavelength of 355 nm or 532 nm is required to use the Rayleigh calibration for estimating the boundary value and to penetrate clouds more effectively, and their detectors are not so limited to saturation from signal returns of thick clouds with high signal amplitudes. Furthermore, the high SNR makes the inversion procedure numerical stable, ensuring trustworthy results.

2. The sampling rate of the AERI should be reduced from 8 min to 20 s, to be able to resolve fast changing cirrus microphysical dynamics on a higher resolution. The costs of higher radiometric calibration uncertainties are negligible in comparison to the retrieval uncertainties.

3. A low altitude site location in the arctic without strong vertical updrafts would also offer dry conditions and allow to exploit the radar doppler velocity via correlation between particle sizes and parameters of the fall velocity–size. Therefore, based on known approaches, it would be possible to include ice crystal habit assumptions in radar-only regions (Matrosov et al., 2002).

4. Calibration of the radar should be ensured by participating in cloud radar calibration network. Is important for the retrieval quality in general and very important for the boundary value estimation with J_{tot} cost function in particular. The Aerosol, Clouds and Trace Gases Research Infrastructure (ACTRIS) is making steps towards uniform calibration strategies (Toledo et al., 2020).

5. Further signal analysis in the cloud masking algorithm is required to identify regions, where the radar misses very small ice crystals. These regions would include usable information content for a ice cloud study.

6. Using mulitfrequency radars and multiwavelength lidars would enrich the information content of the observations in sampling the ice PSD more effectively (Bringi et al., 1986; Gaussiat et al., 2003; Kneifel et al., 2011, 2015; Tridon et al., 2017; Wang et al., 2017; Okamoto et al., 2020; Zhang et al., 2021).

7. The ice crystal roughness can only be assumed in the RT path of the retrieval. To include the roughness in the radar-lidar inversion path, high resolution measurements of the lidar ratio are required (Saito et al., 2022).

8. Adding a passive spectrometer, recording radiances in the solar spectral range, would help to retrieve information about ice crystals. In the solar spectral range short wave scattering is dominant and the ice crystal roughnesses and habits have an impact on the scattering phase function (Yang et al., 2013; Ewald et al., 2021). The spectrometer of the Munich Aerosol Cloud Scanner would be a suitable instrument (Ewald et al., 2016).

9. Usage of in situ data to cross-check the retrieval assumptions about ice crystal habit, roughness and PSD. Although in situ measurements are considered as "ground truth", there are errors and biases that should be considered before comparison with remote sensing data. Baumgardner et al. (2017) stated, that the derivation of size and concentration below ice crystal sizes of 100 µm is uncertain to approximately ±50 % and ±100 %, respectively, with increasing uncertainty as the particle size decreases. Another issue is the size of the sampling volume for collocation between in situ and ground-based instruments. Therefore, Finlon et al. (2016) suggest in situ data should be between 250 m and 500 m, less than 25 m in altitude, and within 5 s of collocated remote sensing data.

10. Reduction of fit errors in $m(D)$ and $A(D)$ expressions, by using second-order polynomials, like suggested in (Erfani and Mitchell, 2016).

11. Usage of radars with a sensitivity of -60 dB would allow to detect 98 % of ice clouds with an optical depth above 0.05 (Illingworth et al., 2007b; Protat et al., 2006).

12. Usage of polarimetric radar and lidar quantities to constrain the wealth of ice microphysical assumptions (Myagkov et al., 2016; Melnikov, 2017).

13. Development of an inverse model at a radar frequency of 36 GHz, to be able to use the iteration method from Tinel et al. (2005) for particle sizes as well.

14. Radiosonde data are not stringently required, but would definitely decrease the uncertainties to some extent for Rayleigh calibration and RT calculations.

15. To include radiative 3D effects and cirrus inhomogeneity Fauchez et al. (2018), the 3D radiative transfer solver MYSTIC could be used (Mayer and Kylling, 2005; Emde et al., 2016),

6. Summary and Conclusion

Ice clouds significantly impact the Earths radiation budget (ERB). They reflect a certain part of incoming shortwave solar radiation back to space (cooling - solar albedo effect), and at the same time they absorb longwave upwelling infrared radiation emitted by Earth's surface (warming - infrared greenhouse effect). To quantify the net effect, cirrus parameters like dominant ice crystal habit, cloud coverage, ice crystal sizes, geographical position, optical thickness values, ice particle size distribution (PSD) and ice crystal roughness should be known. Therefore, knowledge about the ice cloud microphysical properties ice water content (IWC) and effective radius (R_{eff}) is important, because they are very sensitive to the radiation budget and thus climate evolution. However, these quantities are indirect dependent on the PSD and ice crystal habit (Heymsfield et al., 2017). Hence, knowledge of ice crystal properties is important. To gain observational data in order to close gaps in the understanding of ice clouds, these microphysical quantities can be derived by a retrieval algorithm exploiting active and passive remote sensing observations.

Therefore, the aim of this work was the development of an algorithm for a synergistic three instrument retrieval framework, based on active and passive remote sensing, to provide and constrain valuable information about ice clouds. It can be concluded that an operational working algorithm - SynCirrus - was achieved and applied to synthetic and real data from two campaigns.

Scientific objective: Development of a synergistic three-instrument (radar, lidar and infrared spectrometer) retrieval algorithm - *SynCirrus* - for the mapping of radar, lidar and infrared spectrometer measurements to microphysical properties (ice water content IWC and effective radius R_{eff}), including a comprehensive uncertainty consideration.

The first step was to develop a radar-lidar inversion procedure to derive microphysical profiles from the measured profiles. Ground-based radar and lidar are favorable instruments for cloud observations, because they operate at different wavelengths, and therefore they are sensitive to different cloud particle sizes and, hence, to different moments of the cloud's PSD. This difference in particle size sensitivity is an advantage and allows for a well-constrained retrieval of IWC and R_{eff}. Furthermore, they provide substantial vertical and temporal coverage (unlike in situ observations) of microphysically relevant processes, and are capable of vertically resolving the full depth of a cloud at a high temporal coverage (unlike polar-orbiting satellites) (Comstock et al., 2007). The most crucial part, with the largest uncertainty in the retrieval procedure is the inversion of the lidar equation by estimating a boundary value for the Klett-inversion formula of the extinction coefficient. To tackle this, the algorithm uses three different methods from previous studies with different strengths and weaknesses, depending on signal quality and cloud optical thickness, as sketched in Table 5.1. According to the assumptions of an ice crystal microphysical model, the retrieved profiles of β_{ext} and $R_{\text{eff}}^{\text{rali}}$ are converted to profiles of IWC and R_{eff}.

The second step was to use a three-instrument retrieval framework to validate the retrieval results with other observations. For this purpose, an instrument is needed working at other wavelengths than the active sensors, to provide independent measurements for assessment of retrieval performance. Although, the Atmospheric Emitted Radiance Interferometer (AERI), as a passive sensor, only provides the measurement of vertically integrated infrared radiances at the surface, it has many advantages to be used in such an ice cloud study. It has a narrow FOV, which reduces the contributions of 3D effects and better complements the narrow field of views (FOVs) of radar and lidar, and it records downwelling infrared radiances on a high spectral resolution with very low calibration uncertainties. The atmospheric window region around 8 µm to 13 µm of the observed infrared spectrum is kind of transparent for molecular absorption and emission, but water vapour contributes significantly to the measured spectrum. Hence, the AERI location is chosen to be on a mountain site because a high altitude offers extraordinarily dry conditions to obtain data from cirrus clouds (Sussmann et al., 2016; Blanchard et al., 2017). Furthermore, the high-spectral-resolution measurements allow to exploit spectral microwindows, that lie between gaseous absorption lines. Additional to the choice of the site, this further reduces the contribution of water vapour and other trace gases on the recorded infrared radiances. The previous derived IWC and R_{eff} profiles were used for radiative transfer simulations of downwelling infrared radiances with the aim to simulate the spectrum of the AERI device. Now, it was possible to minimise the spectral residuals between measured and simulated spectrum by iterating the possible microphysical assumptions.

The developed retrieval algorithm (SynCirrus) involves preprocessing routines, like cloud masking the lidar signal based on wavelet analysis, correction of the radar signal for gaseous attenuation and the possibility to investigate a radar calibration offset in using radar and AERI data only. The radar-lidar inversion path of SynCirrus exploits power law relationships about mass and projected area for different microphysical assumptions, whereas the radiative transfer (RT) path for the simulation of infrared spectra uses look-up tables for the bulk optical properties for the same microphysical assumptions. This allows to include the same assumptions about ice crystal habit, type, modality and shape parameter of the PSD consistently in both framework paths. The underlying microphysical model is exchangeable, making it possible to compare different models with remote sensing observations. The framework includes a set of different boundary value estimation methods and corresponding uncertainty estimations. The uncertainties of the estimations are derived from look-up tables, based on synthetic simulations. To reduce erroneous extinction spikes (Hogan et al., 2006b), where the lidar runs out of signal, the retrieval uses a numerical stability procedure. The retrieval corrects power law fit deviations caused by changing ice crystal aspect ratios, and multiple-scattering effects of the lidar signal are included iteratively in the inversion procedure. A speed-up for operational usage is achieved by using the REPTRAN parameterisation instead of Line-By-Line calculations for the forward RT simulations of infrared radiation.

The main improvements of the algorithm in comparison to former studies are:

1. Consistency of microphysical models used in both branches of the three-instrument retrieval: radar-lidar inversion and radiative transfer forward model.

2. Improvements in the retrieval workflow. New data preprocessing routines were included, like extension of the wavelet analysis of the lidar signal to include the detection of cloud tops, screening for numerically stable lidar profiles, correction of varying aspect ratios,

and the usage of infrared spectrometer data together with radar signals to estimate possible radar calibration offsets. Improvements in the radar-lidar inversion were achieved by usage of multiple methods to estimate the boundary value to solve the lidar equation.

3. Comprehensive uncertainty quantification of the involved quantities: the microphysical model, the instrument parameter, atmospheric state knowledge and assumptions in the inversion technique, and the identification of main uncertainty contributors.

The three-instrument retrieval SynCirrus was developed to investigate the following (technical) research questions:

Research questions 2: What kind of uncertainties can occur in the retrieval process, and how do these uncertainties impact the interpretation of the retrieved results?

To answer this question, the occurring uncertainties were categorised into uncertainties based on microphysical model assumptions, instrument parameters, atmospheric state assumptions and retrieval technique. Assuming a monomodal gamma distribution for the PSD, the ice crystal habit has the biggest impact on the infrared radiance spectrum. At radar wavelengths the scattering return is dominated by large particles, due to the 6^{th} moment dependence. Therefore, radars can not detect small ice crystals at the cloud boundaries, where ice nucleation creates small crystals. In contrary, at shorter lidar wavelengths, these small ice crystals can be resolved, but the lidar backscattered signal will be quickly attenuated in optically thick parts of the cloud towards the top. Simulations with synthetic data show, that a radar-lidar vertical signal overlap $\gtrsim 90\,\%$ is required, to be able to discriminate the certain habits for different cloud optical thickness values (COTs). It was further demonstrated that without high signal to noise ratio (SNR) values at inversion start the retrieval becomes numerically unstable, producing unreliable profiles. This is because of "memory" effects. They contain the impact of noise at inversion start and the cumulative effect from there to the current point of evaluation (Comerón et al., 2004). The effect of radar noise can be neglected (Hogan et al., 2006b), but it was demonstrated, that for low COTs, the radar calibration uncertainty will exacerbate the determination of ice crystal habits.

The Klett inversion formula has to assume the lidar ratio to be constant with height. For the extreme case, when the true lidar ratio varies strongly at inversion start, this can introduce large retrieval errors for low COTs. However, for cases where it only varies within the cloud but not at inversion start, there will some degree of cancellation in the errors for vertically integrated quantities (Hogan et al., 2006b). The biggest uncertainty within the three-instrument retrieval framework lies in the determination of the boundary value for inverting the lidar equation. The discrimination of certain ice crystal habits would require a very small boundary value error ($R_{\text{eff}}^{\text{rali}}[R_{\text{far}}]$) below $\pm 1\,\%$, but for real data the error is much higher, making it impossible to retrieve ice crystal habits with this three-instrument configuration. Furthermore, the precise uncertainty quantification of this error source is very difficult, and it was only possible to give an error estimation based on look-up tables, calculated with synthetic data.

Research questions 1: What are the accuracy requirements to constrain the microphysical properties of ice clouds, based on synergistic measurements made from radar, lidar and infrared spectrometry?

To answer this question, the developed SynCirrus retrieval was applied on real data from two different campaigns. First, a radar-lidar retrieval intercomparison study with NARVAL-I aircraft data, demonstrated that for high quality lidar signals (high radar-lidar vertical signal overlap and low Rayleigh fit error), the retrieved profiles of SynCirrus and the established retrieval VarCloud (Delanoë and Hogan, 2008) coincided remarkably well, although the two retrieval methods are fundamentally different, following an inversion versus optimal estimate approach, respectively. The application of the complete three-instrument retrieval at Mount Zugspitze showed, that it was possible to achieve an accordance between simulated and measured radiance spectra for the majority of the analysed cases within the uncertainty range. However, the uncertainty range was very large because of the usage of a ceilometer instead of a high power lidar, causing numerical instability in the inversion procedure, due to a low SNR.

Retrievals of microphysical properties, especially ice water content IWC are difficult to be verified precisely because there is no global IWC "truth" on a comparable spatial and temporal grid (Avery et al., 2012). Former studies showed deviations between the mean retrieved IWC and mean predicted IWC between 50 % to 200 % for pure ice clouds (Hogan et al., 2006c; Avery et al., 2012), and mean IWC deviations between different retrieval methods of around 50 % (Stein et al., 2011). The boundary value errors of $R_{\text{eff}}^{\text{rali}}[R_{\text{far}}]$ were in the order of ± 35 % with a ceilometer (UFS data) and around ± 8 % for a high power lidar (NARVAL-I), and resulting in errors for the IWC of the same magnitude because they are proportional to each other. Errors of below ± 10 % for single retrieved profile of IWC would cause lower deviations for further comparisons with the predicted mean IWC from a model. Therefore, the confinement on high quality data can greatly contribute to improve the prediction of ice water content in climate models. In summary, microphysical properties of ice clouds can be constrained with a three instrument retrieval, but high demands on data quality are necessary, like a calibrated radar, a high power lidar, AERI integration times below 1 min and cloud optical thickness values below 2 , and to have a high vertical radar-lidar signal overlap beyond 90 %.

Future developments will need to focus on including more sensors to improve the retrievable information content. Furthermore, in situ data are required for cross-checking the assumptions of ice crystal shape and PSD, made by the retrievals, until they become more reliable. For this goal, optimal estimate approaches are ideal. In optimal estimate approaches additional instruments can easily be incorporated into the measurement state vector of the framework, and they automatically provide a mathematically consistent error propagation (Delanoë and Hogan, 2008). However, physical inversion retrievals with a primary sensitivity, here the 2^{nd} and 6^{th} moment of the PSD, appear to be more "transparent". They are required for cross-checking data with the used primary sensitivities, because it seems, that the mathematical optimal estimation framework sometimes generates too small errors, when an information in form of a measurement is missing.

The developed retrieval could be used on Antarctic sites, if a similar instrumentation as used in this work is available, where satellite data are missing (Howat et al., 2019).

The research presented in this thesis is pertinent and important to the goal of reducing uncertainties related to the description of ice clouds in climate models. The presented three-instrument retrieval SynCirrus can help to narrow down gaps in the understanding of ice clouds, by supplying high resolved and quality flagged microphysical profiles for the development of radiative parameterisations and tuning-constrains for microphysical schemes, both needed in future GCMs. It can not provide information about cirrus ice crystal types, because the errors in the retrieval technique are bigger than the radiative impact from different microphysical assumptions. This prevents the discrimination among different ice crystal habits, and more active and passive sensors, and especially in-situ devices, are indispensable to sample the cirrus PSD more effectively.

7. Outlook

Apart from the focus on remote sensing techniques of ice clouds in this thesis, it would be helpful to extend the focus of future research. To be able to narrow down gaps in the understanding of ice clouds and their role in a future warming climate, a better harmonisation between the needs of climate models and the capability of remote sensing techniques could be achieved with new retrieval design studies.

Modelling

A possible start could be a numerical laboratory for the comparison of two models with different resolutions. The first model is a Global Circulation Model (GCM) and the second model is high-resolved local cloud model, modelling only one grid box of the GCM. Both models will receive the same main input and predict the behavior of a cirrus cloud. The high-resolved cloud model will incorporate important features of ice clouds, like the vertical distribution of different ice crystal habits, roughnesses and particle size distributions (PSDs). Furthermore, the high-resolved cloud model will use instrument simulators, like Silber et al. (2022), to produce a set of remote sensing observations, that will serve as input for a cloud retrieval, like developed in this thesis. Based on the retrieved data, parameterisations could be developed and used in the coarse GCM. The magnitude of the deviations for the model observables in both models could help to identify, which microphysical variables should be known more precisely and what are the maximal errors allowed on the retrieved results of these variables. This could mark clearly the needs a cloud retrieval should be capable of, concerning the required retrieved information content and uncertainty estimations. In a next iteration this will help to clarify, if current remote sensing techniques are able to meet the required uncertainty expectations. For example, would it be useful, that a cloud retrieval makes assumptions about the vertical distribution of ice crystal habits, or is it enough to assume just a dominant habit, because it can not be resolved by a physical parameterisation. It would be helpful to know, how retrieval uncertainties would impact a developed parameterisation, or in other words how big are retrieval errors allowed to be. In any case, it would be very beneficial to constrain the requirements on a cloud retrieval based on model requirements.

Remote Sensing Techniques

For cloud retrieval development, it would be very helpful to have some good high quality reference datasets of ice clouds (optically thin or thick, pure ice or mixed-layer), where different current and future retrievals could be tested. Such datasets should include multiple active sensors on different wavelengths/frequencies to sample the cloud PSD more effectively, multiple remote sensing devices in the solar and thermal spectral range, radiosondes and in situ data from an aircraft or a weather balloon, to get indications about the “real” PSD and ice crystal habits. An analysis on the quality of the retrieval results based on different permutations of used input measurements/devices would be very helpful to define minimal

requirements for a retrieval algorithm to derive certain microphysical variables alongside desired uncertainty quantification. For example, the North Slope of Alaska (NSA) atmospheric observatory at Utqiaġvik (formerly Barrow) provides a promising set of ground-based instruments (Stamnes et al., 1999; Verlinde et al., 2016). These datasets are not only important to compare physically based inversion retrievals with optimal estimation approaches, but will be needed to train machine learning models (Wang et al., 2020) or future retrievals based on deep convolutional neural networks (Schimmel et al., 2022). Good quality reference datasets would definitely help to investigate the strengths and shortcomings of different cloud retrievals and would give promising starting points to improve them (Comstock et al., 2007; Stein et al., 2011).

A. Appendix: Ice Clouds and Climate

Behavior of Clouds in a Warming Climate

Clouds cover roughly 70% of the Earth's surface (Stubenrauch et al., 2013) and due to their frequent occurence, influence weather and climate in multiple ways. For example, they couple hydrological processes in the atmosphere and in the ground through precipitation, they redistribute sensible and latent heat and momentum and have a substantial effect on *Earth's radiation budget* (ERB) through reflection, absorption, and emission of radiation (Arakawa, 1975; Ceppi and Hartmann, 2016).

An understanding of the impact clouds will have on the climate and climate change begins with Earth's energy budget, which describes the flows of energy within the climate system. In a world without global warming the radiative energy fluxes between incoming shortwave (SW) solar (0.2-5 µm) and outgoing longwave (LW) thermal infrared (5-100 µm) radiation would be in balance. To describe an externally imposed perturbation of Earth's radiative energy budget, the IPCC employed the term *radiative forcing* (RF) (in $\mathrm{W\,m^{-2}}$), where a positive radiative forcing has a warming effect and a negative radiative forcing has a cooling effect (Myhre et al., 2013). Furthermore, a distinction is made between forcing agents caused by natural changes, e.g. solar irradiance or stratospheric aerosols from volcanic eruptions, and anthropogenic changes, e.g. greenhouse gases, tropospheric aerosols or land-use. These external forcings are the initial drivers of the climate system, and perturbate Earth's energy balance with space.

Humanity impacts the climatic effect of clouds in a warming climate, mainly via two different processes. The first, is the warming of the surface which increases the greenhouse gas emissions that in turn will change the behavior of clouds. The second anthropogenic activity, is the increased amount of pollutants that have increased the amount of aerosols in the atmosphere. These tiny particles like sulphates can serve as cloud cloud condensation nuclei (CCN) or ice nucleating particle (INP) for cloud formation. In this context there are two important aerosol-cloud interaction processes, the *first indirect effect of aerosols* leads to a larger SW cloud albedo and reflects more sunlight, because cloud droplets have become more in number with smaller sizes (Twomey et al., 1984). Secondly, these smaller droplets may slow down precipitation, and extend the lifetime of a cloud via the *second indirect effect of aerosols* (Albrecht, 1989), which can may influence the hydrological cycle (Rosenfeld et al., 2012).

Because the climate system involves many complex processes which are coupled to each other, the consequences of these climate responses in changing one climate variable can affect another. This creates a feedback loop, where a portion of the output from the process of the climate system is added to the input and subsequently alters the outcome. These changes in the net energy budget at the Top-Of-Atmosphere (TOA) in response to changes of global mean surface temperature are called *climate feedbacks* and can either amplify (positive feedback) or reduce (negative feedback) the effects of climate forcings and their unit is given in $\mathrm{W\,m^{-2}\,K^{-1}}$ (Boucher et al., 2013). The largest positive climate feedback is the *water vapour feedback* with

Table A.1.: Development of important cloud parameter and their uncertainties (Randall et al., 2007; Boucher et al., 2013; Forster et al., 2021).

cloud parameter	**AR4 (2007)**	**AR5 (2013)**	**AR6 (2021)**
net cloud feedback $[\mathrm{W\,m^{-2}\,K^{-1}}]$	not provided	0.6 (-0.2 to 2.0)	0.42 (-0.1 to 0.94)
effective RF aerosol-cloud interaction $[\mathrm{W\,m^{-2}}]$	-0.7 (-1.8 to -0.3)	-0.45 (-1.2 to 0.0)	-0.84 (-1.45 to -0.25)

a value of $1.85 \pm 0.32\ \mathrm{W\,m^{-2}\,K^{-1}}$ as quantified in Liu et al. (2018). Due to his strong infrared absorption bands, water vapour is the most import greenhouse gas and in a warming climate, the concentration of atmospheric water vapour will increase and amplify the greenhouse effect in absorbing more thermal radiation that would otherwise be emitted to space. The main cloud feedback parameters are given in Table A.1.

The coupling between cloudiness and surface air temperature is called *cloud feedback*, and it is the dominant source of spread among GCM climate sensitivity studies, because clouds contribute in creating both, positive and negative feedbacks (Ceppi et al., 2017). Clouds influence the TOA fluxes mainly in two contrary ways: the albedo effect is responsible for enhancing the amount of reflected incoming solar radiation by a cooling of $\sim -50\,\mathrm{W\,m^{-2}}$, whereas the greenhouse effect is leading clouds to trap outgoing LW thermal radiation and therefore reduces the longwave flux leading to a warming of $\sim$30 $\mathrm{W\,m^{-2}}$ (Stephens et al., 2012). This radiative imbalance of $\sim -20\,\mathrm{W\,m^{-2}}$ at TOA, describes the *cloud radiative effect* (CRE) between a cloudy and a clear-sky model atmosphere and shows that Earth would undergo a significant warming (up to 20 K) if there were no clouds present in the atmosphere (Liou and Yang, 2016).

Now, the important question arises, of how the cloud response to anthropogenic greenhouse warming will affect a future climate. At the moment, there are strong evidences (theory, modelling and observations), that there will be, on a globally averaged scale, a positive *net cloud feedback* of $0.42\,\mathrm{W\,m^{-2}\,K^{-1}}$ with a *very likely* but large uncertainty range of -0.10 to $0.94\,\mathrm{W\,m^{-2}\,K^{-1}}$, stating that clouds possibly will amplify global warming (Forster et al., 2021). There are two main underlying cloud processes involved in models to explain this warming. First, the amount of low clouds will decrease (Schneider et al., 2019), leading to less reflection of incoming SW radiation and secondly, in a warming climate the altitude of high clouds will increase (Zelinka et al., 2012), enable them to re-emit the absorbed outgoing LW radiation at colder temperatures and therefore trapping more energy (Norris et al., 2016). The net cloud feedback represents the sum of regional different cloud regimes, because the different SW and LW cloud feedbacks are far from being spatially homogeneous. Especially, the *tropical high-cloud amount feedback*, including ice clouds, is not well specified in models, and it is only possible to assess it with *low confidence*, leading to the largest uncertainty contribution within the cloud feedback framework (Ohno et al., 2019; Forster et al., 2021).

Figure A.1.: Examples of different cirrus types. Cirrus (Ci) are fibrous, threadlike, white feather ice clouds whose form resembles hair curls. Cirrostratus (Cs) are milky, translucent cloud veil of ice crystals, and they can sometimes cause halo appearances around moon and sun. Cirrocumulus (Cc) are fleecy ice clouds of white flakes. These pictures are taken from the 2018 annual report of German Meteorological Service (DWD) at `www.dwd.de`.

Climate Effectiveness of Cirrus Clouds

Cirrus clouds are high-altitude (> 8 km), long-lived ice clouds that have, due to their frequent occurrence, a strong effect on ERB and therefore a considerable contribution to the total cloud feedback as well (Lee et al., 2009b). They form in the upper troposphere in often thermodynamically stable environments with temperatures usually below $-30\,°C$, they have a large average global cloud cover of almost 20% (Sassen et al., 2008), exhibit horizontal inhomogeneity for their bulk ice density (Zhou et al., 2018) and are frequently located near the tropical tropopause (Dessler et al., 2006). For temperatures below $-38\,°C$, clouds consist almost exclusively of ice crystals, and they are called cirrus clouds or just cirrus, whereas clouds for temperatures ranging from $-38\,°C$ to $0\,°C$ are called mixed-phase clouds, due to the coexistence of supercooled liquid droplets and ice crystals. They are also of high atmospheric relevance due to their occurring frequency (Korolev et al., 2017). Dependent on their morphology, the World Meteorological Organization (WMO, 2017) categorised them into three types: cirrus (Ci), cirrostratus (Cs), and cirrocumulus (Cc). Typical examples can be seen in Figure A.1. Mixed-phase or liquid clouds who are lifted by atmospheric updrafts to altitudes where temperatures $< -38\,°C$, are considered as cirrus.

These cirrus clouds have a number of unique features: besides their high-altitude and global occurrence, they consists almost solely of non-spherical ice crystals with manifold different orientations, shapes, surface roughnesses and sizes (Bailey and Hallett, 2004). In contrary to low-altitude liquid clouds, with exclusively spherical droplet particles, the determination of the radiative properties of cirrus clouds is different and much more complex (Yi et al., 2017). These clouds visible optical depths, which is a measure of the attenuation of solar light by cirrus's ice crystals, can range up to 6. However, most values are below 0.1 (Kox et al., 2014). A satellite-based analysis showed, that the cloud feedback, only based on cirrus clouds, is estimated to be positive, with a value of $0.20 \pm 0.21\,\mathrm{W\,m^{-2}\,K^{-1}}$ (Zhou et al., 2014), indicating that the cirrus feedback is a substantial part of the net cloud feedback. The study further indicated, that the amount and altitude of cirrus clouds will may increase as a response of global warming.

Furthermore, air traffic can induce cirrus clouds via line-shaped contrails, developing into extensive contrail cirrus clouds, if they fly in high and cold altitudes. The contribution of air traffic to anthropogenic climate forcing is approximately 5 % (Lee et al., 2009a). The total global net RF associated with aviation-induced cirrus clouds in climate change projections, is estimated to increase by a factor of three to be around $160\,\mathrm{mW\,m^{-2}\,K^{-1}}$, like described in Bock and Burkhardt (2019). On a global scale, there is no observable effect on the mean surface temperature, but these forcings can be much higher regionally (Boucher et al., 2013).

Cirrus clouds play a crucial role in the hydrological circle, because warm rain formation is not enough to explain the most of the global precipitation. In the tropics, subtropics, midlatitude and polar regions 30%, 40%, 80%, and >90%, respectively, of all precipitation events ($>1\,\mathrm{mm\,d^{-1}}$) involve formation and growth processes of ice crystals in cirrus clouds (Field and Heymsfield, 2015). In the tropics, warm rain precipitation is accountable for 31% of the total rain amount (Lau and Wu, 2003), whereas in the mid-latitudes warm rain is only responsible for less than 10% of the total precipitation (Mülmenstädt et al., 2015).

Especially, the behavior of thin cirrus clouds, with very low optical depths (< 0.3), play a key role in RF considerations and subsequently on climate change, due to their large spatial extent and their strong interaction with the radiation field. They significantly modify the SW and LW radiation fluxes. In principle, they can reflect, absorb and transmit the incoming solar radiation and at the same time, they can reflect, transmit and re-emit already absorbed outgoing longwave radiation. Concerning ERB and climate considerations, two processes are competing: the reflection of solar radiation (solar albedo effect) results in a cooling, whereas the trapping of longwave infrared radiation (infrared greenhouse effect) causes a warming (Liou, 1986). Both radiative effects are functions of fundamental cirrus parameters like their coverage, position, thickness, ice crystal size and shape distributions. In contrary to the scattering and absorption by spherical droplets (Lorenz-Mie theory) in water clouds, there is no exact solution for the scattering of light by all the different non-spherical ice crystals, that are present in Earth's atmosphere (Liou and Yang, 2016).

Right now, GCMs show considerable variation and shortcomings in their representations of high cirrus clouds in the upper troposphere, concerning their formation mechanisms and microphysical properties. For example, Mitchell et al. (2008) indicated, that the variation of cirrus parameters like the number of small ice crystals ($<60\,\mu\mathrm{m}$) in a one year simulation can have significant effects on ERB. In detail, they showed a 12% increase of cloud ice as well as a 5.5% increase of global cirrus cloud coverage, causing a net cloud forcing of $-5\,\mathrm{W\,m^{-2}\,K^{-1}}$ in the tropics, which would warm the upper tropical troposphere over 3 °C, comparable to effects of CO_2 doubling. Therefore, there is an urgent need of adequate, high-quality global observations to constrain and calibrate GCM simulations to narrow down uncertainties in the rate and geographical pattern of climate change (Heymsfield et al., 2017).

B. Appendix: Challenges of Modeling Cirrus Clouds in Climate Models

Generally, climate models are required to understand and interpret the effects of greenhouse radiative perturbations on cloud regimes as well as radiative forcings on temperature fields. However, the atmosphere is a complex system with a huge variety of multidimensional coupled processes on different spatial scales. Especially, cloud formation processes range from micrometer scale of CCN/INP, up to evolved clouds with a size of hundreds of kilometers. Such a huge range of scales can not be resolved using numerical simulations on computers, even not in the near future (Boucher et al., 2013, Figure 7.8). Climate models consist of many coupled components. For example, they have a dynamical core to model the movement of air, thermodynamics, as well as heat and use approximations for *radiative transfer* to model the spatial change of the radiation field through the atmosphere (Mayer, B., 2009). There are several quantities to describe a cloud state in a GCM: e.g. there are *macrophysical* properties like horizontal cloud cover, geometrical thickness, altitude, temperature, location and there are *microphysical* properties like the ice water content (IWC), ice water path (IWP), effective ice crystal size (sometimes effective radius R_{eff} or just particle size D), cloud phase, particle size distribution (PSD), ice crystal habit and roughness and *optical* properties like the optical depth and single scattering properties, necessary for radiative transfer calculations (Lynch et al., 2002).

The description of physical phenomena within GCMs relies on the solution of prognostic differential equations and is limited on the size of the spatial (1 km to 100 km) grid, depending on the temporal resolution (1 min to 6 h) (Jansson et al., 2022). However besides those so-called gridscale processes, which are described explicitly, there are relevant processes for future weather and climate, that can not be resolved at this resolution and with these equations. These subgrid-scale physical processes which can not be explicitly resolved by the model grid have to be included as *physical parameterisations*. These schemes provide terms that are added to the prognostic variable, which they are influence, and therefore are often formulated as complex (non-linear) function of the grid box mean value of exactly this prognostic variable (Lynch et al., 2002; Bacer et al., 2018; Stubenrauch et al., 2019). Examples for such unresolved parameterized processes are cloud microphysics, turbulence, and convection (Gu et al., 2003; Ceppi et al., 2017). A further complexity arises, because they are entangled with each other. For example, when tropical cirrus clouds appear optically to be thin, the reason could be that model's convection transports not enough amount of ice into the clouds or the microphysical assumptions are maybe misleading. Furthermore, if convection would be the reason, is it because it occurs not frequently enough or is it simply not strong enough and how are these outcomes related to an overestimation of precipitation in the same region, are questions that could come up (Siebesma et al., 2020; Tully et al., 2021).

In the fifth phase of the Climate Model Intercomparison Project (CMIP6, (Li et al., 2020)), the cloud feedback was still by far the largest source of intermodel spread in equilibrium climate sensitivity (ECS) estimates for the global-mean surface temperature as response to

RF of CO_2 doubling (Ceppi et al., 2017; Stevens et al., 2016). Heymsfield et al. (2017) pointed out, that one possible reason is, that the dynamical processes involved in cirrus formation are different in different geographical areas and lack a proper resolution in GCMs. Related processes, like the transport of very small amounts of water vapour to and within the upper troposphere, suffers the same lack of vertical resolution of only 10-20 model layers. The global annual mean cirrus CRE, estimated by the ECHAM6-HAM2 general circulation model (Gasparini and Lohmann, 2016) has a value of $5.7\,\mathrm{W\,m^{-2}}$, which is larger than estimates from satellite observations, which received values of $1.3\,\mathrm{W\,m^{-2}}$ (Chen et al., 2000) and $2.4\,\mathrm{W\,m^{-2}}$ (Hartmann et al., 1992).

Within the last two decades, a milestone in cirrus cloud modeling was accomplished, by including prognostic equations capable of predicting the IWC of high-altitude cirrus clouds in GCMs. This was important, because it supplied a physically based cloud microphysics scheme, and it provided insights for investigating cirrus-radiation interactions in GCMs (Liou et al., 2008). But, the interaction of ice crystal size, an independent parameter that impacts the radiative transfer within cirrus clouds, was not properly included in GCMs. Therefore, deviations could occur: for a given fixed IWC, smaller ice crystal sizes would reflect more SW radiation than larger ones, due to their larger optical depth. This is similar to what was described by Twomey et al. (1984) for water clouds. Back then, it was a common practice in GCM to use simple and coarse mean effective ice crystal size-approaches or to use temperature to determine ice crystal size, based on ice microphysics observations by aircraft campaigns (Kristjánsson et al., 2005; Gu and Liou, 2006). In their study, Liou et al. (2008) further showed, that the inclusion of ice crystal size-IWC correlations exhibit smaller uncertainties for radiative forcing values, revealing that ice crystal size is an excellent parameter for calculations of the radiation field and much better than temperature based parameterisations. In detail, the significant horizontal and vertical variability inherent in cirrus clouds (Buschmann et al., 2002) will lead to provoke spatial variations concerning radiative heating and cooling rates like investigated from Gu and Liou (2006) in numerical studies with GCMs. Therefore, a profound knowledge of the spatial variability of ice crystal size and IWC would serve as an additional constraint, where the GCM representation of cirrus clouds would benefit from.

To narrow down uncertainties in the predicted cirrus cloud feedback for GCM, innovative ice crystal size-IWC correlation parameterisations based on theory and observation must be developed. To achieve this, *in-situ* measurements and high resolved spatial-temporal profiles from *remote sensing* devices, both from different geographic locations are required, that provide measurement quantities from which profiles of cirrus properties like ice crystal size and IWC can be retrieved.

C. Appendix: Formation of Ice Crystals in Cirrus Clouds

Prerequisites for Ice Formation

Ice particle formation in the upper troposphere happens in regions, where the air is supersaturated with respect to ice. In general, saturation describes a thermodynamic state of equilibrium between water vapour and liquid water or between water vapour and ice (Korolev and Mazin, 2003). This state of equilibrium is characterised by the saturation vapour pressure and shows a non-linear increase with increasing temperature (Clausius-Clapeyron equation). Here, vapour pressure means the partial pressure of water vapour and the sum of all partial pressures is the total atmospheric pressure. Above this equilibrium state, the air is said to be supersaturated with respect to water/ice and water vapour condenses/deposits faster than it evaporates/sublimates, subsequently reducing the water vapour concentration back to the equilibrium value.

In the atmosphere, regions that are supersaturated with respect to ice, occur mainly via large-scale vertical movements along a frontal boundary or at small-scale vertical circulations originated in jet streams, convective clouds, gravity waves or via orographic lifting (Heymsfield et al., 2010b; Gierens and Brinkop, 2012; Heymsfield et al., 2017). In detail, when a moist parcel of air is lifted, it undergoes adiabatic cooling and expansion until it reaches a temperature, where the moist air parcel is supersaturated with respect to water/ice and water vapour is available to participate in different nucleation mechanisms. In an adiabatic process, there will be no exchange of mass with the environment and therefore the specific humidity of the air parcel remains constant during the uplifting process.

In the upper troposphere it is possible for liquid water to remain unfrozen down to temperatures of $-38\,^{\circ}\mathrm{C}$, and this is approximately the threshold temperature for detecting homogeneous freezing (DeMott et al., 2003). This metastable phase, a phase only existent on a limited time scale, of unfrozen cold water is called supercooled. While liquid cloud droplets are formed exclusively via heterogenous condensation of water vapour on aerosol particles, the formation of ice crystals can happen via homogeneous freezing, via heterogenous ice nucleation with the help of INPs, or a mixture of both (Vali et al., 2015). Heterogenous ice nucleation can take place on different pathways, depending on temperature and supersaturation. Nucleation defines the first step in a phase transition, where a cluster of a thermodynamically stable phase (ice nuclei) forms and grows within the surrounding metastable parent phase of supersaturated water vapor (deposition nucleation) or supercooled liquid water (freezing nucleation). The following step (crystal growth) starts, when the microscopic ice nuclei reaches a certain size, they are now activated to ice crystals, and they can grow via accumulation of more water molecules on their surface, until there is a macroscopic crystalline area (Lohmann et al., 2016).

Homogeneous Ice Nucleation

Homogeneous ice nucleation occurs at temperatures below −40 °C and the relative humidity (ice) is between 140 - 170% (Heymsfield et al., 2017). The term "homogeneous" denotes the case, where no foreign substance surface' is available to serve as a catalyser to accelerate the nucleation process by reducing the energy barrier. Due to the thermal molecular movement in supersaturated water vapour or in supercooled water droplets, statistical fluctuations of water molecular arrangement with correct orientations produce a stable, ice-like cluster structure, that can serve as an embryonic ice nuclei, where more water molecules can accumulate onto. Only about 250 molecules are necessary to form such a cluster at temperatures of −40 °C. There are two types of homogeneous nucleation, depending on their parent phase. *Homogeneous deposition nucleation* is the formation of ice based on water vapor. Because of the very high supersaturation necessary for the homogeneous deposition nucleation of ice, it never occurs in the atmosphere. *Homogeneous freezing nucleation* is observed in supercooled liquid droplets without any foreign substance to catalyse the process. Theory and experiments indicated, that droplets smaller than 5 µm will freeze spontaneously at temperatures of about −40 °C, whereas larger droplets will freeze at slightly warmer temperatures (Liou and Yang, 2016).

Heterogenous Ice Nucleation

Heterogenous ice nucleation occurs at temperatures below 0 °C and the relative humidity (ice) is between 100 - 140% and is the dominant ice nucleation process in mixed-phase clouds but also occurs in cirrus clouds (Cziczo et al., 2013). It involves foreign substances as INP to impact the nucleation to the effect, that it takes place at lesser supersaturation or supercooling than the aforementioned homogeneous ice nucleation. The INP provides a surface onto which water molecules can impinge and bond together, and form aggregates with an ice like structure. The larger such an aggregate is, the more likely it is to be stable with a larger lifetime. Heterogeneous ice nucleation is more poorly understood than homogeneous ice nucleation because there is a variety of ways to form ice in the atmosphere. Each of them is fundamentally different from one another. They can be again distinguished by the parent phase: *Heterogenous deposition nucleation* is based on supersaturated water vapor on an INP, whereas *heterogenous freezing nucleation* occurs on INPs within a supercooled liquid droplet.

Heterogenous deposition nucleation is the only mechanism, where liquid water is presumed to be absent and water vapor deposits directly on a deposition nucleus, like mineral dust (Cziczo et al., 2013). The solute effect for liquid droplet nucleation lowered the equilibrium saturation vapor pressure, but is not important for ice nucleation, because salts are excluded from the ice-crystal lattice as water freezes (Brine rejection). Therefore, the size and crystal structure of the ice nucleus is more important and deposition is unlikely to happen on particles of sizes lower than 0.1 µm. Decreasing temperatures and larger supersaturation will increase deposition nucleation.

Heterogenous freezing nucleation can be divided into several modes. *Immersion/condensation freezing* refers to ice nucleation initiated by an INP, located within the body of a liquid droplet, while the air is cooling. There have been minor terminology differences based on the historical description of the immersed INP, but the two mechanisms are now considered to be synonymous (Heymsfield et al., 2017). *Contact freezing* occurs when an uncontaminated supercooled liquid droplet comes into contact with an INP at the air–water interface. If the supercooled

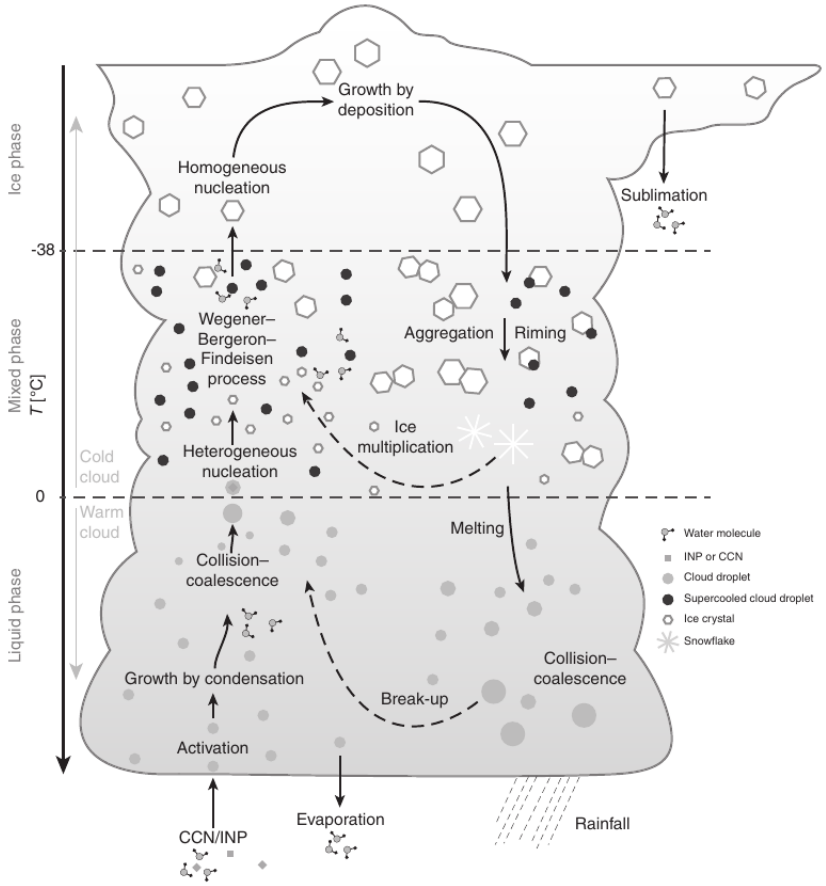

Figure C.1.: Microphysical ice crystal nucleation and growth processes in a convective cloud with all relevant phases of water in the atmosphere. Figure taken from Lohmann et al. (2016).

droplet is colder than the critical temperature of the INP, it will freeze almost instantly. It is defined to be a separate process from immersion freezing because of empirical evidence that some INPs are more effective in this mode, than when immersed in liquid (Shaw et al., 2005; Vali et al., 2015).

Although there is a huge amount of different CCNs in the atmosphere, ice nuclei are rarely to be found, independent of their origin. One of the most effective material being used as an artificial INP is silver iodide, which has been shown to nucleate ice at temperatures of $-3\,°C$ (Vonnegut, 1947; Stull, 2015, Table 7-2).

Growth of Ice Crystals and Secondary Ice Particle Production

Once the ice crystals are nucleated, they can grow via several processes like *diffusion deposition* and *accretion (riming, aggregation, collision–coalescence)* until they reach sizes large enough to precipitate. In dependence of the temperature and supersaturation in the cloud, the ice crystals grow up to different, mainly hexagonal-based forms, called *ice crystal habits*. While first ice crystals have to form on INPs, further ice crystals can be produced by secondary processes where the primary ice crystals are “multiplied” via *ice enhancement* (Pruppacher

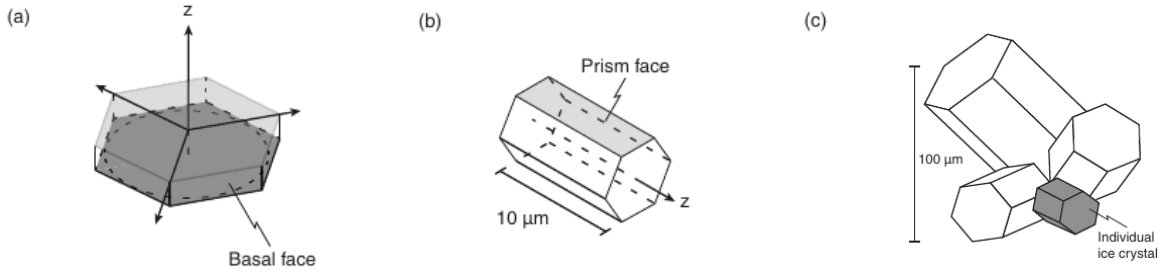

Figure C.2.: Schematic of the most common primary ice crystal habits: (a) plate, (b) column and (c) aggregate. Figure taken and modified from Lohmann et al. (2016).

and Klett, 2010).

Ice crystal growth by *diffusion deposition* is a direct consequence of the differences in the saturation vapor pressure between ice and liquid water. When the first ice crystals in a cloud are nucleated, there will be a mixture of ice crystals, supercooled liquid droplets and water vapour. Due to the higher binding energy in an ice crystal, the saturation vapour pressure over ice will be lower than over liquid water. Therefore, cloud air which is saturated with respect to liquid water is strongly supersaturated with respect to ice. As a result, there will be a vapour pressure gradient and the water vapour moves from the supercooled liquid droplets to the lower pressure surrounding ice crystals, leading them to grow at the expense of supercooled droplets. This action is called Wegener–Bergeron–Findeisen process (Wegener, 1911; Bergeron, 1935; Findeisen, 1938) with a maximum growth rate at a temperature of $-12\,°C$ (Lynch et al., 2002). Subsequently, there will occur a sub-saturation with respect to water and the supercooled liquid droplets evaporate to maintain water saturation, delivering additional water vapour for ice crystal growth.

Ice crystal growth called *accretion (riming, aggregation, collision–coalescence)* takes place after diffusional growth and ensures further grow via collision and coalescence of two different hydrometeors. These collision processes are caused by differences in fall velocities of the involved hydrometeors or by turbulence. After the collision, cloud droplets can freeze onto the ice crystal, it behaves like a collector, and grows in mass. Immediate freezing of droplets on an ice phase hydrometeor is called *riming* and could be the most important explanation for ice enhancement. Typical hydrometeors caused by riming are graupel, if particles stay below 2.5 mm, or hailstones for extreme riming events like convective storms in summer. *Aggregation* denotes the clumping of ice crystals to form snowflakes. When two ice particles collide, the probability of adhesion is governed by temperature and the type of the ice particle, more complex crystals like dendrites, are prone to adhere to one another due to entanglement in collision, whereas two solid plates will tend to deflect on each other (Liou and Yang, 2016).

The aforementioned ice nucleation and growth processes are schematically illustrated in Figure C.1.

Ice Crystal Morphology

When ice crystals fall and move by wind and turbulence in the atmosphere, they enter regions with different temperatures and supersaturation levels, and they are the main parameters who determine the specific shape, also called *habit*, a ice crystal will grow up to. The most common

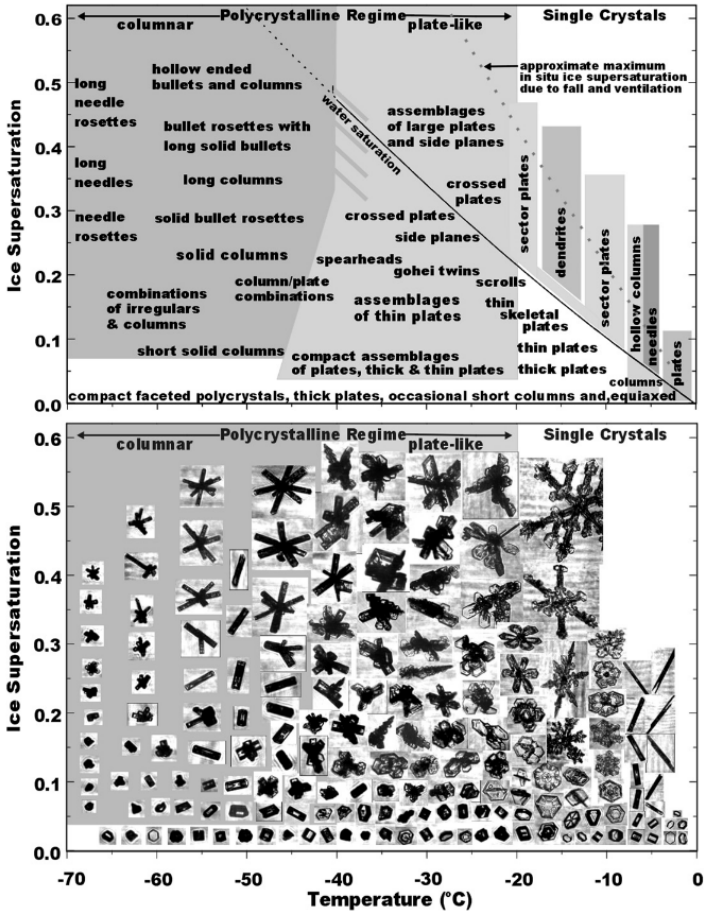

Figure C.3.: Ice crystal habits as a function of temperature and supersaturation with pictures from laboratory and atmospheric field measurements. Figure taken from Bailey and Hallett (2009).

primary habits are *plates* and *columns* and aggregates of them, like illustrated in Figure C.2. When ice crystallisation takes place, the water molecules will form hydrogen bonds with each other, which strongly affects the ice crystal structure, when the molecular tetrahedral arrangements lead to hexagonal based ice lattices. Ice crytals can grow along their basal face as needle or column, or they can grow along their prism face as plate-like crystal, whereas aggregates form via collisions of ice crystals on rather high temperatures. The requirement of minimizing the surface energy per volume controls the temperature and supersaturation dependent growth rate maxima, and shifts the equilibrium shape of the crystal between different ice crystal habits (Nelson, 2001; Pruppacher and Klett, 2010; Lohmann et al., 2016).

Figure C.3 illustrates different regimes of single habit formation as function of temperature and ice supersaturation, which were investigated by Bailey and Hallett (2009) with data from laboratory results and in situ measurements with a CPI. Three major areas of ice crystal habit can be seen at the different temperature intervals. For temperatures between $-70\,°C$ and $-40\,°C$, columnar polycrystals are the dominant habit, whereas between $-40\,°C$ and $-20\,°C$ plate-like polycrystals are the preferable habit. Below $-20\,°C$, the observed crystal morphology shows a mix of plates and short columns for low ice supersaturation. With

increasing supersaturation more complex structures such as hollow columns or dendrites occur as habit.

As in situ and remote sensing measurements indicated, the surfaces of ice crystals are not always exactly smooth, particularly if they undergo collision and riming processes. A famous example is the 22° circular halo, a optical phenomenon, where increasing surface roughness of the ice crystals decreases the halo visibility, as quantified by the so-called halo ratio (Forster et al., 2017).

Both, ice crystal habit and surface roughness are strongly impacting the scattering properties and consequently the radiative properties of cirrus clouds, and should be properly included and represented in climate models and cirrus retrievals to ensure a realistic description.

List of Figures

List of Tables

Glossary

ACTRIS Aerosol, Clouds and Trace Gases Research Infrastructure. 3, 127

ADDA Amsterdam discrete dipole approximation. 17, 18

AERI Atmospheric Emitted Radiance Interferometer. 33, 41, 42, 51, 52, 54, 56, 57, 60–63, 80, 84, 86, 109, 111, 112, 114–120, 124–127, 130, 132

AIRS Atmospheric Infrared Sounder . 61

ARM Atmospheric Radiation Measurement. 3, 29

ARTS Atmospheric Radiative Transfer Simulator. 54

CALIOP Cloud-Aerosol Lidar with Orthogonal Polarisation. 3

CCN cloud condensation nuclei. 137, 141, 145

CKD correlated k-distribution. 57, 58

CMIP6 Climate Model Intercomparison Project phase 6. 141

COT cloud optical thickness. 62, 63, 71, 80, 84, 90, 105, 117, 121, 122, 124, 126, 131

CPI cloud particle imager. 2, 147

CPR cloud profiling radar. 3

CRE cloud radiative effect. 138, 142

CWCT cumulative wavelet covariance transform. 48

DIAL differential absorption lidar. 32, 109

DISORT DIScrete ORdinate Radiative Transfer. 54, 56, 63, 80

DLR German Aerospace Center (Deutsches Zentrum für Luft- und Raumfahrt). 41

DNS direct numerical simulaiton. 27

DWD Deutscher Wetterdienst. 139

ECMWF European Center for Medium-Range Weather Forecasts. 54

ECS equilibrium climate sensitivity. 141

ER-AERI Extended Range Atmospheric Emitted Radiance Interferometer. 43

ERB Earth's radiation budget. 1, 129, 137, 138, 140

FDTD finite-difference time-domain. 17, 18

FIR far infrared. 56

FOV field of view. 75–78, 98, 99, 116, 119, 123, 124, 126, 130

FSSP forward scattering spectrometer probe. 2

FTIR Fourier transform infrared. 30, 32

FTS Fourier transform spectrometer. 30

GCM global circulation models. 1, 2, 6, 27–29, 109, 121, 132, 135, 138, 140–142

HALO High-Altitude LOng-endurance. 41, 42, 102, 103, 107, 111

HAMP HAlo Microwave Package. 42, 49, 111

HITRAN HIgh Resolution TRANsmission, molecular spectroscopic database. 54, 57

HSRL high spectral resolution lidar. 32

IER integrated effective radius. 25

IGOM Improved geometric optics method. 17, 18

ILS instrumental line shape. 31, 87

IMK-IFU Institute of Meteorology and Climate Research Atmospheric Environmental Research. 41, 109

INP ice nucleating particle. 137, 141, 143, 145, 146

IPA independent pixel assumption. 84

IPCC Intergovernmental Panel on Climate Change. 1, 137

IR infrared. 50

ISA independent scattering assumption. 84

IWC ice water content. 3–7, 24, 25, 64, 129, 141, 142

IWP ice water path. 24, 94, 101, 141

LBL Line-By-Line. 54, 57, 58, 86, 87

LES large eddy simulation. 27

libRadtran Library for Radiative Transfer. 18, 42, 54

Lidar Light detection and ranging. 36

LUT lookup table. 59, 60, 97, 105, 123

LW longwave radiation. 3, 13, 19, 28, 137, 138, 140

MIR mid-infrared. 56

MODIS MODerate Resolution Imaging Spectroradiometer. 3

MS multiple-scattering. 77, 78, 99

MYSTIC Monte Carlo code for the phYSically correct Tracing of photons In Cloudy atmospheres. 128

NARVAL Next Generation Remote Sensing for Validation Studies. 8, 41, 42, 49, 75, 85, 102–107, 124, 132

NIR near infrared. 56

NSA North Slope of Alaska. 136

NWP numerical weather prediction. 27, 29

OAP optical array probe. 2

OPD optical path difference. 30, 43, 56

PBL planetary boundary layer. 44–46

PCA principal component analysis. 51

PPA plane-parallel assumption. 84

PSD particle size distribution. 2–4, 6, 7, 23–29, 34, 35, 37–40, 59, 61, 64–69, 80, 83, 85, 87–89, 98, 107, 114, 115, 121, 122, 125–133, 135, 141

pyMPM python implementation of the milimeter wave propagation model MPM. 50, 81

Radar Radio detection and ranging. 34

RCP representative concentration pathway. 1

REPTRAN Representative wavelengths absorption parameterization. 57, 58, 63, 85–87, 130

RF radiative forcing. 137–141

RH relative humidity. 81

RMSE root mean square error. 65, 67, 76

RT radiative transfer. 11, 25, 26, 38, 42, 51, 54, 56, 58, 59, 80, 84–86, 89, 93, 113, 115, 116, 122, 123, 127, 128, 130

RTE radiative transfer equation. 22, 34, 54–56, 59

SHA single habit assumption. 83

SNR signal to noise ratio. 44, 85, 91, 92, 94, 98, 105, 109, 114, 116, 122, 125–127, 131, 132

SS single-scattering. 77, 78

SW shortwave radiation. 3, 13, 28, 137, 138, 140, 142

TCCON Total Carbon Column Observing Network. 126

TOA Top-Of-Atmosphere. 13, 28, 137, 138

UFS Umweltforschungsstation Schneefernerhaus. 8, 41–44, 46, 48, 49, 63, 93, 109–113, 115–119, 124, 126, 132

UV ultraviolet. 50

WALES WAter vapor Lidar Experiment in Space. 42, 103, 105, 114, 124, 125

WCT wavelet covariance transform. 45, 48, 49

Bibliography

Technical data ceilometer chm 15k „nimbus“. Technical report, 2022. URL https://www.lufft.com/products/cloud-height-snow-depth-sensors-288/ceilometer-chm-15k-nimbus-2300/productAction/outputAsPdf/. [Online; accessed 5-December-2022].

Bruce A. Albrecht. Aerosols, cloud microphysics, and fractional cloudiness. *Science*, 245 (4923):1227–1230, 1989. doi: 10.1126/science.245.4923.1227. URL https://www.science.org/doi/abs/10.1126/science.245.4923.1227.

Gail P Anderson, Shepard Anthony Clough, FX Kneizys, James H Chetwynd, and Eric P Shettle. Afgl atmospheric constituent profiles (0.120 km). Technical report, AIR FORCE GEOPHYSICS LAB HANSCOM AFB MA, 1986.

A Arakawa. Modelling clouds and cloud processes for use in climate models. *WMO The Phys. Basis of Climate and Climate Modelling p 183-197(SEE N 76-19675 10-47)*, 1975.

David Atlas. The estimation of cloud parameters by radar. *Journal of Atmospheric Sciences*, 11(4):309–317, 1954.

Melody Avery, David Winker, Andrew Heymsfield, Mark Vaughan, Stuart Young, Yongxiang Hu, and Charles Trepte. Cloud ice water content retrieved from the caliop space-based lidar. *Geophysical Research Letters*, 39(5), 2012. doi: https://doi.org/10.1029/2011GL050545. URL https://agupubs.onlinelibrary.wiley.com/doi/abs/10.1029/2011GL050545.

H. Baars, A. Ansmann, R. Engelmann, and D. Althausen. Continuous monitoring of the boundary-layer top with lidar. *Atmospheric Chemistry and Physics*, 8(23):7281–7296, 2008. doi: 10.5194/acp-8-7281-2008. URL https://acp.copernicus.org/articles/8/7281/2008/.

S. Bacer, S. C. Sullivan, V. A. Karydis, D. Barahona, M. Krämer, A. Nenes, H. Tost, A. P. Tsimpidi, J. Lelieveld, and A. Pozzer. Implementation of a comprehensive ice crystal formation parameterization for cirrus and mixed-phase clouds in the emac model (based on messy 2.53). *Geoscientific Model Development*, 11(10):4021–4041, 2018. doi: 10.5194/gmd-11-4021-2018. URL https://gmd.copernicus.org/articles/11/4021/2018/.

Matthew Bailey and John Hallett. Growth rates and habits of ice crystals between −20° and −70°c. *Journal of the Atmospheric Sciences*, 61(5):514–544, 2004. doi: 10.1175/1520-0469(2004)061<0514:GRAHOI>2.0.CO;2. URL https://journals.ametsoc.org/view/journals/atsc/61/5/1520-0469_2004_061_0514_grahoi_2.0.co_2.xml.

Matthew P. Bailey and John Hallett. A comprehensive habit diagram for atmospheric ice crystals: Confirmation from the laboratory, airs ii, and other field studies. *Journal of the Atmospheric Sciences*, 66(9):2888 – 2899, 2009. doi: 10.1175/2009JAS2883.1. URL https://journals.ametsoc.org/view/journals/atsc/66/9/2009jas2883.1.xml.

Anthony J Baran. A review of the light scattering properties of cirrus. *Journal of Quantitative Spectroscopy and Radiative Transfer*, 110(14-16):1239–1260, 2009.

Anthony J. Baran. From the single-scattering properties of ice crystals to climate prediction: A way forward. *Atmospheric Research*, 112:45–69, 2012. ISSN 0169-8095. doi: https://doi.org/10.1016/j.atmosres.2012.04.010. URL https://www.sciencedirect.com/science/article/pii/S0169809512001160.

Alessandro Battaglia, Simone Tanelli, Satoru Kobayashi, Dusan Zrnic, Robin J. Hogan, and Clemens Simmer. Multiple-scattering in radar systems: A review. *Journal of Quantitative Spectroscopy and Radiative Transfer*, 111(6):917–947, 2010. ISSN 0022-4073. doi: https://doi.org/10.1016/j.jqsrt.2009.11.024. URL https://www.sciencedirect.com/science/article/pii/S0022407309003677.

Bryan A Baum, Ping Yang, Andrew J Heymsfield, Steven Platnick, Michael D King, YX Hu, and Sarah T Bedka. Bulk scattering properties for the remote sensing of ice clouds. part ii: Narrowband models. *Journal of Applied Meteorology*, 44(12):1896–1911, 2005.

Bryan A Baum, Ping Yang, Andrew J Heymsfield, Carl G Schmitt, Yu Xie, Aaron Bansemer, Yong-Xiang Hu, and Zhibo Zhang. Improvements in shortwave bulk scattering and absorption models for the remote sensing of ice clouds. *Journal of Applied Meteorology and Climatology*, 50(5):1037–1056, 2011.

Darrel Baumgardner, L Avallone, Aaron Bansemer, Stephan Borrmann, P Brown, Ulrich Bundke, Patrick Y Chuang, D Cziczo, P Field, Martin Gallagher, et al. In situ, airborne instrumentation: Addressing and solving measurement problems in ice clouds. *Bulletin of the American Meteorological Society*, 93(2):ES29–ES34, 2012.

Darrel Baumgardner, SJ Abel, Duncan Axisa, Richard Cotton, Jonathan Crosier, P Field, Colin Gurganus, A Heymsfield, Alexei Korolev, Martina Kraemer, et al. Cloud ice properties: In situ measurement challenges. *Meteorological monographs*, 58:9–1, 2017.

Omar Bellprat, Virginie Guemas, Francisco Doblas-Reyes, and Markus G. Donat. Towards reliable extreme weather and climate event attribution. *Nature Communications*, 10(1): 1732, Apr 2019. ISSN 2041-1723. doi: 10.1038/s41467-019-09729-2. URL https://doi.org/10.1038/s41467-019-09729-2.

A. Benedetti, G. L. Stephens, and J. M. Haynes. Ice cloud microphysics retrievals from millimeter radar and visible optical depth using an estimation theory approach. *Journal of Geophysical Research: Atmospheres*, 108(D11), 2003. doi: https://doi.org/10.1029/2002JD002693. URL https://agupubs.onlinelibrary.wiley.com/doi/abs/10.1029/2002JD002693.

T. Bergeron. On the physics of clouds and precipitation. *Proc. 5th Assembly U.G.G.I., Lisbon, Portugal, 1935*, pages 156–180, 1935. URL https://ci.nii.ac.jp/naid/10024028214/en/.

Jacob Bernoulli. Explicationes, annotationes & additiones ad ea, quae in actis sup. de curva elastica, isochrona paracentrica, & velaria, hinc inde memorata, & paratim controversa legundur; ubi de linea mediarum directionum, alliisque novis. *Acta Eruditorum*, 1695.

P. Berrisford, D.P. Dee, P. Poli, R. Brugge, Mark Fielding, Manuel Fuentes, P.W. Kållberg, S. Kobayashi, S. Uppala, and Adrian Simmons. *The ERA-Interim archive Version 2.0*. Shinfield Park, Reading, 11/2011 2011.

L. R. Bissonnette, P. Bruscaglioni, A. Ismaelli, G. Zaccanti, A. Cohen, Y. Benayahu, M. Kleiman, S. Egert, C. Flesia, P. Schwendimann, A. V. Starkov, M. Noormohammadian, U. G. Oppel, D. M. Winker, E. P. Zege, I. L. Katsev, and I. N. Polonsky. Lidar multiple scattering from clouds. *Applied Physics B*, 60(4):355–362, Apr 1995. ISSN 1432-0649. doi: 10.1007/BF01082271. URL https://doi.org/10.1007/BF01082271.

Y. Blanchard, A. Royer, N. T. O'Neill, D. D. Turner, and E. W. Eloranta. Thin ice clouds in the arctic: cloud optical depth and particle size retrieved from ground-based thermal infrared radiometry. *Atmospheric Measurement Techniques*, 10(6):2129–2147, 2017. doi: 10.5194/amt-10-2129-2017. URL https://amt.copernicus.org/articles/10/2129/2017/.

L. Bock and U. Burkhardt. Contrail cirrus radiative forcing for future air traffic. *Atmospheric Chemistry and Physics*, 19(12):8163–8174, 2019. doi: 10.5194/acp-19-8163-2019. URL https://acp.copernicus.org/articles/19/8163/2019/.

R Boers, H Russchenberg, J Erkelens, V Venema, ACAP Van Lammeren, A Apituley, and SCHM Jongen. Ground-based remote sensing of stratocumulus properties during clara, 1996. *Journal of Applied Meteorology*, 39(2):169–181, 2000.

Craig F Bohren and Donald R Huffman. *Absorption and scattering of light by small particles*. John Wiley & Sons, 2008.

O. Boucher, D. Randall, P. Artaxo, C. Bretherton, G. Feingold, P. Forster, V.-M. Kerminen, Y. Kondo, H. Liao, U. Lohmann, P. Rasch, S.K. Satheesh, S. Sherwood, B. Stevens, and X.Y. Zhang. *Clouds and Aerosols*, book section 7, page 571–658. Cambridge University Press, Cambridge, United Kingdom and New York, NY, USA, 2013. ISBN ISBN 978-1-107-66182-0. doi: 10.1017/CBO9781107415324.016. URL www.climatechange2013.org.

VN Bringi, J Vivekanandan, and JD Tuttle. Multiparameter radar measurements in colorado convective storms. part ii: Hail detection studies. *Journal of the atmospheric sciences*, 43 (22):2564–2577, 1986.

Ian M. Brooks. Finding boundary layer top: Application of a wavelet covariance transform to lidar backscatter profiles. *Journal of Atmospheric and Oceanic Technology*, 20(8):1092 – 1105, 2003. doi: 10.1175/1520-0426(2003)020<1092:FBLTAO>2.0.CO;2. URL https://journals.ametsoc.org/view/journals/atot/20/8/1520-0426_2003_020_1092_fbltao_2_0_co_2.xml.

P. R. A. Brown, A. J. Illingworth, A. J. Heymsfield, G. M. McFarquhar, K. A. Browning, and M. Gosset. The role of spaceborne millimeter-wave radar in the global monitoring of ice cloud. *Journal of Applied Meteorology and Climatology*, 34(11):2346 – 2366, 1995. doi: 10.1175/1520-0450(1995)034<2346:TROSMW>2.0.CO;2. URL https://journals.ametsoc.org/view/journals/apme/34/11/1520-0450_1995_034_2346_trosmw_2_0_co_2.xml.

Philip R. A. Brown and Peter N. Francis. Improved measurements of the ice water content in cirrus using a total-water probe. *Journal of Atmospheric and Oceanic Technology*, 12(2):410 – 414, 1995. doi: 10.1175/1520-0426(1995)012<0410:IMOTIW>2.0.CO;2. URL https://journals.ametsoc.org/view/journals/atot/12/2/1520-0426_1995_012_0410_imotiw_2_0_co_2.xml.

SA Buehler, VO John, Ajil Kottayil, Mathias Milz, and Patrick Eriksson. Efficient radiative transfer simulations for a broadband infrared radiometer—combining a weighted mean of representative frequencies approach with frequency selection by simulated annealing. *Journal of Quantitative Spectroscopy and Radiative Transfer*, 111(4):602–615, 2010.

Stefan A Buehler, Jana Mendrok, Patrick Eriksson, Agnès Perrin, Richard Larsson, and Oliver Lemke. Arts, the atmospheric radiative transfer simulator–version 2.2. *Geoscientific Model Development*, 11(4):1537–1556, 2018.

J. Bühl, S. Alexander, S. Crewell, A. Heymsfield, H. Kalesse, A. Khain, M. Maahn, K. Van Tricht, and M. Wendisch. Remote sensing. *Meteorological Monographs*, 58:10.1 – 10.21, 2017. doi: 10.1175/AMSMONOGRAPHS-D-16-0015.1. URL https://journals.ametsoc.org/view/journals/amsm/58/1/amsmonographs-d-16-0015.1.xml.

Nicole Buschmann, Greg M. McFarquhar, and Andrew J. Heymsfield. Effects of observed horizontal inhomogeneities within cirrus clouds on solar radiative transfer. *Journal of Geophysical Research: Atmospheres*, 107(D20):AAC 9–1–AAC 9–9, 2002. doi: https://doi.org/10.1029/2001JD001273. URL https://agupubs.onlinelibrary.wiley.com/doi/abs/10.1029/2001JD001273.

Bertrand Cadet, Vincent Giraud, Martial Haeffelin, Philippe Keckhut, Anne Rechou, and Serge Baldy. Improved retrievals of the optical properties of cirrus clouds by a combination of lidar methods. *Applied optics*, 44(9):1726–1734, 2005.

Quitterie Cazenave, Marie Ceccaldi, Julien Delanoë, Jacques Pelon, Silke Groß, and Andrew Heymsfield. Evolution of dardar-cloud ice cloud retrievals: new parameters and impacts on the retrieved microphysical properties. *Atmospheric Measurement Techniques*, 12(5):2819–2835, 2019.

Paulo Ceppi and Dennis L. Hartmann. Clouds and the atmospheric circulation response to warming. *Journal of Climate*, 29(2):783 – 799, 2016. doi: 10.1175/JCLI-D-15-0394.1. URL https://journals.ametsoc.org/view/journals/clim/29/2/jcli-d-15-0394.1.xml.

Paulo Ceppi, Florent Brient, Mark D. Zelinka, and Dennis L. Hartmann. Cloud feedback mechanisms and their representation in global climate models. *WIREs Climate Change*, 8(4):e465, 2017. doi: https://doi.org/10.1002/wcc.465. URL https://wires.onlinelibrary.wiley.com/doi/abs/10.1002/wcc.465.

S. Chandrasekhar. Radiative transfer, 416 dover publications. *New York*, page 393, 1960.

Kai-Wei Chang, Tristan S. L'Ecuyer, Brian H. Kahn, and Vijay Natraj. Information content of visible and midinfrared radiances for retrieving tropical ice cloud properties. *Journal of Geophysical Research: Atmospheres*, 122(9):4944–4966, 2017. doi: https://doi.org/10.1002/2016JD026357. URL https://agupubs.onlinelibrary.wiley.com/doi/abs/10.1002/2016JD026357.

Ting Chen, William B. Rossow, and Yuanchong Zhang. Radiative effects of cloud-type variations. *Journal of Climate*, 13(1):264 – 286, 2000. doi: 10.1175/1520-0442(2000)013<0264:REOCTV>2.0.CO;2. URL https://journals.ametsoc.org/view/journals/clim/13/1/1520-0442_2000_013_0264_reoctv_2.0.co_2.xml.

Wei-Nai Chen, Chih-Wei Chiang, and Jan-Bai Nee. Lidar ratio and depolarization ratio for cirrus clouds. *Applied Optics*, 41(30):6470–6476, 2002.

Nitin R Chopde and Mangesh Nichat. Landmark based shortest path detection by using a* and haversine formula. *International Journal of Innovative Research in Computer and Communication Engineering*, 1(2):298–302, 2013.

M. Collins, R. Knutti, J. Arblaster, J.-L. Dufresne, T. Fichefet, P. Friedlingstein, X. Gao, W.J. Gutowski, T. Johns, G. Krinner, M. Shongwe, C. Tebaldi, A.J. Weaver, and M. Wehner. *Long-term Climate Change: Projections, Commitments and Irreversibility*, book section 12, page 1029–1136. Cambridge University Press, Cambridge, United Kingdom and New York, NY, USA, 2013. ISBN ISBN 978-1-107-66182-0. doi: 10.1017/CBO9781107415324.024. URL www.climatechange2013.org.

Adolfo Comerón, Francesc Rocadenbosch, Miguel Angel López, Alejandro Rodríguez, Constantino Muñoz, David García-Vizcaíno, and Michaël Sicard. Effects of noise on lidar data inversion with the backward algorithm. *Applied Optics*, 43(12):2572–2577, 2004.

Jennifer M Comstock, Robert d'Entremont, Daniel DeSlover, Gerald G Mace, Sergey Y Matrosov, Sally A McFarlane, Patrick Minnis, David Mitchell, Kenneth Sassen, Matthew D Shupe, et al. An intercomparison of microphysical retrieval algorithms for upper-tropospheric ice clouds. *Bulletin of the American Meteorological Society*, 88(2):191–204, 2007.

A. J. Cox, Alan J. DeWeerd, and Jennifer Linden. An experiment to measure mie and rayleigh total scattering cross sections. *American Journal of Physics*, 70(6):620–625, 2002. doi: 10.1119/1.1466815. URL https://doi.org/10.1119/1.1466815.

S. C. Cox and W. H. Munk. Measurement of the roughness of the sea surface from photographs of the sun's glitter. *J. Opt. Soc. Amer.*, 44:838–850, 1954.

Daniel J. Cziczo, Karl D. Froyd, Corinna Hoose, Eric J. Jensen, Minghui Diao, Mark A. Zondlo, Jessica B. Smith, Cynthia H. Twohy, and Daniel M. Murphy. Clarifying the dominant sources and mechanisms of cirrus cloud formation. *Science*, 340(6138):1320–1324, 2013. doi: 10.1126/science.1234145. URL https://www.science.org/doi/abs/10.1126/science.1234145.

Ingrid Daubechies. Orthonormal bases of compactly supported wavelets. *Communications on Pure and Applied Mathematics*, 41(7):909–996, 1988. doi: https://doi.org/10.1002/cpa.3160410705. URL https://onlinelibrary.wiley.com/doi/abs/10.1002/cpa.3160410705.

Dick P Dee, SM Uppala, Adrian J Simmons, Paul Berrisford, Paul Poli, Shinya Kobayashi, U Andrae, MA Balmaseda, G Balsamo, d P Bauer, et al. The era-interim reanalysis: Configuration and performance of the data assimilation system. *Quarterly Journal of the royal meteorological society*, 137(656):553–597, 2011.

Julien Delanoë and Robin J Hogan. Combined cloudsat-calipso-modis retrievals of the properties of ice clouds. *Journal of Geophysical Research: Atmospheres*, 115(D4), 2010.

Julien Delanoë, Alain Protat, Olivier Jourdan, Jacques Pelon, Mathieu Papazzoni, Régis Dupuy, Jean-François Gayet, and Caroline Jouan. Comparison of airborne in situ, airborne radar–lidar, and spaceborne radar–lidar retrievals of polar ice cloud properties sampled during the polarcat campaign. *Journal of Atmospheric and Oceanic Technology*, 30(1): 57–73, 2013.

Julien Delanoë and Robin J. Hogan. A variational scheme for retrieving ice cloud properties from combined radar, lidar, and infrared radiometer. *Journal of Geophysical Research: Atmospheres*, 113(D7), 2008. doi: https://doi.org/10.1029/2007JD009000. URL `https://agupubs.onlinelibrary.wiley.com/doi/abs/10.1029/2007JD009000`.

P. J. DeMott, D. J. Cziczo, A. J. Prenni, D. M. Murphy, S. M. Kreidenweis, D. S. Thomson, R. Borys, and D. C. Rogers. Measurements of the concentration and composition of nuclei for cirrus formation. *Proceedings of the National Academy of Sciences*, 100(25):14655–14660, 2003. ISSN 0027-8424. doi: 10.1073/pnas.2532677100. URL `https://www.pnas.org/content/100/25/14655`.

Wolfgang Demtröder. *Atoms, molecules and photons*, volume 3. Springer, 2010.

Min Deng, Gerald G. Mace, Zhien Wang, and R. Paul Lawson. Evaluation of several a-train ice cloud retrieval products with in situ measurements collected during the sparticus campaign. *Journal of Applied Meteorology and Climatology*, 52(4):1014 – 1030, 2013. doi: 10.1175/JAMC-D-12-054.1. URL `https://journals.ametsoc.org/view/journals/apme/52/4/jamc-d-12-054.1.xml`.

Daniel H. DeSlover, William L. Smith, Paivi K. Piironen, and Edwin W. Eloranta. A methodology for measuring cirrus cloud visible-to-infrared spectral optical depth ratios. *Journal of Atmospheric and Oceanic Technology*, 16(2):251 – 262, 1999. doi: 10.1175/1520-0426(1999)016<0251:AMFMCC>2.0.CO;2. URL `https://journals.ametsoc.org/view/journals/atot/16/2/1520-0426_1999_016_0251_amfmcc_2_0_co_2.xml`.

A. E. Dessler, S. P. Palm, W. D. Hart, and J. D. Spinhirne. Tropopause-level thin cirrus coverage revealed by icesat/geoscience laser altimeter system. *Journal of Geophysical Research: Atmospheres*, 111(D8), 2006. doi: https://doi.org/10.1029/2005JD006586. URL `https://agupubs.onlinelibrary.wiley.com/doi/abs/10.1029/2005JD006586`.

DIN5031. Strahlungsphysik im optischen bereich und lichttechnik; benennung der wellenlängenbereiche. *Deutsches Institut für Normung (Hrsg.): DIN. 5031 Teil 7*, 1984.

DLR. Mira-36 cloud radar at schneefernerhaus, 2022. URL `http://www.pa.op.dlr.de/poldirad/ufsmira.html`. [Online; accessed 5-December-2022].

D. P. Donovan and A. C. A. P. van Lammeren. Cloud effective particle size and water content profile retrievals using combined lidar and radar observations: 1. theory and examples. *Journal of Geophysical Research: Atmospheres*, 106(D21):27425–27448, 2001. doi: https://doi.org/10.1029/2001JD900243. URL `https://agupubs.onlinelibrary.wiley.com/doi/abs/10.1029/2001JD900243`.

D. P. Donovan and A. C. A. P. van Lammeren. First ice cloud effective particle size parameterization based on combined lidar and radar data. *Geophysical Research Letters*, 29(1):6–1–6–4, 2002. doi: https://doi.org/10.1029/2001GL013731. URL https://agupubs.onlinelibrary.wiley.com/doi/abs/10.1029/2001GL013731.

D. P. Donovan, A. C. A. P. van Lammeren, R. J. Hogan, H. W. J. Russchenberg, A. Apituley, P. Francis, J. Testud, J. Pelon, M. Quante, and J. Goddard. Cloud effective particle size and water content profile retrievals using combined lidar and radar observations: 2. comparison with ir radiometer and in situ measurements of ice clouds. *Journal of Geophysical Research: Atmospheres*, 106(D21):27449–27464, 2001. doi: https://doi.org/10.1029/2001JD900241. URL https://agupubs.onlinelibrary.wiley.com/doi/abs/10.1029/2001JD900241.

David Patrick Donovan, Markus Quante, Ingo Schlimme, and Andreas Macke. Use of equivalent spheres to model the relation between radar reflectivity and optical extinction of ice cloud particles. *Appl. Opt.*, 43(25):4929–4940, Sep 2004. doi: 10.1364/AO.43.004929. URL http://www.osapublishing.org/ao/abstract.cfm?URI=ao-43-25-4929.

D.P Donovan, A.C.A.P Van Lammeren, R Hogan, H Russchenburg, A Apituley, P Francis, J Testud, J Pelon, M Quante, and J Agnew. Combined radar and lidar cloud remote sensing: Comparison with ir radiometer and in-situ measurements. *Physics and Chemistry of the Earth, Part B: Hydrology, Oceans and Atmosphere*, 25(10):1049–1055, 2000. ISSN 1464-1909. doi: https://doi.org/10.1016/S1464-1909(00)00151-9. URL https://www.sciencedirect.com/science/article/pii/S1464190900001519. First European Conference on Radar Meteorology.

DP Donovan, GJ van Zadelhoff, O Krasnov, E OĆonner, M Brooks, N Gaussiat, R Hogan, A Illingworth, D Bouniol, H Chepfer, J Delanoë, M Haeffelin, and Y Morille. Cloudnet report (deliverable 10 and wp-3): Development of retrieval algorithms (optimized algorithms and performance). 2005.

Richard J. Doviak and Dušan S. Zrnić. *Doppler Radar and Weather Observations (Second Edition)*. Academic Press, San Diego, second edition edition, 1993.

Eric Durieux and Luca Fiorani. Measurement of the lidar signal fluctuation with a shot-per-shot instrument. *Applied optics*, 37(30):7128–7131, 1998.

Marek Elbaum and Paul Diament. Snr in photocounting images of rough objects in partially coherent light. *Applied Optics*, 15(9):2268–2275, 1976.

Edwin W. Eloranta. Practical model for the calculation of multiply scattered lidar returns. *Appl. Opt.*, 37(12):2464–2472, Apr 1998. doi: 10.1364/AO.37.002464. URL http://opg.optica.org/ao/abstract.cfm?URI=ao-37-12-2464.

C. Emde, R. Buras-Schnell, A. Kylling, B. Mayer, J. Gasteiger, U. Hamann, J. Kylling, B. Richter, C. Pause, T. Dowling, and L. Bugliaro. The libradtran software package for radiative transfer calculations (version 2.0.1). *Geoscientific Model Development*, 9(5):1647–1672, 2016. doi: 10.5194/gmd-9-1647-2016. URL https://gmd.copernicus.org/articles/9/1647/2016/.

Ehsan Erfani and David L Mitchell. Developing and bounding ice particle mass-and area-dimension expressions for use in atmospheric models and remote sensing. *Atmospheric Chemistry and Physics*, 16(7):4379–4400, 2016.

Patrick Eriksson, SA Buehler, CP Davis, C Emde, and Oliver Lemke. Arts, the atmospheric radiative transfer simulator, version 2. *Journal of Quantitative Spectroscopy and Radiative Transfer*, 112(10):1551–1558, 2011.

F Esposito, G Grieco, G Masiello, G Pavese, R Restieri, C Serio, and V Cuomo. Intercomparison of line-parameter spectroscopic databases using downwelling spectral radiance. *Quarterly Journal of the Royal Meteorological Society: A journal of the atmospheric sciences, applied meteorology and physical oceanography*, 133(S3):191–202, 2007.

European-Space-Agency. Earthcare—earth clouds, aerosols and radiation explorer. esa/estec esa sp-1257 (1)—the five candidate earth explorer core missions. page 130 pp., 2001.

F. Ewald, T. Kölling, A. Baumgartner, T. Zinner, and B. Mayer. Design and characterization of specMACS, a multipurpose hyperspectral cloud and sky imager. *Atmospheric Measurement Techniques*, 9(5):2015–2042, 2016. doi: 10.5194/amt-9-2015-2016. URL `https://amt.copernicus.org/articles/9/2015/2016/`.

F. Ewald, S. Groß, M. Wirth, J. Delanoë, S. Fox, and B. Mayer. Why we need radar, lidar, and solar radiance observations to constrain ice cloud microphysics. *Atmospheric Measurement Techniques*, 14(7):5029–5047, 2021. doi: 10.5194/amt-14-5029-2021. URL `https://amt.copernicus.org/articles/14/5029/2021/`.

Florian Ewald. personal communication, 2019.

Florian Ewald, Silke Groß, Martin Hagen, Lutz Hirsch, Julien Delanoë, and Matthias Bauer-Pfundstein. Calibration of a 35 ghz airborne cloud radar: lessons learned and intercomparisons with 94 ghz cloud radars. *Atmospheric Measurement Techniques*, 12(3):1815–1839, 2019.

T Fauchez, S Platnick, O Sourdeval, C Wang, K Meyer, C Cornet, and Frédéric Szczap. Cirrus horizontal heterogeneity and 3-d radiative effects on cloud optical property retrievals from modis near to thermal infrared channels as a function of spatial resolution. *Journal of Geophysical Research: Atmospheres*, 123(19):11–141, 2018.

Frederick G. Fernald. Analysis of atmospheric lidar observations: some comments. *Appl. Opt.*, 23(5):652–653, Mar 1984. doi: 10.1364/AO.23.000652. URL `http://opg.optica.org/ao/abstract.cfm?URI=ao-23-5-652`.

Frederick G. Fernald, Benjamin M. Herman, and John A. Reagan. Determination of aerosol height distributions by lidar. *Journal of Applied Meteorology and Climatology*, 11(3):482 – 489, 1972. doi: 10.1175/1520-0450(1972)011<0482:DOAHDB>2.0.CO;2. URL `https://journals.ametsoc.org/view/journals/apme/11/3/1520-0450_1972_011_0482_doahdb_2_0_co_2.xml`.

P. R. Field and A. J. Heymsfield. Importance of snow to global precipitation. *Geophysical Research Letters*, 42(21):9512–9520, 2015. doi: https://doi.org/10.1002/2015GL065497. URL `https://agupubs.onlinelibrary.wiley.com/doi/abs/10.1002/2015GL065497`.

P. R. Field, R. J. Hogan, P. R. A. Brown, A. J. Illingworth, T. W. Choularton, P. H. Kaye, E. Hirst, and R. Greenaway. Simultaneous radar and aircraft observations of mixed-phase cloud at the 100 m scale. *Quarterly Journal of the Royal Meteorological Society*, 130(600):1877–1904, 2004. doi: https://doi.org/10.1256/qj.03.102. URL `https://rmets.onlinelibrary.wiley.com/doi/abs/10.1256/qj.03.102`.

Walter Findeisen. Kolloid-meteorologische vorgänge bei neiderschlags-bildung. *Meteor. Z*, 55: 121–133, 1938.

Joseph A Finlon, Greg M McFarquhar, Robert M Rauber, David M Plummer, Brian F Jewett, David Leon, and Kevin R Knupp. A comparison of x-band polarization parameters with in situ microphysical measurements in the comma head of two winter cyclones. *Journal of Applied Meteorology and Climatology*, 55(12):2549–2574, 2016.

E. Fontaine, A. Schwarzenboeck, J. Delanoë, W. Wobrock, D. Leroy, R. Dupuy, C. Gourbeyre, and A. Protat. Constraining mass–diameter relations from hydrometeor images and cloud radar reflectivities in tropical continental and oceanic convective anvils. *Atmospheric Chemistry and Physics*, 14(20):11367–11392, 2014. doi: 10.5194/acp-14-11367-2014. URL `https://acp.copernicus.org/articles/14/11367/2014/`.

J. S. Foot. Some observations of the optical properties of clouds. ii: Cirrus. *Quarterly Journal of the Royal Meteorological Society*, 114(479):145–164, 1988. doi: https://doi.org/10.1002/qj.49711447908. URL `https://rmets.onlinelibrary.wiley.com/doi/abs/10.1002/qj.49711447908`.

L. Forster, M. Seefeldner, M. Wiegner, and B. Mayer. Ice crystal characterization in cirrus clouds: a sun-tracking camera system and automated detection algorithm for halo displays. *Atmospheric Measurement Techniques*, 10(7):2499–2516, 2017. doi: 10.5194/amt-10-2499-2017. URL `https://amt.copernicus.org/articles/10/2499/2017/`.

P. Forster, T. Storelvmo, K. Armour, W. Collins, J.-L. Dufresne, D. Frame, D.J. Lunt, T. Mauritsen, M.D. Palmer, M. Watanabe, M. Wild, and H. Zhang. *The Earth's Energy Budget, Climate Feedbacks, and Climate Sensitivity*, book section 7, page X–Y. Cambridge University Press, Cambridge, United Kingdom and New York, NY, USA, 2021.

P. N. Francis, A. Jones, R. W. Saunders, K. P. Shine, A. Slingo, and Zhian Sun. An observational and theoretical study of the radiative properties of cirrus: Some results from ice'89. *Quarterly Journal of the Royal Meteorological Society*, 120(518):809–848, 1994. doi: https://doi.org/10.1002/qj.49712051804. URL `https://rmets.onlinelibrary.wiley.com/doi/abs/10.1002/qj.49712051804`.

PN Francis, P Hignett, and Andreas Macke. The retrieval of cirrus cloud properties from aircraft multi-spectral reflectance measurements during eucrex'93. *Quarterly Journal of the Royal Meteorological Society*, 124(548):1273–1291, 1998.

V. Freudenthaler, H. Linné, A. Chaikovski, D. Rabus, and S. Groß. Earlinet lidar quality assurance tools. *Atmospheric Measurement Techniques Discussions*, 2018:1–35, 2018. doi: 10.5194/amt-2017-395. URL `https://amt.copernicus.org/preprints/amt-2017-395/`.

Volker Freudenthaler. personal communication, 2019.

C Fröhlich and Glenn E Shaw. New determination of rayleigh scattering in the terrestrial atmosphere. *Applied Optics*, 19(11):1773–1775, 1980.

Qiang Fu and K. N. Liou. Parameterization of the radiative properties of cirrus clouds. *Journal of Atmospheric Sciences*, 50(13):2008 – 2025, 1993. doi: 10.1175/1520-0469(1993)050<2008:POTRPO>2.0.CO;2. URL https://journals.ametsoc.org/view/journals/atsc/50/13/1520-0469_1993_050_2008_potrpo_2_0_co_2.xml.

Qiang Fu and KN Liou. On the correlated k-distribution method for radiative transfer in nonhomogeneous atmospheres. *Journal of Atmospheric Sciences*, 49(22):2139–2156, 1992.

Qiang Fu, B Carlin, and G Mace. Cirrus horizontal inhomogeneity and olr bias. *Geophysical research letters*, 27(20):3341–3344, 2000.

J. P. Fugal and R. A. Shaw. Cloud particle size distributions measured with an airborne digital in-line holographic instrument. *Atmospheric Measurement Techniques*, 2(1):259–271, 2009. doi: 10.5194/amt-2-259-2009. URL https://amt.copernicus.org/articles/2/259/2009/.

Nimal Gamage and Carl Hagelberg. Detection and analysis of microfronts and associated coherent events using localized transforms. *Journal of Atmospheric Sciences*, 50(5):750 – 756, 1993. doi: 10.1175/1520-0469(1993)050<0750:DAAOMA>2.0.CO;2. URL https://journals.ametsoc.org/view/journals/atsc/50/5/1520-0469_1993_050_0750_daaoma_2_0_co_2.xml.

Blaž Gasparini and Ulrike Lohmann. Why cirrus cloud seeding cannot substantially cool the planet. *Journal of Geophysical Research: Atmospheres*, 121(9):4877–4893, 2016. doi: https://doi.org/10.1002/2015JD024666. URL https://agupubs.onlinelibrary.wiley.com/doi/abs/10.1002/2015JD024666.

J Gasteiger, Claudia Emde, Bernhard Mayer, Robertl Buras, SA Buehler, and Oliver Lemke. Representative wavelengths absorption parameterization applied to satellite channels and spectral bands. *Journal of Quantitative Spectroscopy and Radiative Transfer*, 148:99–115, 2014.

Nicolas Gaussiat, Henri Sauvageot, and Anthony J Illingworth. Cloud liquid water and ice content retrieval by multiwavelength radar. *Journal of Atmospheric and Oceanic Technology*, 20(9):1264–1275, 2003.

Andrew Gettelman, Hugh Morrison, and Greg Thompson. *Cloud Microphysics Across Scales for Weather and Climate*, pages 71–94. Springer Singapore, Singapore, 2019. ISBN 978-981-13-3396-5. doi: 10.1007/978-981-13-3396-5_4. URL https://doi.org/10.1007/978-981-13-3396-5_4.

K. Gierens and S. Brinkop. Dynamical characteristics of ice supersaturated regions. *Atmospheric Chemistry and Physics*, 12(24):11933–11942, 2012. doi: 10.5194/acp-12-11933-2012. URL https://acp.copernicus.org/articles/12/11933/2012/.

Google Maps. Zugspitze on Google Maps, imagery ©2023 cnes/airbus, geocontent, maxar technologies, map data ©2023 geobasics-de/bkg(©2009), 2023. URL https://goo.gl/maps/HvL7pqivCvRSodCEA. [Online; accessed 7-February-2023].

Diego Gouveia, Holger Baars, Patric Seifert, Ulla Wandinger, Henrique Barbosa, Boris Barja, Paulo Artaxo, Fabio Lopes, Eduardo Landulfo, and Albert Ansmann. Application of a multiple scattering model to estimate optical depth, lidar ratio and ice crystal effective radius of cirrus clouds observed with lidar. In *EPJ Web of Conferences*, volume 176, page 05037. EDP Sciences, 2018.

Thomas C. Grenfell, Steven P. Neshyba, and Stephen G. Warren. Representation of a nonspherical ice particle by a collection of independent spheres for scattering and absorption of radiation: 3. hollow columns and plates. *Journal of Geophysical Research: Atmospheres*, 110(D17), 2005. doi: https://doi.org/10.1029/2005JD005811. URL `https://agupubs.onlinelibrary.wiley.com/doi/abs/10.1029/2005JD005811`.

Peter R. Griffiths and James A. De Haseth. *Fourier transform infrared spectrometry*. Number ARRAY(0x55b5c5e98590) in Chemical analysis. Wiley-Interscience, Hoboken, NJ, 2. ed. edition, 2007. ISBN 0-471-19404-2 and 978-0-471-19404-0. Previous ed.: 1986 ; Literaturangaben.

A Grossman. R. kronland-martinet, and j. *Morlet," Reading and Understanding Continuous Wavelet Transforms," in Wavelets, Time-Frequency Mettds and Phase Space, JM Combes, A. Grossman, and Ph. Tchamitchian (Eds.). Springer-Verlag*, 1989.

Y. Gu, J. Farrara, K. N. Liou, and C. R. Mechoso. Parameterization of cloud–radiation processes in the ucla general circulation model. *Journal of Climate*, 16(20):3357 – 3370, 2003. doi: 10.1175/1520-0442(2003)016<3357:POCPIT>2.0.CO;2. URL `https://journals.ametsoc.org/view/journals/clim/16/20/1520-0442_2003_016_3357_pocpit_2.0.co_2.xml`.

Yu Gu and K. N. Liou. Cirrus cloud horizontal and vertical inhomogeneity effects in a gcm. *Meteorology and Atmospheric Physics*, 91(1):223–235, Jan 2006. ISSN 1436-5065. doi: 10.1007/s00703-004-0099-2. URL `https://doi.org/10.1007/s00703-004-0099-2`.

Guang Guo, Qiang Ji, Ping Yang, and Si-Chee Tsay. Remote sensing of cirrus optical and microphysical properties from ground-based infrared radiometric measurements-part ii: retrievals from crystal-face measurements. *IEEE Geoscience and Remote Sensing Letters*, 2 (2):132–135, 2005. doi: 10.1109/LGRS.2005.844734.

Ulrich Görsdorf, Volker Lehmann, Matthias Bauer-Pfundstein, Gerhard Peters, Dmytro Vavriv, Vladimir Vinogradov, and Vadim Volkov. A 35-ghz polarimetric doppler radar for long-term observations of cloud parameters—description of system and data processing. *Journal of Atmospheric and Oceanic Technology*, 32(4):675 – 690, 2015. doi: 10.1175/JTECH-D-14-00066.1. URL `https://journals.ametsoc.org/view/journals/atot/32/4/jtech-d-14-00066_1.xml`.

Seung-Hee Ham, Seiji Kato, and Fred G. Rose. Examining impacts of mass-diameter (m-d) and area-diameter (a-d) relationships of ice particles on retrievals of effective radius and ice water content from radar and lidar measurements. *Journal of Geophysical Research: Atmospheres*, 122(6):3396–3420, 2017. doi: https://doi.org/10.1002/2016JD025672. URL `https://agupubs.onlinelibrary.wiley.com/doi/abs/10.1002/2016JD025672`.

S. Häme, G. Saporano, N. Kivekäs, M. Kaukolehto, and E. Rodriguez, editors. *ACTRIS stakeholder handbook 2018*. 2018. ISBN 978-952-336-066-2. URL https://www.actris.eu/sites/default/files/Documents/ACTRIS%20PPP/Deliverables/ACTRIS%20PPP_WP1_D1.5_2nd%20ACTRIS%20Stakeholder%20Handbook.pdf.

James E Hansen and Larry D Travis. Light scattering in planetary atmospheres. *Space science reviews*, 16(4):527–610, 1974.

Axel Häring. Synergistic cloud observations with cloud radar and satellite instruments, 2016.

Dennis L. Hartmann, Maureen E. Ockert-Bell, and Marc L. Michelsen. The effect of cloud type on earth's energy balance: Global analysis. *Journal of Climate*, 5 (11):1281 – 1304, 1992. doi: 10.1175/1520-0442(1992)005<1281:TEOCTO>2.0.CO;2. URL https://journals.ametsoc.org/view/journals/clim/5/11/1520-0442_1992_005_1281_teocto_2_0_co_2.xml.

B. Heese, H. Flentje, D. Althausen, A. Ansmann, and S. Frey. Ceilometer lidar comparison: backscatter coefficient retrieval and signal-to-noise ratio determination. *Atmospheric Measurement Techniques*, 3(6):1763–1770, 2010. doi: 10.5194/amt-3-1763-2010. URL https://amt.copernicus.org/articles/3/1763/2010/.

Andrew Heymsfield, Dave Winker, Melody Avery, Mark Vaughan, Glenn Diskin, Min Deng, Valentin Mitev, and Renaud Matthey. Relationships between ice water content and volume extinction coefficient from in situ observations for temperatures from 0° to -86°c: Implications for spaceborne lidar retrievals. *Journal of Applied Meteorology and Climatology*, 53(2):479 – 505, 2014. doi: 10.1175/JAMC-D-13-087.1. URL https://journals.ametsoc.org/view/journals/apme/53/2/jamc-d-13-087.1.xml.

Andrew J. Heymsfield. On measurements of small ice particles in clouds. *Geophysical Research Letters*, 34(23), 2007. doi: https://doi.org/10.1029/2007GL030951. URL https://agupubs.onlinelibrary.wiley.com/doi/abs/10.1029/2007GL030951.

Andrew J. Heymsfield, Carl Schmitt, Aaron Bansemer, and Cynthia H. Twohy. Improved representation of ice particle masses based on observations in natural clouds. *Journal of the Atmospheric Sciences*, 67(10):3303 – 3318, 2010a. doi: 10.1175/2010JAS3507.1. URL https://journals.ametsoc.org/view/journals/atsc/67/10/2010jas3507.1.xml.

Andrew J. Heymsfield, Carl Schmitt, and Aaron Bansemer. Ice cloud particle size distributions and pressure-dependent terminal velocities from in situ observations at temperatures from 0° to -86°c. *Journal of the Atmospheric Sciences*, 70(12):4123 – 4154, 2013. doi: 10.1175/JAS-D-12-0124.1. URL https://journals.ametsoc.org/view/journals/atsc/70/12/jas-d-12-0124.1.xml.

Andrew J. Heymsfield, Martina Krämer, Anna Luebke, Phil Brown, Daniel J. Cziczo, Charmaine Franklin, Paul Lawson, Ulrike Lohmann, Greg McFarquhar, Zbigniew Ulanowski, and Kristof Van Tricht. Cirrus clouds. *Meteorological Monographs*, 58:2.1 – 2.26, 2017. doi: 10.1175/AMSMONOGRAPHS-D-16-0010.1. URL https://journals.ametsoc.org/view/journals/amsm/58/1/amsmonographs-d-16-0010.1.xml.

Gerald M. Heymsfield, Lin Tian, Andrew J. Heymsfield, Lihua Li, and Stephen Guimond. Characteristics of deep tropical and subtropical convection from nadir-viewing high-altitude airborne doppler radar. *Journal of the Atmospheric Sciences*, 67(2):285 – 308, 2010b. doi: 10.1175/2009JAS3132.1. URL https://journals.ametsoc.org/view/journals/atsc/67/2/2009jas3132.1.xml.

Edward E. Hindman and David B. Johnson. Numerical simulation of ice particle growth in a cloud of supercooled water droplets. *Journal of Atmospheric Sciences*, 29(7):1313 – 1321, 1972. doi: 10.1175/1520-0469(1972)029<1313:NSOIPG>2.0.CO;2. URL https://journals.ametsoc.org/view/journals/atsc/29/7/1520-0469_1972_029_1313_nsoipg_2_0_co_2.xml.

Walter Hitschfeld and Jack Bordan. Errors inherent in the radar measurement of rainfall at attenuating wavelengths. *Journal of the Atmospheric Sciences*, 11(1):58–67, 1954.

Stefan Hofer, Andrew J. Tedstone, Xavier Fettweis, and Jonathan L. Bamber. Cloud microphysics and circulation anomalies control differences in future greenland melt. *Nature Climate Change*, 9(7):523–528, Jul 2019. ISSN 1758-6798. doi: 10.1038/s41558-019-0507-8. URL https://doi.org/10.1038/s41558-019-0507-8.

Lars Hoffmann, Gebhard Günther, Dan Li, Olaf Stein, Xue Wu, Sabine Griessbach, Yi Heng, Paul Konopka, Rolf Müller, Bärbel Vogel, et al. From era-interim to era5: the considerable impact of ecmwf's next-generation reanalysis on lagrangian transport simulations. *Atmospheric Chemistry and Physics*, 19(5):3097–3124, 2019.

RJ Hogan, AJ Illingworth, EJ O'Connor, D Bouniol, ME Brooks, J Delanoë, DP Donovan, JD Eastment, N Gaussiat, JWF Goddard, et al. Cloudnet: Evaluation of model clouds using ground-based observations. In *Proceedings of the ECMWF Workshop on Parametrization of clouds in large-scale models, Reading, UK*, pages 13–15, 2006a.

Robin Hogan. What are the errors due to differences in the spaceborne radar and lidar footprints? (part i), 2001a. URL http://www.met.rdg.ac.uk/radar/esa/radarlidar.html. [Online; accessed 12-February-2022].

Robin Hogan. What are the errors due to differences in the spaceborne radar and lidar footprints? (part ii), 2001b. URL http://www.met.rdg.ac.uk/radar/esa/radarlidar2.html. [Online; accessed 12-February-2022].

Robin Hogan. What are the errors due to differences in the spaceborne radar and lidar footprints? (part iii), 2001c. URL http://www.met.rdg.ac.uk/radar/esa/radarlidar3.html. [Online; accessed 12-February-2022].

Robin Hogan and Ewan O'Connor. Facilitating cloud radar and lidar algorithms: the cloudnet instrument synergy/target categorization product. 2004a.

Robin J. Hogan. Fast approximate calculation of multiply scattered lidar returns. *Appl. Opt.*, 45(23):5984–5992, Aug 2006. doi: 10.1364/AO.45.005984. URL http://opg.optica.org/ao/abstract.cfm?URI=ao-45-23-5984.

Robin J. Hogan. Fast lidar and radar multiple-scattering models. part i: Small-angle scattering using the photon variance–covariance method. *Journal of the Atmospheric Sciences*, 65

(12):3621 – 3635, 2008. doi: 10.1175/2008JAS2642.1. URL https://journals.ametsoc.org/view/journals/atsc/65/12/2008jas2642.1.xml.

Robin J. Hogan and Alessandro Battaglia. Fast lidar and radar multiple-scattering models. part ii: Wide-angle scattering using the time-dependent two-stream approximation. *Journal of the Atmospheric Sciences*, 65(12):3636 – 3651, 2008. doi: 10.1175/2008JAS2643.1. URL https://journals.ametsoc.org/view/journals/atsc/65/12/2008jas2643.1.xml.

Robin J Hogan and Anthony J Illingworth. The potential of spaceborne dual-wavelength radar to make global measurements of cirrus clouds. *Journal of Atmospheric and Oceanic Technology*, 16(5):518–531, 1999.

Robin J Hogan and Anthony J Illingworth. Parameterizing ice cloud inhomogeneity and the overlap of inhomogeneities using cloud radar data. *Journal of the atmospheric sciences*, 60 (5):756–767, 2003.

Robin J Hogan and Ewan J O'Connor. Facilitating cloud radar and lidar algorithms: the cloudnet instrument synergy/target categorization product. *Cloudnet documentation*, 14, 2004b.

Robin J Hogan, Nicolas Gaussiat, and Anthony J Illingworth. Stratocumulus liquid water content from dual-wavelength radar. *Journal of Atmospheric and Oceanic Technology*, 22 (8):1207–1218, 2005.

Robin J. Hogan, Malcolm E. Brooks, Anthony J. Illingworth, David P. Donovan, Claire Tinel, Dominique Bouniol, and J. Pedro V. Poiares Baptista. Independent evaluation of the ability of spaceborne radar and lidar to retrieve the microphysical and radiative properties of ice clouds. *Journal of Atmospheric and Oceanic Technology*, 23(2):211 – 227, 2006b. doi: 10.1175/JTECH1837.1. URL https://journals.ametsoc.org/view/journals/atot/23/2/jtech1837_1.xml.

Robin J. Hogan, Marion P. Mittermaier, and Anthony J. Illingworth. The retrieval of ice water content from radar reflectivity factor and temperature and its use in evaluating a mesoscale model. *Journal of Applied Meteorology and Climatology*, 45(2):301 – 317, 2006c. doi: 10.1175/JAM2340.1. URL https://journals.ametsoc.org/view/journals/apme/45/2/jam2340.1.xml.

Hogan, R. J. Blind test of radar/lidar retrieval algorithms, 2003. URL http://www.met.rdg.ac.uk/radar/esa/blind_test.html. [Online; accessed 20-January-2022].

Gang Hong, Ping Yang, Bryan A. Baum, Andrew J. Heymsfield, and Kuan-Man Xu. Parameterization of shortwave and longwave radiative properties of ice clouds for use in climate models. *Journal of Climate*, 22(23):6287 – 6312, 2009. doi: 10.1175/2009JCLI2844.1. URL https://journals.ametsoc.org/view/journals/clim/22/23/2009jcli2844.1.xml.

Frédéric Hourdin, Thorsten Mauritsen, Andrew Gettelman, Jean-Christophe Golaz, Venkatramani Balaji, Qingyun Duan, Doris Folini, Duoying Ji, Daniel Klocke, Yun Qian, Florian Rauser, Catherine Rio, Lorenzo Tomassini, Masahiro Watanabe, and Daniel Williamson. The art and science of climate model tuning. *Bulletin of the American Meteorological Society*, 98(3):589 – 602, 2017. doi: 10.1175/BAMS-D-15-00135.1. URL https://journals.ametsoc.org/view/journals/bams/98/3/bams-d-15-00135.1.xml.

I. M. Howat, C. Porter, B. E. Smith, M.-J. Noh, and P. Morin. The reference elevation model of antarctica. *The Cryosphere*, 13(2):665–674, 2019. doi: 10.5194/tc-13-665-2019. URL https://tc.copernicus.org/articles/13/665/2019/.

Y. X. Hu and K. Stamnes. An accurate parameterization of the radiative properties of water clouds suitable for use in climate models. *Journal of Climate*, 6(4):728 – 742, 1993. doi: 10.1175/1520-0442(1993)006<0728:AAPOTR>2.0.CO;2. URL https://journals.ametsoc.org/view/journals/clim/6/4/1520-0442_1993_006_0728_aapotr_2_0_co_2.xml.

H. C. van de Hulst. *Light scattering by small particles*. Dover classics of science and mathematics. Dover Publ., New York, 1981. ISBN 0-486-64228-3 and 978-0-486-64228-4. Unabr. and corr. republication of the work originally published in 1957 by Wiley.

D. L. Hutt, L. R. Bissonnette, and L. Durand. Multiple field of view lidar returns from atmospheric aerosols. *Appl. Opt.*, 33(12):2338–2348, Apr 1994. doi: 10.1364/AO.33.002338. URL http://opg.optica.org/ao/abstract.cfm?URI=ao-33-12-2338.

A. J. Illingworth, R. J. Hogan, E.J. O'Connor, D. Bouniol, M. E. Brooks, J. Delanoé, D. P. Donovan, J. D. Eastment, N. Gaussiat, J. W. F. Goddard, M. Haeffelin, H. Klein Baltink, O. A. Krasnov, J. Pelon, J.-M. Piriou, A. Protat, H. W. J. Russchenberg, A. Seifert, A. M. Tompkins, G.-J. van Zadelhoff, F. Vinit, U. Willén, D. R. Wilson, and C. L. Wrench. Cloudnet: Continuous evaluation of cloud profiles in seven operational models using ground-based observations. *Bulletin of the American Meteorological Society*, 88(6):883 – 898, 2007a. doi: 10.1175/BAMS-88-6-883. URL https://journals.ametsoc.org/view/journals/bams/88/6/bams-88-6-883.xml.

A. J. Illingworth, R. J. Hogan, E.J. O'Connor, D. Bouniol, M. E. Brooks, J. Delanoé, D. P. Donovan, J. D. Eastment, N. Gaussiat, J. W. F. Goddard, M. Haeffelin, H. Klein Baltink, O. A. Krasnov, J. Pelon, J.-M. Piriou, A. Protat, H. W. J. Russchenberg, A. Seifert, A. M. Tompkins, G.-J. van Zadelhoff, F. Vinit, U. Willén, D. R. Wilson, and C. L. Wrench. Cloudnet: Continuous evaluation of cloud profiles in seven operational models using ground-based observations. *Bulletin of the American Meteorological Society*, 88(6):883 – 898, 2007b. doi: 10.1175/BAMS-88-6-883. URL https://journals.ametsoc.org/view/journals/bams/88/6/bams-88-6-883.xml.

A. J. Illingworth, H. W. Barker, A. Beljaars, M. Ceccaldi, H. Chepfer, N. Clerbaux, J. Cole, J. Delanoë, C. Domenech, D. P. Donovan, S. Fukuda, M. Hirakata, R. J. Hogan, A. Huenerbein, P. Kollias, T. Kubota, T. Nakajima, T. Y. Nakajima, T. Nishizawa, Y. Ohno, H. Okamoto, R. Oki, K. Sato, M. Satoh, M. W. Shephard, A. Velázquez-Blázquez, U. Wandinger, T. Wehr, and G.-J. van Zadelhoff. The earthcare satellite: The next step forward in global measurements of clouds, aerosols, precipitation, and radiation. *Bulletin of the American Meteorological Society*, 96(8):1311 – 1332, 2015. doi: 10.1175/BAMS-D-12-00227.1. URL https://journals.ametsoc.org/view/journals/bams/96/8/bams-d-12-00227.1.xml.

Anthony J. Illingworth and T. Mark Blackman. The need to represent raindrop size spectra as normalized gamma distributions for the interpretation of polarization radar observations. *Journal of Applied Meteorology*, 41(3):286 – 297, 2002. doi: 10.1175/1520-0450(2002)041<0286:TNTRRS>2.0.CO;2. URL https://journals.ametsoc.org/view/journals/apme/41/3/1520-0450_2002_041_0286_tntrrs_2.0.co_2.xml.

Janet M. Intrieri, Graeme L. Stephens, Wynn L. Eberhard, and Taneil Uttal. A method for determining cirrus cloud particle sizes using lidar and radar backscatter technique. *Journal of Applied Meteorology and Climatology*, 32(6):1074 – 1082, 1993. doi: 10.1175/1520-0450(1993)032<1074:AMFDCC>2.0.CO;2. URL https://journals.ametsoc.org/view/journals/apme/32/6/1520-0450_1993_032_1074_amfdcc_2_0_co_2.xml.

ITU. Attenuation by atmospheric gases. *Recommendation ITU-R*, pages 676–10, 2013. URL https://www.itu.int/dms_pubrec/itu-r/rec/p/R-REC-P.676-10-201309-S!!PDF-E.pdf.

Dorothea Ivanova, David L Mitchell, W.Patrick Arnott, and Michael Poellot. A gcm parameterization for bimodal size spectra and ice mass removal rates in mid-latitude cirrus clouds. *Atmospheric Research*, 59-60:89–113, 2001. ISSN 0169-8095. doi: https://doi.org/10.1016/S0169-8095(01)00111-9. URL https://www.sciencedirect.com/science/article/pii/S0169809501001119. 13th International Conference on Clouds and Precipitation.

Fredrik Jansson, Gijs Van Den Oord, Inti Pelupessy, Maria Chertova, Johanna H Grönqvist, A Pier Siebesma, and Daan Crommelin. Representing cloud mesoscale variability in superparameterized climate models. *Journal of Advances in Modeling Earth Systems*, 14(8): e2021MS002892, 2022.

Michael P Jensen, Donna J Holdridge, Petteri Survo, Raisa Lehtinen, Shannon Baxter, Tami Toto, and Karen L Johnson. Comparison of vaisala radiosondes rs41 and rs92 at the arm southern great plains site. *Atmospheric Measurement Techniques*, 9(7):3115–3129, 2016.

Gustav Robert Kirchhoff. *Untersuchungen über das Sonnenspectrum und die Spectren der chemischen Elemente*. Dümmler, 1866.

James D. Klett. Stable analytical inversion solution for processing lidar returns. *Appl. Opt.*, 20(2):211–220, Jan 1981. doi: 10.1364/AO.20.000211. URL http://opg.optica.org/ao/abstract.cfm?URI=ao-20-2-211.

James D Klett. Lidar inversion with variable backscatter/extinction ratios. *Applied optics*, 24(11):1638–1643, 1985.

Stefan Kneifel, MS Kulie, and R Bennartz. A triple-frequency approach to retrieve microphysical snowfall parameters. *Journal of Geophysical Research: Atmospheres*, 116(D11), 2011.

Stefan Kneifel, Annakaisa von Lerber, Jussi Tiira, Dmitri Moisseev, Pavlos Kollias, and Jussi Leinonen. Observed relations between snowfall microphysics and triple-frequency radar measurements. *Journal of Geophysical Research: Atmospheres*, 120(12):6034–6055, 2015.

R. O. Knuteson, H. E. Revercomb, F. A. Best, N. C. Ciganovich, R. G. Dedecker, T. P. Dirkx, S. C. Ellington, W. F. Feltz, R. K. Garcia, H. B. Howell, W. L. Smith, J. F. Short, and D. C. Tobin. Atmospheric emitted radiance interferometer. part i: Instrument design. *Journal of Atmospheric and Oceanic Technology*, 21(12):1763 – 1776, 2004a. doi: 10.1175/JTECH-1662.1. URL https://journals.ametsoc.org/view/journals/atot/21/12/jtech-1662_1.xml.

R. O. Knuteson, H. E. Revercomb, F. A. Best, N. C. Ciganovich, R. G. Dedecker, T. P. Dirkx, S. C. Ellington, W. F. Feltz, R. K. Garcia, H. B. Howell, W. L. Smith, J. F. Short, and D. C. Tobin. Atmospheric emitted radiance interferometer. part ii: Instrument performance. *Journal of Atmospheric and Oceanic Technology*, 21(12):1777 – 1789, 2004b. doi: 10.1175/JTECH-1663.1. URL https://journals.ametsoc.org/view/journals/atot/21/12/jtech-1663_1.xml.

L. R. Koenig. Numerical modeling of ice deposition. *Journal of Atmospheric Sciences*, 28(2):226 – 237, 1971. doi: 10.1175/1520-0469(1971)028<0226:NMOID>2.0.CO;2. URL https://journals.ametsoc.org/view/journals/atsc/28/2/1520-0469_1971_028_0226_nmoid_2_0_co_2.xml.

Alexander Kokhanovsky, editor. *Springer Series in Light Scattering*. Springer Series in Light Scattering. Springer International Publishing, Cham, 1st ed. 2021. edition, 2021. ISBN 978-3-030-71254-9. doi: 10.1007/978-3-030-71254-9. URL https://doi.org/10.1007/978-3-030-71254-9.

Heike Konow, Marek Jacob, Felix Ament, Susanne Crewell, Florian Ewald, Martin Hagen, Lutz Hirsch, Friedhelm Jansen, Mario Mech, and Bjorn Stevens. Halo microwave package measurements during next-generation remote sensing for validation studies - north (narval-north), 2018. URL https://doi.org/10.1594/WDCC/HALO_measurements_1.

A. Korolev, G. McFarquhar, P. R. Field, C. Franklin, P. Lawson, Z. Wang, E. Williams, S. J. Abel, D. Axisa, S. Borrmann, J. Crosier, J. Fugal, M. Krämer, U. Lohmann, O. Schlenczek, M. Schnaiter, and M. Wendisch. Mixed-phase clouds: Progress and challenges. *Meteorological Monographs*, 58:5.1 – 5.50, 2017. doi: 10.1175/AMSMONOGRAPHS-D-17-0001.1. URL https://journals.ametsoc.org/view/journals/amsm/58/1/amsmonographs-d-17-0001.1.xml.

Alexei V. Korolev and Ilia P. Mazin. Supersaturation of water vapor in clouds. *Journal of the Atmospheric Sciences*, 60(24):2957 – 2974, 2003. doi: 10.1175/1520-0469(2003)060<2957:SOWVIC>2.0.CO;2. URL https://journals.ametsoc.org/view/journals/atsc/60/24/1520-0469_2003_060_2957_sowvic_2.0.co_2.xml.

S. Kox, L. Bugliaro, and A. Ostler. Retrieval of cirrus cloud optical thickness and top altitude from geostationary remote sensing. *Atmospheric Measurement Techniques*, 7(10):3233–3246, 2014. doi: 10.5194/amt-7-3233-2014. URL https://amt.copernicus.org/articles/7/3233/2014/.

J. E. Kristjánsson, T. Iversen, A. Kirkevåg, Ø. Seland, and J. Debernard. Response of the climate system to aerosol direct and indirect forcing: Role of cloud feedbacks. *Journal of Geophysical Research: Atmospheres*, 110(D24), 2005. doi: https://doi.org/10.1029/2005JD006299. URL https://agupubs.onlinelibrary.wiley.com/doi/abs/10.1029/2005JD006299.

B. Kärcher, J. Hendricks, and U. Lohmann. Physically based parameterization of cirrus cloud formation for use in global atmospheric models. *Journal of Geophysical Research: Atmospheres*, 111(D1), 2006. doi: https://doi.org/10.1029/2005JD006219. URL https://agupubs.onlinelibrary.wiley.com/doi/abs/10.1029/2005JD006219.

K. M. Lau and H. T. Wu. Warm rain processes over tropical oceans and climate implications. *Geophysical Research Letters*, 30(24), 2003. doi: https://doi.org/10.1029/2003GL018567. URL https://agupubs.onlinelibrary.wiley.com/doi/abs/10.1029/2003GL018567.

David S. Lee, David W. Fahey, Piers M. Forster, Peter J. Newton, Ron C.N. Wit, Ling L. Lim, Bethan Owen, and Robert Sausen. Aviation and global climate change in the 21st century. *Atmospheric Environment*, 43(22):3520–3537, 2009a. ISSN 1352-2310. doi: https://doi.org/10.1016/j.atmosenv.2009.04.024. URL https://www.sciencedirect.com/science/article/pii/S1352231009003574.

Joonsuk Lee, Ping Yang, Andrew E. Dessler, Bo-Cai Gao, and Steven Platnick. Distribution and radiative forcing of tropical thin cirrus clouds. *Journal of the Atmospheric Sciences*, 66 (12):3721 – 3731, 2009b. doi: 10.1175/2009JAS3183.1. URL https://journals.ametsoc.org/view/journals/atsc/66/12/2009jas3183.1.xml.

Roger Lhermitte. Attenuation and scattering of millimeter wavelength radiation by clouds and precipitation. *Journal of Atmospheric and Oceanic Technology*, 7(3):464–479, 1990.

JL F Li, Kuan-Man Xu, Mark Richardson, Wei-Liang Lee, Jonathan H Jiang, Jia-Yuh Yu, Yi-Hui Wang, Eric Fetzer, Li-Chiao Wang, Graeme Stephens, et al. Annual and seasonal mean tropical and subtropical precipitation bias in cmip5 and cmip6 models. *Environmental Research Letters*, 15(12):124068, 2020.

Shunlin Liang. *Quantitative remote sensing of land surfaces*. Wiley series in remote sensing. Wiley-Interscience, Hoboken, NJ [u.a.], 2004. ISBN 0-471-28166-2 and 978-0-471-28166-5. Includes bibliographical references and index.

HJ Liebe, GA Hufford, and MG Cotton. Propagation modeling of moist air and suspended water/ice particles at frequencies below 1000 ghz. *In AGARD*, 1993.

K. N. Liou, Y. Gu, Q. Yue, and G. McFarguhar. On the correlation between ice water content and ice crystal size and its application to radiative transfer and general circulation models. *Geophysical Research Letters*, 35(13), 2008. doi: https://doi.org/10.1029/2008GL033918. URL https://agupubs.onlinelibrary.wiley.com/doi/abs/10.1029/2008GL033918.

Kuo-Nan Liou. Influence of cirrus clouds on weather and climate processes: A global perspective. *Monthly Weather Review*, 114(6):1167 – 1199, 1986. doi: 10.1175/1520-0493(1986)114<1167:IOCCOW>2.0.CO;2. URL https://journals.ametsoc.org/view/journals/mwre/114/6/1520-0493_1986_114_1167_ioccow_2_0_co_2.xml.

Kuo-Nan Liou and Ping Yang. *Light Scattering by Ice Crystals*, pages iii–iii. Cambridge University Press, 2016.

Run Liu, Hui Su, Kuo-Nan Liou, Jonathan H. Jiang, Yu Gu, Shaw Chen Liu, and Chein-Jung Shiu. An assessment of tropospheric water vapor feedback using radiative kernels. *Journal of Geophysical Research: Atmospheres*, 123(3):1499–1509, 2018. doi: https://doi.org/10.1002/2017JD027512. URL https://agupubs.onlinelibrary.wiley.com/doi/abs/10.1002/2017JD027512.

Gary Lloyd, Martin Gallagher, Thomas Choularton, Martina Krämer, Petzold Andreas, and Darrel Baumgardner. In situ measurements of cirrus clouds on a global scale. *Atmosphere*,

12(1), 2021. ISSN 2073-4433. doi: 10.3390/atmos12010041. URL https://www.mdpi.com/2073-4433/12/1/41.

Ulrike Lohmann, Felix Lüönd, and Fabian Mahrt. *An Introduction to Clouds: From the Microscale to Climate*. Cambridge University Press, 2016. doi: 10.1017/CBO9781139087513.

D. K. Lynch, K. Sassen, G. Stephens, and D. O. Starr. *Cirrus*. Oxford University Press Inc, New York, 2002. ISBN 978-0195130720.

Gerald G. Mace and Elizabeth Berry. Using active remote sensing to evaluate cloud-climate feedbacks: a review and a look to the future. *Current Climate Change Reports*, 3(3):185–192, Sep 2017. ISSN 2198-6061. doi: 10.1007/s40641-017-0067-9. URL https://doi.org/10.1007/s40641-017-0067-9.

AA Maryott and G Birnbaum. Collision-induced microwave absorption in compressed gases. i. dependence on density, temperature, and frequency in co2. *The Journal of Chemical Physics*, 36(8):2026–2032, 1962.

S. L. Mason, R. J. Hogan, A. Bozzo, and N. L. Pounder. A unified synergistic retrieval of clouds, aerosols, and precipitation from earthcare: the acm-cap product. *Atmospheric Measurement Techniques*, 16(13):3459–3486, 2023. doi: 10.5194/amt-16-3459-2023. URL https://amt.copernicus.org/articles/16/3459/2023/.

Sergey Y Matrosov, Alexei V Korolev, and Andrew J Heymsfield. Profiling cloud ice mass and particle characteristic size from doppler radar measurements. *Journal of Atmospheric and Oceanic Technology*, 19(7):1003–1018, 2002.

Sergey Y Matrosov, AJ Heymsfield, and Z Wang. Dual-frequency radar ratio of nonspherical atmospheric hydrometeors. *Geophysical research letters*, 32(13), 2005.

I. P Mattis and Wagner F. Clough. E-profile: Glossary of lidar and ceilometer variables. Technical report, 2014.

B. Mayer. Satellitengestützte verfahren zur ableitung von wolkenparametern. *Promet*, 36: 129 – 143, 2010. URL https://www.dwd.de/DE/leistungen/pbfb_verlag_promet/pdf_promethefte/36_3_4_pdf.pdf;jsessionid=B60B6AE40C484303EF25B6968117ED7B.live11042?__blob=publicationFile&v=10.

B. Mayer and A. Kylling. Technical note: The libradtran software package for radiative transfer calculations - description and examples of use. *Atmospheric Chemistry and Physics*, 5(7):1855–1877, 2005. doi: 10.5194/acp-5-1855-2005. URL https://acp.copernicus.org/articles/5/1855/2005/.

Mayer, B. Radiative transfer in the cloudy atmosphere. *EPJ Web of Conferences*, 1:75–99, 2009. doi: 10.1140/epjconf/e2009-00912-1. URL https://doi.org/10.1140/epjconf/e2009-00912-1.

Greg M. McFarquhar and Andrew J. Heymsfield. The definition and significance of an effective radius for ice clouds. *Journal of the Atmospheric Sciences*, 55(11):2039 – 2052, 1998. doi: 10.1175/1520-0469(1998)055<2039:TDASOA>2.0.CO;2. URL https://journals.ametsoc.org/view/journals/atsc/55/11/1520-0469_1998_055_2039_tdasoa_2.0.co_2.xml.

Greg M. McFarquhar, Darrel Baumgardner, Aaron Bansemer, Steven J. Abel, Jonathan Crosier, Jeff French, Phil Rosenberg, Alexei Korolev, Alfons Schwarzoenboeck, Delphine Leroy, Junshik Um, Wei Wu, Andrew J. Heymsfield, Cynthia Twohy, Andrew Detwiler, Paul Field, Andrea Neumann, Richard Cotton, Duncan Axisa, and Jiayin Dong. Processing of ice cloud in situ data collected by bulk water, scattering, and imaging probes: Fundamentals, uncertainties, and efforts toward consistency. *Meteorological Monographs*, 58:11.1 – 11.33, 2017a. doi: 10.1175/AMSMONOGRAPHS-D-16-0007.1. URL `https://journals.ametsoc.org/view/journals/amsm/58/1/amsmonographs-d-16-0007.1.xml`.

Greg M. McFarquhar, Darrel Baumgardner, and Andrew J. Heymsfield. Background and overview. *Meteorological Monographs*, 58:v – ix, 2017b. doi: 10.1175/AMSMONOGRAPHS-D-16-0018.1. URL `https://journals.ametsoc.org/view/journals/amsm/58/1/amsmonographs-d-16-0018.1.xml`.

M. Mech, M. Maahn, S. Kneifel, D. Ori, E. Orlandi, P. Kollias, V. Schemann, and S. Crewell. Pamtra 1.0: the passive and active microwave radiative transfer tool for simulating radiometer and radar measurements of the cloudy atmosphere. *Geoscientific Model Development*, 13(9):4229–4251, 2020. doi: 10.5194/gmd-13-4229-2020. URL `https://gmd.copernicus.org/articles/13/4229/2020/`.

Valery Melnikov. Parameters of cloud ice particles retrieved from radar data. *Journal of Atmospheric and Oceanic Technology*, 34(3):717–728, 2017.

Y. Meyer. Orthonormal wavelets. In Jean-Michel Combes, Alexander Grossmann, and Philippe Tchamitchian, editors, *Wavelets*, pages 21–37, Berlin, Heidelberg, 1989. Springer Berlin Heidelberg. ISBN 978-3-642-97177-8.

Albert A Michelson and Edward W Morley. On the relative motion of the earth and of the luminiferous ether. *Sidereal Messenger, vol. 6, pp. 306-310*, 6:306–310, 1887.

Gustav Mie. Beiträge zur optik trüber medien, speziell kolloidaler metallösungen. *Annalen der Physik*, 330(3):377–445, 1908. doi: https://doi.org/10.1002/andp.19083300302. URL `https://onlinelibrary.wiley.com/doi/abs/10.1002/andp.19083300302`.

M. A. Miller, K. Nitschke, T. P. Ackerman, W. R. Ferrell, N. Hickmon, and M. Ivey. The arm mobile facilities. *Meteorological Monographs*, 57:9.1 – 9.15, 2016. doi: 10.1175/AMSMONOGRAPHS-D-15-0051.1. URL `https://journals.ametsoc.org/view/journals/amsm/57/1/amsmonographs-d-15-0051.1.xml`.

M. I. Mishchenko. Light scattering by randomly oriented axially symmetric particles. *J. Opt. Soc. Am. A*, 8(6):871–882, Jun 1991. doi: 10.1364/JOSAA.8.000871. URL `http://www.osapublishing.org/josaa/abstract.cfm?URI=josaa-8-6-871`.

Michael I. Mishchenko. Vector radiative transfer equation for arbitrarily shaped and arbitrarily oriented particles: a microphysical derivation from statistical electromagnetics. *Appl. Opt.*, 41(33):7114–7134, Nov 2002. doi: 10.1364/AO.41.007114. URL `http://opg.optica.org/ao/abstract.cfm?URI=ao-41-33-7114`.

Michael I. Mishchenko. “independent” and “dependent” scattering by particles in a multi-particle group. *OSA Continuum*, 1(1):243–260, Sep 2018.

doi: 10.1364/OSAC.1.000243. URL http://www.osapublishing.org/osac/abstract.cfm?URI=osac-1-1-243.

Michael I. Mishchenko and Larry D. Travis. T-matrix computations of light scattering by large spheroidal particles. *Optics Communications*, 109(1):16–21, 1994. ISSN 0030-4018. doi: https://doi.org/10.1016/0030-4018(94)90731-5. URL https://www.sciencedirect.com/science/article/pii/0030401894907315.

David L. Mitchell. Effective diameter in radiation transfer: General definition, applications, and limitations. *Journal of the Atmospheric Sciences*, 59(15):2330 – 2346, 2002. doi: 10.1175/1520-0469(2002)059<2330:EDIRTG>2.0.CO;2. URL https://journals.ametsoc.org/view/journals/atsc/59/15/1520-0469_2002_059_2330_edirtg_2.0.co_2.xml.

David L. Mitchell, Steven K. Chai, Yangang Liu, Andrew J. Heymsfield, and Yayi Dong. Modeling cirrus clouds. part i: Treatment of bimodal size spectra and case study analysis. *Journal of Atmospheric Sciences*, 53(20):2952 – 2966, 1996a. doi: 10.1175/1520-0469(1996)053<2952:MCCPIT>2.0.CO;2. URL https://journals.ametsoc.org/view/journals/atsc/53/20/1520-0469_1996_053_2952_mccpit_2_0_co_2.xml.

David L. Mitchell, Yangang Liu, and Andreas Macke. Modeling cirrus clouds. part ii: Treatment of radiative properties. *Journal of Atmospheric Sciences*, 53(20):2967 – 2988, 1996b. doi: 10.1175/1520-0469(1996)053<2967:MCCPIT>2.0.CO;2. URL https://journals.ametsoc.org/view/journals/atsc/53/20/1520-0469_1996_053_2967_mccpit_2_0_co_2.xml.

David L. Mitchell, Philip Rasch, Dorothea Ivanova, Greg McFarquhar, and Timo Nousiainen. Impact of small ice crystal assumptions on ice sedimentation rates in cirrus clouds and gcm simulations. *Geophysical Research Letters*, 35(9), 2008. doi: https://doi.org/10.1029/2008GL033552. URL https://agupubs.onlinelibrary.wiley.com/doi/abs/10.1029/2008GL033552.

Hugh Morrison, Marcus van Lier-Walqui, Ann M. Fridlind, Wojciech W. Grabowski, Jerry Y. Harrington, Corinna Hoose, Alexei Korolev, Matthew R. Kumjian, Jason A. Milbrandt, Hanna Pawlowska, Derek J. Posselt, Olivier P. Prat, Karly J. Reimel, Shin-Ichiro Shima, Bastiaan van Diedenhoven, and Lulin Xue. Confronting the challenge of modeling cloud and precipitation microphysics. *Journal of Advances in Modeling Earth Systems*, 12(8):e2019MS001689, 2020. doi: https://doi.org/10.1029/2019MS001689. URL https://agupubs.onlinelibrary.wiley.com/doi/abs/10.1029/2019MS001689. e2019MS001689 2019MS001689.

K. Mroz, B. P. Treserras, A. Battaglia, P. Kollias, A. Tatarevic, and F. Tridon. Cloud and precipitation microphysical retrievals from the earthcare cloud profiling radar: the c-cld product. *Atmospheric Measurement Techniques*, 16(11):2865–2888, 2023. doi: 10.5194/amt-16-2865-2023. URL https://amt.copernicus.org/articles/16/2865/2023/.

Alexander Myagkov, Patric Seifert, Ulla Wandinger, Johannes Bühl, and Ronny Engelmann. Relationship between temperature and apparent shape of pristine ice crystals derived from polarimetric cloud radar observations during the accept campaign. *Atmospheric Measurement Techniques*, 9(8):3739–3754, 2016.

G. Myhre, D. Shindell, F.-M. Bréon, W. Collins, J. Fuglestvedt, J. Huang, D. Koch, J.-F. Lamarque, D. Lee, B. Mendoza, T. Nakajima, A. Robock, G. Stephens, T. Takemura, and H. Zhang. *Anthropogenic and Natural Radiative Forcing*, book section 8, page 659–740. Cambridge University Press, Cambridge, United Kingdom and New York, NY, USA, 2013. ISBN ISBN 978-1-107-66182-0. doi: 10.1017/CBO9781107415324.018. URL www.climatechange2013.org.

Johannes Mülmenstädt, O. Sourdeval, J. Delanoë, and J. Quaas. Frequency of occurrence of rain from liquid-, mixed-, and ice-phase clouds derived from a-train satellite retrievals. *Geophysical Research Letters*, 42(15):6502–6509, 2015. doi: https://doi.org/10.1002/2015GL064604. URL https://agupubs.onlinelibrary.wiley.com/doi/abs/10.1002/2015GL064604.

Teruyuki Nakajima and Michael D. King. Determination of the optical thickness and effective particle radius of clouds from reflected solar radiation measurements. part i: Theory. *Journal of Atmospheric Sciences*, 47(15):1878 – 1893, 1990. doi: 10.1175/1520-0469(1990)047<1878:DOTOTA>2.0.CO;2. URL https://journals.ametsoc.org/view/journals/atsc/47/15/1520-0469_1990_047_1878_dotota_2_0_co_2.xml.

J. Nelson. Growth mechanisms to explain the primary and secondary habits of snow crystals. *Philosophical Magazine A*, 81(10):2337–2373, 2001. doi: 10.1080/01418610108217152. URL https://doi.org/10.1080/01418610108217152.

Joel R. Norris, Robert J. Allen, Amato T. Evan, Mark D. Zelinka, Christopher W. O'Dell, and Stephen A. Klein. Evidence for climate change in the satellite cloud record. *Nature*, 536(7614):72–75, Aug 2016. ISSN 1476-4687. doi: 10.1038/nature18273. URL https://doi.org/10.1038/nature18273.

Tomoki Ohno, Masaki Satoh, and Akira Noda. Fine vertical resolution radiative-convective equilibrium experiments: Roles of turbulent mixing on the high-cloud response to sea surface temperatures. *Journal of Advances in Modeling Earth Systems*, 11(6):1637–1654, 2019. doi: https://doi.org/10.1029/2019MS001704. URL https://agupubs.onlinelibrary.wiley.com/doi/abs/10.1029/2019MS001704.

Hajime Okamoto, Suginori Iwasaki, Motoaki Yasui, Hiroaki Horie, Hiroshi Kuroiwa, and Hiroshi Kumagai. An algorithm for retrieval of cloud microphysics using 95-ghz cloud radar and lidar. *Journal of Geophysical Research: Atmospheres*, 108(D7), 2003.

Hajime Okamoto, Kaori Sato, Anatoli Borovoi, Hiroshi Ishimoto, Kazuhiko Masuda, Alexander Konoshonkin, and Natalia Kustova. Wavelength dependence of ice cloud backscatter properties for space-borne polarization lidar applications. *Optics Express*, 28(20):29178–29191, 2020.

Grant W. Petty. *A first course in atmospheric radiation.* Sundog Publ., Madison, 2. ed. edition, 2006. ISBN 0-9729033-1-3 and 978-0-9729033-1-8.

M Planck. Zur theorie des gesetzes der energieverteilung im normalspectrumverhandlungen der deutschen physikalischen gesellschaft2, 237–45. *English translation by D. ter Haar 1967The Old Quantum Theory (PergamonPress]*, 1900.

C. M. R. Platt. Lidar and radiometric observations of cirrus clouds. *Journal of Atmospheric Sciences*, 30(6):1191 – 1204, 1973. doi: 10.1175/1520-0469(1973)030<1191:LAROOC>2.0.CO;2. URL https://journals.ametsoc.org/view/journals/atsc/30/6/1520-0469_1973_030_1191_larooc_2_0_co_2.xml.

C. M. R. Platt. Remote sounding of high clouds. iii: Monte carlo calculations of multiple-scattered lidar returns. *Journal of Atmospheric Sciences*, 38(1):156 – 167, 1981. doi: 10.1175/1520-0469(1981)038<0156:RSOHCI>2.0.CO;2. URL https://journals.ametsoc.org/view/journals/atsc/38/1/1520-0469_1981_038_0156_rsohci_2_0_co_2.xml.

J. R. Probert-Jones. The radar equation in meteorology. *Quarterly Journal of the Royal Meteorological Society*, 88(378):485–495, 1962. doi: https://doi.org/10.1002/qj.49708837810. URL https://rmets.onlinelibrary.wiley.com/doi/abs/10.1002/qj.49708837810.

Alain Protat, A Armstrong, Martial Haeffelin, Yohann Morille, Jacques Pelon, Julien Delanoë, and Dominique Bouniol. Impact of conditional sampling and instrumental limitations on the statistics of cloud properties derived from cloud radar and lidar at sirta. *Geophysical research letters*, 33(11), 2006.

Hans R. Pruppacher and James D. Klett. *Microphysics of clouds and precipitation*. Number ARRAY(0x564da06fa148) in Atmospheric and oceanographic sciences library. Springer, Dordrecht ; Heidelberg [u.a.], 2., rev. and enl. ed., [nachdr.] edition, 2010. ISBN 978-0-7923-4211-3.

Stefan Rahmstorf. A new view on sea level rise. *Nature Climate Change*, 1(1004):44–45, Apr 2010. ISSN 1758-6798. doi: 10.1038/climate.2010.29. URL https://doi.org/10.1038/climate.2010.29.

D.A. Randall, R.A. Wood, S. Bony, R. Colman, T. Fichefet, J. Fyfe, V. Kattsov, A. Pitman, J. Shukla, J. Srinivasan, R.J. Stouffer, A. Sumi, and K.E. Taylor. *Climate Models and Their Evaluation*, book section 8, page 589–662. Cambridge University Press, Cambridge, United Kingdom and New York, NY, USA, 2007. doi: 10.1017/CBO9781107415324.016. URL www.climatechange2013.org.

David A Randall. *General circulation model development: past, present, and future*. Elsevier, 2000.

A. Reichert, M. Rettinger, and R. Sussmann. The zugspitze radiative closure experiment for quantifying water vapor absorption over the terrestrial and solar infrared – part 2: Accurate calibration of high spectral-resolution infrared measurements of surface solar radiation. *Atmospheric Measurement Techniques*, 9(9):4673–4686, 2016. doi: 10.5194/amt-9-4673-2016. URL https://amt.copernicus.org/articles/9/4673/2016/.

Andreas Reichert and Ralf Sussmann. The zugspitze radiative closure experiment for quantifying water vapor absorption over the terrestrial and solar infrared–part 3: Quantification of the mid-and near-infrared water vapor continuum in the 2500 to 7800 cm- 1 spectral range under atmospheric conditions. *Atmospheric Chemistry and Physics*, 16(18):11671–11686, 2016.

Tong Ren, Dongchen Li, Jake Muller, and Ping Yang. Sensitivity of radiative flux simulations to ice cloud parameterization over the equatorial western pacific ocean region. *Journal of the Atmospheric Sciences*, 78(8):2549–2571, 2021.

Markus Rettinger. personal communication, 2019.

Henry E. Revercomb, H. Buijs, Hugh B. Howell, D. D. LaPorte, William L. Smith, and L. A. Sromovsky. Radiometric calibration of ir fourier transform spectrometers: solution to a problem with the high-resolution interferometer sounder. *Appl. Opt.*, 27(15):3210–3218, Aug 1988. doi: 10.1364/AO.27.003210. URL `http://opg.optica.org/ao/abstract.cfm?URI=ao-27-15-3210`.

Jacobo Riccati. Animadversiones in aequationes differentiales secundi gradus. *Actorum Eruditorum Supplementa*, 8(1724):66–73, 1724.

Ronald E Rinehart. *Radar for meteorologists*. University of North Dakota, Office of the President, 1991.

Erich Roeckner, G Bäuml, Luca Bonaventura, Renate Brokopf, Monika Esch, Marco Giorgetta, Stefan Hagemann, Ingo Kirchner, Luis Kornblueh, Elisa Manzini, et al. The atmospheric general circulation model echam 5. part i: Model description. 2003.

D. Rosenfeld, E. Williams, M. O. Andreae, E. Freud, U. Pöschl, and N. O. Rennó. The scientific basis for a satellite mission to retrieve ccn concentrations and their impacts on convective clouds. *Atmospheric Measurement Techniques*, 5(8):2039–2055, 2012. doi: 10.5194/amt-5-2039-2012. URL `https://amt.copernicus.org/articles/5/2039/2012/`.

Laurence S Rothman, Iouli E Gordon, Alain Barbe, D Chris Benner, Peter F Bernath, Manfred Birk, Vincent Boudon, Linda R Brown, Alain Campargue, J-P Champion, et al. The hitran 2008 molecular spectroscopic database. *Journal of Quantitative Spectroscopy and Radiative Transfer*, 110(9-10):533–572, 2009.

L.S. Rothman, D. Jacquemart, A. Barbe, D. Chris Benner, M. Birk, L.R. Brown, M.R. Carleer, C. Chackerian, K. Chance, L.H. Coudert, V. Dana, V.M. Devi, J.-M. Flaud, R.R. Gamache, A. Goldman, J.-M. Hartmann, K.W. Jucks, A.G. Maki, J.-Y. Mandin, S.T. Massie, J. Orphal, A. Perrin, C.P. Rinsland, M.A.H. Smith, J. Tennyson, R.N. Tolchenov, R.A. Toth, J. Vander Auwera, P. Varanasi, and G. Wagner. The hitran 2004 molecular spectroscopic database. *Journal of Quantitative Spectroscopy and Radiative Transfer*, 96 (2):139–204, 2005. ISSN 0022-4073. doi: https://doi.org/10.1016/j.jqsrt.2004.10.008. URL `https://www.sciencedirect.com/science/article/pii/S0022407305001081`.

Masanori Saito, Ping Yang, Lei Bi, Jens Reichardt, Bastiaan Van Diedenhoven, Kaori Sato, and Zhien Wang. Quantifying the impact of the surface roughness of ice crystals on the backscattering properties for lidar-based remote sensing applications. *Authorea Preprints*, 2022.

Yasuhiro Sasano, Edward V. Browell, and Syed Ismail. Error caused by using a constant extinction/backscattering ratio in the lidar solution. *Appl. Opt.*, 24(22):3929–3932, Nov 1985. doi: 10.1364/AO.24.003929. URL `http://opg.optica.org/ao/abstract.cfm?URI=ao-24-22-3929`.

Kenneth Sassen, Zhien Wang, and Dong Liu. Global distribution of cirrus clouds from cloudsat/cloud-aerosol lidar and infrared pathfinder satellite observations (calipso) measurements. *Journal of Geophysical Research: Atmospheres*, 113(D8), 2008. doi: https://doi.org/10.1029/2008JD009972. URL https://agupubs.onlinelibrary.wiley.com/doi/abs/10.1029/2008JD009972.

Kaori Sato and Hajime Okamoto. Characterization of ze and ldr of nonspherical and inhomogeneous ice particles for 95-ghz cloud radar: Its implication to microphysical retrievals. *Journal of Geophysical Research: Atmospheres*, 111(D22), 2006. doi: https://doi.org/10.1029/2005JD006959. URL https://agupubs.onlinelibrary.wiley.com/doi/abs/10.1029/2005JD006959.

Willi Schimmel, Heike Kalesse-Los, Maximilian Maahn, Teresa Vogl, Andreas Foth, Pablo Saavedra Garfias, and Patric Seifert. Identifying cloud droplets beyond lidar attenuation from vertically pointing cloud radar observations using artificial neural networks. *Atmospheric Measurement Techniques*, 15(18):5343–5366, 2022.

G. A. Schmidt, D. Bader, L. J. Donner, G. S. Elsaesser, J.-C. Golaz, C. Hannay, A. Molod, R. B. Neale, and S. Saha. Practice and philosophy of climate model tuning across six us modeling centers. *Geoscientific Model Development*, 10(9):3207–3223, 2017. doi: 10.5194/gmd-10-3207-2017. URL https://gmd.copernicus.org/articles/10/3207/2017/.

Tapio Schneider, Colleen M. Kaul, and Kyle G. Pressel. Possible climate transitions from breakup of stratocumulus decks under greenhouse warming. *Nature Geoscience*, 12(3):163–167, Mar 2019. ISSN 1752-0908. doi: 10.1038/s41561-019-0310-1. URL https://doi.org/10.1038/s41561-019-0310-1.

Andreas Schäfler, George Craig, Heini Wernli, Philippe Arbogast, James D. Doyle, Ron McTaggart-Cowan, John Methven, Gwendal Rivière, Felix Ament, Maxi Boettcher, Martina Bramberger, Quitterie Cazenave, Richard Cotton, Susanne Crewell, Julien Delanoë, Andreas Dörnbrack, André Ehrlich, Florian Ewald, Andreas Fix, Christian M. Grams, Suzanne L. Gray, Hans Grob, Silke Groß, Martin Hagen, Ben Harvey, Lutz Hirsch, Marek Jacob, Tobias Kölling, Heike Konow, Christian Lemmerz, Oliver Lux, Linus Magnusson, Bernhard Mayer, Mario Mech, Richard Moore, Jacques Pelon, Julian Quinting, Stephan Rahm, Markus Rapp, Marc Rautenhaus, Oliver Reitebuch, Carolyn A. Reynolds, Harald Sodemann, Thomas Spengler, Geraint Vaughan, Manfred Wendisch, Martin Wirth, Benjamin Witschas, Kevin Wolf, and Tobias Zinner. The north atlantic waveguide and downstream impact experiment. *Bulletin of the American Meteorological Society*, 99(8):1607 – 1637, 2018. doi: 10.1175/BAMS-D-17-0003.1. URL https://journals.ametsoc.org/view/journals/bams/99/8/bams-d-17-0003.1.xml.

Axel Seifert and Klaus D. Beheng. A double-moment parameterization for simulating autoconversion, accretion and selfcollection. *Atmospheric Research*, 59-60:265–281, 2001. ISSN 0169-8095. doi: https://doi.org/10.1016/S0169-8095(01)00126-0. URL https://www.sciencedirect.com/science/article/pii/S0169809501001260. 13th International Conference on Clouds and Precipitation.

Raymond A. Shaw, Adam J. Durant, and Youshi Mi. Heterogeneous surface crystallization observed in undercooled water. *The Journal of Physical Chemistry B*, 109(20):9865–9868,

May 2005. ISSN 1520-6106. doi: 10.1021/jp0506336. URL https://doi.org/10.1021/jp0506336.

A. Pier Siebesma, Sandrine Bony, Christian Jakob, and Bjorn Stevens, editors. *Clouds and Climate: Climate Science's Greatest Challenge*. Cambridge University Press, Cambridge, 2020. ISBN 9781107061071. doi: 10.1017/9781107447738. URL https://doi.org/10.1017/9781107447738.

I. Silber, R. C. Jackson, A. M. Fridlind, A. S. Ackerman, S. Collis, J. Verlinde, and J. Ding. The earth model column collaboratory (emc^2) v1.1: an open-source ground-based lidar and radar instrument simulator and subcolumn generator for large-scale models. *Geoscientific Model Development*, 15(2):901–927, 2022. doi: 10.5194/gmd-15-901-2022. URL https://gmd.copernicus.org/articles/15/901/2022/.

Knut Stamnes, S-Chee Tsay, Warren Wiscombe, and Kolf Jayaweera. Numerically stable algorithm for discrete-ordinate-method radiative transfer in multiple scattering and emitting layered media. *Appl. Opt.*, 27(12):2502–2509, Jun 1988. doi: 10.1364/AO.27.002502. URL http://opg.optica.org/ao/abstract.cfm?URI=ao-27-12-2502.

Knut Stamnes, Si-Chee Tsay, Warren Wiscombe, and Istvan Laszlo. Disort, a general-purpose fortran program for discrete-ordinate-method radiative transfer in scattering and emitting layered media: documentation of methodology. 2000.

Knut H. Stamnes, Gary E. Thomas, and Jakob J. Stamnes. *Radiative transfer in the atmosphere and ocean*. Cambridge University Press, Cambridge, United Kingdom, second edition edition, 2017. ISBN 978-1-107-09473-4. Previous edition: published as by Gary E. Thomas and Knut Stamnes. 1999.

KRGE Stamnes, RG Ellingson, JA Curry, JE Walsh, and BD Zak. Review of science issues, deployment strategy, and status for the arm north slope of alaska–adjacent arctic ocean climate research site. *Journal of Climate*, 12(1):46–63, 1999.

Thorwald H. M. Stein, Julien Delanoë, and Robin J. Hogan. A comparison among four different retrieval methods for ice-cloud properties using data from cloudsat, calipso, and modis. *Journal of Applied Meteorology and Climatology*, 50(9):1952 – 1969, 2011. doi: 10.1175/2011JAMC2646.1. URL https://journals.ametsoc.org/view/journals/apme/50/9/2011jamc2646.1.xml.

Graeme L. Stephens, Deborah G. Vane, Ronald J. Boain, Gerald G. Mace, Kenneth Sassen, Zhien Wang, Anthony J. Illingworth, Ewan J. O'connor, William B. Rossow, Stephen L. Durden, Steven D. Miller, Richard T. Austin, Angela Benedetti, and Cristian Mitrescu. The cloudsat mission and the a-train: A new dimension of space-based observations of clouds and precipitation. *Bulletin of the American Meteorological Society*, 83(12):1771–1790, 2002. doi: 10.1175/BAMS-83-12-1771. URL https://doi.org/10.1175/BAMS-83-12-1771.

Graeme L. Stephens, Juilin Li, Martin Wild, Carol Anne Clayson, Norman Loeb, Seiji Kato, Tristan L'Ecuyer, Paul W. Stackhouse, Matthew Lebsock, and Timothy Andrews. An update on earth's energy balance in light of the latest global observations. *Nature Geoscience*, 5(10):691–696, Oct 2012. ISSN 1752-0908. doi: 10.1038/ngeo1580. URL https://doi.org/10.1038/ngeo1580.

Bjorn Stevens, Marco Giorgetta, Monika Esch, Thorsten Mauritsen, Traute Crueger, Sebastian Rast, Marc Salzmann, Hauke Schmidt, Jürgen Bader, Karoline Block, Renate Brokopf, Irina Fast, Stefan Kinne, Luis Kornblueh, Ulrike Lohmann, Robert Pincus, Thomas Reichler, and Erich Roeckner. Atmospheric component of the mpi-m earth system model: Echam6. *Journal of Advances in Modeling Earth Systems*, 5(2):146–172, 2013. doi: https://doi.org/10.1002/jame.20015. URL `https://agupubs.onlinelibrary.wiley.com/doi/abs/10.1002/jame.20015`.

Bjorn Stevens, Steven C. Sherwood, Sandrine Bony, and Mark J. Webb. Prospects for narrowing bounds on earth's equilibrium climate sensitivity. *Earth's Future*, 4(11):512–522, 2016. doi: https://doi.org/10.1002/2016EF000376. URL `https://agupubs.onlinelibrary.wiley.com/doi/abs/10.1002/2016EF000376`.

Bjorn Stevens, Felix Ament, Sandrine Bony, Susanne Crewell, Florian Ewald, Silke Gross, Akio Hansen, Lutz Hirsch, Marek Jacob, Tobias Kölling, Heike Konow, Bernhard Mayer, Manfred Wendisch, Martin Wirth, Kevin Wolf, Stephan Bakan, Matthias Bauer-Pfundstein, Matthias Brueck, Julien Delanoë, André Ehrlich, David Farrell, Marvin Forde, Felix Gödde, Hans Grob, Martin Hagen, Evelyn Jäkel, Friedhelm Jansen, Christian Klepp, Marcus Klingebiel, Mario Mech, Gerhard Peters, Markus Rapp, Allison A. Wing, and Tobias Zinner. A high-altitude long-range aircraft configured as a cloud observatory: The narval expeditions. *Bulletin of the American Meteorological Society*, 100(6):1061 – 1077, 2019. doi: 10.1175/BAMS-D-18-0198.1. URL `https://journals.ametsoc.org/view/journals/bams/100/6/bams-d-18-0198.1.xml`.

Gerald M. Stokes and Stephen E. Schwartz. The atmospheric radiation measurement (arm) program: Programmatic background and design of the cloud and radiation test bed. *Bulletin of the American Meteorological Society*, 75(7):1201 – 1222, 1994. doi: 10.1175/1520-0477(1994)075<1201:TARMPP>2.0.CO;2. URL `https://journals.ametsoc.org/view/journals/bams/75/7/1520-0477_1994_075_1201_tarmpp_2_0_co_2.xml`.

Hans von Storch, Stefan Güss, and Martin Heimann. *Das Klimasystem und seine Modellierung*. Springer, Berlin ; Heidelberg [u.a.], 1999. ISBN 3-540-65830-0 and 978-3-540-65830-6. Literaturverz. S. [239] - 247.

Hon. J.W. Strutt. Xv. on the light from the sky, its polarization and colour. *The London, Edinburgh, and Dublin Philosophical Magazine and Journal of Science*, 41(271):107–120, 274–279, 447–454, 1871. doi: 10.1080/14786447108640452. URL `https://doi.org/10.1080/14786447108640452`.

Hon. J.W. Strutt. Xxxiv. on the transmission of light through an atmosphere containing small particles in suspension, and on the origin of the blue of the sky. *The London, Edinburgh, and Dublin Philosophical Magazine and Journal of Science*, 47(287):375–384, 1899. doi: 10.1080/14786449908621276. URL `https://doi.org/10.1080/14786449908621276`.

C. J. Stubenrauch, W. B. Rossow, S. Kinne, S. Ackerman, G. Cesana, H. Chepfer, L. Di Girolamo, B. Getzewich, A. Guignard, A. Heidinger, B. C. Maddux, W. P. Menzel, P. Minnis, C. Pearl, S. Platnick, C. Poulsen, J. Riedi, S. Sun-Mack, A. Walther, D. Winker, S. Zeng, and G. Zhao. Assessment of global cloud datasets from satellites: Project

and database initiated by the gewex radiation panel. *Bulletin of the American Meteorological Society*, 94(7):1031 – 1049, 2013. doi: 10.1175/BAMS-D-12-00117.1. URL https://journals.ametsoc.org/view/journals/bams/94/7/bams-d-12-00117.1.xml.

Claudia J. Stubenrauch, Marine Bonazzola, Sofia E. Protopapadaki, and Ionela Musat. New cloud system metrics to assess bulk ice cloud schemes in a gcm. *Journal of Advances in Modeling Earth Systems*, 11(10):3212–3234, 2019. doi: https://doi.org/10.1029/2019MS001642. URL https://agupubs.onlinelibrary.wiley.com/doi/abs/10.1029/2019MS001642.

Roland Stull. *Practical Meteorology - An Algebra-based Survey of Atmospheric Science*. 2015.

R. Sussmann, A. Reichert, and M. Rettinger. The zugspitze radiative closure experiment for quantifying water vapor absorption over the terrestrial and solar infrared – part 1: Setup, uncertainty analysis, and assessment of far-infrared water vapor continuum. *Atmospheric Chemistry and Physics*, 16(18):11649–11669, 2016. doi: 10.5194/acp-16-11649-2016. URL https://acp.copernicus.org/articles/16/11649/2016/.

Ingo Sölch and Bernd Kärcher. A large-eddy model for cirrus clouds with explicit aerosol and ice microphysics and lagrangian ice particle tracking. *Quarterly Journal of the Royal Meteorological Society*, 136(653):2074–2093, 2010. doi: https://doi.org/10.1002/qj.689. URL https://rmets.onlinelibrary.wiley.com/doi/abs/10.1002/qj.689.

Jacques Testud, Stéphane Oury, Robert A. Black, Paul Amayenc, and Xiankang Dou. The concept of "normalized" distribution to describe raindrop spectra: A tool for cloud physics and cloud remote sensing. *Journal of Applied Meteorology*, 40(6):1118 – 1140, 2001. doi: 10.1175/1520-0450(2001)040<1118:TCONDT>2.0.CO;2. URL https://journals.ametsoc.org/view/journals/apme/40/6/1520-0450_2001_040_1118_tcondt_2.0.co_2.xml.

David W. J. Thompson, Sandrine Bony, and Ying Li. Thermodynamic constraint on the depth of the global tropospheric circulation. *Proceedings of the National Academy of Sciences*, 114(31):8181–8186, 2017. ISSN 0027-8424. doi: 10.1073/pnas.1620493114. URL https://www.pnas.org/content/114/31/8181.

Claire Tinel. *Restitution des propriétés microphysiques et radiatives des nuages froids et mixtes à partir des données du système RALI (radar-lidar)*. PhD thesis, Université Paris-Diderot-Paris VII, 2002.

Claire Tinel, Jacques Testud, Jacques Pelon, Robin J. Hogan, Alain Protat, Julien Delanoë, and Dominique Bouniol. The retrieval of ice-cloud properties from cloud radar and lidar synergy. *Journal of Applied Meteorology*, 44(6):860 – 875, 2005. doi: 10.1175/JAM2229.1. URL https://journals.ametsoc.org/view/journals/apme/44/6/jam2229.1.xml.

DC Tobin, FA Best, PD Brown, SA Clough, RG Dedecker, RG Ellingson, RK Garcia, HB Howell, RO Knuteson, EJ Mlawer, et al. Downwelling spectral radiance observations at the sheba ice station: Water vapor continuum measurements from 17 to 26μm. *Journal of Geophysical Research: Atmospheres*, 104(D2):2081–2092, 1999.

F. Toledo, J. Delanoë, M. Haeffelin, J.-C. Dupont, S. Jorquera, and C. Le Gac. Absolute calibration method for frequency-modulated continuous wave (fmcw) cloud radars based on corner reflectors. *Atmospheric Measurement Techniques*, 13(12):6853–6875, 2020. doi: 10.5194/amt-13-6853-2020. URL https://amt.copernicus.org/articles/13/6853/2020/.

Frederic Tridon, Alessandro Battaglia, E Luke, and P Kollias. Rain retrieval from dual-frequency radar doppler spectra: Validation and potential for a midlatitude precipitating case-study. *Quarterly Journal of the Royal Meteorological Society*, 143(704):1364–1380, 2017.

C. Tully, D. Neubauer, N. Omanovic, and U. Lohmann. Cirrus cloud thinning using a more physically-based ice microphysics scheme in the echam-ham gcm. *Atmospheric Chemistry and Physics Discussions*, 2021:1–42, 2021. doi: 10.5194/acp-2021-685. URL https://acp.copernicus.org/preprints/acp-2021-685/.

D. D. Turner. Arctic mixed-phase cloud properties from aeri lidar observations: Algorithm and results from sheba. *Journal of Applied Meteorology*, 44(4):427 – 444, 2005. doi: 10.1175/JAM2208.1. URL https://journals.ametsoc.org/view/journals/apme/44/4/jam2208.1.xml.

D. D. Turner, D. C. Tobin, S. A. Clough, P. D. Brown, R. G. Ellingson, E. J. Mlawer, R. O. Knuteson, H. E. Revercomb, T. R. Shippert, W. L. Smith, and M. W. Shephard. The qme aeri lblrtm: A closure experiment for downwelling high spectral resolution infrared radiance. *Journal of the Atmospheric Sciences*, 61(22):2657 – 2675, 2004. doi: 10.1175/JAS3300.1. URL https://journals.ametsoc.org/view/journals/atsc/61/22/jas3300.1.xml.

D. D. Turner, R. O. Knuteson, H. E. Revercomb, C. Lo, and R. G. Dedecker. Noise reduction of atmospheric emitted radiance interferometer (aeri) observations using principal component analysis. *Journal of Atmospheric and Oceanic Technology*, 23(9):1223 – 1238, 2006. doi: 10.1175/JTECH1906.1. URL https://journals.ametsoc.org/view/journals/atot/23/9/jtech1906_1.xml.

S. A. Twomey, M. Piepgrass, and T. L. Wolfe. An assessment of the impact of pollution on global cloud albedo. *Tellus B*, 36B(5):356–366, 1984. doi: https://doi.org/10.1111/j.1600-0889.1984.tb00254.x. URL https://onlinelibrary.wiley.com/doi/abs/10.1111/j.1600-0889.1984.tb00254.x.

G. Vali, P. J. DeMott, O. Möhler, and T. F. Whale. Technical note: A proposal for ice nucleation terminology. *Atmospheric Chemistry and Physics*, 15(18):10263–10270, 2015. doi: 10.5194/acp-15-10263-2015. URL https://acp.copernicus.org/articles/15/10263/2015/.

Bastiaan Van Diedenhoven and Brian Cairns. A flexible parameterization for shortwave and longwave optical properties of ice crystals and derived bulk optical properties for climate models. *Journal of the Atmospheric Sciences*, 77(4):1245–1260, 2020.

Mark A. Vaughan, Stuart A. Young, David M. Winker, Kathleen A. Powell, Ali H. Omar, Zhaoyan Liu, Yongxiang Hu, and Chris A. Hostetler. Fully automated analysis of space-based lidar data: an overview of the CALIPSO retrieval algorithms and data products. In Upendra N. Singh, editor, *Laser Radar Techniques for Atmospheric Sensing*, volume 5575, pages 16 – 30. International Society for Optics and Photonics, SPIE, 2004. doi: 10.1117/12.572024. URL https://doi.org/10.1117/12.572024.

J Verlinde, BD Zak, MD Shupe, MD Ivey, and K Stamnes. The arm north slope of alaska (nsa) sites. *Meteorological Monographs*, 57:8–1, 2016.

Thomas von Clarmann and Georg Echle. Selection of optimized microwindows for atmospheric spectroscopy. *Appl. Opt.*, 37(33):7661–7669, Nov 1998. doi: 10.1364/AO.37.007661. URL http://opg.optica.org/ao/abstract.cfm?URI=ao-37-33-7661.

B. Vonnegut. The nucleation of ice formation by silver iodide. *Journal of Applied Physics*, 18 (7):593–595, 1947. doi: 10.1063/1.1697813. URL https://doi.org/10.1063/1.1697813.

John M. Wallace and Peter Victor Hobbs. *Atmospheric science*. Number ARRAY(0x561771633b20) in International geophysics series. Academic Press, Amsterdam ; Heidelberg [u.a.], 2. ed. edition, 2006. ISBN 0-12-732951-X and 978-0-12-732951-2.

Ulla Wandinger. Multiple-scattering influence on extinction-and backscatter-coefficient measurements with raman and high-spectral-resolution lidars. *Applied optics*, 37(3):417–427, 1998.

C. Wang, S. Platnick, K. Meyer, Z. Zhang, and Y. Zhou. A machine-learning-based cloud detection and thermodynamic-phase classification algorithm using passive spectral observations. *Atmospheric Measurement Techniques*, 13(5):2257–2277, 2020. doi: 10.5194/amt-13-2257-2020. URL https://amt.copernicus.org/articles/13/2257/2020/.

Lian-Ping Wang, Bogdan Rosa, Hui Gao, Guowei He, and Guodong Jin. Turbulent collision of inertial particles: Point-particle based, hybrid simulations and beyond. *International Journal of Multiphase Flow*, 35(9):854–867, 2009. ISSN 0301-9322. doi: https://doi.org/10.1016/j.ijmultiphaseflow.2009.02.012. URL https://www.sciencedirect.com/science/article/pii/S030193220900024X. Special Issue: Point-Particle Model for Disperse Turbulent Flows.

Zhenzhu Wang, VA Shishko, AV Konoshonkin, NV Kustova, AG Borovoi, GG Matvienko, Chenbo Xie, Dong Liu, and Yingjian Wang. The study of cirrus clouds with the polarization lidar in the south-east china (hefei). *Atmospheric and Oceanic Optics*, 30:234–235, 2017.

Zhien Wang and Kenneth Sassen. Cloud type and macrophysical property retrieval using multiple remote sensors. *Journal of Applied Meteorology*, 40(10):1665 – 1682, 2001. doi: 10.1175/1520-0450(2001)040<1665:CTAMPR>2.0.CO;2. URL https://journals.ametsoc.org/view/journals/apme/40/10/1520-0450_2001_040_1665_ctampr_2.0.co_2.xml.

Stephen G. Warren and Richard E. Brandt. Optical constants of ice from the ultraviolet to the microwave: A revised compilation. *Journal of Geophysical Research: Atmospheres*, 113(D14), 2008. doi: https://doi.org/10.1029/2007JD009744. URL https://agupubs.onlinelibrary.wiley.com/doi/abs/10.1029/2007JD009744.

Alfred Wegener. *Thermodynamik der Atmosphaäre*. Leipzig: Verlag Von Johann Ambrosius Barth, 1911.

J. A. Weinman. Effects of multiple scattering on light pulses reflected by turbid atmospheres. *Journal of Atmospheric Sciences*, 33(9):1763 – 1771, 1976. doi: 10.1175/1520-0469(1976)033<1763:EOMSOL>2.0.CO;2. URL https://journals.ametsoc.org/view/journals/atsc/33/9/1520-0469_1976_033_1763_eomsol_2_0_co_2.xml.

Claus Weitkamp. *Lidar: range-resolved optical remote sensing of the atmosphere*, volume 102. Springer Science & Business, 2006.

M. Wiegner, F. Madonna, I. Binietoglou, R. Forkel, J. Gasteiger, A. Geiß, G. Pappalardo, K. Schäfer, and W. Thomas. What is the benefit of ceilometers for aerosol remote sensing? an answer from earlinet. *Atmospheric Measurement Techniques*, 7(7):1979–1997, 2014. doi: 10.5194/amt-7-1979-2014. URL https://amt.copernicus.org/articles/7/1979/2014/.

Matthias Wiegner. *Lidarvorlesung - Sommersemester 2017*. 2017.

Matthias Wiegner. personal communication, 2018.

Wikipedia contributors. Atmospheric window — Wikipedia, the free encyclopedia, 2022. URL https://en.wikipedia.org/w/index.php?title=Atmospheric_window&oldid=1066283486. [Online; accessed 20-January-2022].

M. Wirth, A. Fix, P. Mahnke, H. Schwarzer, F. Schrandt, and G. Ehret. The airborne multi-wavelength water vapor differential absorption lidar wales: system design and performance. *Applied Physics B*, 96(1):201, Feb 2009. ISSN 1432-0649. doi: 10.1007/s00340-009-3365-7. URL https://doi.org/10.1007/s00340-009-3365-7.

WMO. *International Cloud Atlas - Manual on the observation of clouds and other meteors*, volume 407. World Meteorological Organization, 2017.

Thomas Wriedt. Light scattering theories and computer codes. *Journal of Quantitative Spectroscopy and Radiative Transfer*, 110(11):833–843, 2009. ISSN 0022-4073. doi: https://doi.org/10.1016/j.jqsrt.2009.02.023. URL https://www.sciencedirect.com/science/article/pii/S0022407309000831. Light Scattering: Mie and More Commemorating 100 years of Mie's 1908 publication.

Klaus Wyser and Ping Yang. Average ice crystal size and bulk short-wave single-scattering properties of cirrus clouds. *Atmospheric research*, 49(4):315–335, 1998.

P. Yang, K. N. Liou, K. Wyser, and D. Mitchell. Parameterization of the scattering and absorption properties of individual ice crystals. *J. Geophys. Res.*, 105:4699–4718, 2000.

Ping Yang, Si-Chee Tsay, Heli Wei, Guang Guo, and Qiang Ji. Remote sensing of cirrus optical and microphysical properties from ground-based infrared radiometric measurements-part i: a new retrieval method based on microwindow spectral signature. *IEEE Geoscience and Remote Sensing Letters*, 2(2):128–131, 2005a. doi: 10.1109/LGRS.2005.844733.

Ping Yang, Heli Wei, Hung-Lung Huang, Bryan A. Baum, Yong X. Hu, George W. Kattawar, Michael I. Mishchenko, and Qiang Fu. Scattering and absorption property database for nonspherical ice particles in the near- through far-infrared spectral region. *Appl. Opt.*, 44(26):5512–5523, Sep 2005b. doi: 10.1364/AO.44.005512. URL http://opg.optica.org/ao/abstract.cfm?URI=ao-44-26-5512.

Ping Yang, Lei Bi, Bryan A. Baum, Kuo-Nan Liou, George W. Kattawar, Michael I. Mishchenko, and Benjamin Cole. Spectrally consistent scattering, absorption, and polarization properties of atmospheric ice crystals at wavelengths from 0.2 to 100 μm. *Journal of the Atmospheric Sciences*, 70(1):330 – 347, 2013. doi: 10.1175/JAS-D-12-039.1. URL https://journals.ametsoc.org/view/journals/atsc/70/1/jas-d-12-039.1.xml.

Ping Yang, Souichiro Hioki, Masanori Saito, Chia-Pang Kuo, Bryan A. Baum, and Kuo-Nan Liou. A review of ice cloud optical property models for passive satellite remote sensing, 2018. ISSN 2073-4433. URL https://doi.org/10.3390/atmos9120499.

Bingqi Yi, Anita D. Rapp, Ping Yang, Bryan A. Baum, and Michael D. King. A comparison of aqua modis ice and liquid water cloud physical and optical properties between collection 6 and collection 5.1: Cloud radiative effects. *Journal of Geophysical Research: Atmospheres*, 122(8):4550–4564, 2017. doi: https://doi.org/10.1002/2016JD025654. URL https://agupubs.onlinelibrary.wiley.com/doi/abs/10.1002/2016JD025654.

John E. Yorks, Patrick A. Selmer, Andrew Kupchock, Edward P. Nowottnick, Kenneth E. Christian, Daniel Rusinek, Natasha Dacic, and Matthew J. McGill. Aerosol and cloud detection using machine learning algorithms and space-based lidar data. *Atmosphere*, 12 (5), 2021. ISSN 2073-4433. doi: 10.3390/atmos12050606. URL https://www.mdpi.com/2073-4433/12/5/606.

Qing Yue, K. N. Liou, S. C. Ou, B. H. Kahn, P. Yang, and G. G. Mace. Interpretation of airs data in thin cirrus atmospheres based on a fast radiative transfer model. *Journal of the Atmospheric Sciences*, 64(11):3827 – 3842, 2007. doi: 10.1175/2007JAS2043.1. URL https://journals.ametsoc.org/view/journals/atsc/64/11/2007jas2043.1.xml.

Mark D. Zelinka, Stephen A. Klein, and Dennis L. Hartmann. Computing and partitioning cloud feedbacks using cloud property histograms. part ii: Attribution to changes in cloud amount, altitude, and optical depth. *Journal of Climate*, 25(11):3736 – 3754, 2012. doi: 10.1175/JCLI-D-11-00249.1. URL https://journals.ametsoc.org/view/journals/clim/25/11/jcli-d-11-00249.1.xml.

Yinchao Zhang, Su Chen, Wangshu Tan, Siying Chen, He Chen, Pan Guo, Zhuoran Sun, Rui Hu, Qingyue Xu, Mengwei Zhang, et al. Retrieval of water cloud optical and microphysical properties from combined multiwavelength lidar and radar data. *Remote Sensing*, 13(21): 4396, 2021.

C. Zhou, A. E. Dessler, M. D. Zelinka, P. Yang, and T. Wang. Cirrus feedback on interannual climate fluctuations. *Geophysical Research Letters*, 41(24):9166–9173, 2014. doi: https://doi.org/10.1002/2014GL062095. URL https://agupubs.onlinelibrary.wiley.com/doi/abs/10.1002/2014GL062095.

Yongbo Zhou, Xuejin Sun, Tero Mielonen, Haoran Li, Riwei Zhang, Yan Li, and Chuanliang Zhang. Cirrus cloud optical thickness and effective diameter retrieved by modis: Impacts of single habit assumption, 3-d radiative effects, and cloud inhomogeneity. *Journal of Geophysical Research: Atmospheres*, 123(2):1195–1210, 2018. doi: https://doi.org/10.1002/2017JD027232. URL https://agupubs.onlinelibrary.wiley.com/doi/abs/10.1002/2017JD027232.

Acknowledgements

Working on such an interesting, stimulating and challenging interdisciplinary research topic would not be possible without outstanding support and assistance from a large number of people, and I wish to express my deepest thanks to them with these final lines.

For giving me this interesting topic, fruitful discussions and the possibility to present my work at conferences, I want to thank

- Prof. Dr. Bernhard Mayer.

For writing the second review for this thesis, I want to thank

- Prof. Dr. Markus Rapp.

For careful proofreading and productive comments on this thesis, I want to thank

- Dr. Rianne Lous,
- Dr. Tobias Kölling,
- Dr. Adrian Walser and
- Dr. Tobias Zinner.

For sharing his great enthusiasm and wide range of expertise in signal processing, scientific computation and software development patterns, I want to thank

- Dr. Tobias Kölling.

For supplying the data, I want to thank

- Dr. Matthias Wiegner (Ceilometer UFS),
- Dr. Martin Hagen (MIRA-36 UFS),
- Dr. Ralf Sussmann, Markus Rettinger (AERI Mount Zugspitze),
- Dr. Silke Gross and Dr. Florian Ewald (NARVAL-I).

For scientific support and fruitful discussions, I want to thank

- Dr. Tobias Zinner,
- Dr. Tobias Kölling,
- Dr. Claudia Emde,
- Dr. Matthias Wiegner,

- Dr. Volker Freudenthaler,
- Dr. Adrian Walser and
- Dr. Josef Gasteiger.

For technical and IT support, I want to thank

- Dr. Robert Redl and
- Heinz Lößlein.

For organisational support, I want to thank

- Barbara Baumann,
- Markus Garhammer and
- Dr. Audine Laurian.

For funding this thesis as part of the Virtual Alpine Observatory project (VAO), I want to thank

- Bayerische Forschungsallianz GmbH (BayFOR).

The greatest thanks I owe, and I want to deeply express here goes to my family, especially my parents. Their continuous support, love and encouragement has always been an invaluable gift throughout my whole life. I feel deep gratitude for my girlfriend's empathy, time and company, her mental support carried me through some phases. Furthermore, I am very thankful for all my friends, for sharing countless great conversations, laughs and sporting activities apart from working on this project.